# SIMULATING THE CHEMICAL ENRICHMENT OF THE INTERGALACTIC MEDIUM

# SIMULATING THE CHEMICAL ENRICHMENT OF THE INTERGALACTIC MEDIUM

Proefschrift

ter verkrijging van
de graad van Doctor aan de Universiteit Leiden,
op gezag van de Rector Magnificus prof. mr. P.F. van der Heijden,
volgens besluit van het College voor Promoties
te verdedigen op woensdag 22 september 2010
te klokke 15.00 uur

door

Robert P.C. Wiersma

geboren te Collingwood in 1978

Promotiecommissie

Promotor: Prof. dr. Tim de Zeeuw

Co-promotor: Dr. J. Schaye

Overige leden: Dr. J. Brinchman
Prof. dr. S. Portegies Zwart
Prof. dr. K. Kuijken
Dr. T. Theuns (Durham University)
Prof. dr. E. Tolstoy (Rijksuniversiteit Groningen)

*The heavens proclaim the glory of God.*
*The skies display his craftsmanship.*
PSALM 19:1, NLT

# Contents

# CHAPTER 1

# Introduction

IN this chapter we introduce the basic concepts used in this thesis. We give a brief overview of structure formation theory, stressing the importance of baryonic physics. Chemical evolution models - beginning with simple analytic but moving on to numeric models - are described and their strengths and weaknesses discussed. Having established a context, the contents of this thesis are outlined, briefly describing the contents and findings of each chapter. We conclude by considering the outlook for the field.

For over one hundred years now astronomers have been able to study the universe on the largest scales. Recently, this field has become particularly exciting as we have entered an era of 'precision cosmology'. Due in large part to the very detailed mapping of the sky in the microwave band (e.g., *COBE*[1], *WMAP*[2]) and wide field extragalactic surveys such as the *Sloan Digital Sky Survey (SDSS)*[3], a solid understanding of large scale structure in the universe can be obtained. On the other hand, sophisticated computer simulations of the universe such as the *Millennium Simulation*[4] have yielded a number of clues as to how this structure formed. Both of these aspects of research in this area have benefited greatly from recent technological advancements that have only now made these projects possible.

These developments have been built upon a solid foundation of cosmological theory that emerged in the first half of the twentieth century. The starting point of this theory is the Cosmological Principle, which assumes that the Universe is homogeneous and isotropic. This principle appears to be true on the very largest scales.

Given the Cosmological Principle, Einstein's equations of General Relativity can be solved for a fluid with energy density $\rho c^2$ and pressure $p$. This solution is typically written in the form of the Friedmann equations:

$$\ddot{a} + \frac{4}{3}\pi G\left(p + \frac{3\rho}{c^2}\right)a = 0, \tag{1.1}$$

$$\dot{a}^2 + Kc^2 - \frac{8}{3}\pi G\rho a^2 = 0, \tag{1.2}$$

where $G$ is the gravitational constant, $K$ is the curvature of space-time, and $a$ is the expansion factor of the Universe (we have used a dot to indicate a derivative with respect to proper time). The expansion factor is a parameter that relates comoving distances to proper distances measured at the present day viz. $d_p = ad_c$. The expansion factor is also used to define the Hubble parameter: $H \equiv \dot{a}/a$.

Observations over the past decade have shown that the universe is remarkably close to, if not completely flat (e.g. Spergel et al. 2007). In this case, the equations simplify slightly as the curvature $K$ is zero. The matter-energy density of the universe can then be written as:

$$\rho_m = \rho_{\mathrm{crit}} = \frac{3H^2}{8\pi G}. \tag{1.3}$$

One can then predict the growth of structures from primordial fluctuations in the linear regime (typically referred to as linear theory). Considering only gravity, a matter density perturbation in an expanding universe is governed by:

$$\ddot{\delta} + 2H\dot{\delta} - \frac{3}{2}\Omega H^2\delta = 0, \tag{1.4}$$

where $\delta$ is the magnitude of the density perturbation and $\Omega$ is the ratio of the density to the critical density of the universe. This formalism breaks down if $\delta$ is significant

---

[1] http://lambda.gsfc.nasa.gov/product/cobe/

[2] http://map.gsfc.nasa.gov/

[3] http://www.sdss.org/

[4] http://www.mpa-garching.mpg.de/galform/millennium/

compared to unity, at which point more sophisticated modelling is required, often in the form of computer simulations. Note that structures of interest to most astronomers (galaxies, clusters of galaxies, etc.) are highly non-linear.

As such models became more sophisticated, astronomers soon became aware that the budget of matter in the universe is dominated by some unseen form, called 'dark matter'. Although other explanations exist (e.g., Modified Newtonian Dynamics - MOND), dark matter provides a solution on a wide range of scales, accounting for structure formation as well as galactic rotation curves. Since dark matter is so dominant, much work has been done with exclusively dark matter simulations.

These simulations have been very instructive, describing the hierarchical nature of structure formation. In this picture, haloes are assembled via mergers of smaller haloes rather than a monolithic collapse. The resulting correlation functions and halo statistics from such simulations match well with the observed distribution of matter on large scales[5].

To gain further insight, we must however move beyond the collapse of matter into haloes by gravity. While dark matter is thought to feel only gravity, the baryons (which in most cases are visible) in the universe can interact using other forces as well and are what is directly observed by astronomers. These baryons collapse into galaxies hosted by dark matter haloes, a process that involves a great deal of physical processes, including but not limited to hydrodynamics, gas heating and cooling, star formation, radiative, mechanical, and chemical[6] feedback from stars, and feedback from active galactic nuclei (AGN). The task in interpreting extra-galactic observations beyond the large-scale distribution of matter then becomes increasingly complicated.

To first order, structure formation is a competition between gravitational collapse and kinetic energy. When considering the collapse of dark matter haloes, one can simply apply the virial theorem:

$$2K = -U, \tag{1.5}$$

where $K$ and $U$ represent the total kinetic and potential energy of the system respectively. A halo will then typically collapse to fulfill this condition.

Since a gas cloud contains pressure forces, this is not the only condition that dictates how baryonic structures form. Under solely adiabatic conditions, the increasing thermal velocity dispersion of a collapsing cloud will at some point halt its formation. By equating the free-fall timescale ($t_{\rm ff} \simeq 1/\sqrt{G\rho}$, where $\rho$ is the mean density of the medium and $G$ is the gravitational constant) and the sound crossing timescale ($t_{\rm sc} \simeq L/c_{\rm s}$, where $L$ is the mean diameter of the cloud, and $c_{\rm s}$ is the sound speed of the medium) we can arrive at the Jeans length, $L_{\rm J}$:

$$L_{\rm J} \simeq \frac{c_{\rm s}}{\sqrt{G\rho}}. \tag{1.6}$$

---

[5] Note that such simulations predict the large scale distribution of the dark matter - the connection to observable, visible matter is made via a halo population model.

[6] Note that here and throughout this thesis, we have use the word 'chemical' somewhat loosely since we are referring to nucleosynthesis and redistribution of elements, ignoring almost entirely chemical reactions between atoms and molecules.

Given a spherical cloud, this can be converted into a mass:

$$M_{\rm J} \simeq \frac{c_{\rm S}^3}{G^{3/2}\rho^{1/2}}, \tag{1.7}$$

above which a concentration of matter can collapse under the forces of gravity or fragment and below which said concentration will reach equilibrium by either expanding or evaporating.

The energy that is used to support the system can be radiated away via cooling. In this way we introduce another timescale, the cooling time:

$$t_{\rm cool} \equiv \frac{T}{dT/dt} \propto \frac{\rho T}{\Lambda}, \tag{1.8}$$

where $\Lambda$ is the radiative cooling rate per unit volume. We can then consider three regimes: The first is where $t_{\rm cool} > t_H$, the Hubble time, defined as $1/H$, or roughly the age of the universe. In this regime, objects stay at the Jeans mass and evolve neither in density or temperature. For $t_{\rm ff} < t_{\rm cool} < t_H$, the gas can adjust itself in reaction to the cooling. In this case, an object undergoes a steady, monolithic collapse on a timescale of $t_{\rm cool}$. Finally, when $t_{\rm cool} < t_{\rm ff} < t_H$, the gas cannot adjust itself and collapses on a free-fall timescale. Such a cloud can fragment to form substructures which themselves would be subject to their own timescales.

There are currently two approaches to the modelling of baryonic physics in galaxy formation. One is semi-analytical modelling, which typically employs existing dark matter simulations[7] and uses numerical prescriptions for the various physical processes occurring at a given time. Such prescriptions are often physically motivated, with the uncertainties quantified using free parameters. The entire model is then tuned to match observations of the local universe. This method has its advantages and has had many successes (e.g., Kauffmann et al. 1993; Somerville & Primack 1999; Croton et al. 2006) over the past two decades. There are two main disadvantages to this method however. One problem is that such models tend to involve many free parameters, making interpretation troublesome (is a given effect real, or could another arbitrary set of parameters reproduce it?). Perhaps more important is that semi-analytical models incorporate highly simplified aspects of the physics involved in galaxy formation. For instance, rather than modeling haloes as intersections in the cosmic web, these models assume that haloes are spherically symmetric. This often results in the absence of crucial processes, such as accretion of cold gas in the form of filaments.

Another way to model the physics of baryons is to perform hydrodynamical simulations. Unfortunately, introducing baryonic physics into fully numerical simulations is far from straightforward. One must always be conscious of possible resolution effects as well as the limitations of the implementation of a given physical recipe. It is often necessary to concede one's ability to directly resolve a process and to use a so-called 'sub-grid' recipe to simulate the effects of said process on a larger scale. For example, current cosmological simulations can at best resolve objects of gas mass $\sim 10^5~{\rm M}_\odot$. The

---

[7] Although halo mass functions (e.g., Press-Schechter formalism) and Monte-Carlo merging are also sometimes employed.

formation of a star takes place on scales many orders of magnitude below that, say $\sim 1\ \mathrm{M}_\odot$. As a result of this discrepancy in scales, simulations must invoke some law that approximates star formation on galactic scales without introducing some bias.

These processes often feed back into other processes as well as into structure formation. Ionizing photons from star formation, for instance, can inhibit further structure formation by heating the surrounding gas, thereby changing the typical mass of a collapsed object (e.g., Shapiro et al. 1994; Gnedin & Hui 1998). Other forms of feedback include energy and chemical feedback from supernovae and stellar winds.

Chemical feedback plays a prominent role in astrophysical studies on a wide range of scales. Despite the fact that 'metals' (elements heavier than helium) have abundances more than an order of magnitude lower than hydrogen and helium, they can profoundly influence objects ranging from protostars to galaxy clusters. A large amount of work, both theoretical and observational has been done in order to investigate the causes and the effects of chemical feedback (see for example table 3.5). Metals can act as tracers for various processes, as well as enrich gas clouds and impact their cooling (Sutherland & Dopita 1993), which in turn determine the timescale on which structures can form.

Metal production occurs during a large part of the history of the universe. After the Big Bang produced trace amounts of lithium and other light elements, there was a gap until the first stars formed. From then on, stars, supernovae, and exotic events such as neutron star mergers contributed to the enrichment of the almost pristine hydrogen and helium mix in the Universe.

These metals can indicate how star formation occurred, and as such can yield clues to the assembly of galaxies and clusters, fundamental questions deeply important to our understanding of the universe. We must therefore understand how metals are created, transported and how various quantities can give us information about the state of the system.

## 1.1 'SIMPLE' MODELS

### 1.1.1 Purely Analytical Calculations

The idea of studying the chemical evolution of the universe is by no means new. Once astronomers realised that heavy elements are produced in stars, they could use analytic formulations to account for the current metal distribution. This involves some assumptions about the star formation rate/efficiency as well as the yield of such stars, but can provide some insight as to the nature of the enriched gas. The following treatment draws on Binney & Merrifield (1998).

#### The Closed Box

First considered by Talbot & Arnett (1971), the closed box model considers a system where no gas enters or leaves the system, but is recycled for new stars to be born. As galaxies are known to generate super-winds and have gas accreted from filaments, it serves only as a toy model when applied to them. Galaxy clusters however, retain a large fraction of their gas and are reasonably well approximated by such a model. Naturally, the Universe as a whole is a truly a closed box. On the other hand, in both of these instances the instantaneous mixing approximation is unlikely to be valid.

In addition to the assumption of a closed box, we also make two more assumptions: the instantaneous mixing approximation and the instantaneous recycling approximation. The former simply means that the gas is always well mixed, while the latter means that stars that pollute the ISM do so immediately (i.e., the stellar lifetimes are zero).

We begin by considering a mass of gas $M_g$, with metal mass $M_Z$ such that the metallicity is:

$$Z_g = M_Z/M_g. \tag{1.9}$$

Our total stellar mass $M_*$ increases by $\Delta' M_*$ in some time interval. Let us consider $\Delta M_*$, the amount of mass converted into stars *that stays in stars*, that is after stellar mass loss has been accounted for. Since the metal mass that is ejected is some constant fraction of $\Delta' M_*$ and $\Delta M_*$ will also be some constant factor times $\Delta' M_*$, we may denote the amount of heavy elements ejected as $y\Delta M_*$ (i.e., proportional to the amount that stays in stars) and we call $y$ the yield. Thus the change in the gas phase metal mass in some time interval is just the amount of metals locked up in stars in that interval subtracted from the metal mass ejected in that interval:

$$\Delta M_Z = y\Delta M_* - Z\Delta M_* = (y - Z_g)\Delta M_*. \tag{1.10}$$

What we usually want to know is the metallicity, which changes as:

$$\Delta Z_g = \Delta\left(\frac{M_Z}{M_g}\right) = \frac{\Delta M_Z}{M_g} - \frac{M_Z}{M_g^2}\Delta M_g = \frac{1}{M_g}\left(\Delta M_Z - Z_g \Delta M_g\right). \tag{1.11}$$

Since mass is approximately[8] conserved, $\Delta M_* = -\Delta M_g$ this works out to

$$\Delta Z_g = \frac{1}{M_g}\left(\Delta M_Z - Z_g\Delta M_g\right) = \frac{1}{M_g}\left(-(y - Z_g)\Delta M_g - Z_g \Delta M_g\right) = -y\frac{\Delta M_g}{M_g}. \tag{1.12}$$

If we integrate over time, imposing that all of the mass is initially in metal-free gas, we get:

$$Z_g(t) = -y \ln\left(\frac{M_g(t)}{M_g(0)}\right) = -y \ln f_g, \tag{1.13}$$

where $f_g$ is the gas fraction (we show $Z_g$ as a function of $f_g$ in figure 1.1). Since $Z_g$ and $f_g$ are observables, it is sometimes convenient to define an *effective yield*:

$$y_{\mathit{eff}} \equiv -\frac{Z_g(t)}{\ln f_g}. \tag{1.14}$$

---

[8] Nuclear fusion converts some mass into energy, but the amount of mass that is converted negligible in this argument.

### The Leaky Box

A number of processes can cause mass loss from a bound system, such as, winds produced by supernovae and massive stars as well as AGN. This happens for example in starburst environments where a large fraction of the gas is driven out by high mass, short lived stars. If the amount of mass that is expelled is proportional to the star formation rate, we can write:

$$\dot{M}_{\rm tot} = -\alpha \dot{M}_{*}. \tag{1.15}$$

Thus, at any time, $M_{\rm tot}(t) = M_{\rm tot}(0) - \alpha M_{*}(t)$. The implication for the gas mass is clear:

$$M_g(t) = M_{\rm tot}(t) - M_{*}(t) = M_{\rm tot}(0) - (1+\alpha)M_{*}(t). \tag{1.16}$$

We can proceed from equation 1.11 if we combine $\Delta M_{*} + \Delta M_g + \alpha\Delta' M_{*} = 0$ with the assumption that the expelled gas is of the same metallicity: $\Delta M_Z = y\Delta M_{*} - Z_g \Delta M_{*} - \alpha Z_g \Delta' M_{*}$.

$$\begin{aligned} \Delta Z_g &= \frac{1}{M_g}\left(y\Delta M_{*} - Z_g\Delta M_{*} - \alpha Z_g \Delta' M_{*} - Z_g(-\Delta M_{*} - \alpha\Delta' M_{*})\right) && (1.17) \\ \frac{dZ_g}{dM_{*}} &= \frac{y}{M_g} = \frac{y}{M_{\rm tot}(0) - (1+\alpha)M_{*}(t)}. && (1.18) \end{aligned}$$

Integrating this we get:

$$Z_g(t) = -\frac{y}{1+\alpha}\left\{\ln\left[M_{\rm tot}(0) - (1+\alpha)M_{*}(t)\right] - \ln\left[M_{\rm tot}(0) - (1+\alpha)M_{*}(0)\right]\right\}. \tag{1.19}$$

Assuming the initial composition is gas ($M_{\rm tot}(0) = M_g(0), M_{*}(0) = 0$)

$$Z_g(t) = -\frac{y}{1+\alpha}\ln\left[\frac{M_{\rm tot}(0) - (1+\alpha)M_{*}(t)}{M_{\rm tot}(0)}\right], \tag{1.20}$$

which can be combined with the integral form of equation 1.15 ($M_{\rm tot}(t) = M_{\rm tot}(0) - \alpha M_{*}(t)$):

$$\begin{aligned} Z_g(t) &= -\frac{y}{1+\alpha}\ln\left[\frac{M_{\rm tot}(t) - M_{*}(t)}{M_{\rm tot}(0)}\right] && (1.21) \\ &= -\frac{y}{1+\alpha}\ln\left[\frac{M_g(t)}{M_g(0)}\right]. && (1.22) \end{aligned}$$

This reduces to equation 1.13 when $\alpha = 0$. Shown in figure 1.1 is the behaviour of the metallicity as a function of consumed/expelled gas. Note that the increase of outflow strength has a similar effect as decreasing the stellar yield.

### The Accreting Box

Galaxies do not only expel mass, they build up through gas accretion. Here we neglect outflows and assume that the inflowing gas has a metallicity of 0. Since the infalling gas can either be turned into stars or left as gas, we have:

$$\Delta M_{\rm tot} = \Delta M_{*} + \Delta M_g. \tag{1.23}$$

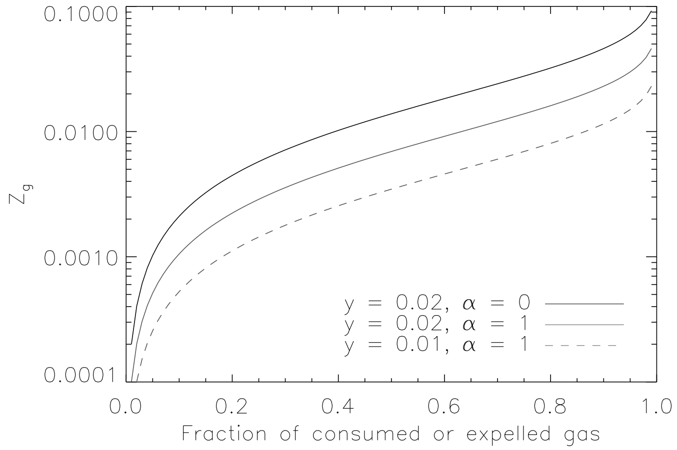

**Figure 1.1**: Gas Metallicity as a function of consumed/expelled gas for a closed box model (solid black), a leaky box model (solid grey), and a leaky box model with a lower yield (dashed grey). Note that the x axis corresponds to the stellar mass fraction for the closed box model only.

We can combine equations 1.23 and 1.10 with equation 1.11, giving:

$$\Delta Z_g = \frac{1}{M_g}\left[(y - Z_g)(\Delta M_{\rm tot} - \Delta M_g) - Z_g \Delta M_g\right], \tag{1.24}$$

$$= \frac{1}{M_g}\left[(y - Z_g)\Delta M_{\rm tot} - y\Delta M_g\right], \tag{1.25}$$

and dividing by $\Delta M_{\rm tot}$ and switching to differentials yields:

$$\frac{dZ_g}{dM_{\rm tot}} = \frac{1}{M_g}\left[y - Z_g - y\frac{dM_g}{dM_{\rm tot}}\right]. \tag{1.26}$$

If we now let $u = \int \frac{dM_{\rm tot}}{M_g}$, the above equation becomes

$$\frac{dZ_g}{du} + Z_g = y\left(1 - \frac{d\ln M_g}{du}\right), \tag{1.27}$$

whose solution is:

$$Z_g = y\left(1 - Ce^{-u} - e^{-u}\int_0^u e^{u'}\frac{d\ln M_g}{du'}\right). \tag{1.28}$$

In the case that the accretion rate plus the gas return rate is equal to the star formation rate (i.e., $\Delta M_g = 0$) we can return to equation 1.26:

$$dM_{\rm tot} = M_g\left(\frac{1}{y - Z_g}\right)dZ_g. \tag{1.29}$$

Integrating and assuming that the system is initially composed of metal-free gas ($Z_g(0) = 0$ and $M_{\rm tot}(0) = M_g(0)$):

$$\frac{M_{\rm tot}}{M_g} - 1 = \ln\frac{y}{y - Z_g}, \tag{1.30}$$

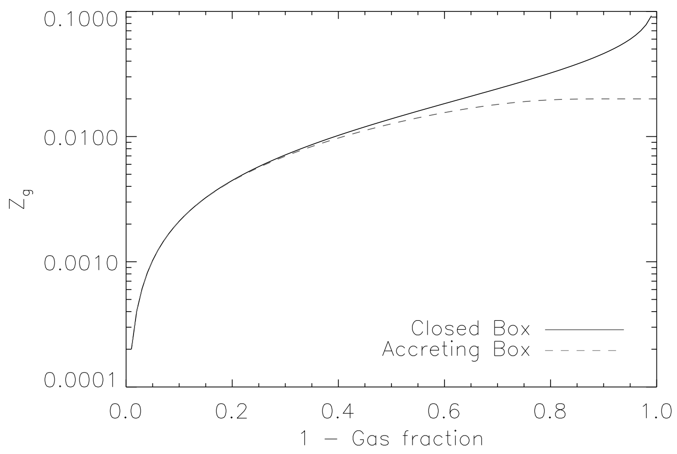

**Figure 1.2**: Gas Metallicity as a function of stellar fraction for a closed box model (solid black) and an accreting box model (dashed grey)

which becomes,

$$Z_g = y\left[1 - exp\left(1 - \frac{M_{\rm tot}}{M_g}\right)\right]. \tag{1.31}$$

As figure 1.2 shows, $Z_g$ asymptotes to $y$ for small gas fractions.

We present these models to guide the reader through the established framework in this field. We find however, the assumptions to be too restrictive, so we leave the analytic models behind while keeping in mind some of the limits and relations expressed here.

### 1.1.2 Numerical Calculations

If we wish to relax the instantaneous recycling approximation or consider the yields of stars of different masses/metallicities, we almost certainly need to turn to numerical methods. With a simple numerical model one can feed the chemical makeup of the recently enriched gas back into the stellar evolution of newly formed stars. Since stars of different masses lose their mass on different timescales, considering said timescales is very important when attempting to model the chemical evolution of a system.

The chemical makeup of the ejecta from a star is strongly dependent on mass. Massive stars ($M \gtrsim 8 \mathrm{M}_\odot$), for instance, experience a phase of strong mass loss before ending their lives as type II (core-collapse) supernova (SNII) explosions. Such explosions occur when the energy from nuclear reactions at the star's core can no longer support the weight of the star. The outer layers collapse onto the core until electron degeneracy pressure forces the collapsing material to 'bounce' back. In general, the contributions of massive stars to cosmic pollution are mainly in the form of so-called alpha elements, such as oxygen, neon, magnesium, and silicon.

Intermediate mass stars ($0.8\ \mathrm{M}_\odot \lesssim M \lesssim 8\ \mathrm{M}_\odot$) contribute to chemical enrichment in two ways: as asymptotal giant branch (AGB) stars and type Ia supernova (SNIa). After a main sequence star has completely burned the hydrogen in its core, the star's core begins to contract while the outer layers expand as they cool. These stars are on the red giant branch (RGB) in the Hertzsprung—Russell (HR) diagram of luminosity and temperature. When the temperature at the core of the star is high enough, helium begins to be the primary source of nuclear fusion, stalling a star's progress up the giant branch. When the helium core is exhausted, the star's envelope begins to expand again in a similar fashion to the RGB phase. The star takes a path in the HR diagram that *asymptotes* to the RGB. The instabilities resulting from hydrogen and helium burning in shells around the core, the majority of the star's mass may be lost in the AGB phase (see Herwig 2005, for an excellent review of AGB stellar evolution). This mass loss is rich in helium, carbon, and nitrogen.

Following this period of mass loss, the core (composed of mainly carbon and oxygen) of the star will be left to cool down in what is known as the white dwarf phase. During this phase, the star remains relatively inactive unless it comes into contact with another star. A merger (typically as a result of binary stellar evolution), that puts the object above the Chandrasekhar mass ($\sim 1.38\mathrm{M}_{\odot}$) will cause runaway nuclear fusion. This results because the star uses electron degeneracy pressure to support itself and does not use thermal pressure to respond to increases in temperature and therefore cannot add more pressure to counteract the heat generated from the nuclear activity. Eventually, the energy from nuclear reactions will unbind the star, resulting in what is called a type Ia supernova. The ejecta from this explosion are heavily enriched in metals, in particular iron.

Since the amount of time that stars spend on the main sequence is significant compared to the star formation timescale, it is useful to define the stellar lifetime, $\tau(M)$, as the time from stellar birth until the point at which the star leaves the main sequence. Because gravity is able to hasten the evolution of a star, its lifetime is a monotonically decreasing function of mass. The result is that high mass stars end their lives relatively quickly, while low mass stars can live for billions of years. Note that this discussion ignores the time from when a star leaves the main sequence to when it loses most of its mass (as either a SNII or an AGB star). The duration of this period is negligible with respect to the other timescales discussed here.

Type Ia supernovae, on the other hand, occur in evolved stellar systems (i.e., after one or more of the stars is already 'dead'). For SNIa, a separate rate function must be calculated since its occurrence is governed by binary as well as stellar evolution. Typically these supernovae occur over a long period of time.

Since we now have the power to follow different elements (since they are created by different processes), we must redefine the term 'yield' slightly. Recall that earlier we defined the yield $y$, as the metal mass ejected divided by the amount of amount of mass remaining in stars. We now use yield to refer to the elemental mass ejected from a star of a given mass and metallicity. That is, for a given stellar mass and metallicity we specify the abundance of a given element leaving the star. While this prevents us from presenting a neat analytical solution, our analysis becomes significantly more versatile.

The details of our numerical model are as follows. We begin with a reservoir of gas with arbitrary metallicity. During a given timestep $t_i + \Delta t$, we lock a certain amount of mass into stars based on a prescribed star formation rate. These stars have the metallicity of the gas out of which they formed. We then integrate the contributions from each stellar population formed in preceding timesteps (i.e., from $t = 0$ to $t = t_i$) based on the characteristics (mass, metal content) of the stars born at that timestep. To do this, we convert time into mass using the lifetime function, then look up in yield tables the corresponding asymptotic giant branch star, supernova type II, and supernova type Ia yields. This can be written in equation form (as in chapter 3) to show the mass expelled by stars $\Delta m_*$ during a single time step $(t_i, t_i + \Delta t)$ by a stellar population of initial mass $m_{*,0}$ and metallicity $Z$ that was created at time $t_* < t_i$:

$$\begin{aligned} \Delta m_* &= m_*(t_i) - m_*(t_i + \Delta t) && (1.32) \\ &= m_{*,0} \int_{M_Z(t_i - t_* + \Delta t)}^{M_Z(t_i - t_*)} \Phi(M) m_{\rm ej}(M, Z)\, dM, && (1.33) \end{aligned}$$

where $M_Z(\tau)$ is the inverse of the lifetime function $\tau_Z(M)$, $m_{\rm ej}(M, Z)$ is the mass ejected by a single star and $\Phi(M)$ is the stellar initial mass function (IMF), normalized such that $\int M\Phi(M)dM = 1$. It is straightforward to generalize the above equations to give $\Delta m_{*,j}$, the mass ejected in the form of element $j$. The functions $\tau_Z(M)$ and $m_{j,\rm ej}(M, Z)$ need to be taken from stellar evolution and nucleosynthesis calculations provided in the literature. This methodology allows us to compare yields (that is, $m_{j,\rm ej}(M, Z)$), IMFs, and type Ia supernova rates under various conditions relatively quickly.

All of the following calculations are done with our default yield set and type Ia lifetime model (Marigo 2001; Portinari et al. 1998; Thielemann et al. 2003, exponential delay function, see chapter 3). The first thing we try is to turn all of the gas into stars in one step. In that way we are simply looking at the ejecta from the stars.

In figure 1.3 we show the behaviour of this model. Notice that some elements are ejected on different timescales, corresponding to the lifetimes of the stars that produce these elements. We see that for primordial abundances, carbon, nitrogen, and iron are all produced with a delay. The former two are mainly produced by AGB stars while a significant portion of the iron comes from SNIa. These effects diminish as the initial metallicity increases since a larger fraction of the ejecta is composed of metals present at the time the star is formed. Note that here we compare to solar by using the notation $[X/\mathrm{H}] \equiv \mathrm{Log}(m_X/m_\mathrm{H}) - \mathrm{Log}(m_X/m_\mathrm{H})_\odot$, as is commonly done in the literature.

We next try an efolding star formation history (that is, exponentially decaying), which is similar to what is used by those who have in recent years been studying stellar populations of individual galaxies. For this calculation we have not assumed that the initial gas cloud is immediately converted into stars, as we did in the previous example. Stars are formed with a characteristic timescale of 1 Gyr (with a normalization of 1 - after 1 Gyr, $1/e$ of the gas has been turned into stars). These parameters are arbitrarily chosen to show the behaviour of such a star formation history, but this also illustrates a degree of freedom in this type of calculation. Since stars return gas to the ISM, the stellar mass fraction does not increase monotonically in this model, but peaks at approximately $40\%$.

In figure 1.4 we compare this model with a closed box calculation explored in the previous section (using a yield, $y = 0.02$, and the gas fraction obtained from the numerical model). The closed box model predicts the shape of the metallicity evolution well. Note that when the gas is initially not metal-free, equation 1.13 becomes:

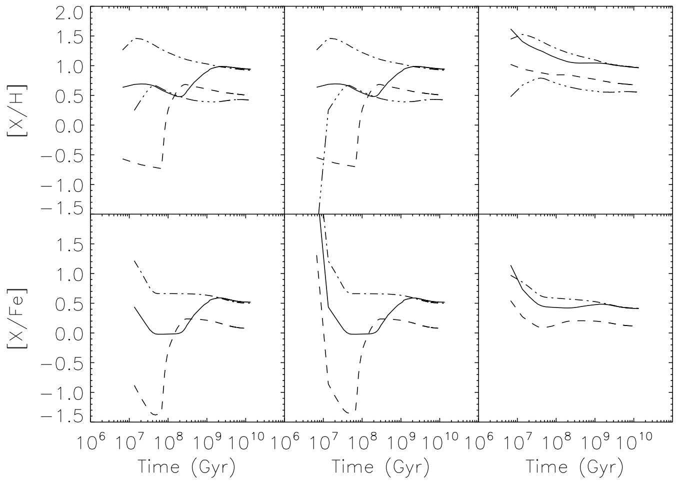

**Figure 1.3**: Our numerical chemical evolution model with an initial burst of star formation and a Chabrier (2003) IMF. Shown are ratios of gas abundance of element $X$ to hydrogen (top) and iron (bottom) as a function of time. Since the burst consumes 100% of the gas, this figure effectively shows the ejecta of a single stellar population as a function of time. The left, centre, and right columns begin with primordial, 1% solar, and solar gas metallicity respectively. Elements shown are Carbon (solid), Nitrogen (dashed), Oxygen (dot-dashed) and Iron (dot-dot-dot-dashed).

$Z_g(t) = -y \ln f_g + Z_g(0)$. There is of course, a slight offset between the closed box model and the numerical result for the first time step because the closed box model assumes that the gas is instantaneously recycled while the in the numerical model there will be a delay of *at least* one time step. Many of the differences between the relative abundances seen in figure 1.3 have now disappeared since the ejecta initially make up relatively little of the gas. These differences can be seen when the abundance ratios are plotted with respect to iron, indicating that this can be an important way of evaluating chemical evolution models. We note that the final abundances do not converge to the solar values, as one might expect. It shall be seen later that uncertainties in stellar yields and SNIa rates can more than account for the difference from solar seen in figure 1.4.

Finally, we use a Strolger et al. (2004) star formation rate, which is an analytic estimation of the cosmic star formation rate. In figure 1.5 we see that with this star formation history, the initial metallicity of the gas appears to be much more important. This is only because this star formation rate results in much less stellar mass. Again, we see that the closed box model predicts the numerical solution very well. The fact that the estimates of metallicity fall below solar does not give cause for concern since this would be averaged over the entire universe and there are indeed regions of very low metallicity in the Universe at $z = 0$.

## 1.2 THE OWLS PROJECT

Ultimately, studying the chemical evolution of the universe is best approached using cosmological, hydrodynamical, chemodynamical simulations. Cosmological because large scales are necessary to capture the different types of objects which contribute

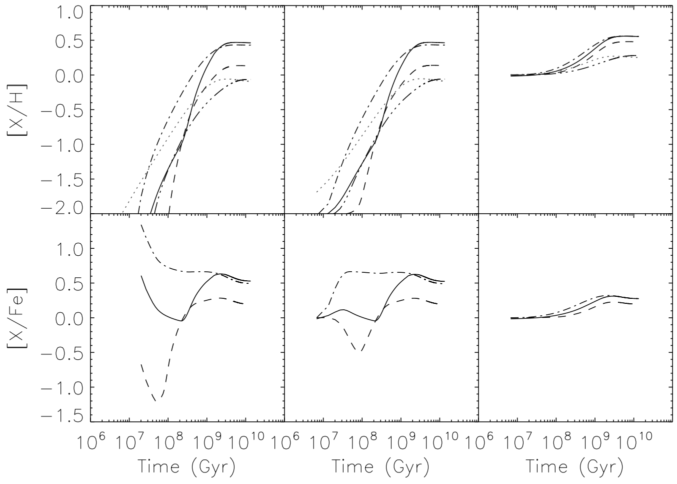

**Figure 1.4**: Our numerical chemical evolution model with an efolding star formation rate and a Chabrier (2003) IMF. The left, centre, and right columns begin with primordial, 1% solar, and solar gas metallicity respectively. Elements shown are Carbon (solid), Nitrogen (dashed), Oxygen (dot-dashed), and Iron (dot-dot-dot-dashed). Also shown in the top panel is the prediction from the analytical closed box model (grey dotted).

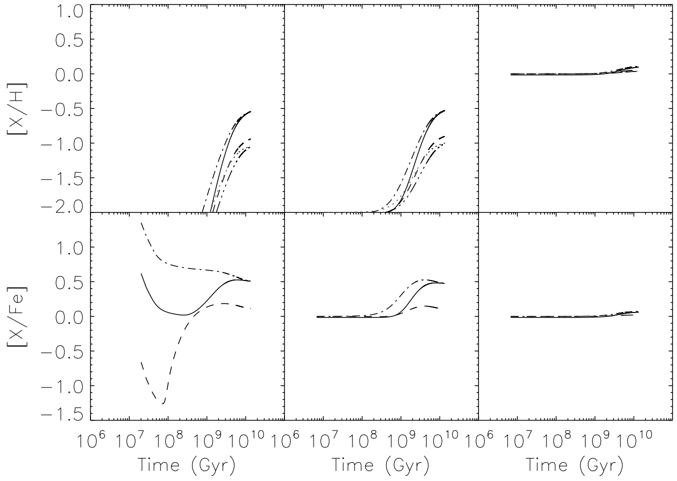

**Figure 1.5**: Our numerical chemical evolution model with a Strolger et al. (2004) star formation rate and a Chabrier (2003) IMF. The left, centre, and right columns begin with primordial, 1% solar, and solar gas metallicity respectively. Elements shown are Carbon (solid), Nitrogen (dashed), Oxygen (dot-dashed), and Iron (dot-dot-dot-dashed). Also shown in the top panel is the prediction from the analytical closed box model (grey dotted).

to the chemical enrichment of the universe. Hydrodynamical because gas forces play an important role in chemical evolution. Chemodynamical because it is important to follow where the produced metals originate and where they go. This method allows one to relax the instantaneous mixing approximation on large scales, as well as to investigate the chemical state of the gas in density/temperature phase space. Such an undertaking introduces new parameters that require tuning and are subject to difficulties in the interpretation of the results. Nevertheless, we will find that the chemical makeup of the IGM is complex enough that such an approach is warranted.

The idea behind the OverWhelmingly Large Simulations (OWLS) project Schaye et al. (2009) was to run a large suite of simulations, each with slightly different physical implementations or numerical parameters. Some of the aims it was conceived with are as follows:

- Quantify uncertainties due to numerical parameters.

- Quantify uncertainties due to sub-resolution physics.
- Determine which physical processes are influential in a given regime.
- Test observational/sampling biases in a controlled environment.

The process of comparing simulations with different physical models can be very instructive. It may allow us to clearly understand the physics involved in certain phenomena, or it may simply allow us determine, to first order, what is important and needs further study.

## 1.3 THIS THESIS

This thesis is heavily based on the OWLS project. The first half describes some of the physics that has gone into the reference model of the project, while the second half focuses more on the analysis of the simulations.

### 1.3.1 Chapter 2

Chapter 2 discusses how metals and a photoionizing background can effect the radiative cooling of cosmic gas. This is presented in the context of gas typical (in density, temperature, and ionizing background) of the intergalactic medium and protogalaxies. Metal enrichment typically serves to enhance cooling rates (due to the increased number of bound electrons) and photoionization typically serves to decrease cooling rates (due to the decreased number of bound electrons available and through photoheating). Although both of these effects had been previously discussed in isolation, we combine the two and explore the relative contribution of both effects for a range of densities and temperatures. We find that the density at which gas can cool in a Hubble time changes by up to an order of magnitude for given metallicity and ionization conditions. This effect occurs in a non-trivial manner, indicating self-consistent calculations are necessary for accurate cooling rates.

We demonstrate how to calculate the contributions of each element to the cooling, allowing us to relax the assumption that the relative abundances of the elements in the gas are that of solar. Even in well mixed gas, relative abundances can change by a factor of a few as it gets enriched by different processes (see the previous section). This is very important since the individual peaks of the cooling curve are very sensitive to abundances and ionization state. The cooling calculations presented in this chapter are used in the simulations presented in the rest of this thesis.

### 1.3.2 Chapter 3

In chapter 3 we describe the chemodynamics that goes into our simulations. We take care to consider every ingredient in turn, illustrating the uncertainties involved. The uncertainties in the stellar yields, and particularly in the supernova type Ia rates, can amount to differences of factors of a few in metal production. We then examine the distribution of metals in the reference runs of the OWLS project, which incorporates our method. We find that simply changing the definition of the metallicity in the simulations can result in up to a factor of one and a half difference in stellar mass at $z = 0$, illustrating some of the numerical difficulties inherent to such a calculation.

The metals in our simulations are distributed relatively evenly among the cosmic gas phases at $z = 2$ and they do not follow the relative distributions of baryons, which tend to either be in a shock-heated, warm-hot phase surrounding galaxies and haloes or in a cold, diffuse phase. At $z = 0$, most of the metals are locked up in stars.

### 1.3.3 Chapter 4

The power of the OWLS project is finally realised in chapter 4. Here we compare the different physical models used in the various simulations in the context of the cosmic metal distribution. We examine in detail the effect of cooling, galactic wind model, stellar IMF, and feedback from AGN.

We find that strong feedback is needed to efficiently eject metals from haloes of all masses. This can come in the form of a particularly strong supernova wind model, a top-heavy IMF in high pressure regions, or feedback from AGN. In accordance with previous work, we find that the metallicity of the Warm-Hot Intergalactic Medium (WHIM) - where a large portion of the baryons in the local universe reside - to be of order $10^{-1}Z_{\odot}$, experiencing little evolution. Among all of the models this value varies by less than 0.5 dex. The only exception is the models that do not include energy feedback in the form of stellar winds and supernovae.

The metallicity of the lowest density regions - the diffuse IGM - is very sensitive the precise parameters and implementation of the feedback. This dependence can be therefore useful in gauging the validity of the different models.

We find in all models that the average stellar metallicity of the Universe is rather high ($[Z_*] \sim -1$) at high redshift ($z \sim 6$).

### 1.3.4 Chapter 5

The final chapter considers the origin of the $z = 0$ (that is, present day) metals. We construct an enrichment history for different gas phases at $z = 0$ in the highest resolution reference model. As expected, we find a strong density dependence, with gas of higher density being enriched later. We not only consider *when* this gas was enriched, but also by *what*. A group finder is used to determine the characteristic halo mass which enriches gas of a given density and temperature. Here too, we find a strong density gradient. Low mass haloes enrich the low density IGM while high mass haloes enrich hot gas of medium densities. This is independent of the feedback model. The cold, diffuse, underdense IGM contains very few metals, the metals that are there come mainly from intergalactic stars. The fact that much of the IGM enrichment is driven by the lowest mass haloes that we can resolve, suggests that the characteristic halo mass by which the IGM is enriched may be dependent on resolution.

## 1.4 OUTLOOK

Improvement on this work will come via computer code development. Ideally we would like to be able to resolve more physics without making the simulation unfeasible, in terms of run time, data storage, or memory management. Currently run time is typically not limited by processor speed, but by communication. Since communication is not likely to improve much in the near future, better codes need to be introduced. Data storage will need to become more efficient since analysing the data is quickly becoming a computer science problem itself. Finally, if we wish to achieve higher resolutions (which may be necessary if we introduce more physics), we shall need more memory since this limits the number of particles that can be employed.

Aside from these problems, development also needs to continue for the hydrodynamical aspect of these codes. Specific to Smoothed Particle Hydrodynamics (SPH - a popular method of performing hydrodynamics calculations) it has recently become apparent that a number of 'tweaks' may need to be made to reduce numerical problems such as discreteness and lack of diffusion (e.g., Wadsley et al. 2008; Greif et al. 2009; Kawata et al. 2009). Perhaps novel approaches to hydrodynamics need to considered (e.g., Springel 2009).

New codes will hopefully also include the transfer of radiation from galactic sources throughout the IGM. While the simulations presented here assume a uniform radiation field, in reality the gas will be embedded in an inhomogeneous radiation field - particularly during reionization. This could have a large impact on the temperature structure of the IGM.

More related to the chemodynamics, the uncertainties in stellar evolution/nucleosynthesis models will hopefully be diminished in the future. Models of type Ia supernova in particular have been getting much attention as their explosion rate/mechanism is also uncertain. If we are to maintain any hope of performing any useful science with individual abundances (beyond reproducing general trends), progress in the above areas is a necessity. The uncertainties in the type Ia supernova rate in particular, result in a wide range of values for iron abundances. On the other hand these uncertainties can also be reduced observationally.

There currently exist a number of mechanisms to drive galactic winds. Such winds are thought to carry metals from the galaxies that they are produced in to the low density IGM. The only direct constraint on the nature of such winds is the energy of a supernova (assuming supernovae do indeed drive galactic winds). When attempting to account for this process in simulations, it is unclear how efficient this energy couples to the surrounding medium. At some point, a certain fraction of this energy is converted into kinetic energy as an outflow is formed. Whether this results in a large amount of mass moving at a low velocity or a small amount of mass at a fast velocity is another source of uncertainty. If one also considers other mechanisms for galactic winds (radiation pressure on dust grains, cosmic ray pressure, active galactic nucleii), then there is even more freedom available. While one may try to constrain these models indirectly with other signatures (the galactic mass-metallicity relation, IGM metallicity measurements, galactic mass functions, etc.), these tend to be degenerate with other uncertain/unresolved processes. A sound, first principles, understanding of galactic winds is clearly necessary.

Encouragingly new instruments and telescopes will continually become available. In the next decade, a number of instruments are coming online that will be able to measure abundances for a number of temperatures and densities in the IGM. It is hoped that new X-ray instruments will finally detect and analyse the WHIM - a phase oft predicted in simulations, but not yet detected with instruments. This phase is thought to hold a good fraction of the baryons and metals in the local universe. Further measurements of abundances to greater radii in clusters will also help sort through the models. Lastly, more sensitive detectors will allow absorption lines to be measured in more and more galaxy spectra, offering a probe of the coldest portions of the IGM.

We present here a thorough treatment of the physics of the numerical models in the hope that we can understand what processes are influential so that the path ahead may become clearer.

## REFERENCES

Binney J., Merrifield M., 1998, Galactic astronomy. Galactic astronomy / James Binney and Michael Merrifield. Princeton, NJ : Princeton University Press, 1998. (Princeton series in astrophysics) QB857 .B522 1998 ($35.00)

Chabrier G., 2003, PASP, 115, 763

Croton D. J., Springel V., White S. D. M., De Lucia G., Frenk C. S., Gao L., Jenkins A., Kauffmann G., Navarro J. F., Yoshida N., 2006, MNRAS, 365, 11

Gnedin N. Y., Hui L., 1998, MNRAS, 296, 44

Greif T. H., Glover S. C. O., Bromm V., Klessen R. S., 2009, MNRAS, 392, 1381

Herwig F., 2005, ARA&A, 43, 435

Kauffmann G., White S. D. M., Guiderdoni B., 1993, MNRAS, 264, 201

Kawata D., Okamoto T., Cen R., Gibson B. K., 2009, ArXiv e-prints

Marigo P., 2001, A&A, 370, 194

Portinari L., Chiosi C., Bressan A., 1998, A&A, 334, 505

Schaye J., Dalla Vecchia C., Booth C. M., Wiersma R. P. C., Theuns T., Haas M. R., Bertone S., Duffy A. R., McCarthy I. G., van de Voort F., 2009, ArXiv e-prints

Shapiro P. R., Giroux M. L., Babul A., 1994, ApJ, 427, 25

Somerville R. S., Primack J. R., 1999, MNRAS, 310, 1087

Spergel D. N., Bean R., Doré O., Nolta M. R., Bennett C. L., Dunkley J., Hinshaw G., Jarosik J. L., Wollack E., Wright E. L., 2007, ApJS, 170, 377

Springel V., 2009, ArXiv e-prints

Strolger L.-G., Riess A. G., Dahlen T., Livio M., Panagia N., Challis P., Tonry J. L., Filippenko A. V., Chornock R., Ferguson H., Koekemoer A., Mobasher B., Dickinson M., 2004, ApJ, 613, 200

Sutherland R. S., Dopita M. A., 1993, ApJS, 88, 253

Talbot Jr. R. J., Arnett W. D., 1971, ApJ, 170, 409

Thielemann F.-K., Argast D., Brachwitz F., Hix W. R., Höflich P., Liebendörfer M., Martinez-Pinedo G., Mezzacappa A., Nomoto K., Panov I., 2003, in From Twilight to Highlight: The Physics of Supernovae Supernova Nucleosynthesis and Galactic Evolution. pp 331–+

Wadsley J. W., Veeravalli G., Couchman H. M. P., 2008, MNRAS, 387, 427

# CHAPTER 2

# Photoionization and the cooling rates of enriched, astrophysical plasmas

Robert P.C. Wiersma, Joop Schaye and Britton D. Smith

Monthly Notices of the Royal Astronomical Society, 393, 99, 2009

RADIATIVE cooling is central to a wide range of astrophysical problems. Despite its importance, cooling rates are generally computed using very restrictive assumptions, such as collisional ionization equilibrium and solar relative abundances. We simultaneously relax both assumptions and investigate the effects of photo-ionization of heavy elements by the meta-galactic UV/X-ray background and of variations in relative abundances on the cooling rates of optically thin gas in ionization equilibrium. We find that photo-ionization by the meta-galactic background radiation reduces the net cooling rates by up to an order of magnitude for gas densities and temperatures typical of the shock-heated intergalactic medium and proto-galaxies ($10^4\,\mathrm{K} \lesssim T \lesssim 10^6\,\mathrm{K}$, $\rho/\langle\rho\rangle \lesssim 100$). In addition, photo-ionization changes the relative contributions of different elements to the cooling rates. We conclude that photo-ionization by the ionizing background and heavy elements both need to be taken into account in order for the cooling rates to be correct to order of magnitude. Moreover, if the rates need to be known to better than a factor of a few, then departures of the relative abundances from solar need to be taken into account. We propose a method to compute cooling rates on an element-by-element basis by interpolating pre-computed tables that take photo-ionization into account. We provide such tables for a popular model of the evolving UV/X-ray background radiation, computed using the photo-ionization package CLOUDY.

## 2.1 INTRODUCTION

Dissipation of energy via radiative cooling plays a central role in many different astrophysical contexts. In general the cooling rate depends on a large number of parameters, such as the gas density, temperature, chemical composition, ionization balance, and the radiation field. In the absence of radiation, however, the equilibrium ionization balance depends only on the temperature. In that case the cooling rate in the low density regime, which is dominated by collisional processes, is simply proportional to the gas density squared, for a given composition. Thus, the cooling rates for a plasma in collisional ionization equilibrium (CIE) can be conveniently tabulated as a function of the temperature and composition (metallicity) of the gas (e.g., Cox & Tucker 1969; Raymond et al. 1976; Shull & van Steenberg 1982; Gaetz & Salpeter 1983; Boehringer & Hensler 1989; Sutherland & Dopita 1993; Landi & Landini 1999; Benjamin et al. 2001; Gnat & Sternberg 2007; Smith et al. 2008), and such tables are widely used for a large variety of problems.

Although it is convenient to ignore radiation when calculating cooling rates, radiation is generally important for the thermal and ionization state of astrophysical plasmas. For example, Efstathiou (1992) investigated the effect of the extragalactic UV background on the cooling rates for gas of primordial composition (in practice this means a pure H/He plasma) and found that including photo-ionization can suppress the cooling rates of gas in the temperature range $T \sim 10^4 - 10^5\,\mathrm{K}$ by a large factor. Although the effects of radiation are often taken into account for gas of primordial composition, photo-ionization of heavy elements is usually ignored in the calculation of cooling rates (but see Leonard 1998; Benson et al. 2002).

In this chapter we will investigate the dependence of cooling rates of gas enriched with metals on the presence of ionizing radiation, focusing on the temperature range $T \sim 10^4 - 10^8\,\mathrm{K}$ and optically thin plasmas. We will show that, as is the case for gas of primordial composition (Efstathiou 1992), photo-ionization can suppress the metallic cooling rates by a large factor. Moreover, the suppression of the cooling rate is significant up to much higher temperatures than for the primordial case.

We will also investigate the relative contributions of various elements to the cooling rates. If the relative abundances are similar to solar, then oxygen, neon, and iron dominate the cooling in the temperature range $T \sim 10^4 - 10^7\,\mathrm{K}$. However, we will show that the relative contributions of different elements to the cooling rate are sensitive to the presence of ionizing radiation.

Although we will illustrate the results using densities and radiation fields that are relevant for studies of galaxy formation and the intergalactic medium (IGM), the conclusion that photo-ionization significantly reduces the cooling rates of enriched gas is valid for a large variety of astrophysical problems. For example, for $T \sim 10^5\,\mathrm{K}$ and $T \sim 10^6\,\mathrm{K}$ the reduction of metal-line cooling rates is significant as long as the dimensionless ionization parameter[1] $U \gtrsim 10^{-3}$ and $U \gtrsim 10^{-1}$, respectively. We will focus on the temperature range $10^4 - 10^8\,\mathrm{K}$ because gas in this temperature range is usually

---

[1] $U \equiv \Phi_{\mathrm{H}}/(n_{\mathrm{H}}c)$, where $\Phi_{\mathrm{H}}$ is the flux of hydrogen ionizing photons (i.e., photons per unit area and time), $n_{\mathrm{H}}$ is the total hydrogen number density and $c$ is the speed of light.

optically thin and because the effects of photo-ionization are generally unimportant at higher temperatures.

Tables containing cooling rates and several other useful quantities as a function of density, temperature, redshift, and composition, appropriate for gas exposed to the models for the evolving meta-galactic UV/X-ray background of Haardt & Madau (2001) are available on the following web site:
`http://www.strw.leidenuniv.nl/WSS08/`. The web site also contains a number of videos that illustrate the dependence of the cooling rates on various parameters.

This chapter is organized as follows. In Section 2.2 we present our method for calculating element-by-element cooling rates including photo-ionization and we compare the limiting case of CIE to results taken from the literature. Section 2.3 shows how metals and ionizing radiation affect the cooling rates. Section 2.4 demonstrates the importance for the low-redshift shock-heated IGM, which is thought to contain most of the baryons. In this section we also illustrate the effect of changing the intensity and spectral shape of the ionizing radiation. We investigate the effect of photo-ionization on the relative contributions of individual elements in Section 2.5 and we summarize and discuss our conclusions in Section 2.6.

Throughout this chapter we use the cosmological parameters from Komatsu et al. (2008): $(\Omega_{\rm m}, \Omega_\Lambda, \Omega_{\rm b}, h) = (0.279, 0.721, 0.0462, 0.701)$ and a primordial helium mass fraction $X_{\rm He} = 0.248$. Densities will be expressed both as proper hydrogen number densities $n_{\rm H}$ and density contrasts $\delta \equiv \rho_{\rm b}/\langle\rho_{\rm b}\rangle - 1$, where $\langle\rho_{\rm b}\rangle$ is the cosmic mean baryon density. The two are related by

$$n_{\rm H} \approx 1.9 \times 10^{-7}\,{\rm cm}^{-3}\ (1+\delta)\,(1+z)^3 \left(\frac{X_{\rm H}}{0.752}\right). \tag{2.1}$$

## 2.2 METHOD

All radiative cooling and heating rates were computed by running large grids of photo-ionization models using the publicly available photo-ionization package CLOUDY[2] (version 07.02 of the code last described by Ferland et al. 1998). CLOUDY contains most of the atomic processes that are thought to be important in the temperature range of interest here ($T \sim 10^4 - 10^8$ K) and the reader is referred to the online documentation for details about the atomic physics and data used.

The gas was exposed to the cosmic microwave background radiation (CMB) and the Haardt & Madau (2001, hereafter HM01) model[3] for the UV/X-ray background radiation from galaxies (assuming a 10 percent escape fraction for H-ionizing photons) and quasars. We assumed the gas to be dust-free, optically thin and in ionization equilibrium. We discuss the limitations and the effects of the last two assumptions in section 2.6. All cooling rates are tabulated as a function of $\log n_{\rm H}$ (total hydrogen number density), $\log T$ (temperature), and $z$ (redshift).

---

[2] `http://www.nublado.org/`

[3] `http://pitto.mib.infn.it/~haardt/refmodel.html`

**Table 2.1**: Default CLOUDY solar abundances

| Element | $n_i/n_{\rm H}$ | Mass Fraction |
|---|---|---|
| H | 1 | 0.7065 |
| He | 0.1 | 0.2806 |
| C | $2.46 \times 10^{-4}$ | $2.07 \times 10^{-3}$ |
| N | $8.51 \times 10^{-5}$ | $8.36 \times 10^{-4}$ |
| O | $4.90 \times 10^{-4}$ | $5.49 \times 10^{-3}$ |
| Ne | $1.00 \times 10^{-4}$ | $1.41 \times 10^{-3}$ |
| Mg | $3.47 \times 10^{-5}$ | $5.91 \times 10^{-4}$ |
| Si | $3.47 \times 10^{-5}$ | $6.83 \times 10^{-4}$ |
| S | $1.86 \times 10^{-5}$ | $4.09 \times 10^{-4}$ |
| Ca | $2.29 \times 10^{-6}$ | $6.44 \times 10^{-5}$ |
| Fe | $2.82 \times 10^{-5}$ | $1.10 \times 10^{-3}$ |

When studying the effect of changes in the relative abundances of elements, we compute the cooling rates on an element-by-element basis. The cooling rate $\Lambda_i$ (in $\rm erg\,s^{-1}\,cm^{-3}$) due to element $i$, where element $i$ is heavier than helium, is defined as the difference between the cooling rate computed using all elements (assuming solar abundances) and the cooling rate computed after setting the abundance of element $i$ to zero, while keeping all other abundances (i.e., number densities relative to H) the same. This is a valid approximation provided element $i$ does not contribute significantly to the free electron density, which is the case for all elements heavier than helium and if the metallicity $Z \lesssim Z_\odot$.

The combined contributions from hydrogen and helium are computed by interpolating in the four dimensions $\log n_{\rm H}$, $\log T$, $z$, and $n_{\rm He}/n_{\rm H}$ from tables of CLOUDY models that contain only H and He.

Thus, the total net cooling rate,

$$\Lambda = \Lambda_{\rm H,He} + \sum_{i>{\rm He}} \Lambda_i, \tag{2.2}$$

could be obtained from

$$\Lambda = \Lambda_{\rm H,He} + \sum_{i>{\rm He}} \frac{n_i/n_{\rm H}}{(n_i/n_{\rm H})_\odot} \Lambda_{i,\odot}, \tag{2.3}$$

where $(n_i/n_{\rm H})_\odot$ is the solar abundance of element $i$ (the default CLOUDY solar abundances are given in Table 2.1) and $\Lambda_{i,\odot}$ is the contribution of heavy element $i$ to the radiative cooling rate for solar abundances, which we have tabulated as a function of $\log n_{\rm H}$, $\log T$, and $z$. Note that we use $\Lambda$ to denote the cooling rate per unit volume ($\rm erg\,s^{-1}\,cm^{-3}$).

We can, however, do better than equation (2.3) by taking the dependence of the free electron density on He/H, into account (in equation (2.3), the electron density is implicitly assumed to be that corresponding to solar abundances - $n_{\rm He}/n_{\rm H} = 0.1$). Since cooling rates due to metals are dominated by collisions between ions and free electrons, $\Lambda_i$ scales as the product of the free electron and ion densities, $\Lambda_i \propto n_{\rm e} n_i$. Hence,

$$\begin{aligned}\Lambda &= \Lambda_{\rm H,He} + \sum_{i>{\rm He}} \Lambda_{i,\odot} \left(\frac{n_{\rm e}}{n_{{\rm e},\odot}}\right) \left(\frac{n_i}{n_{i,\odot}}\right), \\ &= \Lambda_{\rm H,He} + \sum_{i>{\rm He}} \Lambda_{i,\odot} \frac{n_{\rm e}/n_{\rm H}}{(n_{\rm e}/n_{\rm H})_\odot} 10^{[i/{\rm H}]} \end{aligned} \tag{2.4}$$

where $10^{[i/{\rm H}]} \equiv (n_i/n_{\rm H})/(n_i/n_{\rm H})_\odot$ and we used the fact that $n_{\rm H} = n_{{\rm H},\odot}$ (since we tabulate as a function of $n_{\rm H}$). While $(n_{\rm e}/n_{\rm H})_\odot$ is obtained by interpolating the solar abundance table for $n_{\rm e}/n_{\rm H}$ in $(n_{\rm H}, T, z)$, $(n_{\rm e}/n_{\rm H})$ must be obtained by interpolating in $((n_{\rm He}/n_{\rm H}), n_{\rm H}, T, z)$. Note that we tabulate the electron density in the absence of metals. This is a valid approximation given that heavy elements only contribute significantly to the free electron density for $Z \gg Z_\odot$.

In practice we tabulate $\log \Lambda_{i,\odot}/n_{\rm H}^2$ over the range $\log[n_{\rm H}\,({\rm cm}^{-3})] = -8.0$, -7.9, . . ., 0.0 and $\log[T\ ({\rm K})] = 2.00$, 2.02, . . ., 9.00. In addition, the quantities $\log \Lambda_{\rm H,He}/n_{\rm H}^2$, $n_{\rm e}/n_{\rm H}$ and the mean particle mass are all tabulated as a function of density and temperature for each of the values $n_{\rm He}/n_{\rm H} = 0.0787$, 0.0830, 0.0876, 0.0922, 0.970, 0.102, 0.107 which correspond to mass fractions $X_{\rm He}/(X_{\rm H} + X_{\rm He}) = 0.238$, 0.248, 0.258, 0.268, 0.278, 0.288, 0.298. Finally, for each value of the ratio $n_{\rm He}/n_{\rm H}$ we tabulate the temperature as a function of density and internal energy per unit mass to enable simulation codes that parametrize thermal energy in terms of the latter quantity to use the cooling tables. We have computed these tables for each of the 49 redshifts spanning $z = 0-9$ for which the HM01 models are defined. All tables are in HDF5 format and together they result in upwards of 232 MB of storage. Reducing the resolution in $n_{\rm H}$ and $T$ by a factor of two does reduce the accuracy of interpolated rates significantly[4], but reduces the storage requirements to 61 MB.

We find that for metallicities $Z \lesssim Z_\odot$ equation (2.4) closely matches the true cooling rate (i.e., including all elements) with very good accuracy[5] if the following 11 elements are included: H, He, C, N, O, Ne, Mg, Si, S, Ca, and Fe.

For redshift $z = 0$ and over the full range of densities and temperatures, the median relative errors in the absolute net cooling rates are 0.33%, 1.6%, and 6.1% for $Z = 0.1Z_\odot$, $Z_\odot$, and $10Z_\odot$, respectively (we have scaled $n_{\rm He}/n_{\rm H}$ with metallicity). For higher redshifts the median errors are smaller than for $z = 0$ because Compton cooling off the CMB, which is modelled accurately, becomes increasingly important. Hence, even

---

[4] Reducing the temperature resolution by a factor of two roughly doubles the interpolation errors near the thermal equilibrium solution, but in this regime the cooling times are in any case effectively infinite.

[5] While the error in the total cooling rates is small, the relative errors in the contribution of individual elements can be larger if the element contributes negligibly to the total cooling rate (see e.g., the noise in the Fe contour at $T < 10^5$ K in the left-hand panel of figure 2.6). This is because the tables for individual elements were computed by taking the difference between the total cooling rate for solar abundances including and excluding the element. Hence, if the element does not contribute significantly to the cooling rate for a particular density, temperature, and redshift, then its contribution will be computed as the difference between two nearly equal numbers. Because this can only occur if the contribution is negligible, we do not consider this to be a problem.

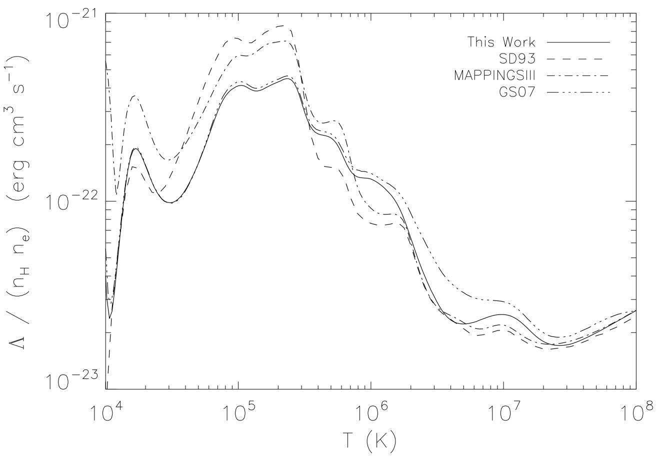

**Figure 2.1**: Comparison of normalized CIE cooling rates for various studies. All curves use the solar abundances of Gnat & Sternberg (2007), which differ somewhat from our default solar abundances. Shown are CLOUDY version 07.02 (solid), Sutherland & Dopita (1993) (dashed), MAPPINGS III (dot-dashed), and Gnat & Sternberg (2007) (dot-dot-dot-dashed). MAPPINGS gives significantly higher cooling rates for $T \sim 10^5$ K, but the differences are typically smaller than a factor of two. Note that for this comparison the cooling rates were divided by $n_{\rm H} n_{\rm e}$, but that we divide by $n_{\rm H}^2$ in our tables and in figure 2.6. The upturn in the normalized cooling rates below $10^4$ K is caused by the sharp decrease in $n_{\rm e}$ with decreasing temperature.

for metallicities as extreme as 10 times solar, using equation (2.4) and including 11 elements gives errors of only a few percent. As we shall see below, this is much smaller than the differences between different photo-ionization codes. Using equation (2.3) rather than (2.4) gives similar errors for low metallicities, but the median errors are a factor 2–3 higher for $Z > 10^{0.5}\ Z_\odot$.

Excluding temperatures within 0.1 dex of the thermal equilibrium solution (where the relative errors in the net cooling rate, which is computed as the absolute difference between heating and cooling, become large because we are subtracting two nearly identical numbers), the maximum errors in the net cooling rates are 32%, 29%, and 39% for $Z = 0.1 Z_\odot$, $Z_\odot$, and $10 Z_\odot$, respectively. Thus, even for extreme metallicities the maximum difference between the estimated and true rates is well within a factor of two. These maxima are reached near the 0.1 dex exclusion zone, so the maximum errors for temperatures that differ substantially from the equilibrium values are much smaller.

We have also tabulated the combined cooling rates of all elements heavier than helium, assuming solar relative abundances. While scaling all heavy elements simultaneously reduces the accuracy (relative to scaling the contribution of each element individually), these tables may be convenient in the absence of a complete set of elemental abundances. In this case, the total cooling rate becomes:

$$\Lambda = \Lambda_{\mathrm{H,He}} + \Lambda_{Z,\odot} \frac{n_\mathrm{e}/n_\mathrm{H}}{(n_\mathrm{e}/n_\mathrm{H})_\odot} \frac{Z}{Z_\odot}. \tag{2.5}$$

Although cooling rates including photo-ionization have not yet been tabulated, CIE cooling rates have been published by various authors. In Figure 2.1 we compare our CIE results (i.e., CLOUDY version 07.02) with those of Gnat & Sternberg (2007) (who used CLOUDY version 06.02), Sutherland & Dopita (1993) (who used MAPPINGS) and also with MAPPINGS III (version r; Groves et al. 2008). The calculations generally differ in terms of the code, the atomic rates, and the solar abundances that were used. In order to focus the comparison on codes and rates, we used the solar abundances assumed by Gnat & Sternberg (2007) when computing the cooling rates for all curves in this figure[6]. Note that these abundances differ somewhat from the solar abundances that we use in the rest of this chapter.

The differences in the cooling rates shown in Figure 2.1 are typically smaller than 0.3 dex suggesting that the cooling rates are known to better than a factor of two, at least for CIE. The differences are largest for $T \sim 10^5$ K, with MAPPINGS giving higher cooling rates than CLOUDY.

## 2.3 PHOTO-IONIZATION, METALS, AND COOLING RATES

The cooling rates in photo-ionization equilibrium are not proportional to the density squared, as is the case for CIE. As a consequence, the cooling curve changes dramatically with density. This is illustrated in Fig. 2.2 which shows normalized, net cooling, rates ($|\Lambda/n_\mathrm{H}^2|$), as a function of temperature for solar abundances. Different curves correspond to different densities, as indicated in the legend.

The calculation includes the CMB and the HM01 background at redshift three. The $z = 3$ HM01 background corresponds to a hydrogen photo-ionization rate $\Gamma_{12} \equiv \Gamma/10^{-12}\ \mathrm{s}^{-1} = 1.1$ and an ionization parameter $U = 1.6 \times 10^{-5}/n_\mathrm{H}$. We stress that in the vicinity of ionizing sources the radiation field may be much more intense, which would enhance its effect on the cooling rates compared to the results presented here.

As the density decreases the gas becomes more highly ionized and the cooling peaks due to collisional excitation of various ions disappear. For very low densities and high temperatures the normalized cooling rates actually increase as they become dominated by Compton cooling off the CMB, which scales as $\Lambda \propto n_\mathrm{e} T$. For the two lowest densities shown, the equilibrium temperature, for which the net cooling rate $\Lambda \rightarrow 0$, exceeds $10^4$ K. In these cases, curves corresponding to net heating appear to the left of the thermal equilibrium temperature.

Note that for the lowest densities shown here, adiabatic cooling due to the expansion of the Universe becomes important. We have not included this effect here since cooling rates at these densities are often considered in the context of cosmological models which implicitly take this into account. The rates however, are a complex interplay

---

[6] Sutherland & Dopita (1993) only give the cooling rates as a function of the abundance of iron, which we interpolated to the corresponding Gnat & Sternberg (2007) value.

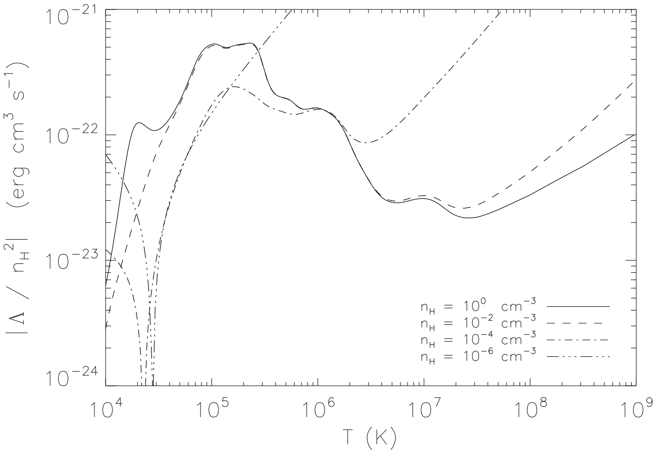

**Figure 2.2**: Normalized, absolute, net cooling rates ($|\Lambda/n_{\rm H}^2|$) as a function of temperature for solar abundances. Different curves correspond to different gas densities, as indicated in the legend. The gas in all models is exposed to the $z = 3$ CMB and the $z = 3$ HM01 UV/X-ray background. Note that the cooling rates were divided by $n_{\rm H}^2$, but that we divided by $n_{\rm H} n_{\rm e}$ in Fig. 2.1.

of photo-heating (dominant at low temperatures), adiabatic expansion of the Universe (dominant at medium temperatures), and Compton cooling off the CMB (dominant at high temperatures).

Figure 2.3 shows how the presence of heavy elements and radiation affects the radiative cooling time. Each panel shows contours of constant cooling time in the density-temperature plane for two models. The top panels illustrate well known results, while the bottom panels demonstrate the importance of radiation on the cooling due to metal lines.

Here and throughout the cooling time refers to the absolute value of the net radiative cooling time at a fixed hydrogen density,

$$t_{\rm cool} \equiv \frac{T}{dT/dt} = \frac{\frac{3}{2} n k T}{|\Lambda_{\rm heat} - \Lambda_{\rm cool}|}. \tag{2.6}$$

For temperatures below the thermal equilibrium temperature, $t_{\rm cool}$ corresponds to a heating timescale. The calculation includes the CMB and, optionally, the HM01 background at redshift three.

Note that adiabatic cooling due to the expansion of the Universe is not included, but would dominate over radiative cooling for sufficiently low densities. For example, the universal Hubble expansion (appropriate for densities around the cosmic mean, i.e., $n_{\rm H} \sim 10^{-5}\,{\rm cm}^{-3}$ at $z = 3$) corresponds to an adiabatic cooling time $t_{\rm cool,adiab} = 1/(2H) \approx 1.6 \times 10^9$ yr at $z = 3$.

The top-left panel shows that for a metal-free[7] gas, ionizing radiation drastically reduces the cooling rates for $10^4\,{\rm K} < T \lesssim 10^5{\rm K}$ (Efstathiou 1992). This happens because the peaks in the cooling rate due to collisional excitation of neutral hydrogen and singly ionized helium (followed by Ly$\alpha$ emission) are removed when the gas is photo-ionized.

In the presence of ionizing radiation (solid curves) there are actually two contours for each net cooling time, corresponding to net heating (left of the thermal equilibrium

---

[7] We use $n_{\rm He}/n_{\rm H} = 0.083$ for primordial abundances.

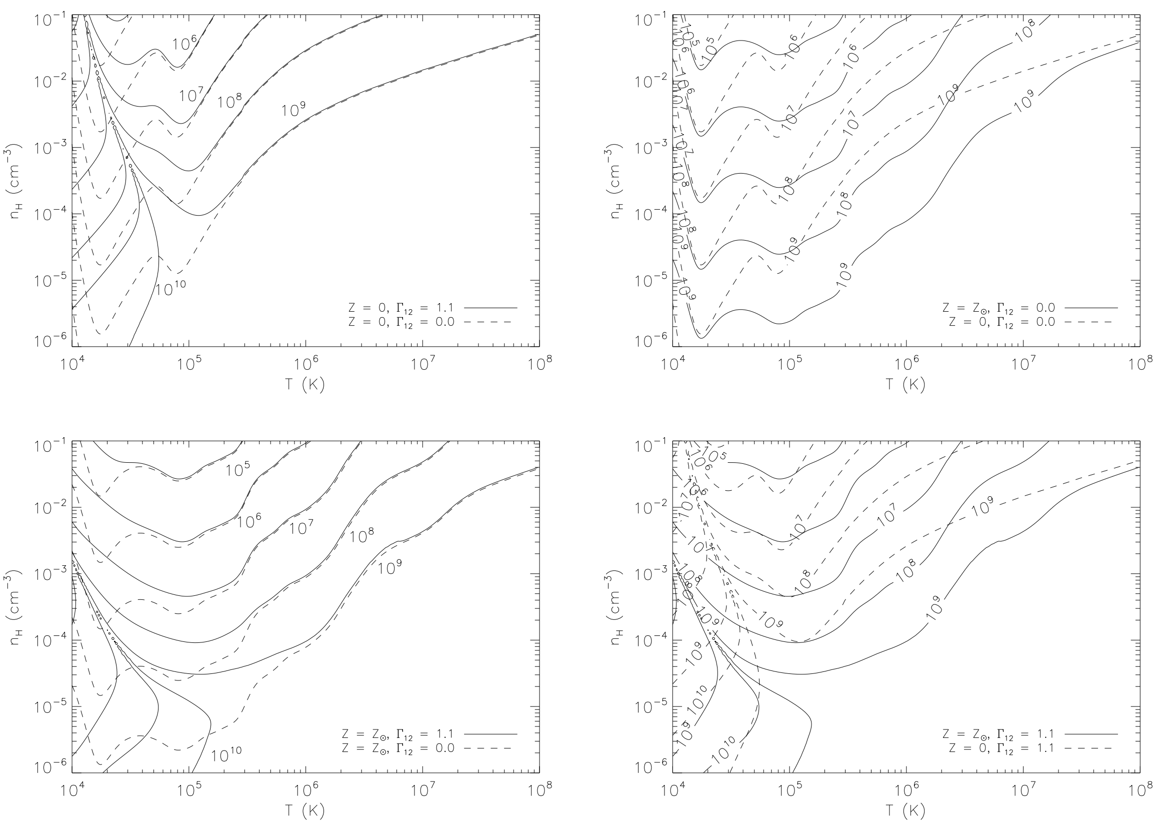

**Figure 2.3**: Contour plots of the net cooling time in years as a function of temperature and total hydrogen number density (note that the mean baryon density corresponds to $n_{\rm H} \sim 10^{-5}\,{\rm cm}^{-3}$ at $z = 3$). For temperatures below the equilibrium temperature, the contours indicate negative net cooling times, that is, heating times (see text). The gas in all models is exposed to the $z = 3$ CMB. In addition, models for which the legend indicates $\Gamma_{12} = 1.1$ use the $z = 3$ HM01 UV/X-ray background. The figure confirms that both metals and photo-ionization affect the cooling rates significantly, and shows their combined effect. *Top-left:* The effect of photo-ionization for zero metallicity; *Top-right:* The effect of metallicity for a purely collisionally ionized plasma; *Bottom-left:* The effect of photo-ionization for solar metallicity; *Bottom-right:* The effect of metallicity for a photo-ionized plasma.

asymptote) and net cooling (right of the equilibrium asymptote). These two contours nearly merge[8] near the (density-dependent) thermal equilibrium temperature, slightly above $10^4$ K, where the net cooling time goes to infinity. Below this temperature, the heating time is dictated by the photo-heating rate.

For $T \gg 10^5$ K photo-ionization has no effect on a metal-free gas because the plasma is already fully ionized by collisional processes. In this regime the plasma cools predominantly via the emission of Bremsstrahlung and/or inverse Compton scattering of CMB photons. The latter process is the dominant cooling mechanism for most of the

---

[8] The fact that the contours really do merge and then disappear at high densities is due to the limitations of our plotting package and the finite resolution of our grid.

baryons at high redshift ($z > 7$). In the plot inverse Compton cooling off the CMB dominates the radiative cooling rate at low densities and high temperatures, but the corresponding cooling time exceeds the Hubble time.

For diffuse, intergalactic gas (i.e., for density contrasts $\delta \ll 10^2$, corresponding to $n_{\rm H} \ll 10^{-3}\,{\rm cm}^{-3}$ at $z = 3$, much lower than expected in virialized objects, e.g., Coles & Lucchin 2002) of primordial composition, radiation increases the cooling time at $10^5\,{\rm K}$ by at least an order of magnitude and by much more at lower temperatures. Since the cooling times in this regime are comparable to the Hubble time, radiation will have a large effect on the fraction of the baryons that are hot. At densities corresponding to collapsed objects ($\delta \gtrsim 10^2$ or $n_{\rm H} \gtrsim 10^{-3}\,{\rm cm}^{-3}$ at $z = 3$), the increase in the cooling time is generally smaller, although it can still easily be an order of magnitude at temperatures as high as $10^{4.5}\,{\rm K}$.

The top-right panel shows that heavy elements strongly increase the cooling rate of a collisionally ionized plasma for $10^4\,{\rm K} \ll T \lesssim 10^7\,{\rm K}$ (e.g., Boehringer & Hensler 1989). Comparing the model with primordial abundances (dashed contours) to the one assuming solar metallicity (solid contours), we see that the cooling times typically differ by about an order of magnitude. The presence of metals allows radiative cooling through collisional excitation of a large number of ions at a variety of temperatures. For $T > 10^7\,{\rm K}$ the difference is smaller because there are few lines to excite since most elements are collisionally ionized to a very high degree. Bremsstrahlung is the dominant cooling mechanism at these very high temperatures.

The bottom-left panel demonstrates that ionizing radiation also strongly reduces the cooling rates when heavy elements dominate the cooling. This happens for the same reason as in the primordial case. The radiation field ionizes the plasma to a higher degree than it would be in CIE. Hence, the ions that are typically collisionally excited are not present, reducing the cooling rates.

Note that a similar thing happens when a collisionally ionized plasma is cooling more quickly than it can recombine. In that case the ionization balance shifts out of equilibrium leaving the gas too highly ionized for its temperature. As for photoionization, the associated reduction of the number of bound electrons with excitation energies low enough to be collisionally excited, reduces the cooling rate (e.g., Kafatos 1973; Shapiro & Moore 1976; Schmutzler & Tscharnuter 1993; Sutherland & Dopita 1993).

Comparing the models with (solid contours) and without ionizing radiation (dashed contours), we see that for densities characteristic of the diffuse IGM ($\delta \ll 10^2$ corresponding to $n_{\rm H} \ll 10^{-3}\,{\rm cm}^{-3}$ at $z = 3$), radiation significantly reduces the cooling rates for $T \lesssim 10^6\,{\rm K}$ and that the reduction typically exceeds one order of magnitude for $T \lesssim 3 \times 10^5\,{\rm K}$. For densities $n_{\rm H} \gtrsim 10^{-3}\,{\rm cm}^{-3}$ the cooling rates are only suppressed substantially for $T < 3 \times 10^4\,{\rm K}$. However, we stress that what matters here is the ionization parameter. Hence, a stronger radiation field will affect the cooling rates up to higher densities. Gas with a density characteristic of collapsed objects will typically be close to sources of ionizing radiation and may thus be exposed to a radiation field that is more intense than the meta-galactic UV background.

Finally, the bottom-right panel shows that metals strongly increase the cooling rates in the presence of an ionizing radiation field, as was the case for a collisionally ionized gas (top-right panel). For solar metallicity the cooling rate at $T < 10^7\,\mathrm{K}$ is typically an order of magnitude higher than for a primordial composition.

Note that for very low densities ($n_\mathrm{H} \lesssim 10^{-5}\,\mathrm{cm}^{-3}$) metals increase the equilibrium temperature (towards the left side of the region where the net cooling time is above $10^{10}$ years) because their presence boosts the photo-heating (via oxygen and iron[9]) but does not significantly affect the cooling because it is dominated by Compton cooling off the CMB.

## 2.4 EFFECT ON THE WHIM

The fraction of gas that has been shock-heated to temperatures of $10^5\,\mathrm{K} \lesssim T < 10^7\,\mathrm{K}$ is currently of great interest, mainly because this so-called warm-hot intergalactic medium (WHIM) is hard to detect, yet may contain a large fraction of the baryons in the low-redshift Universe (e.g., Cen & Ostriker 1999). There are two reasons why the WHIM becomes more important at lower redshift. First, as structure formation progresses, larger structures form, leading to stronger gravitational accretion shocks and a greater fraction of the baryons are heated to temperatures in the WHIM range. Second, as the universe expands, the density of the diffuse gas decreases as[10] $(1 + z)^3$ and the cooling time due to collisional processes (which dominate for $z < 7$) will thus increase as $(1 + z)^{-3}$. Hence, the cooling time increases faster than the Hubble time and more and more of the shock-heated gas is unable to cool.

Since the cooling times are of order the Hubble time for much of the WHIM, the precise values of the cooling rate is particularly important. Because the cooling of the WHIM tends to be dominated by line radiation, because its density is low ($\delta \sim 10 - 10^2$; e.g., Bertone et al. 2008), and because the WHIM gas may well be enriched to values of 10% of solar or higher, both metals and photo-ionization by the UV background may be important. Figure 2.4 demonstrates that this is indeed the case.

Figure 2.4 shows a contour plot of the cooling time in the density contrast-temperature plane for redshift $z = 0$. Each contour corresponds to the same net cooling time, namely the Hubble time. Dashed contours are for a purely collisionally ionized gas, while the solid contours include photo-ionization by the $z = 0$ UV/X-ray background radiation from galaxies and quasars, which corresponds to a hydrogen photo-ionization rate $\Gamma_{12} = 0.08$ and an ionization parameter $U = 9 \times 10^{-7}/n_\mathrm{H}$. Metallicity increases from the top down from zero (i.e., primordial abundances), to 10% solar (grey contours) to solar (black), as indicated in the figure. Gas above a given contour is able to cool, while gas below it will remain hot.

For a primordial composition (grey contours), turning on the ionizing radiation raises the density contrast above which the gas can cool from $\delta \lesssim 10$ to $\delta \sim 10^2$ for $T < 10^5\,\mathrm{K}$. For solar metallicity, the UV radiation becomes important for $T < 10^6\,\mathrm{K}$ and raises the critical density required for cooling within a Hubble time by about an order

---

[9] The increased He/H ratio also boosts the photo-heating rate, but its contribution is smaller than that of the metals.

[10] In reality the density will decrease slightly less fast with time if the gas is overdense and collapsing.

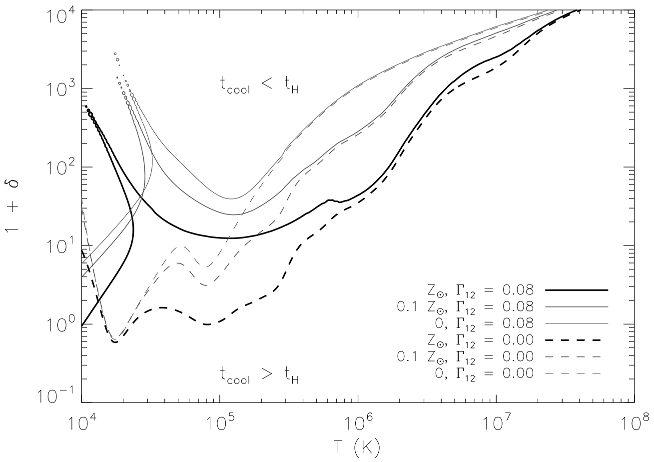

**Figure 2.4**: Contours show where the net cooling time equals the Hubble time in the density contrast - temperature plane at $z = 0$. From top to bottom, metallicity increases with increasing line thickness, from primordial to solar. Dashed contours are for collisional ionization only, while solid contours are for gas exposed to the HM01 model for the $z = 0$ UV/X-ray background. Each solid contour comprises two components, corresponding to net heating (low temperature component) and net cooling (high temperature component), respectively, which merge near the (density-dependent) thermal equilibrium temperature. Both photo-ionization and metallicity determine whether gas is able to cool and it is therefore crucial to take both into account when predicting the fraction of the baryons that reside in the WHIM.

of magnitude for $T \lesssim 10^5\,$K. Increasing the metallicity from zero to solar decreases the critical density contrast by about an order of magnitude over the full range of WHIM temperatures. Clearly, both photo-ionization and metals are important for the thermal evolution of the WHIM.

Figure 2.5 shows how the intensity and the spectral shape of the ionizing radiation affect the results for solar abundances. The solid contour indicates the density contrasts and temperatures for which the cooling time equals the Hubble time for the $z = 0$ HM01 model for the UV/X-ray radiation from quasars and galaxies (model QG). It is identical to the black, solid contour in Figure 2.4. The dashed contour shows the $t_{\rm cool} = t_H$ contour after we have multiplied the entire HM01 radiation field by a factor of 10 (model 10$*$QG). Increasing the intensity reduces the cooling rates, shifting the contour to higher densities.

The dot-dashed contour corresponds to the quasar only HM01 model (model Q), which we have rescaled such as to give the same hydrogen ionization rate as model QG. Since the average energy of H-ionizing photons is higher for model Q than for QG, the difference between the dot-dashed and solid contours reflects the effect of changing the spectral hardness. Comparing these two contours, we see that, at a fixed H ionization rate, harder spectra tend to inhibit the cooling more than softer spectra

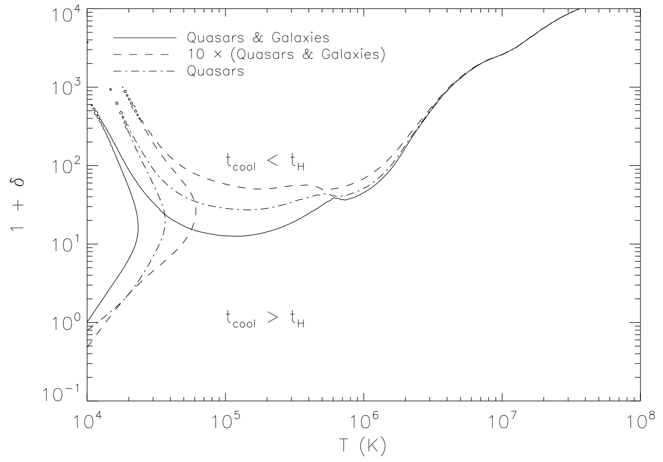

**Figure 2.5**: Contours show where the net cooling time equals the Hubble time in the density contrast - temperature plane for gas of solar metallicity at $z = 0$. The solid contour is for the HM01 model for the $z = 0$ UV/X-ray background from galaxies and quasars (model QG), the dashed contour is for a radiation field with the same spectral shape as model QG, but 10 times the intensity, and the dot-dashed contour is for the HM01 quasars only radiation field, scaled to the same hydrogen ionization rate as model QG. Each contour comprises two components, corresponding to net heating (low temperature component) and net cooling (high temperature component), respectively, which merge near the (density-dependent) thermal equilibrium temperature.

for temperatures above the equilibrium value (the $t_{\rm cool} = t_H$ contour moves to higher densities for harder spectra). This happens because collisional excitation of heavy ions involves electrons with higher ionization energies than hydrogen. The extra high energy photons will remove many of those electrons, thus reducing the cooling rates further. For temperatures below the equilibrium value, however, the net cooling time actually decreases (the lower-left of the left contour moves to lower densities for harder spectra) because the photo-heating rates are larger for harder spectra.

In summary, for densities and temperatures characteristic of the WHIM the nature of the ionizing radiation field as well as the metallicity of the gas may have a significant impact. Accurate cooling rates therefore require a correct treatment of the composition of the gas, the spectral hardness, and the radiation intensity. Simple models may result in a poor estimate of the amount of baryons in the WHIM phase.

## 2.5 THE RELATIVE IMPORTANCE OF DIFFERENT ELEMENTS

For solar abundances, a large number of elements contribute to the radiative cooling rate. The black, solid curve in the left-hand panel of Figure 2.6 shows the normalized cooling rate ($\Lambda/n_{\rm H}^2$) as a function of temperature for a plasma in pure CIE and for solar abundances, reproducing previous work done on this subject (e.g., Cox & Tucker 1969;

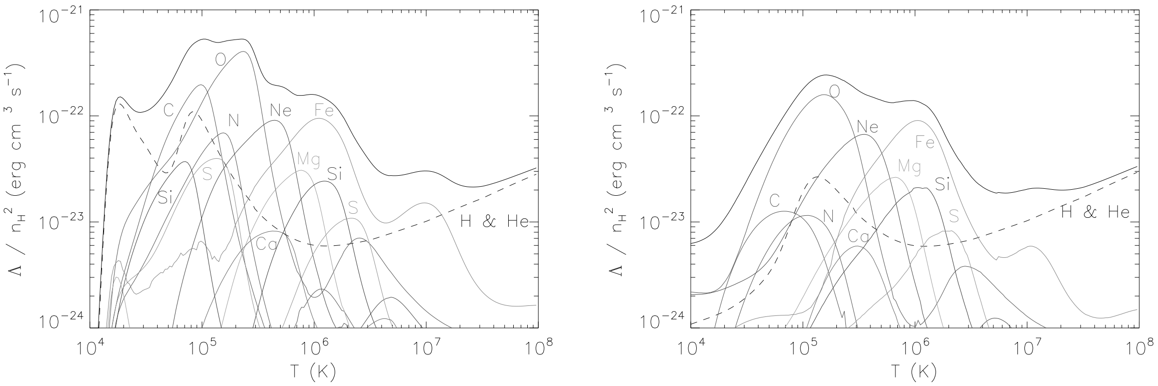

**Figure 2.6**: Normalized cooling rates as a function of temperature for solar abundances, assuming either CIE (*left-hand panel*) or photo-ionization equilibrium for $n_{\rm H} = 10^{-4}\,{\rm cm}^{-3}$ and an optically thin gas exposed to the $z = 3$ HM01 model for the meta-galactic UV/X-ray background from quasars and galaxies (*right-hand panel*). Note that normalized cooling rates are independent of the density for CIE, but not for photo-ionization equilibrium. The black, solid curve indicates the total cooling rate and the thin, grey, solid curves show the contributions from individual elements. The black, dashed curve shows the contribution from H and He.

Raymond et al. 1976; Shull & van Steenberg 1982; Gaetz & Salpeter 1983; Boehringer & Hensler 1989; Sutherland & Dopita 1993; Landi & Landini 1999; Benjamin et al. 2001; Gnat & Sternberg 2007; Smith et al. 2008). The thin, coloured, solid curves show the contributions from individual elements, while the black, dashed curve shows the total cooling rate due to H and He. For $T \gg 10^7$ K Bremsstrahlung (i.e., H & He) dominates, but at lower temperatures line radiation is most important. Going down from $10^7$ K to $10^4$ K the cooling rate is successively dominated by iron, neon, oxygen, carbon, and hydrogen.

If the cooling rate is dominated by a single element, as is for example the case for oxygen at $T \approx 2 \times 10^5$ K and for iron at $T \sim 10^6$ K, then the total cooling rate will be sensitive to the relative abundances of those elements. For instance, since $[{\rm O/Fe}]$ is observed to vary with environment by factors of two or so at a fixed metallicity (e.g., Shetrone et al. 2003), we can expect similar variations in the cooling rates.

We next turn on the HM01 ionizing background and illustrate the results for $n_{\rm H} = 10^{-4}\,{\rm cm}^{-3}$ and $z = 3$ in the right-hand panel of Figure 2.6 (recall that the left-hand panel is independent of both density and redshift). For this figure we have excluded Compton cooling off the CMB to isolate the impact of the ionizing radiation and because the former is only important at high redshift. We can see that photo-ionization affects some elements more than others. As we have seen before, the effect is stronger for lower temperatures. Although we show the results for only a single density here, we note that the importance of photo-ionization increases with decreasing density.

Comparing the cooling rates including photo-ionization (right-hand panel of figure 2.6) to those for CIE (left-hand panel of figure 2.6) shows that photo-ionization increases the relative importance of oxygen and decreases that of carbon, helium, and especially hydrogen. It is also clear that many of the peaks of the various elements shift to lower temperatures when an ionizing radiation field is present. This shift occurs because a photo-ionized gas is overionized for its temperature compared to a collisionally ionized plasma. If the ion fractions peak at lower temperatures, then so will the cooling rates due to collisional excitation of those ions.

This last figure illustrates the central result of this work: photo-ionization changes both the total cooling rates and the relative importance of individual elements. For a more complete visualization of this point, we kindly refer the interested reader to our web site[11], where we host a number of videos, plots, and the tables themselves for download.

## 2.6 DISCUSSION

Radiative cooling is an essential ingredient of hydrodynamical models of a wide range of astrophysical objects, ranging from the IGM to (proto-)galaxies and molecular clouds. While numerical simulations of objects with a primordial composition often compute non-equilibrium radiative cooling rates explicitly and sometimes even include the effect of ionizing background radiation, the treatment of cooling of chemically enriched material is typically much more approximate. For example, simulations of galaxy formation typically either ignore metal-line cooling altogether or include it assuming pure CIE. In addition, the abundances of all heavy elements are typically scaled by the same factor (the metallicity) (but see Martínez-Serrano et al. 2008 and Maio et al. 2007 for recent exceptions). In this simplified treatment metal-line cooling depends only on temperature and metallicity, allowing straightforward interpolation from pre-computed two-dimensional tables.

We have used CLOUDY to investigate the effects of heavy elements and ionizing radiation on the radiative cooling of gas with properties characteristic of (proto-)galaxies and the IGM, i.e., optically thin gas with densities $n_{\rm H} \lesssim 1\,{\rm cm}^{-3}$ and temperatures $T \gtrsim 10^4\,{\rm K}$, assuming ionization equilibrium. We presented a method to incorporate radiative cooling on an element-by-element basis including photo-ionization by an evolving UV/X-ray background, using precomputed tables, which for heavy elements are functions of density, temperature, and redshift and for H&He (which must be considered together because they are important contributors to the free electron density) depend additionally on the He/H ratio. Using the 11 elements H, He, C, N, O, Ne, Mg, Si, S, Ca, and Fe, the redshift $z = 0$ median absolute errors in the net cooling rate range from 0.33%, at $Z = 0.1 Z_\odot$ to 6.1% for the extreme metallicity $Z = 10 Z_\odot$, and the errors are smaller for higher redshifts.

The tables as well as some scripts that illustrate how to use them are available from the following web site: `http://www.strw.leidenuniv.nl/WSS08/`. We also include tables for solar relative abundances which can be used if metallicity, but not the abundances of individual elements are known, as in equation (2.5). This web site also contains a number of videos that may be helpful to gain intuition on the importance of various parameters on the cooling rates.

---

[11] `http://www.strw.leidenuniv.nl/WSS08/`.

We confirmed that, assuming CIE, heavy elements greatly enhance the cooling rates for metallicities $Z \gtrsim 10^{-1}\ Z_\odot$ and temperatures $T \lesssim 10^7\,\mathrm{K}$. We demonstrated that this remains true in the presence of photo-ionization by the meta-galactic UV/X-ray background.

The background radiation removes electrons that would otherwise be collisionally excited, thus reducing the cooling rates. The effect is stronger for higher ionization parameters (i.e., higher radiation intensities or lower densities) and if the spectral shape of the radiation field is harder. Considering only the meta-galactic radiation field, which provides a lower limit to the intensity of the radiation to which optically thin gas may be exposed, the reduction of the metal-line cooling rates becomes important below $10^6\,\mathrm{K}$ for ionization parameters $U \gtrsim 10^{-1}$ and below $10^5\,\mathrm{K}$ for $U \gtrsim 10^{-3}$ (note that for the HM01 background $U = 9 \times 10^{-7}/n_\mathrm{H}$ and $2 \times 10^{-5}/n_\mathrm{H}$ at $z = 0$ and $z = 3$, respectively).

As an example of the potential importance of including the effects of both photo-ionization and heavy elements, we considered the so-called warm-hot intergalactic medium (WHIM), which is thought to contain a large fraction of the baryons at redshifts $z < 1$. We demonstrated that the overdensities for which gas at typical WHIM metallicities ($Z \sim 10^{-1}\ Z_\odot$) and temperatures ($T \sim 10^5 - 10^7\,\mathrm{K}$) can cool within a Hubble time, can shift by an order of magnitude depending on whether photo-ionization and metal-line cooling are taken into account. Hence, photo-ionization of heavy elements may have important consequences for predictions of the amount of matter contained in this elusive gas phase.

Because chemical enrichment happens in a number of stages, involving a number of processes with different timescales, the relative abundances of the heavy elements varies with redshift and environment by factors of a few. Hence, computing cooling rates on an element-by-element basis rather than scaling all elements by the metallicity, will change the cooling rates by factors of a few. The difference is therefore typically somewhat smaller than the effect of neglecting metals or photo-ionization altogether, but still highly significant.

While it was known that different elements dominate the cooling for different temperatures in CIE, we showed that photo-ionization both shifts the peaks due to individual elements to smaller temperatures and reduces their amplitude. Note that since photo-ionization over-ionizes the gas, this effect is similar (but not equivalent to) that found in non-equilibrium calculations without ionizing radiation (e.g., Sutherland & Dopita 1993; Gnat & Sternberg 2007). Because the importance of photo-ionization depends on the ionization parameter, the relative contributions of individual elements exposed to a fixed ionizing radiation field depends also on the gas density.

Would dropping our assumption of ionization equilibrium have a large effect on the cooling rates? Ionizing radiation results in a plasma that is overionized relative to its temperature. Its effect is therefore similar to that of non-equilibrium ionization following rapid cooling (i.e., if the cooling time is shorter than the recombination times of the ions dominating the cooling, see e.g., Kafatos 1973; Shapiro & Moore 1976). We therefore anticipate that the effect of non-equilibrium ionization will be much smaller for our cooling rates than for those that assume CIE.

The assumptions that the gas is optically thin and exposed only to the meta-galactic background radiation are likely to be more important than the assumption of ionization equilibrium, particularly since non-equilibrium collisional cooling rates only differ from those assuming CIE by factors of a few or less (e.g., Schmutzler & Tscharnuter 1993; Sutherland & Dopita 1993; Gnat & Sternberg 2007). For column densities $N_{\rm HI} > 10^{17}\,{\rm cm}^{-2}$ self-shielding becomes important and only part of the H-ionizing radiation will penetrate the gas cloud, which would particularly affect the cooling rates for $T \lesssim 10^5\,{\rm K}$. At higher temperatures line cooling is dominated by heavier ions, which can only be ionized by higher energy photons and which therefore remain optically thin up to much higher column densities. This is because the photo-ionization cross sections of H and He drop rapidly with increasing frequency for energies exceeding their ionization potentials. Moreover, for $T \gg 10^4$ K hydrogen is collisionally ionized to a high degree and consequently the optical depth for ionizing radiation will be significantly reduced.

It is, however, far from clear that high column densities would reduce the effect of radiation. For self-shielded clouds the cooling radiation may itself be trapped, providing a source of ionizing radiation even in the absence of an external one (e.g., Shapiro & Moore 1976; Gnat & Sternberg 2007). Moreover, gas clouds with columns that exceed $10^{17}$ cm$^{-2}$ are on average expected to be sufficiently close to a galaxy that local sources of ionizing radiation dominate over the background (Schaye 2006; Miralda-Escudé 2005).

Ultimately, these issues can only be resolved if non-equilibrium cooling rates are computed including radiative transfer and if the locations of all relevant sources of ionizing radiation are known. It will be some time before it is feasible to carry out such a calculation in, say, a cosmological hydrodynamical simulation. In the mean time, we believe that our element-by-element calculation of the equilibrium cooling rates for an optically thin gas exposed to the CMB and an evolving UV/X-ray background provides a marked improvement over earlier treatments. In future publications we will present cosmological, hydrodynamical simulations using these cooling rates.

## ACKNOWLEDGMENTS

We are grateful to the anonymous referee whose helpful comments greatly improved the manuscript. We are also grateful to Gary Ferland for help with CLOUDY and to Brent Groves for help with MAPPINGS III. We would also like to thank Tom Abel and the members of the OWLS collaboration for discussions. In particular, we are grateful to Tom Theuns for showing us the benefits of HDF5. This work was supported by Marie Curie Excellence Grant MEXT-CT-2004-014112.

## REFERENCES

Benjamin R. A., Benson B. A., Cox D. P., 2001, ApJ, 554, L225

Benson A. J., Lacey C. G., Baugh C. M., Cole S., Frenk C. S., 2002, MNRAS, 333, 156

Bertone S., Schaye J., Dolag K., 2008, Space Science Reviews, 134, 295

Boehringer H., Hensler G., 1989, A&A, 215, 147

Cen R., Ostriker J. P., 1999, ApJ, 514, 1

Coles P., Lucchin F., 2002, Cosmology: The Origin and Evolution of Cosmic Structure, Second Edition. Cosmology: The Origin and Evolution of Cosmic Structure, Second Edition, by Peter Coles, Francesco Lucchin, pp. 512. ISBN 0-471-48909-3. Wiley-VCH , July 2002.

Cox D. P., Tucker W. H., 1969, ApJ, 157, 1157

Efstathiou G., 1992, MNRAS, 256, 43P

Ferland G. J., Korista K. T., Verner D. A., Ferguson J. W., Kingdon J. B., Verner E. M., 1998, PASP, 110, 761

Gaetz T. J., Salpeter E. E., 1983, ApJS, 52, 155

Gnat O., Sternberg A., 2007, ApJS, 168, 213

Groves B., Dopita M. A., Sutherland R. S., Kewley L. J., Fischera J., Leitherer C., Brandl B., van Breugel W., 2008, ApJS, 176, 438

Haardt F., Madau P., 2001, in Neumann D. M., Tran J. T. V., eds, Clusters of Galaxies and the High Redshift Universe Observed in X-rays Modelling the UV/X-ray cosmic background with CUBA

Kafatos M., 1973, ApJ, 182, 433

Komatsu E., Dunkley J., Nolta M. R., Bennett C. L., Gold B., Hinshaw G., Jarosik N., Larson D., Limon M., Page L., Spergel D. N., Halpern M., Hill R. S., Kogut A., Meyer S. S., Tucker G. S., Weiland J. L., Wollack E., Wright E. L., 2008, ArXiv e-prints, 803

Landi E., Landini M., 1999, A&A, 347, 401

Leonard A., 1998, PhD thesis, University of Oxford

Maio U., Dolag K., Ciardi B., Tornatore L., 2007, MNRAS, 379, 963

Martínez-Serrano F. J., Serna A., Domínguez-Tenreiro R., Mollá M., 2008, ArXiv e-prints, 804

Miralda-Escudé J., 2005, ApJ, 620, L91

Raymond J. C., Cox D. P., Smith B. W., 1976, ApJ, 204, 290

Schaye J., 2006, ApJ, 643, 59

Schmutzler T., Tscharnuter W. M., 1993, A&A, 273, 318

Shapiro P. R., Moore R. T., 1976, ApJ, 207, 460

Shetrone M., Venn K. A., Tolstoy E., Primas F., Hill V., Kaufer A., 2003, AJ, 125, 684

Shull J. M., van Steenberg M., 1982, ApJS, 48, 95

Smith B., Sigurdsson S., Abel T., 2008, MNRAS, 385, 1443

Sutherland R. S., Dopita M. A., 1993, ApJS, 88, 253

# CHAPTER 3

# Chemical enrichment in cosmological, SPH simulations

Robert P. C. Wiersma, Joop Schaye, Tom Theuns, Claudio Dalla Vecchia,
and Luca Tornatore

Monthly Notices of the Royal Astronomical Society, 399, 574, 2009

We present an implementation of stellar evolution and chemical feedback for smoothed particle hydrodynamics (SPH) simulations. We consider the timed release of individual elements by both massive and intermediate mass stars. We contrast two reasonable definitions of the metallicity of a resolution element and find that while they agree for high metallicities, there are large differences at low metallicities. We argue the discrepancy is indicative of the lack of metal mixing caused by the fact that metals are stuck to particles. We argue that since this is a (numerical) sampling problem, solving it using a poorly constrained physical process such as diffusion could have undesired consequences. We demonstrate that the two metallicity definitions result in redshift $z = 0$ stellar masses that can differ by up to a factor of one and a half, because of the sensitivity of the cooling rates to the elemental abundances.

Finally, we use several $512^3$ particle simulations to investigate the evolution of the distribution of heavy elements, which we find to be in reasonably good agreement with available observational constraints. We find that by $z = 0$ most of the metals are locked up in stars. The gaseous metals are distributed over a very wide range of gas densities and temperatures. The shock-heated warm-hot intergalactic medium has a relatively high metallicity of $\sim 10^{-1}\,Z_\odot$ that evolves only weakly and is therefore an important reservoir of metals. Any census aiming to account for most of the metal mass will have to take a wide variety of objects and structures into account.

## 3.1 INTRODUCTION

Nucleosynthetic processes within stars and supernovae (SNe) change the abundances of elements in the Universe over time. As stars release these elements back into the diffuse interstellar medium (ISM) that surrounds them, subsequent generations of stars are born with different chemical compositions. On larger scales, winds driven out of galaxies by the energy released by dying stars and/or active galactic nuclei modify the composition of the intergalactic medium (IGM) and hence that of future galaxies. The IGM within groups and clusters of galaxies exerts a ram-pressure on their member galaxies as they move along their orbits. This head-wind can be sufficiently strong to strip the ISM from the galaxies, thus mixing the elements that were present in the ISM into the IGM. These and other processes make the (re-)cycling of elements over time through stars, galaxies and diffuse gas a complicated problem that is well-suited for studies using hydrodynamical simulations.

Simulating the exchange of elements between stars, galaxies, and their environments is the subject of this chapter. Specifically, this chapter describes and tests a method to follow the timed release and subsequent spreading of elements by stellar populations formed in cosmological, hydrodynamical simulations.

The elemental abundances of stars, galaxies, and diffuse gas are of great interest for a variety of reasons. First, the dissipation of binding energy by the emission of "cooling" radiation is a fundamental ingredient of models of the formation of both stars and galaxies. Because radiative cooling rates are very sensitive to abundance variations, the rate at which gas can collapse into galaxies is to a large extent determined by its chemical composition. Similarly, the initial mass function (IMF) of stars may well depend on the chemical composition of the gas from which they formed.

Second, knowledge of elemental abundances can give great insight into a variety of key astrophysical processes. For example, the distribution of elements in the IGM provides stringent constraints on models of galactic winds and ram-pressure stripping in clusters. The relative abundances of elements can tell us about the IMF of the stars that produced them. The abundance of alpha elements - which are released on short time-scales through core collapse SNe - relative to iron - most of which is released much later when intermediate mass stars explode as type Ia SNe - tells us about the time-scale on which stars have been formed. On the other hand, the absolute abundances of metals provide us with a measure of the integral of past star formation.

Third, emission and absorption lines of individual elements constitute key diagnostics of physical conditions, such as gas densities, temperatures, radiation fields and dust content. The strengths of said lines depend on a number of factors, but invariably the abundances play an important role.

Fourth, individual lines are the only observable signatures for most of the diffuse gas in the Universe. For example, oxygen lines are the most promising tools to detect the warm-hot IGM that may host a large fraction of the cosmic baryons. To verify this prediction of structure formation in a cold dark matter universe, it is necessary to know the abundance of oxygen in this elusive gas phase.

Clearly, following the timed release of the elements by stars and their subsequent dispersal through space, a collection of processes sometimes referred to as "chemodynamics", is a critical ingredient of any realistic simulation of the formation and evolution of galaxies. The implementation of chemodynamics into cosmological simulations is a challenging problem, mainly because such models lack the resolution to resolve many of the relevant physical processes and hence require "sub-grid" recipes.

The first study to implement metal enrichment into a Smoothed Particle Hydrodynamics (SPH) code did not distinguish between different elements and only considered enrichment by core collapse SNe in the instantaneous recycling approximation (Steinmetz & Mueller 1994). Since then many authors have implemented more sophisticated recipes for chemodynamics into SPH codes (e.g. Raiteri et al. 1996; Berczik 1999; Mosconi et al. 2001; Kawata 2001; Lia et al. 2002; Kawata & Gibson 2003; Valdarnini 2003; Kobayashi 2004a; Sommer-Larsen et al. 2005; Tornatore et al. 2007; Oppenheimer & Davé 2008), ranging from recipes that distinguish only between SN type Ia and SN type II elements to models that follow large numbers of individual elements released by AGB stars, SNe Ia, SNe II, and the winds from their progenitors. Three-dimensional chemodynamical simulations have so far been used most often for the study of individual objects such as galaxies (e.g. Theis et al. 1992; Raiteri et al. 1996; Berczik 1999; Recchi et al. 2001; Kawata 2001; Kawata & Gibson 2003; Kobayashi 2004a; Mori & Umemura 2006; Governato et al. 2007) and clusters of galaxies (e.g. Lia et al. 2002; Valdarnini 2003; Tornatore et al. 2004; Sommer-Larsen et al. 2005; Romeo et al. 2006; Tornatore et al. 2007; see Borgani et al. 2008 for a review), but in recent years chemodynamical cosmological simulations have also become more common (e.g. Mosconi et al. 2001; Scannapieco et al. 2005; Kobayashi et al. 2007; Oppenheimer & Davé 2008). Note that several recent cosmological works (Scannapieco et al. 2005; Kobayashi et al. 2007; Oppenheimer & Davé 2008) use our hydrodynamical code of choice, namely the SPH code GADGET (Springel 2005), although they use different implementations of chemodynamics, star formation, galactic winds, and radiative cooling.

Here we present a new implementation of chemodynamics that follows the timed release – by AGB stars, SNe Ia, SNe II, and the winds from their progenitors – of the 11 elements that we found in chapter 2 to contribute significantly to the radiative cooling at $T > 10^4$ K. We present a subset of high-resolution cosmological, hydrodynamical simulations taken from the OverWhelmingly Large Simulations (OWLS) project (Schaye et al. 2009) and use them to test the robustness of our prescription to numerical parameters and to make some predictions regarding the large-scale distribution of heavy elements. These simulations include element-by-element cooling, a first for cosmological chemodynamical simulations, and they take the effect of photo-ionization by the UV/X-ray background radiation on the cooling rates into account, which is normally either ignored or included only for hydrogen and helium. While this chapter focuses on a single implementation of the relevant physics, we will present the effects of varying the physical parameters (e.g., stellar IMF, star formation, cooling, feedback from star formation) and make use of a larger fraction of the OWLS data set in chapter 4.

This chapter is organized as follows. The simulations and the prescriptions used for star formation, feedback from star formation, and radiative cooling are summarized in §3.2. In §3.3 we discuss in some detail the ingredients that we take from models of

**Table 3.1**: Adopted solar abundances.

| Element | $n_i/n_{\rm H}$ | Mass Fraction |
|---|---|---|
| H | 1 | 0.7065 |
| He | 0.1 | 0.2806 |
| C | $2.46 \times 10^{-4}$ | $2.07 \times 10^{-3}$ |
| N | $8.51 \times 10^{-5}$ | $8.36 \times 10^{-4}$ |
| O | $4.90 \times 10^{-4}$ | $5.49 \times 10^{-3}$ |
| Ne | $1.00 \times 10^{-4}$ | $1.41 \times 10^{-3}$ |
| Mg | $3.47 \times 10^{-5}$ | $5.91 \times 10^{-4}$ |
| Si | $3.47 \times 10^{-5}$ | $6.83 \times 10^{-4}$ |
| S | $1.86 \times 10^{-5}$ | $4.09 \times 10^{-4}$ |
| Ca | $2.29 \times 10^{-6}$ | $6.44 \times 10^{-5}$ |
| Fe | $2.82 \times 10^{-5}$ | $1.10 \times 10^{-3}$ |

stellar evolution or observations, including the IMF, stellar lifetimes, stellar yields, and SN Ia rates. In §3.5 we discuss how we combine all these ingredients to predict the mass released by a simple stellar population as a function of its age and present some results. Our implementation of chemodynamics into SPH is discussed in §3.6. This section also contrasts two possible definitions of elemental abundances in SPH and demonstrates that the choice of definition can be extremely important due to limitations intrinsic to SPH. In §3.7 we use our simulations to address the question "Where are the metals?" and we show how the answer is influenced by the definition of metallicity that is used. Finally, we provide a detailed summary in §3.8 and investigate convergence with the size of the simulation box and with resolution in appendices 3.A and 3.B, respectively.

For the solar abundance we use the metal mass fraction $Z_\odot = 0.0127$, corresponding to the value obtained using the default abundance set of CLOUDY (version 07.02; last described by Ferland et al. 1998). This abundance set (see Table 3.1) combines the abundances of Allende Prieto et al. (2001, 2002) for C and O, Holweger (2001) for N, Ne, Mg, Si, and Fe, and assumes $n_{\rm He}/n_{\rm H} = 0.1$ which is a typical value for nebular with near-solar compositions. Note that much of the literature assumes $Z_\odot = 0.02$, which is 0.2 dex higher than the value used here.

## 3.2 SIMULATIONS

We performed cosmological, gas-dynamical simulations using a modified version of the $N$-body Tree-PM, SPH code GADGET III, which is a modified version of the code GADGET II (Springel 2005). Our prescriptions for star formation, for feedback from core collapse supernovae and for radiative cooling and heating are summarized below. Our prescription for stellar evolution, which is the subject of this chapter, is described in detail in the next section.

We use the suite of simulations of varying box sizes and particle numbers listed in Table 3.2 together with the corresponding particle masses and gravitational force

**Table 3.2**: List of simulations used. The columns give the comoving size of the box $L$, the total number of particles per component $N$ (dark matter and baryons), the initial baryonic particle mass $m_{\rm b}$, the dark matter particle mass $m_{\rm dm}$, the (Plummer-equivalent) comoving softening length $\epsilon_{\rm com}$, the maximum (Plummer-equivalent) proper softening length $\epsilon_{\rm prop}$, and the redshift at which the simulation was stopped $z_{\rm end}$.

| Simulation | $L$ $(h^{-1}\,\rm Mpc)$ | $N$ | $m_{\rm b}$ $(h^{-1}\,\rm M_\odot)$ | $m_{\rm dm}$ $(h^{-1}\,\rm M_\odot)$ | $\epsilon_{\rm com}$ $(h^{-1}\,\rm kpc)$ | $\epsilon_{\rm prop}$ $(h^{-1}\,\rm kpc)$ | $z_{\rm end}$ |
|---|---|---|---|---|---|---|---|
| L006N128 | 6.25 | $128^3$ | $1.4 \times 10^6$ | $6.3 \times 10^6$ | 1.95 | 0.5 | 2 |
| L012N256 | 12.50 | $256^3$ | $1.4 \times 10^6$ | $6.3 \times 10^6$ | 1.95 | 0.5 | 2 |
| L025N128 | 25.00 | $128^3$ | $8.7 \times 10^7$ | $4.1 \times 10^8$ | 7.81 | 2.0 | 0 |
| L025N256 | 25.00 | $256^3$ | $1.1 \times 10^7$ | $5.1 \times 10^7$ | 3.91 | 1.00 | 2 |
| L025N512 | 25.00 | $512^3$ | $1.4 \times 10^6$ | $6.3 \times 10^6$ | 1.95 | 0.5 | 1 |
| L050N256 | 50.00 | $256^3$ | $8.7 \times 10^7$ | $4.1 \times 10^8$ | 7.81 | 2.0 | 0 |
| L050N512 | 50.00 | $512^3$ | $1.1 \times 10^7$ | $5.1 \times 10^7$ | 3.91 | 1.0 | 0 |
| L100N128 | 100.00 | $128^3$ | $5.5 \times 10^9$ | $2.6 \times 10^{10}$ | 31.25 | 8.0 | 0 |
| L100N256 | 100.00 | $256^3$ | $6.9 \times 10^8$ | $3.2 \times 10^9$ | 15.62 | 4.0 | 0 |
| L100N512 | 100.00 | $512^3$ | $8.7 \times 10^7$ | $4.1 \times 10^8$ | 7.81 | 2.0 | 0 |

softening scales [1]. We use fixed comoving softening scales down to $z = 2.91$ below which we switch to a fixed proper scale. Our largest simulations use $2 \times 512^3$ particles in boxes of comoving size $L = 25$, $50$, and $100\ h^{-1}\,\rm Mpc$.

The initial particle positions and velocities are obtained from glass-like (White 1994) initial conditions using CMBFAST (version 4.1; Seljak & Zaldarriaga 1996) and employing the Zeldovich approximation to linearly evolve the particles down to redshift $z = 127$. We assume a flat ΛCDM universe and employ the set of cosmological parameters $[\Omega_m, \Omega_b, \Omega_\Lambda, \sigma_8, n_s, h] = [0.238, 0.0418, 0.762, 0.74, 0.951, 0.73]$, as determined from the WMAP 3-year data and consistent[2] with the WMAP 5-year data (Komatsu et al. 2008). In addition, the primordial helium mass fraction was set to $X_{\rm H} = 0.248$.

We employ the star formation recipe of Schaye & Dalla Vecchia (2008), to which we refer the reader for details. Briefly, gas with densities exceeding the critical density for the onset of the thermo-gravitational instability ($n_{\rm H} \sim 10^{-2} - 10^{-1}\ \rm cm^{-3}$) is expected to be multiphase and star-forming (Schaye 2004). We therefore impose an effective equation of state with pressure $P \propto \rho_g^{\gamma_{\rm eff}}$ for densities exceeding $n_{\rm H} = 0.1\ \rm cm^{-3}$, normalized to $P/k = 10^3\ \rm cm^{-3}\,K$ for an atomic gas at the threshold density. We use $\gamma_{\rm eff} = 4/3$ for which both the Jeans mass and the ratio of the Jeans length and the SPH kernel are independent of the density, thus preventing spurious fragmentation due to a lack of numerical resolution.

The local Kennicutt-Schmidt star formation law is analytically converted and implemented as a pressure law. As we demonstrated in Schaye & Dalla Vecchia (2008),

---

[1] We give the Plummer equivalent values, that is to say, that the Newtonian potential of a point mass in non-periodic space is $Gm/\epsilon$, the same as for a Plummer 'sphere' of size $\epsilon$ (see Springel 2005, for more details)

[2] Our value of $\sigma_8$ is $1.6\,\sigma$ lower than allowed by the WMAP 5-year data.

our method allows us to reproduce arbitrary input star formation laws for any equation of state without tuning any parameters. We use the observed Kennicutt (1998) law,

$$\dot{\Sigma}_* = 1.5 \times 10^{-4}\,\mathrm{M_\odot yr^{-1} kpc^{-2}} \left( \frac{\Sigma_\mathrm{g}}{1\ \mathrm{M_\odot pc^{-2}}} \right)^{1.4}, \tag{3.1}$$

where we divided Kennicutt's normalization by a factor 1.65 to account for the fact that it assumes a Salpeter IMF whereas we are using a Chabrier (2003) IMF.

Galactic winds are implemented as described in Dalla Vecchia & Schaye (2008). Briefly, after a short delay of $t_\mathrm{SN} = 3\times 10^7$ yr, corresponding to the maximum lifetime of stars that end their lives as core-collapse supernovae, newly-formed star particles inject kinetic energy into their surroundings by kicking a fraction of their neighbours in a random direction. The simulations presented here use the default parameters of Dalla Vecchia & Schaye (2008), which means that each SPH neighbour $i$ of a newly-formed star particle $j$ has a probability of $\eta m_j / \sum_{i=1}^{N_\mathrm{ngb}} m_i$ of receiving a kick with a velocity $v_\mathrm{w}$. We choose $\eta = 2$ and $v_\mathrm{w} = 600\ \mathrm{km\,s^{-1}}$ (i.e., if all baryonic particles had equal mass, each newly formed star particle would kick, on average, two of its neighbours). Assuming that each star with initial mass in the range $6 - 100\ \mathrm{M_\odot}$ injects $10^{51}$ erg of kinetic energy, these parameters imply that the total wind energy accounts for 40 per cent of the available kinetic energy for a Chabrier IMF and a stellar mass range $0.1 - 100\ \mathrm{M_\odot}$ (if we consider only stars in the mass range $8 - 100\ \mathrm{M_\odot}$ for type II SNe, this works out to be 60 per cent). The value $\eta = 2$ was chosen to roughly reproduce the peak in the cosmic star formation rate. Note that contrary to the widely-used kinetic feedback recipe of Springel & Hernquist (2003), the kinetic energy is injected *locally* and the wind particles are *not* decoupled hydrodynamically. As discussed by Dalla Vecchia & Schaye (2008), these differences have important consequences.

Radiative cooling was implemented according to chapter 2[3]. In brief, net radiative cooling rates are computed element-by-element in the presence of the cosmic microwave background (CMB) and a Haardt & Madau (2001, hereafter HM01) model for the UV/X-ray background radiation from quasars and galaxies. The contributions of the eleven elements hydrogen, helium, carbon, nitrogen, oxygen, neon, magnesium, silicon, sulphur, calcium, and iron are interpolated as a function of density, temperature, and redshift from tables that have been pre-computed using the publicly available photo-ionization package CLOUDY, last described by Ferland et al. (1998), assuming the gas to be optically thin and in (photo-)ionization equilibrium.

Hydrogen reionization is implemented by turning on the evolving, uniform ionizing background at redshift $z = 9$. Prior to this redshift the cooling rates are computed using the CMB and a photo-dissociating background which we obtain by cutting off the $z = 9$ HM01 spectrum at 1 Ryd. Note that the presence of a photo-dissociating background suppresses $H_2$ cooling at all redshifts.

Our assumption that the gas is optically thin may lead to an underestimate of the temperature of the IGM shortly after reionization (e.g. Abel & Haehnelt 1999). Moreover, it is well known that without extra heat input, hydrodynamical simulations underestimate the temperature of the IGM at $z \gtrsim 3$, the redshift around which helium

---

[3] We used their equation (3) rather than (4) and CLOUDY version 05.07 rather than 07.02.

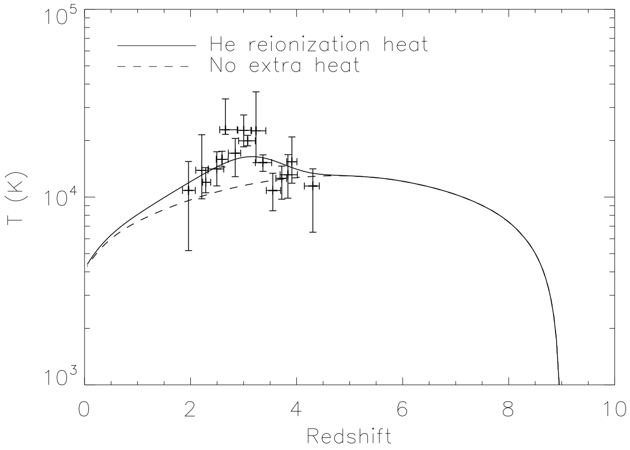

**Figure 3.1**: A comparison between the simulated and observed evolution of the temperature of gas with density equal to the cosmic mean. The dashed curve indicates the temperature evolution for a gas parcel undergoing Hubble expansion, computed using the same radiative cooling and heating rates as are used in our simulations for gas of primordial composition. These net cooling rates include the effects of the CMB and, below $z = 9$, of the evolving UV/X-ray background (UVB) from galaxies and quasars as modeled by HM01, assuming the gas to be optically thin and in ionization equilibrium. The redshift of hydrogen reionization was set to $z = 9$ by turning on the UVB at this redshift, resulting in a steep increase of the temperature to $T \sim 10^4$ K. A comparison with with the data points of Schaye et al. (2000), which were derived from the widths of Ly$\alpha$ absorption lines, shows that the simulation underestimates the temperature at $z \approx 3$, the redshift around which the reionization of helium is thought to have ended. To mimic the expected extra heat input, relative to the optically thin limit, during helium reionization, the solid curve shows the result of injecting an extra $2$ eV per proton, smoothed with a $\sigma(z) = 0.5$ Gaussian centered at $z = 3.5$. The reduced $\chi^2$ for the solid and dashed curves is 1.1 and 4.5, respectively.

reionization is thought to have ended (e.g. Theuns et al. 1998, 1999; Bryan et al. 1999; Schaye et al. 2000; Ricotti et al. 2000). We therefore inject $2$ eV per proton, smoothed with a $\sigma(z) = 0.5$ Gaussian centered at $z = 3.5$. Figure 3.1 shows that with this extra energy, the predicted temperature at the mean density agrees well with the measurements of Schaye et al. (2000).

## 3.3 INGREDIENTS FROM STELLAR EVOLUTION

Cosmological simulations cannot at present resolve individual stars. Instead, a single particle is taken to represent a population of stars of a single age, a so-called simple stellar population (SSP), with some assumed stellar initial mass function (IMF). The task of stellar evolution modules in cosmological hydrodynamical simulations is to implement the timed release of kinetic energy and mass by star particles. The feedback processes originating from stellar evolution that we will consider are winds from asymptotic giant branch (AGB) stars, type Ia supernovae (SNe), type II (i.e. core collapse) SNe[4] and the winds from their progenitors. The above stellar processes differ in a number of ways, such as their nucleosynthetic production, their energetic output, and the timescale on which they act.

Progenitors associated with AGB stars are typically intermediate mass ($0.8~\mathrm{M}_\odot \leq M \leq 8~\mathrm{M}_\odot$) stars which have long ($10^8~\mathrm{yr} \lesssim \tau \lesssim 10^{10}~\mathrm{yr}$) main sequence lifetimes (see Kippenhahn & Weigert 1994). For AGB stars the mass loss occurs during a period that is very short compared with both their lifetimes and the dynamical timescales in cosmological simulations and we therefore assume the mass loss for an AGB star of given mass to happen within a single simulation time step at the end of the main sequence lifetime. The kinetic energy injected by AGB stars is assumed to be unimportant, which is an excellent approximation both because observed AGB wind velocities are not large compared to the velocity dispersion in the ISM and because it takes an SSP billions of years for all the energy to be released. AGB stars are major producers of carbon and nitrogen, both of them being among the few elements that can be detected in the diffuse IGM (e.g. Schaye et al. 2003; Fechner & Richter 2008).

Since type II SNe (SNII) only result from massive stars (see Crowther & Smartt 2007, and references therein), most of these events take place within tens of millions of years after the birth of a stellar population. For SNII progenitors mass loss on the main sequence can be substantial. However, since their main sequence lifetimes are short compared with the dynamical timescales in cosmological simulations, it is still a good approximation to release all the mass ejected by stars of a fixed initial mass in a single time step at the end of their lifetimes. Note that if the time step governing a star particle is shorter than the lifetime of the least massive SNII progenitor, then the mass will still be ejected over multiple time steps.

Type II SNe explosions dump so much energy in the ISM ($\sim 10^{51}$ erg of kinetic energy per SN) in a short time that they may drive galactic-scale outflows from starburst-

---

[4] Type Ib and Ic SN are also core collapse supernova, but we follow other authors and use type II to refer to the entire class of core collapse SN.

ing galaxies (e.g. Veilleux et al. 2005). The implementation of these winds is troublesome since simulations lack the resolution to implement them correctly (e.g. Ceverino & Klypin 2007; Dalla Vecchia & Schaye 2008). In our simulations forty percent of the kinetic energy from SNII is injected in kinetic form as discussed in section 3.2 and in more detail in Dalla Vecchia & Schaye (2008). The remainder is assumed to be lost radiatively on scales below the resolution limit of the simulation.

Unlike type II SNe and AGB stars, type Ia SNe are a result of binary stellar evolution, and consequently somewhat complicated to model. Currently there are two major theories for the progenitors of type Ia SNe. The most common is the single degenerate model. In this model, a white dwarf experiences enough mass transfer via a main sequence or giant companion to bring its mass above the Chandrasekhar limit, inducing an explosion. According to the double degenerate model, two white dwarfs merge after a long period of binary evolution. In order to predict the type Ia SN rate from a stellar population, one must consider a wide range of relatively uncertain processes (e.g. binary stellar evolution) and poorly constrained parameters (e.g. binary fraction, binary separation, binary mass function).

Although each SNIa is thought to inject a similar amount of kinetic energy as a type II SN, they are thought to be much less efficient at driving galactic outflows, mainly because the energy of a stellar population is released over billions of years rather than the tens of millions of years over which core collapse SNe release their energy. SNIa may, however, dominate the stellar energy feedback in galaxies with very low specific star formation rates. We therefore do include energy feedback by SNIa, which we distribute in thermal form among the SPH neighbours of star particles.

These two types of supernovae also have different chemical signatures. Type II SNe produce copious amounts of oxygen and so-called 'alpha elements' (neon, magnesium, silicon, etc.). These elements are primarily a result of $\alpha$-capture reactions and, in addition to oxygen, make up the bulk of the metal mass ejected from type II SNe (Woosley & Weaver 1995). What is known about type Ia SNe (SNIa) is that they are a major source of iron in the Universe and that a large fraction of them involve relatively old ($\gtrsim 10^9$ yr) stars (see Greggio & Renzini 1983). Because of the time difference between the release of $\alpha$ elements by type II SNe and iron by SN Ia, the $\alpha$/Fe ratio can provide information about the time since the last starburst, at least for the case of closed box models.

Before discussing our implementation of mass transfer from star particles, we briefly discuss all the ingredients of our stellar evolution module: the IMF, the stellar lifetimes, the type Ia SN rate and the stellar yields.

### 3.3.1 Stellar initial mass function

The stellar IMF has long been a subject of debate. Salpeter (1955) made the first attempt to derive an IMF from local stellar counts and his formulation is still widely used today. As star formation is still not understood well enough to predict the IMF from first principles, a wide range of IMFs are available in the literature (e.g., Romano et al. 2005). Although there is consensus about the fact that the IMF is less steep than

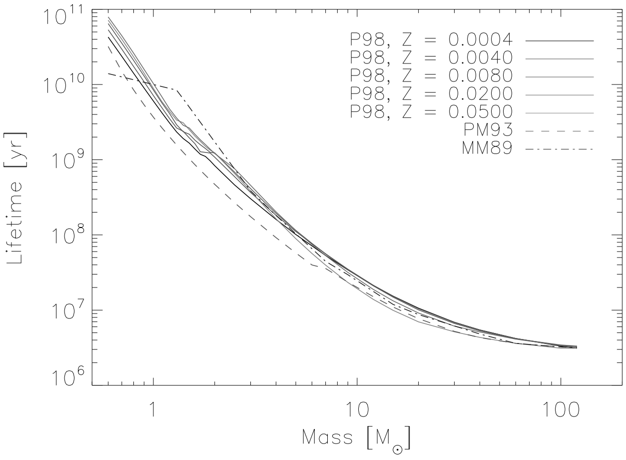

**Figure 3.2**: Stellar lifetime as a function of initial mass for various metallicities (metal mass fractions). Solid lines show lifetimes as given by Portinari et al. (1998), while the dot-dashed line shows calculations from Padovani & Matteucci (1993), who compiled results from the literature for a unspecified metallicity, and the dashed line shows the lifetimes given by Maeder & Meynet (1989a), who assumed solar abundances. Lifetime is a strongly decreasing function of mass, but it is only weakly dependent on metallicity.

Salpeter below $1\ \mathrm{M}_\odot$, there are many uncertainties. In addition, the IMF may depend on redshift or on properties of the environment such as metallicity, gas pressure, or the local radiation field.

For our purposes, the particularly interesting IMFs are the Salpeter IMF - because it serves as a reference model and because it is still used in many simulations - and the Chabrier (2003) IMF - because it is an example of an IMF with a low mass turnover that fits the observations much better than the Salpeter IMF. In this work we will assume a Chabrier IMF.

The Salpeter mass function takes a very simple power-law form,

$$\Phi(M) \equiv \frac{dN}{dM} = AM^{-2.35}, \tag{3.2}$$

where the normalization constant $A$ is chosen such that:

$$\int M\Phi(M)dM = 1\ \mathrm{M}_\odot. \tag{3.3}$$

While the Chabrier IMF has the advantage that it does not overproduce low mass stars, it is slightly more complicated:

$$M\Phi(M) = \begin{cases} Ae^{-(\log M - \log M_\mathrm{c})^2/2\sigma^2} & \text{if } M \leq 1\mathrm{M}_\odot \\ BM^{-1.3} & \text{if } M > 1\mathrm{M}_\odot \end{cases} \tag{3.4}$$

where $M_\mathrm{c} = 0.079$, $\sigma = 0.69$, and the coefficients $A$ and $B$ are set by requiring continuity at $1\ \mathrm{M}_\odot$ and by the normalization condition (3.3). Although the shape of the IMF above $1\ \mathrm{M}_\odot$ is very similar to Salpeter, the lognormal decrease at the low mass end results in a much lower stellar mass-to-light ratio.

Besides the shape of the IMF, we also need to specify the mass limits. The lower limit is defined by the hydrogen burning limit of a star (typically cited as $0.08\ \mathrm{M}_\odot$; e.g.

**Table 3.3**: AGB yield references and grids

| Ref. | Initial stellar mass ($M_\odot$) | Metallicity |
|---|---|---|
| HG97 | [0.8, 0.9, 1, 1.3, 1.5, 1.7, 2, 2.5, 3, 3.5, 4, 4.5, 5, 6, 7, 8] | [0.001, 0.004, 0.008, 0.02, 0.04] |
| M01 | (various) [0.85 - 5] | [0.004, 0.008, 0.019] |
| I04 | [0.5, 1, 1.5, 2, 2.5, 3, 3.5, 4, 4.5, 5, 5.5, 6, 6.5, 7, 7.5, 8] | [0.0001, 0.004, 0.008, 0.02] |

Kippenhahn & Weigert 1994), while the upper limit is significantly more uncertain, and the value most often found in the literature of $100\ M_\odot$ roughly reflects the current upper limit of observed stars. For consistency with previous studies, we choose mass limits of $0.1\ M_\odot$ and $100\ M_\odot$.

### 3.3.2 Stellar lifetimes

Although a star can be active (via accretion) for an indefinite period of time, it is useful to define its stellar 'lifetime' as the time a star takes to move from the zero age main sequence up the giant branch and through any subsequent giant evolution. Using this definition, most stellar mass loss occurs at the end of the star's lifetime during the AGB/SN phase.

There is no easy way to determine the lifetime function for a stellar population observationally. As a result, the published lifetimes are functional fits to the results of stellar evolution models (e.g., Maeder & Meynet 1989a and Padovani & Matteucci 1993; see Romano et al. 2005 for an overview).

Portinari et al. (1998) have published metallicity-dependent lifetimes from their stellar evolution calculations in tabular form and we show their results in figure 3.2 together with the widely used lifetimes of Maeder & Meynet (1989a), who assumed solar abundances, and Padovani & Matteucci (1993), who presented a compilation taken from the literature but did not specify the assumed metallicity. The different lifetime sets agree well at high mass, but differ by nearly an order of magnitude for stars of a few solar masses with Padovani & Matteucci (1993) giving systematically lower values.

Lifetime is a strongly decreasing function of mass and only weakly dependent on metallicity. Although metallicity seems to make little difference, it is attractive to be consistent in treating stellar evolution (in that we use yields based on the same calculations). We thus employ the metallicity-dependent lifetime tables of Portinari et al. (1998).

### 3.3.3 Stellar yields

The mass ejected in each element must be obtained from stellar evolution and (explosive) nucleosynthesis calculations. Differing treatments of physics can often lead to drastically different results in yield calculations. For instance, is it largely unknown what determines the convection boundaries and hot-bottom burning in AGB stars,

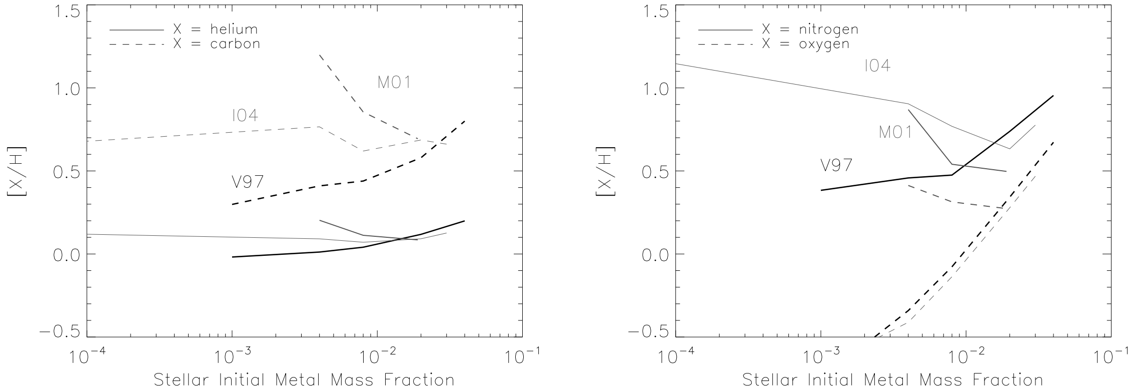

**Figure 3.3**: Composition of the integrated AGB ejecta of an SSP at time $t = \infty$ as a function of its initial stellar metal mass fraction, assuming the yields of van den Hoek & Groenewegen (1997) (black, thick lines), Marigo (2001) (grey, medium thick lines), or Izzard et al. (2004) (grey, thin lines). Shown are the abundances of helium (*left, solid*), carbon (*left, dashed*), nitrogen (*right, solid*) and oxygen (*right, dashed*) relative to hydrogen in solar units. The calculations assume a Chabrier IMF and integrate the yields over the stellar initial mass range $[0.8, 6]$ $\mathrm{M}_\odot$. The different yield sets agree around solar metallicity, but differ significantly for lower metallicities. A colour version of this figure can be found on page ???.

leading to discrepancies between yields sets[5], as we will see below. Hirschi et al. (2005) found that adding rotation to type II SN models changes the yields by factors ranging from two to an order of magnitude. These problems are most evident in the fact that the yields of individual elements are often rescaled in order to get chemical evolution models to match observations. In fact, some authors (e.g. François et al. 2004) use observations and chemical evolution models to derive stellar yields for a number of elements, and the results show marked differences from yields derived from nucleosynthetic calculations.

Another important point to make sure of when using yields from various processes, is that the theoretical assumptions made in the models match. For instance, if one uses AGB yields for masses up to $8\ \mathrm{M}_\odot$, then one must take care to use type II SNe yields that begin higher than $8\ \mathrm{M}_\odot$ (Marigo 2001). The problem is more often than not in reverse, however, since most yield sets for massive stars are tabulated down to $\approx 10\ \mathrm{M}_\odot$, but most intermediate mass yield sets only go up to at most $8\ \mathrm{M}_\odot$, leaving it up to the user to decide what to do for the transition masses. Ideally, one would like to use a consistent set of yields, in the sense that the same stellar evolution model is used for both intermediate mass stars and the progenitors of core collapse SNe.

### AGB stars

The asymptotic giant branch phase of stellar evolution occurs in intermediate mass stars near the very end of their lifetimes. During this phase the envelope of the star

---

[5] In this section we use the term yield in the generic sense, referring to stellar ejecta. We will define it more rigorously in section 3.5.1.

puffs up and is eventually shed, causing the star to lose up to 60 % of its mass. Prior to the AGB phase, material in the core (where most of the heavy elements reside) is dredged up into the envelope via convection. As a result, the ejecta are particularly rich in carbon and nitrogen.

Building on pioneering work by Iben & Truran (1978) and Renzini & Voli (1981), various groups have published AGB yields (e.g. Forestini & Charbonnel 1997; van den Hoek & Groenewegen 1997; Marigo 2001; Chieffi et al. 2001; Karakas et al. 2002; Izzard et al. 2004). Table 3.3 outlines the extent of the resolution (in mass and metallicity) of the AGB yields of van den Hoek & Groenewegen (1997), Marigo (2001) and Izzard et al. (2004), which are some of the most complete sets for our purposes. These yields are compared in Fig. 3.3, which shows the abundance relative to hydrogen, in solar units[6], of various elements in the ejecta as a function of stellar metallicity. These calculations are for an SSP with a Chabrier IMF and the mass range $[0.8, 6]$ $\mathrm{M}_\odot$ at time $t = \infty$. The yields agree very well at solar metallicity, and for the case of helium, this agreement extends to lower metallicities. However, for nitrogen, oxygen, and particularly carbon, different yields sets give very different results at low metallicities.

We show in Fig. 3.4, for each yield set, the integrated fraction of the initial SSP mass ejected by stars in the mass range $[0.8, 6]$ $\mathrm{M}_\odot$ at time $t = \infty$, normalized to the total initial stellar mass over the range $[0.1, 100]$ $\mathrm{M}_\odot$. The ejected mass fractions are very similar for the different yield sets.

In this work we use the yields of Marigo (2001). Although these only go up to $5\ \mathrm{M}_\odot$, they form a complete set with the SN Type II yields of Portinari et al. (1998) since they are both based on the Padova evolutionary tracks. Indeed, there are very few yield pairings that form a consistent set across the full mass range.

### Type II Supernovae

Although major advances have been made in modelling type II SNe, theorists have yet to come up with a model that self-consistently explodes. As a result, the yields are very sensitive to the location of the mass cut, i.e., the explosion radius. The material interior to this radius is assumed to end up in the stellar remnant, while the mass exterior to this radius is assumed to be ejected in the explosion. Unfortunately, the mass cut is very uncertain, thus creating another degree of freedom. Although uncertainties in the explosion radius do not affect the oxygen yields much, the yields of heavier elements such as iron are very sensitive to this choice.

A large number of groups have published tables of type II SN yields (e.g., Maeder 1992; Woosley & Weaver 1995; Portinari et al. 1998; Rauscher et al. 2002; Hirschi et al. 2005; Nomoto et al. 2006). Although the more recent models tend to be more sophisticated, for example including the effects of improved stellar and nuclear physics and rotation, the Woosley & Weaver (1995) yields are still the most widely used. Portinari et al. (1998) combine models of pre-SN stellar mass loss with the nucleosynthesis explosion calculations of Woosley & Weaver (1995), who ignored pre-SN mass loss. To do this they link the carbon-oxygen core mass predicted by their models with those of

---

[6] We use the notation $[\mathrm{X/H}] \equiv \log(\mathrm{X/H}) - \log(\mathrm{X/H})_\odot$.

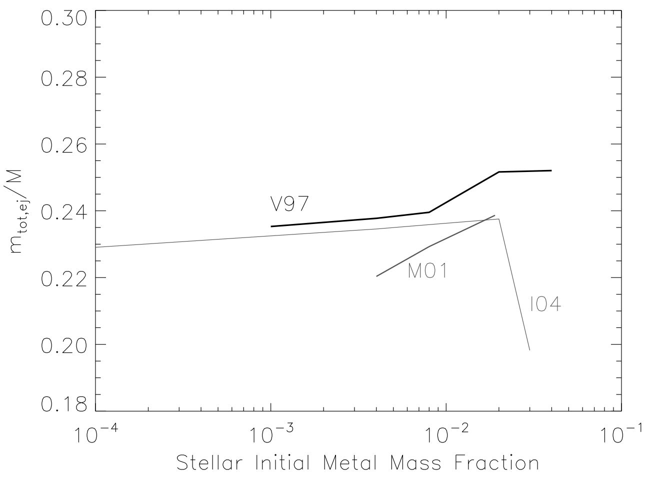

**Figure 3.4**: Total fraction of the initial mass of an SSP ejected by AGB stars at time $t = \infty$ as a function of initial stellar metal mass fraction, assuming the yields of van den Hoek & Groenewegen (1997) (black, thick lines), Marigo (2001) (grey, medium thick lines), or Izzard et al. (2004) (grey, thin lines). The calculations assume a Chabrier IMF and integrate the yields over a stellar initial mass range $[0.8, 6]$ $\mathrm{M}_{\odot}$, but the fractions are normalized to the mass range $[0.1, 100]$ $\mathrm{M}_{\odot}$. Different yield sets predict similar ejected mass fractions. The ejected mass fraction is insensitive to metallicity. A colour version of this figure can be found on page ???.

**Table 3.4**: SN type II yield references and grids

| Ref. | Initial stellar mass ($\mathrm{M}_{\odot}$) | Metallicity |
|---|---|---|
| WW95 | [11, 12, 13, 15, 18, 19, 20, 22, 25, 30, 35, 40] | [0.0, 0.000002, 0.0002, 0.002, 0.02] |
| P98 | [6, 7, 9, 12, 15, 20, 30, 60, 100, 120, 150, 200, 300, 500, 1000] | [0.0004, 0.004, 0.008, 0.02, 0.05] |
| CL04 | [13, 15, 20, 25, 30, 35] | [0.0, 0.000001, 0.0001, 0.001, 0.006, 0.02] |

Woosley & Weaver (1995). They find low metallicity, massive stars to have very inefficient mass loss for these large core masses (for which there are no type II SN yields), they only consider mass loss by winds and assume the rest of the star collapses directly into a black hole.

Table 3.4 and Figure 3.5 compare the SN type II yields of Woosley & Weaver (1995), Portinari et al. (1998), and Chieffi & Limongi (2004). Figure 3.5 shows the abundance relative to hydrogen, in solar units, of various elements in the ejecta as a function of stellar metallicity. The elements shown are those that, together with hydrogen, dominate the radiative cooling of (photo-)ionized plasmas chapter 2. These calculations are for an SSP with a Chabrier IMF in the mass range $[8, 40]$ $\mathrm{M}_{\odot}$ at time $t = \infty$. It is clear that the yields of elements that are produced by type II SNe depend only weakly on metallicity, unless the metallicity is supersolar. However, except for very low metallicities, the nitrogen abundance in the ejecta is proportional to the stellar metallicity, indicating that it is simply passing through rather than being produced.

The different yield sets agree well for helium, carbon, and nitrogen, but there are large differences for heavier elements. The difference between Portinari et al. (1998)

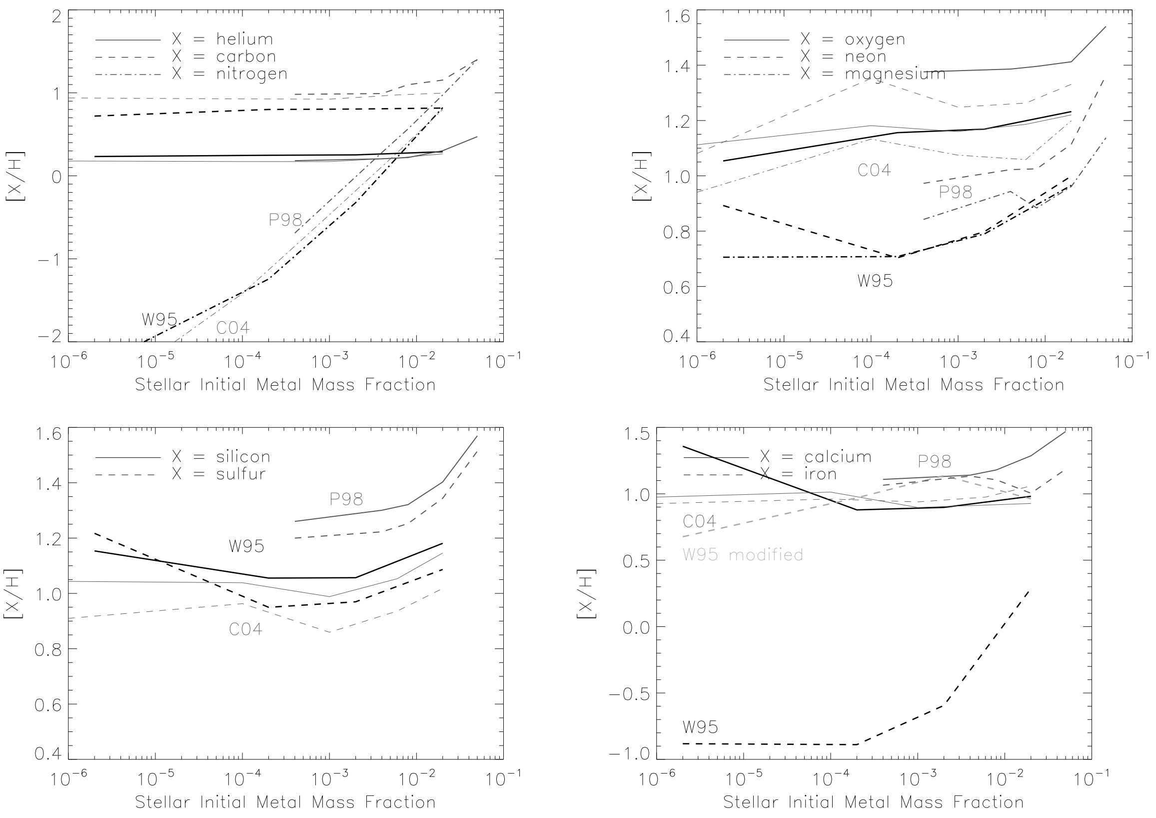

**Figure 3.5**: Composition of the integrated SN type II ejecta of an SSP at time $t = \infty$ as a function of its initial stellar metal mass fraction, assuming the yields of Woosley & Weaver (1995) (black, thick lines), Portinari et al. (1998) (grey, medium thick lines), or Chieffi & Limongi (2004) (grey, thin lines). Shown are the abundances of helium, carbon, nitrogen, oxygen, neon, magnesium, silicon, sulphur, calcium, and iron, as indicated in the legends. The calculations assume a Chabrier IMF and integrate the yields over the stellar initial mass range $[8, 40]\ \mathrm{M}_{\odot}$. The grey thick dashed line in the lower right panel indicates the result of transferring the $^{56}$Ni to the Iron yield of Woosley & Weaver (1995). While the different yield sets agree well for the lightest elements (upper panels), there are large differences for elements heavier than nitrogen.

and Woosley & Weaver (1995) is due to the fact that the former add their stellar evolution to the Woosley & Weaver (1995) nucleosynthesis calculations. The difference between Chieffi & Limongi (2004) and Woosley & Weaver (1995) is caused mostly by the difference in the assumed mass cut.

The yields presented in Woosley & Weaver (1995) consider the state of the ejecta $10^5$ s after the explosion. Because a number of isotopes have rather short decay times, it is customary to consider – as most recent yield sets have done – the state of the ejecta at a much later time ($10^8$ s in the case of Chieffi & Limongi 2004). This is especially important for $^{56}$Ni, which decays rapidly into $^{56}$Fe. When Portinari et al. (1998) incorporate the Woosley & Weaver (1995) yields into their calculations, they simply add the $^{56}$Ni to the $^{56}$Fe. We have added an additional magenta line to figure 3.5 to show the iron yield from Woosley & Weaver (1995) with this adjustment. This agrees much better with the other two yield sets.

Figure 3.6 shows the integrated fraction of the initial mass of an SSP that is ejected by type II SNe at time $t = \infty$ as a function of metallicity. These calculations again assume a Chabrier IMF and integrate the yields over the mass range $[8, 40]\ \mathrm{M}_{\odot}$, but normalize the mass fraction to the mass range $[0.1, 100]\ \mathrm{M}_{\odot}$. The ejected mass is insensitive to metallicity and the three yield sets are in excellent agreement.

We use the yields of Portinari et al. (1998) since they include mass loss from massive stars and because they form a self-consistent set together with the stellar lifetimes of these authors and the AGB yields of Marigo (2001). Their models allow for the possibility of electron capture supernova for intermediate mass stars ($7 - 9\ \mathrm{M}_{\odot}$). Unfortunately, nucleosynthesis calculations for these stars have only recently been performed (e.g., Wanajo et al. 2008). The Portinari et al. (1998) yields therefore only consider the shedding of the envelope and the mass loss up to that stage. While both Chieffi & Limongi (2004) and Woosley & Weaver (1995) evolve their models until the point of supernova and then begin supernova calculations, they do not include mass loss in their yield tables (since the goal of their studies was to investigate explosive nucleosynthesis).

Following the recommendation of L. Portinari (private communication), we have adjusted the massive star yields by the factors inferred from comparisons of chemodynamical models and current Galactic abundances. Following Portinari et al. (1998), we have multiplied the type II SN yields of C, Mg, and Fe for all masses and metallicities by factors of 0.5, 2, and 0.5, respectively. Note that these factors were *not* included in Fig. 3.5, but have been implemented for the rest of this work. The adjustments to Mg and Fe can be justified due to uncertainties in the explosive nucleosynthesis models by Woosley & Weaver (1995) as discussed by a number of authors (e.g. Timmes et al. 1995; Lindner et al. 1999; Carigi 2000; Goswami & Prantzos 2000; Carigi 2003; Gavilán et al. 2005; Nykytyuk & Mishenina 2006). These adjustments have also been incorporated into other studies (e.g. Liang et al. 2001; Lia et al. 2002; Portinari et al. 2004; Nagashima et al. 2005). These *ad hoc* adjustments reveal just how uncertain the yields are.

### Type Ia Supernovae

Despite the fact that the progenitors of type Ia SNe are still uncertain, yield calculations can be made based on an explosion of a Chandrasekhar mass carbon-oxygen dwarf. While most models assume the progenitor to be a binary system, the yields usually consider just the explosion of the white dwarf itself, ignoring the companion completely.

It is instructive to anticipate a few features of these calculations. First, since a type Ia SN explosion occurs as soon as the compact object reaches the Chandrasekhar mass, the yields from this process will be independent of the initial stellar mass. Second, by the time a star gets to the white dwarf phase, it is almost completely composed of carbon, nitrogen and oxygen, and while the balance between these elements may depend on initial mass or composition, the models assume such a dependence is insignificant.

Several research groups have published yields from type Ia SNe. Their calculations range from one- to three-dimensional calculations (Travaglio et al. 2004). The standard to which most results are compared is the spherically symmetric calculation dubbed

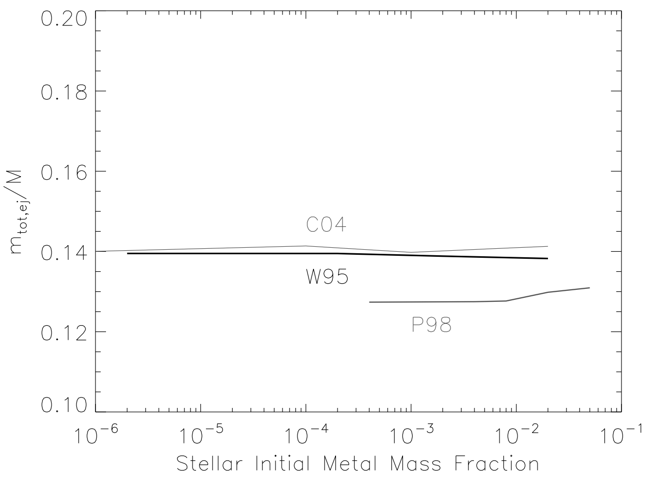

**Figure 3.6**: Total fraction of the initial mass of an SSP ejected by SNe type II at time $t = \infty$ as a function of initial stellar metal mass fraction, assuming the yields of Woosley & Weaver (1995) (black, thick lines), Portinari et al. (1998) (grey, medium thick lines), or Chieffi & Limongi (2004) (grey, thin lines). The calculations assume a Chabrier IMF and integrate the yields over the stellar initial mass range $[8, 40]$ $\mathrm{M}_\odot$, but the fractions are normalized tot he mass range $[0.1, 100]$ $\mathrm{M}_\odot$. The ejected mass fraction is insensitive to metallicity and different yields sets predict very similar results.

"W7" (Nomoto et al. 1984, 1997; Iwamoto et al. 1999; Brachwitz et al. 2000; Thielemann et al. 2003). We use the latest incarnation (at the time of code development) of the W7 model, i.e., Thielemann et al. (2003).

### 3.3.4 SN type Ia rates

The recipes for the release of mass by AGB stars and SNII are quite simple because these processes are direct results of stars reaching the ends of their lifetimes. Hence, one merely needs to combine the IMF with the stellar lifetime function and the yields and integrate over the time interval specified. The recipe for SNIa is, however, somewhat more complex.

Two SNIa channels are thought to be most plausible (see, e.g., Podsiadlowski et al. 2008 for a review). According to the single degenerate scenario, SNIa result when accretion onto a white dwarf by a binary companion pushes the former over the Chandrasekhar mass. The double degenerate scenario, on the other hand, involves the merger of two white dwarfs, thus putting the merger product over the Chandrasekhar mass.

The SNIa rate of an SSP as a function of its age can be determined using late age stellar and binary evolution theory. The formulation that is used most often is given by Greggio & Renzini (1983). This formulation requires knowledge of the distribution of secondary masses in binaries and makes some assumptions about binary evolution. These are poorly constrained and may therefore be subject to large uncertainties. Hence, it is attractive to take an alternative, more empirical approach. Guided by observations of SNIa rates, we can simplify the prescription by specifying a functional form for the empirical delay time function $\xi(t)$, which gives the SNIa rate as a function of the age of an SSP, normalized such that $\int_0^\infty \xi(t)dt = 1$. The parameters of this function can then be determined by fitting to observations of SNIa rates (e.g., Barris & Tonry 2006; Förster et al. 2006).

The number of SNIa explosions per unit stellar mass in a time step $\Delta t$ for a given SSP is then

$$N_{\rm SNIa}(t; t+\Delta t) = \nu \int_t^{t+\Delta t} \xi(t')dt', \tag{3.5}$$

where $\nu$ is the number of SNe per unit formed stellar mass that will ever occur. While this approach is attractive since it does not require us to make any assumptions regarding the progenitors, we will employ yields that correspond to a scenario involving at least one white dwarf so the SNIa rate should take that into account (i.e., we should not have any SNIa before the white dwarfs have evolved). We therefore take an approach similar to Mannucci et al. (2006) and write:

$$N_{\rm SNIa}(t; t+\Delta t) = a \int_t^{t+\Delta t} f_{\rm wd}(t')\xi(t')dt', \tag{3.6}$$

where $a$ is a normalization parameter and $f_{\rm wd}(t)$ is the number of stars that have evolved into white dwarfs up until time $t$ (i.e., the age of the SSP) per unit initial stellar mass:

$$f_{\rm wd}(t) = \begin{cases} 0 & \text{if } M_Z(t) > m_{\rm wdhigh} \\ \displaystyle\int_{m_{\rm SNIalow}(t)}^{m_{\rm wdhigh}} \Phi(M)dM & \text{otherwise} \end{cases} \tag{3.7}$$

Here $m_{\rm wdhigh}$ and $m_{\rm wdlow}$ are the maximum and minimum white dwarf masses respectively, $M_Z(\tau)$ is the inverse[7] of the lifetime function $\tau_Z(M)$, and

$$m_{\rm SNIalow}(t) = \max(M_Z(t), m_{\rm wdlow}). \tag{3.8}$$

Note that the shape of the SNIa rate as a function of time differs between equations (3.5) and (3.6).

It is thought that stars with main sequence masses between $3\ {\rm M}_\odot$ and $8\ {\rm M}_\odot$ evolve into a SNIa progenitor white dwarf. Note that while our type II SN yields range to masses as low as $6\ {\rm M}_\odot$, the models used in the yield calculations of Portinari et al. (1998) for stars of $6$ and $7\ {\rm M}_\odot$ do not incorporate any explosive nucleosynthesis. They note that stars of these masses could explode as electron capture SNe *or* evolve to a thermally-pulsing AGB phase, thus simply shedding their envelopes.

The form of the delay function $\xi$ has generated particular interest recently (e.g., Dahlen et al. 2004). The two types of delay functions that are most often considered, the so-called e-folding delay and Gaussian delay functions, are shown in figure 3.7. The e-folding delay function takes the form:

$$\xi(t) = \frac{e^{-t/\tau_{\rm Ia}}}{\tau_{\rm Ia}} \tag{3.9}$$

---

[7] The lifetime function is invertible because it is a monotonic function of mass for a fixed metallicity.

where $\tau_{\mathrm{Ia}}$ is the characteristic delay time. This delay approximates predictions made for the single degenerate scenario via population synthesis models.

The Gaussian delay function was motivated by high redshift observations by Dahlen et al. (2004), which show a marked decline in the SNIa rate beyond $z = 1$. It takes the form:

$$\xi(t) = \frac{1}{\sqrt{2\pi\sigma^2}} e^{-\frac{(t-\tau_{\mathrm{Ia}})^2}{2\sigma^2}} \tag{3.10}$$

where $\sigma = 0.2\tau_{\mathrm{Ia}}$ for 'narrow' distributions and $\sigma = 0.5\tau_{\mathrm{Ia}}$ for 'wide' distributions. Note that the integral of this particular function ($\int_0^\infty \xi(t)dt$ is only normalised to unity for $\sigma \ll \tau_{\mathrm{Ia}}$. Gaussian delay functions often feature long characteristic times ($\tau_{\mathrm{Ia}} = 4$ Gyr) in order to fit the data. Strengths and weaknesses exist for both delay functions, and are discussed in the references cited above. Unfortunately, the choice of distribution (including all the ensuing parameters) is rather poorly constrained. In particular, both the cosmic star formation rate and the type Ia rate contain large uncertainties beyond a redshift of 1. For instance, the type Ia rate quoted at $z = 1.6$ by Dahlen et al. (2004) is based on only two detection events.

In addition to the cosmic SNIa rate, Mannucci et al. (2006) attempt to use other observations to constrain the shape of the delay function. They cite the dependence of the SNIa rate on galaxy colour observed in the local universe (Mannucci et al. 2005) as well as a dependence on radio loudness observed by Della Valle et al. (2005). Their analysis suggests that the delay time function could have two components, a "prompt" mode and a "tardy" mode (see also Scannapieco & Bildsten 2005a). These modes may have physical counterparts with the two progenitor channels, but this is still uncertain. Using such a delay function could improve our fits to the observations marginally, but would introduce another unknown parameter (the ratio of contributions of the modes). Moreover, the e-folding delay function also includes significant prompt and late contributions. We therefore chose to use an e-folding delay function with $\tau_{\mathrm{Ia}} = 2$ Gyr, but have also performed one simulation with a Gaussian delay function using $\tau_{\mathrm{Ia}} = 3.3$ Gyr and $\sigma = 0.66$ Gyr. These parameter values were chosen to roughly agree with the constraints mentioned above. The coefficient $a$ appearing in equation (3.6) was chosen to roughly match observations of the cosmic SNIa rate.

We plot the current measurements of the cosmic SNIa rate in figure 3.7. We have self-consistently adjusted all data points to our cosmology of choice[8], $(h, \Omega_m, \Omega_\Lambda) = (0.73, 0.238, 0.762)$. Note that the different SNIa measurements are strongly discrepant, indicating that the statistical errors have been underestimated and/or that some rates suffer from systematic errors.

The solid, black curve in Figure 3.7 shows the evolution of the SNIa rate in our L100N512 simulation, which used the e-folding time delay function and $a = 0.01$. Also shown (dashed, black curve) is the predicted type Ia rate for another simulation that is identical to L100N512 except for the fact that it uses the Gaussian delay function and

---

[8] Correcting for cosmology is important since observations are taken over a volume in co-moving space. For instance, the highest redshift point of Poznanski et al. (2007) is greater than that of Dahlen et al. (2004) when using their cosmology, but when converting to our cosmology the Dahlen et al. (2004) point is reduced by a greater amount since it was taken over a larger redshift range. Thus, our plot shows the Dahlen et al. (2004) point to be greater than the Poznanski et al. (2007) point.

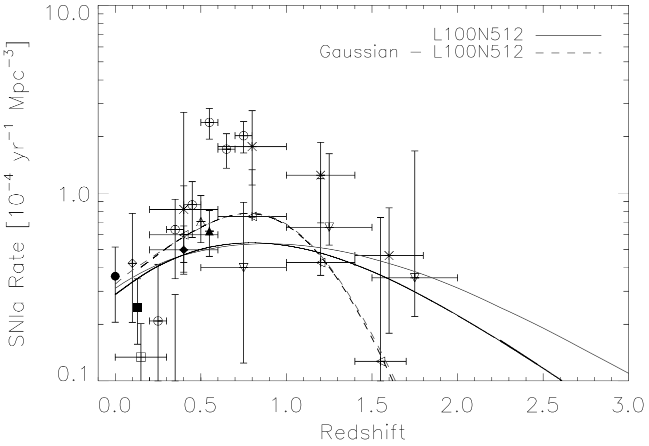

**Figure 3.7**: Volumetric Type Ia supernova rate as a function of redshift from our simulations (black) using either an e-folding (*solid*) or a Gaussian (*dashed*) delay function. Also shown are approximate fits using a "standard formulation" of the cosmic SNIa rate, calculated using equation (3.5) and the star formation history predicted by the simulations and a Chabrier IMF (grey). The data points correspond to observations reported by Cappellaro et al. (1999) (filled circle), Madgwick et al. (2003) (open square), Blanc (2004) (filled square), Hardin (2000) (open diamond), Neill (2006) (filled diamond), Tonry (2003) (open black triangle), Pain (2002) (filled triangle), Dahlen et al. (2004) (crosses), Barris & Tonry (2006) (open circles), Poznanski et al. (2007) (upright triangles), and Kuznetsova et al. (2008) (left pointing triangles).

$a = 0.0069$. The e-folding and Gaussian models result in reduced $\chi^2$ values of 2.6 and 2.2, respectively. We consider this acceptable since the data are internally inconsistent. Note that the predicted SNIa rates agree better with the more recent measurements.

While preparing this publication, we encountered a bug in the code that resulted in $m_{\rm wdlow}$ being set to zero in equation (3.8). The net result is a shift in the effective delay time to lower redshifts and an increase in the effective value of $a$. Because this error complicates the interpretation of our parameter values and because most of the literature uses equation (3.5) rather than (3.6) we have tried to approximately match the SNIa rates predicted by our L100N512 simulations using equation (3.5), taking the star formation history predicted by the simulations as input and using the same (Chabrier) IMF as was used in the simulation. We expect the effects of this bug to be nominal, causing an increase in iron production at late times - increasing cooling slightly and releasing more metals from old stellar populations - but note that our rates still pass comfortably though the observations. Moreover, a simulation with a Gaussian delay function (which we will present in a later publication) showed negligible difference to the e-folding model in nearly all respects (e.g., star formation history, distribution of metals). The difference between the type Ia rates is much greater than the difference between the bugged and unbugged versions.

The matching "standard formulation" SNIa rates are shown as the red curves in figure 3.7. The e-folding delay function (solid, red curve) uses $\tau_{\rm Ia} = 3$ Gyr while the Gaussian delay function (dashed, red curve) uses $\tau_{\rm Ia} = 3.3\ {\rm Gyr}, \sigma = 0.66\ {\rm Gyr}$ (which is identical to the original delay function used in combination with equation 3.6). When using equation (3.5) it is useful to parametrize the normalization in terms of $\eta$, the fraction of white dwarfs that eventually explode as SNIa, or the *Type Ia efficiency*, which is related to $\nu$, the number of SNIa per unit formed stellar mass via

$$\eta \int_3^8 \Phi(M) dM = \nu \int_{0.1}^{100} M\Phi(M) dM. \tag{3.11}$$

The red curves in figure 3.7 correspond to $\eta = 2.50\ \%$ for the e-folding model and $\eta = 2.56\ \%$ for the Gaussian model. Note that these efficiencies correspond to our Chabrier IMF, whereas much of the literature quotes efficiencies for a Salpeter IMF. For a Salpeter IMF, these efficiencies work out to $\eta = 3.25\ \%$ and $\eta = 3.33\ \%$ for the e-folding model and the Gaussian model respectively.

We end the discussion by noting that we match another constraint in that we find iron abundances in our galaxies to be roughly solar at $z = 0$ (McCarthy et al. 2009).

## 3.4 PREVIOUS WORK

Several authors have used similar chemodynamical models in previous studies. While these simulations are useful to compare to, it is important to pay close attention to the various parameters in each work. The earliest treatment that could truly be deemed chemodynamics was by Theis et al. (1992). While most of the subsequent codes (including ours) used SPH, they used a mesh code, and they explicitly tracked the evolution of metals as produced from stars, and even considered their impact on cooling.

Table 3.5 outlines the differences between a selection of previous simulations. It is important to note that some of these simulations were only run for individual galaxies while others used a large cosmological box. Note that in this table we only refer to the first paper in a series, but that the parameters shown are from the most recent incarnation of the model. We also include the type of model used for winds driven by supernovae.

It is useful to notice the trends that exist among the various authors. For the initial mass function Salpeter (1955) is regularly used as well as Arimoto & Yoshii (1987) (Kobayashi 2004b uses a simple power law of 1.10). Lia et al. (2002) published a formulation of the type Ia supernova rate given by Greggio & Renzini (1983), and many authors use this because it is concise and easy to follow. Others, however, follow very different recipes, such as Scannapieco et al. (2005) who use a type Ia supernova rate that is constant in time. The choice of a particular set of stellar lifetimes could have a strong effect on simulations since all of the feedback processes directly depend on it. Fortunately, the differences between the lifetimes are modest (see Romano et al. 2005 for a good review).

The treatment of cooling also has a significant impact on the outcome of the simulation. While cooling tables from Sutherland & Dopita (1993) are widely used, some authors (Kawata & Gibson 2003; Kobayashi 2004b) have made their own cooling tables using the software package MAPPINGS III (Sutherland & Dopita (1993) used MAPPINGS II, and wrote both packages). None of the calculations published to date allow the relative contributions of the elements to vary, nor do they consider the effect of UV background on the metals.

Winds also play an important role. Some authors choose to inject gas surrounding a supernova event with thermal energy (often suppressing the cooling for sometime in order to ensure the feedback is effective) while others impart kinetic energy to the gas. Navarro & White (1993) proposed a hybrid method in which some fraction of the energy is given thermally and the remaining energy given kinetically.

Our simulations are similar in some respects to the previous works (i.e., stellar yields and lifetimes) but also have some new aspects such the way in which radiative cooling is implemented.

**Table 3.5**: Parameters of Previous Chemodynamical Simulations

| Type | Year | Paper[a] | Code | IMF | SN Ia Rates | Lifetimes | Yields (SNII, Ia, AGB) | Cooling | Wind model |
|---|---|---|---|---|---|---|---|---|---|
| Galaxy | 1992 | TBH92[1] | TBH92[1] | S55[2] | immediate at death | MM89[3] | constant Z fractions | analytic | thermal |
| Galaxy | 1995 | SM95[4] | SM95[4] | MS79[5] | n/a | n/a | M87[6], n/a, n/a | n/a | thermal |
| Galaxy | 1996 | RVN96[7] | NW93[8] | KTG93[9] | GR83[10] | A93[11] | WW95[12], TNH93[13], n/a | n/a | NW93[8] |
| Galaxy | 1999 | B99[14] | CD-SPH | KTG93[9] | GR83[10] | RVN96[7] | WW95[12], NTY84[15], vdHG97[16] | DM72[17] | thermal |
| Galaxy | 2001 | K01[18] | K99[19] | S55[2] | T95[20] | constant | n/a | TBH92[1] | NW93[8] |
| Galaxy | 2001 | RME01[21] | RME01[21] | S55[2] | BMD98[22] | PM93[23] | WW95[12], NTY84[15], RV81[24] | n/a | kinetic |
| Cosmological | 2001 | M01[25] | APHMSPH | S55[2] | GR83[10] | immediate at death | WW95[12]/PCB98[26], TNH93[13], n/a | n/a | none |
| Galaxy | 2002 | LPC02[27] | LPC02[27] | S55[2]/AY87[28] | LPC02[27] | PCB98[26] | PCB98[26], I99[29], M01[30] | n/a | thermal |
| Galaxy | 2003 | KG03[31] | GCD+ | S55[2] M = {0.2-60} | HKN99[32] | K97[33] | WW95[12], I99[29], vdHG97[16] | mpIII[34] | NW93[8] |
| Cluster | 2003 | V03[35] | n/a | various | LPC02[27] | n/a | WW95[12], I99[29], n/a | SD93[36] | thermal |
| Galaxy | 2004 | K04[37] | GRAPE-SPH | $M^{\alpha}$, $\alpha = 1.10$ | KTN00[38] | DFJ90[39] | N97[40], N97[41] | mpIII[34] | NW93[8] |
| Cluster | 2004 | T04[42] | GADGET-2 | S55[2]/AY87[28] | M01[43] | PM93[23] | WW95[12], NIK97[44], RV81[24] | SD93[36] | kinetic |
| Cosmological | 2005 | C05[45] | GADGET-2 | S55[2] | constant | constant | WW95[8], TNH93[9], n/a | SD93[36] | C05[45] |
| Galaxy | 2006 | MU06[46] | n/a | S55[2] | n/a | n/a | T95[20] | SD93[36] | thermal |
| Cluster | 2006 | R06[47] | FLY | S55[2]/AY87[28] | LPC02[27] | PCB98[26] | PCB98[26], I99[29], M01[30] | SD93[36] | thermal |
| Galaxy/Cosmological | 2006 | S06[48] | GASOLINE | MS79[5] | GR83[10] | A93[11] | WW95[12], TNH93[13], n/a | SD93[36] | thermal |
| Cosmological | 2006 | OD06[49] | GADGET-2 | C03[50] | SB05[51] | BC03[52] | CL04[53], T95[20], M01[30] | SD93[36] | kinetic |
| Galaxy/Cosmological | 2007 | KSW07[54] | GADGET-2 | S55[2] | KTN00[38] | DFJ90[39] | N97[40], N97[41] | mpIII[34] | thermal |
| This Work | | | | | | | | | |
| Cosmological | 2008 | W09b[55] | GADGET-3 | C03[50] | W09b[55] | PCB98[26] | PCB98[26], T03[56], M01[30] | W09a[57] | kinetic |

[a] Here we cite only the first paper of the project, [1] Theis et al. (1992) (Eulerean code), [2] Salpeter (1955), [3] Maeder & Meynet (1989b), [4] Steinmetz & Muller (1995) ,[5] Miller & Scalo (1979), [6] Maeder (1987) , [7] Raiteri et al. (1996) , [8] Navarro & White (1993) , [9] Kroupa et al. (1993) , [10] Greggio & Renzini (1983) , [11] Alongi et al. (1993), [12] Woosley & Weaver (1995) , [13] Thielemann et al. (1993) , [14] Berczik (1999), [15] Nomoto et al. (1984), [16] van den Hoek & Groenewegen (1997), [17] Dalgarno & McCray (1972), [18] Kawata (2001) , [19] Kawata (1999), [20] Tsujimoto et al. (1995), [21] Recchi et al. (2001) (2 dimensional) , [22] Bradamante et al. (1998), [23] Padovani & Matteucci (1993), [24] Renzini & Voli (1981) , [25] Mosconi et al. (2001), [26] Portinari et al. (1998) , [27] Lia et al. (2002) , [28] Arimoto & Yoshii (1987) , [29] Iwamoto et al. (1999) , [30] Marigo (2001) , [31] Kawata & Gibson (2003) , [32] Hachisu et al. (1999) , [33] Kodama (1997) , [34] Tables made with Mappings III software, [35] Valdarnini (2003), [36] Sutherland & Dopita (1993), [37] Kobayashi (2004b), [38] Kobayashi et al. (2000), [39]David et al. (1990), [40] Nomoto et al. (1997), [41] Nomoto et al. (1997), [42] Tornatore et al. (2004), [43] Matteucci (2001) [44] Nomoto et al. (1997),[45] Scannapieco et al. (2005), [46] Mori & Umemura (2006), [47] Romeo et al. (2006), [48] Stinson et al. (2006), [49] Oppenheimer & Davé (2006), [50] Chabrier (2003), [51] Scannapieco & Bildsten (2005b), [52] Bruzual & Charlot (2003), [53] Chieffi & Limongi (2004), [54] Kobayashi et al. (2007), [55] Chapter 3, [56] Thielemann et al. (2003), [57] Chapter 2

## 3.5 THE MASS EJECTED BY A SIMPLE STELLAR POPULATION

The mass that is ejected during a single time step $(t, t+\Delta t)$ by a star particle of initial mass $m_{*,0}$ and metallicity $Z$ that was created at time $t_* < t$ is given by

$$\begin{aligned}
\Delta m_* &= m_*(t) - m_*(t+\Delta t) && (3.12)\\
&= m_{*,0} \int_{M_Z(t-t_*+\Delta t)}^{M_Z(t-t_*)} \Phi(M) m_{\rm ej}(M,Z)\, dM, && (3.13)
\end{aligned}$$

where $M_Z(\tau)$ is the inverse of the lifetime function $\tau_Z(M)$, $m_{\rm ej}(M,Z)$ is the mass ejected by a single star and $\Phi(M)$ is the IMF, normalized such that $\int M\Phi(M)dM = 1$. It is straightforward to generalize the above equations to give $\Delta m_{*,j}$, the mass ejected in the form of element $j$. The functions $\tau_Z(M)$ and $m_{j,{\rm ej}}(M,Z)$ need to be taken from stellar evolution and nucleosynthesis calculations provided in the literature.

### 3.5.1 Implementation

Since stellar evolution and nucleosynthesis depend on initial composition, a correct treatment of chemodynamics would require yields (i.e. the ejected mass of various elements) to be tabulated in a space with dimensionality equal to the number of elements. Most yields are, however, given only as a function of metallicity, where metallicity is the total mass fraction in metals. The models used to compute the yields assume implicitly that the relative abundances of the heavy elements are initially solar.

One way to implement the release of elements is to interpolate the ejected masses, which are given as a function of metallicity, to the metallicity of the star particle and to ignore possible differences between the relative abundances assumed by the yield calculation and the actual relative abundances of the star particle. However, this can have some very undesirable consequences. For example, because iron does not participate in the nucleosynthesis of intermediate mass stars, the iron that these stars eject was already present when the star was born. If an intermediate mass star has a high iron abundance for its metallicity, then simple interpolation of the yield tables with respect to metallicity would lead to a large underestimate of the ejected iron mass. That is, it would result in the spurious destruction of iron.

A more accurate way to implement chemodynamics would thus be to distinguish metals that were produced/destroyed from those that pass through the star without participating in the nucleosynthesis. If we knew, for each ejected element, what fraction of the ejected mass resulted from net nucleosynthetic production (i.e., production minus destruction) and what fraction simply passed through the star (the two fractions should add up to one), then it would make sense to assume that the mass that passed through the star is proportional to the star's initial abundance. In that case we would still neglect the effect of relative abundances on the nucleosynthesis itself (this can only be done by repeating the nucleosynthesis calculations or using the somewhat cumbersome Q-matrix formalism, e.g. Portinari et al. 1998), but we would take into account the consequences of varying relative abundances on metals that do not participate in the nucleosynthesis.

We have adopted this strategy - as is often done (e.g. Recchi et al. 2001; Lia et al. 2002; Sommer-Larsen et al. 2005; Romeo et al. 2006; Tornatore et al. 2007) - and have implemented it as follows[9]. For a star of given initial mass and metallicity, we can write the mass of element $j$ that is ejected into the surrounding medium, $m_{j,\rm ej}$, as the sum of two parts:

$$m_{j,\rm ej} = m_{j,\rm 0:ej} + m_{j,\rm p:ej}. \tag{3.14}$$

Here $m_{j,\rm 0:ej}$ is the mass in element $j$ that would have been ejected if no nucleosynthesis had taken place and if the star were well-mixed,

$$m_{j,\rm 0:ej} = \left(\frac{m_{j,\rm 0:star}}{m_{\rm tot,0:star}}\right)_{\rm sim} (m_{\rm tot,ej})_{\rm tbl}\,, \tag{3.15}$$

where $(m_{j,\rm 0:star}/m_{\rm tot,0:star})_{\rm sim}$ is the initial mass fraction of element $j$ in the star *as tracked by the simulation* and $(m_{\rm tot,ej})_{\rm tbl}$ is the total ejected mass according to the yield table. Note that we use the subscript "sim" to indicate values predicted by the simulation and the subscript "tbl" to indicate values that are published by authors presenting a particular set of stellar yields. The second term of equation (3.14) represents the ejected mass in element $j$ that was produced minus destroyed. Assuming that the star is well-mixed, we can write it as

$$m_{j,\rm p:ej} = (m_{j,\rm ej})_{\rm tbl} - \left(\frac{m_{j,\rm 0:star}}{m_{\rm tot,0:star}}\right)_{\rm tbl} (m_{\rm tot,ej})_{\rm tbl}\,, \tag{3.16}$$

where $(m_{j,\rm 0:star}/m_{\rm tot,0:star})_{\rm tbl}$ is the initial mass fraction of element $j$ that was used for the nucleosynthesis calculation. This term, which is often referred to as the yield of element $j$, will be negative if an element effectively gets destroyed (this is for example the case for hydrogen).

Combining equations (3.14), (3.15), and (3.16), we obtain:

$$\begin{aligned} m_{j,\rm ej} = {} & (m_{j,\rm ej})_{\rm tbl} + \\ & \left[\left(\frac{m_{j,\rm 0:star}}{m_{\rm tot,0:star}}\right)_{\rm sim} - \left(\frac{m_{j,\rm 0:star}}{m_{\rm tot,0:star}}\right)_{\rm tbl}\right] (m_{\rm tot,ej})_{\rm tbl}. \end{aligned} \tag{3.17}$$

Note that this expression behaves as expected in the limit that the simulated abundances agree with the ones assumed by the yield tables (i.e. the second term vanishes). Note also that although the abundances appearing in equation (3.17) are absolute, it is the abundance relative to other heavy elements that is important because we interpolate the yield tables to the metallicity (i.e. $\sum_j m_{j,0}/m_{\rm tot,0}$ where the sum is over all elements heavier than helium) of the simulation star particle.

The ejected mass predicted by equation (3.17) can in principle be negative if the simulated relative abundance of some element is much lower than the relative abundance assumed in the yield calculation and if the element is not produced in significant amounts. To prevent stellar particles from obtaining negative total abundances,

---

[9] Note that this strategy applies directly for our chosen yields since they are presented as what is produced minus what was initially in the star. Some yields (e.g. Woosley & Weaver 1995) would have to be modified to implement this approach.

we therefore impose that for each element $j$, the *total* ejected mass, which consists of the sum of the mass ejected by intermediate mass stars and SNe of types Ia and II, is non-negative at each time step. If it happens to be negative, we set it to zero. In practice we have, however, not observed this to occur in any of our simulations.

If some $m_{j,\mathrm{ej}}$ has been set to zero, as in the scenario described in the previous paragraph, or if the simulated abundances $(m_{j,0:\mathrm{star}}/m_{\mathrm{tot},0:\mathrm{star}})_{\mathrm{sim}}$ do not add up to unity (which can happen when using smoothed abundances; see section 3.6.2), then the sum of the ejected masses, $\sum_j m_{j,\mathrm{ej}}$, may differ from the total ejected mass, $(m_{\mathrm{tot,ej}})_{\mathrm{tbl}}$, predicted by the yield tables. To ensure that we release the correct amount of mass, we therefore normalise the mass released from each element, including the total metal mass (see section 3.5.1), such that the total mass released agrees with the value found in the yield tables.

### Tracking the total metal mass

Of the many elements tracked by stellar evolution calculations, only a fraction contribute significantly to the radiative cooling rates. These elements tend to be the most abundant and thus the most observed. We therefore only track 9 elements individually: H, He, C, N, O, Ne, Mg, Si, and Fe (plus we take Ca and S, whose contributions to the cooling rates can be significant (see chapter 2), to be proportional to Si). Because we only track a finite number of elements, we cannot define the metallicity to be $Z = \sum_j m_j/m_{\mathrm{tot}}$ where the sum is over all elements heavier than He that are tracked by the simulation. Using $Z = 1-(m_{\mathrm{H}}+m_{\mathrm{He}})/m_{\mathrm{tot}}$ is also problematic since this definition is susceptible to round-off errors.

We therefore treat the total metal mass in the same manner as we treat individual elements, i.e., we include it as an additional array, as has also been done by others (e.g. Lia et al. 2002; Kawata & Gibson 2003; Valdarnini 2003; Sommer-Larsen et al. 2005; Romeo et al. 2006). There are a number of ways to determine the yield of the total metals released by a stellar population, $Y_Z \equiv m_{Z,\mathrm{p:ej}}$. Since the sum of all $Y_j \equiv m_{j,\mathrm{p:ej}}$ (including hydrogen and helium) should be zero (see eq. 3.16), one could simply define $Y_Z = -(Y_{\mathrm{H}} + Y_{\mathrm{He}})$. Unfortunately, yield tables often give $\sum_j Y_j < 0$, which implies that more mass is destroyed than produced. This is mainly due to non-conservation of nucleons and round-off errors (L. Portinari, private communication). We choose therefore to define $Y_{\mathrm{Z}}$ as the sum of the yields of all elements heavier than helium and redefine the hydrogen yield as:

$$Y_{\mathrm{H}} \equiv -(Y_{\mathrm{He}} + Y_{\mathrm{Z}}). \tag{3.18}$$

Note that $Y_{\mathrm{Z}}$ will differ from the sum of the metal yields of all elements tracked by the simulation if the yield tables contain more elements than are tracked by the simulation. The differences and round-off errors may not be significant in light of the uncertainties in our method (e.g., different yield sets, the definition of metallicity, etc.), but we choose to try to minimize the uncertainties at each step.

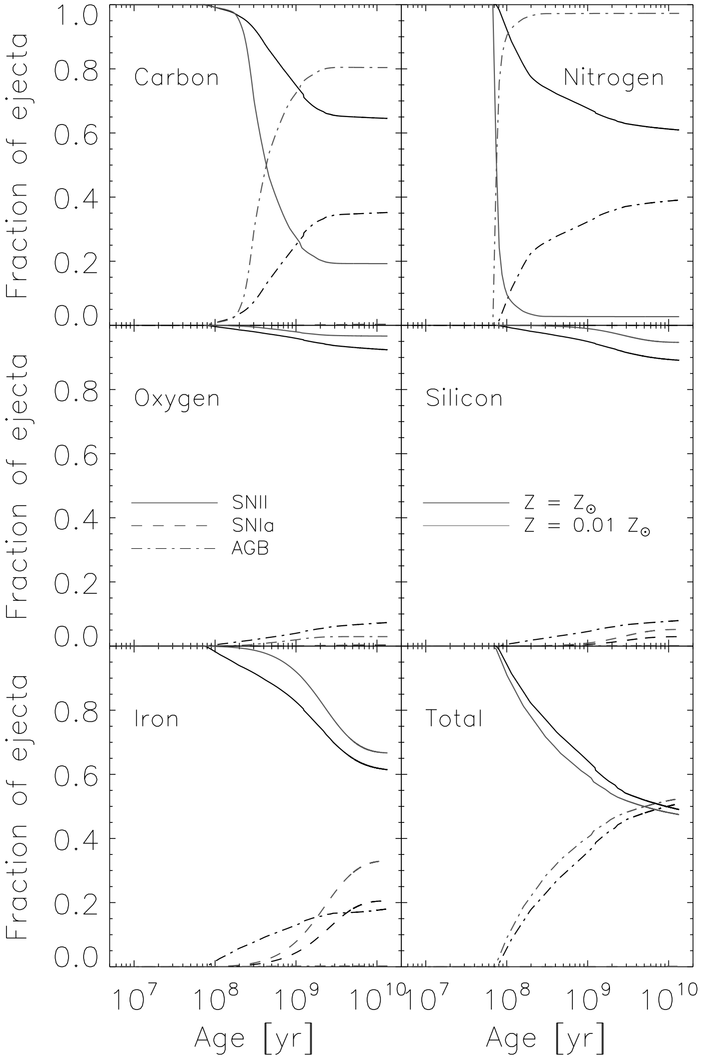

**Figure 3.8**: The fraction of the integrated mass ejected by an SSP that is due to SNII (solid), SNIa (dashed), and AGB (dot-dashed) as a function of the age of the SSP for two initial stellar metallicities: solar (black) and one per cent of solar (grey). All curves assume a Chabrier IMF. The bottom-right panel corresponds to the total ejected mass, whereas the other panels correspond to individual elements, as indicated in the plot. While nearly all the ejecta come initially from SNII, for ages $\tau \gtrsim 10^8$ yr the contributions from AGB stars become significant for carbon, nitrogen and, if the metallicity is high, for other elements as well. The contribution from SNIa very important for iron for $\tau \gtrsim 10^9$ yr. Note that the predictions are uncertain at the factor of two level, mainly due to the freedom in the normalization of the SNIa rate and the uncertainty in the yields.

### 3.5.2 Results

Figures 3.8 and 3.9 show the result of combining all the ingredients described in section 3.3 using the implementation described in this section. Both figures provide information about the composition of the integrated (i.e., cumulative in time) ejecta of an SSP as a function of its age. While figure 3.8 shows the fraction of the mass due to SNII, AGB and SNIa, figure 3.9 plots the abundance of a few elements relative to iron.

At early times, $\tau \lesssim 10^8$ yr, the integrated ejecta are totally dominated by SNII and consequently the abundances relative to iron of elements such as carbon, nitrogen, oxygen, and silicon are highly supersolar. As the stellar population ages, the contributions of AGB stars become very important for carbon and nitrogen and those of SNIa for iron. Higher initial stellar metallicities tend to result in larger abundances relative to iron, although the effect becomes smaller at late times because the yields of SNIa are independent of metallicity.

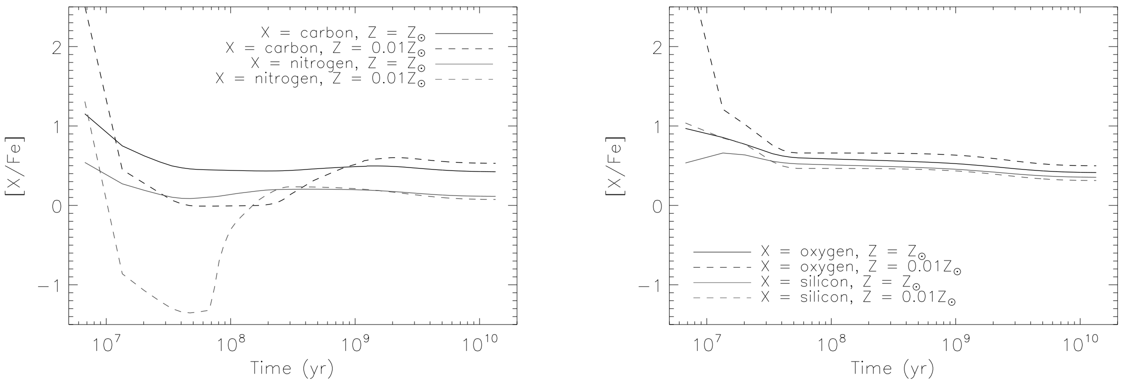

**Figure 3.9**: The abundances of various elements relative to iron in the integrated ejecta of an SSP as a function of its age for two metallicities: solar (solid) and one per cent of solar (dashed). All curves assume a Chabrier IMF. The abundances of all elements shown are initially enhanced relative to iron, particularly for lower stellar metallicities. The integrated abundances decrease relative to that of iron for $\tau \gtrsim 10^9$ yr when large amounts of iron are ejected by SNIa. Note that the predictions are uncertain at the factor of two level, mainly due to the freedom in the normalization of the SNIa rate and the uncertainty in the yields.

Note that these figures show the properties of the mass released integrated over time rather than at a particular time. For ages $\tau > 10^8$ yr all mass loss comes from AGB stars and SNIa and the elemental abundances relative to iron of the instantaneous ejecta are therefore much lower than those in the integrated ejecta that are shown here.

We emphasize that the predictions shown in these figures are very uncertain, even for a fixed IMF. As we discuss in section 3.3.3, the yields are uncertain at the factor of two level. For example, we rescaled the SNII yields as discussed in section 3.3.3). The relative contribution of SNIa is proportional to the normalization of the SNIa rate, which, as discussed in section 3.3.4, is also highly uncertain. As shown in Fig. 3.8, this is particularly important for iron.

We assumed a Chabrier IMF, but the results presented in this section would be similar for other IMFs as long as they have similar slopes for stellar masses above a few solar masses, as is for example the case for the Salpeter IMF.

## 3.6 IMPLEMENTATION INTO SPH

### 3.6.1 Enrichment scheme

Having determined the ejected masses $m_{j,\mathrm{ej}}$ for each stellar particle during a given time step, we still need to define how much of this mass should go to each of the surrounding gas particles. We would like the mass transfer to be isotropic, but it is not obvious how to accomplish this. As discussed in detail in appendix A of Pawlik &

Schaye (2008), the transport of mass[10] from a source particle to its SPH neighbours is in general highly biased towards the direction of the centre of mass of the neighbours. In essence this is a consequence of the fact that particle-to-particle transport is only possible in directions where there are particles.

Pawlik & Schaye (2008) demonstrate that using an SPH kernel transport scheme, as for example laid out by Mosconi et al. (2001), results in a statistical bias that is much smaller than alternative schemes such as equal weighting or solid angle weighting. It should be noted, however, that while SPH weighting results in only a small statistical bias, the transport from individual source particles is still highly anisotropic. As in previous works (e.g. Steinmetz & Mueller 1994; Kawata 2001; Kawata & Gibson 2003; Tornatore et al. 2004; Scannapieco et al. 2005; Stinson et al. 2006; Kobayashi et al. 2007; Tornatore et al. 2007), we choose to employ SPH weights and transfer to each SPH neighbour $k$ of a given star particle the fraction of the ejected mass given by

$$w_k = \frac{\frac{m_k}{\rho_k} W(r_k, h)}{\sum_i \frac{m_i}{\rho_i} W(r_i, h)}, \tag{3.19}$$

where $h$ is the smoothing length of the star particle (which we determine in the same manner as for gas particles), $r_i$ is the distance from the star particle to neighbour $i$, $W$ is the SPH kernel, and the sum in the denominator is over all SPH neighbours of the star particle. Tornatore et al. (2007) have investigated changing the number of neighbours and kernel length used for distribution of heavy elements. They found that doubling the amount of neighbours results in an increase of stellar mass fraction by about $10\%$, presumably because more particles are affected by metal-line cooling. We choose to use 48 neighbours, the same number as is used in the other SPH calculations.

Finally, we note that we do not change the entropy or, equivalently, the internal energy per unit mass of the receiving gas particles. The total internal energy of a receiving particle therefore increases when its mass increases. The thermal energy of the gas surrounding a star undergoing mass loss will change as a result of the mass transfer, but not necessarily by the amount that we implicitly assume. In the case of SN explosions we inject (part of) this energy explicitly (see §3.2) but it is possible that the mismatch of energy could be important. Assuming all star particles lose 100 per cent of their mass and that all this mass is transferred to non-star-forming particles with $T = 10^4\,\mathrm{K}$, the total energy per unit stellar mass that we implicitly use to heat the transferred mass to this temperature is only $(c_\mathrm{s}/v_\mathrm{w})^2/\eta \sim 10^{-4}$ of the kinetic energy released by core collapse SNe, where $c_s$ is the sound speed of the ambient medium. Thus, the energy that we implicitly use in the mass transfer is negligible. Furthermore, many of the receiving gas particles may be star-forming, in which case we impose an effective equation of state (see §3.2).

Similarly, we also neglect the change in the momentum of star particles and their gaseous neighbours as a result of the change in the particle masses. We made this choice partly because we also do not attempt to follow the actual momentum of the ejecta except for core collapse SNe, in which case we inject the kinetic energy explicitly.

---

[10] Pawlik & Schaye (2008) considered photon transport, but the analysis is equivalent for mass transport.

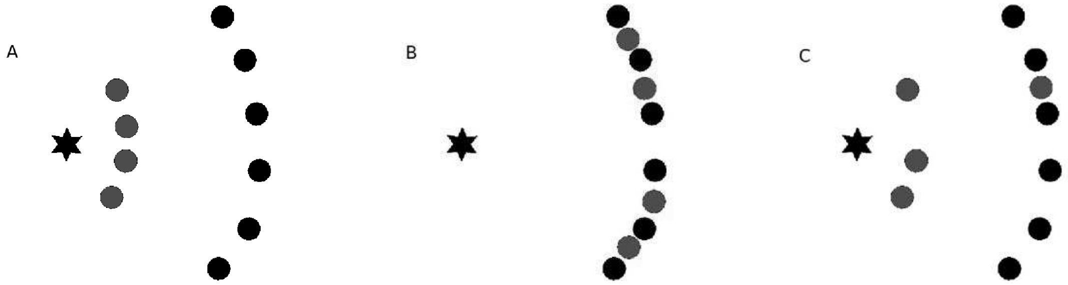

**Figure 3.10**: The enrichment sampling problem. *A*: A star particle enriches its neighbouring gas particles (grey). *B*: The energy released by massive stars within the star particle drives its neighbours away. Because metals are stuck to particle the local metallicity in the shell fluctuates. *C*: Using kinetic feedback the problem is worse because only a small fraction of the neighbours are kicked.

Neglecting momentum transfer from AGB stars and SNIa can be justified for the star particles if the mass transfer is isotropic, which it is in our case. For the receiving gas particles this argument does not apply, even when averaged over many mass transfer events, if the stars and gas have systematically different bulk flows. However, even in that case the energy associated with this momentum transfer is negligible compared with the kinetic energy injected by core collapse SNe unless the bulk flow velocities of the stars differ systematically from those of the gas by $\gtrsim 10^2\,\mathrm{km\,s^{-1}}$.

### 3.6.2 Smoothed metallicities

The elemental abundances of a particle are not only of interest in the analysis of the simulations, they are also required during the simulation itself because gas cooling rates depend on them. Furthermore, the lifetimes and yields of star particles depend on their metallicities.

Having tracked and transferred the total metal mass released by star particles during all time steps (see section 3.5.1), we could simply define the metallicity of a particle to be

$$Z_{\rm part} \equiv \frac{m_Z}{m}. \tag{3.20}$$

We will refer to metallicities computed using the above expression as "particle metallicities". Alternatively, we could define the metallicity as the ratio of the SPH smoothed metal mass density and the SPH smoothed gas mass density (as in Okamoto et al. 2005; Tornatore et al. 2007),

$$Z_{\rm sm} \equiv \frac{\rho_Z}{\rho}, \tag{3.21}$$

where the gas and metal mass densities of particle $i$ are given by the standard SPH expressions

$$\rho_i \;=\; \sum_j m_j W(r_i - r_j, h_i), \tag{3.22}$$

$$\rho_{\mathrm{Z},i} = \sum_j m_{\mathrm{Z},j} W(r_i - r_j, h_i), \tag{3.23}$$

where the sum is over all SPH neighbours $j$ and $h_i$ is the smoothing length of particle $i$. We will refer to metallicities computed using (3.21) as "smoothed metallicities". Similarly, we will make use of particle and smoothed abundances of individual elements. Note that while particle abundances can only change when a particle gains or loses mass, smoothed abundances will generally vary from time step to time step because they depend on the distances between particles and their SPH neighbours. Although most studies do not explicitly define what they mean by "metallicity", particle metallicities are generally used.

The use of smoothed abundances has the advantage that it is most consistent with the SPH formalism. For example, in the absence of metals gas cooling rates depend on $\rho$ and it therefore makes sense for the metallic cooling rates to depend on $\rho_Z \equiv Z_{\mathrm{sm}}\rho$, computed in the same manner as $\rho$. Another advantage of smoothed abundances is that they partially counter the lack of metal mixing that is inherent to SPH. In particular, there will be many less particles with zero metallicity if smoothed abundances are used because every neighbour of a particle with a non-zero particle metallicity will have a non-zero smoothed metallicity.

The reason SPH underestimates metal mixing is that, in the absence of some implementation of diffusion, metals are stuck to particles. Even in the absence of microscopic diffusion processes, this will result in a lack of metal mixing due to a straightforward sampling problem. This sampling problem is most easily illustrated by imagining a shell of constant thickness swept up by a spherically symmetric explosion driven by a single stellar particle in a uniform, initially primordial gas, just after it has completed the transfer of metals produced by massive stars to its SPH neighbours (see Fig. 3.10). As the metal-rich bubble expands, the local metal density should decrease as $1/r^2$. However, because the metals are stuck to a fixed number of particles, the local metal density will instead fluctuate strongly within the swept-up shell (Fig. 3.10, middle panel). The situation may actually be even worse in practice because we are using kinetic feedback which implies that only a subset of the SPH neighbours of the star particle are kicked (Fig. 3.10, right panel). Note that this sampling problem does not become smaller when the resolution is increased.

The metal sampling problem of SPH can be reduced by implementing diffusion (and tuning the diffusion coefficient). We have, however, decided not to do this because diffusion is a physical process whereas the sampling problem is in essence a numerical problem. Attempting to solve it with a poorly constrained physical mechanism may have undesired consequences. Depending on the severity of the sampling problem, it may for example require an unphysical amount of diffusion. The addition of diffusion may also lead to the introduction of new physical scales (through the choice of a particular value for the diffusion coefficient).

We therefore consider the problem of (turbulent) diffusion separate from the sampling problem described here. While diffusion processes may well be important and have a significant impact on our results (e.g. de Avillez & Breitschwerdt 2007), subgrid recipes are required to implement them as they relevant physical processes are unresolved in cosmological simulations.

Note that a static gas will not suffer from the sampling problem but diffusion will still alter its metallicity distribution. A possible way out may therefore be to implement a recipe for (turbulent) diffusion that depends explicitly on the relative velocities of neighbouring particles (Greif et al. 2008). Although this will still implicitly use physical processes (e.g. hydrodynamical instabilities) to get around a numerical problem, it does have the important advantage that it asymptotes to the standard, no mixing, solution for the case of a static gas. We intend to test such sub-grid mixing prescriptions in the future. For now, we note that our use of smoothed abundances decreases the severity of – but does not solve – the sampling aspect of the mixing problem, leaving the physical aspect of the problem unaddressed.

We decided to use smoothed abundances in the calculation of the cooling rates, the stellar lifetimes and the yields. When a gas particle is converted into a stellar particle its smoothed abundances are frozen. Note that because the smoothed abundances of gas particles are recalculated at every time step from the metal mass fractions, we need to store both smoothed and particle abundances and can thus compare the two.

It is important to note that metal mass is only approximately conserved when smoothed abundances are used using the "gather approach", equation (3.23). The non-conservation is exacerbated by the fact that the smoothed abundances of a particle are frozen when it is converted from a gas into a star particle. Metal conservation could be enforced by using a "scatter" approach,

$$\rho_{\mathrm{Z},i} = \sum_j m_{\mathrm{Z},j} W'(r_i - r_j, h_j), \tag{3.24}$$

normalized such that $\sum_i W'(r_i - r_j, h_j) = 1$ for every particle $j$. However, this is computationally more expensive and would in any case only conserve metal mass if the time steps of all particles were synchronized, which is not the case for GADGET.

It is a well known problem that the SPH technique overestimates densities of low density gas in regions where the density gradient is steep, which may result in overcooling (Pearce et al. 1999). By using smoothed metal densities we are vulnerable to a similar problem that may result in an overestimate of the metal mass and hence increased overcooling. Indeed, in our low resolution L025N128 and L100N128 runs the final total smoothed metal masses are, respectively, 3.6% and 18% greater than the final total particle metal masses. However, as expected, the difference decreases rapidly with increasing resolution. For the L100N256, L100N512, and L025N512 runs the total smoothed metal mass is 8.3% higher, 3.7% higher, and 0.14% lower than the total particle metal mass in the respective simulations. Thus, metal mass conservation errors are negligible for our highest resolution simulations.

However, note that we compared total smoothed and particle metal masses in simulations that always used smoothed abundances to compute the cooling rates, stellar lifetimes and yields. Because increased metal abundances will result in increased cooling and thus increased star formation and increased metal production, we expect the difference to increase if we compare the total smoothed metal mass predicted by a simulation employing smoothed abundances with the total particle metal mass pre-

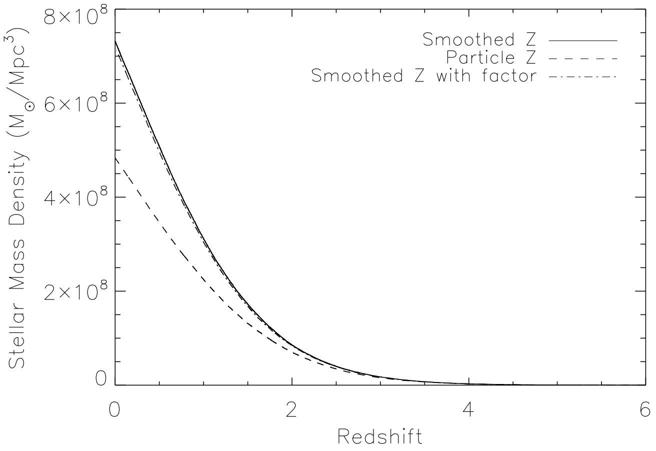

**Figure 3.11**: Stellar mass density as a function of redshift for $256^3$, $100\ h^{-1}\,\mathrm{Mpc}$ runs. The solid curve shows the total stellar mass density in L100N256 which employs smoothed abundances in the calculation of the cooling rates. The dashed curve indicates the total stellar mass in a simulation that used particle abundances for the cooling rates. The use of smoothed abundances increases the stellar mass produced by $z = 0$ by 51 %. The dash-dot curve used smoothed abundances for the cooling after multiplying them by a factor $1/1.08$ to correct for the increase in the total metal mass, at fixed stellar mass, due to the use of smoothed abundances. The fact that the dash-dot curve is close to the black one indicates that the increase in the stellar mass when using smoothed abundances is mostly due to the increased metal mixing rather than the small increase in the total metal mass.

dicted by a simulation employing particle abundances. We have tested this by comparing two L100N256 (and two L100N128) simulations. One simulation used smoothed abundances while the other used particle abundances for the calculation of the cooling rates. Indeed, we found that at $z = 0$ the total smoothed metal mass in the L100N256 (L100N128) simulation using smoothed abundances was 49% (82%) higher than the total particle metal mass in the corresponding simulation using particle abundances.

As can be seen from Figure 3.11, the simulation that uses smoothed abundances (black curve) produces about 1.5 times as many stars as the simulation that used particle abundances (red curve) for the calculation of the cooling rates. We performed a further test to determine if the increase in the stellar mass resulting from our use of smoothed abundances is due to the non-conservation of metal mass or to the increased metal mixing (i.e., metal cooling affects more particles). To this end we ran another version of the L100N256 simulation that used smoothed abundances but in which the smoothed abundances were multiplied by a factor $1/1.08$, which is the ratio between the final total particle and smoothed metal mass in the simulation that used smoothed abundances for the cooling, before passing them to the cooling routine. As can be

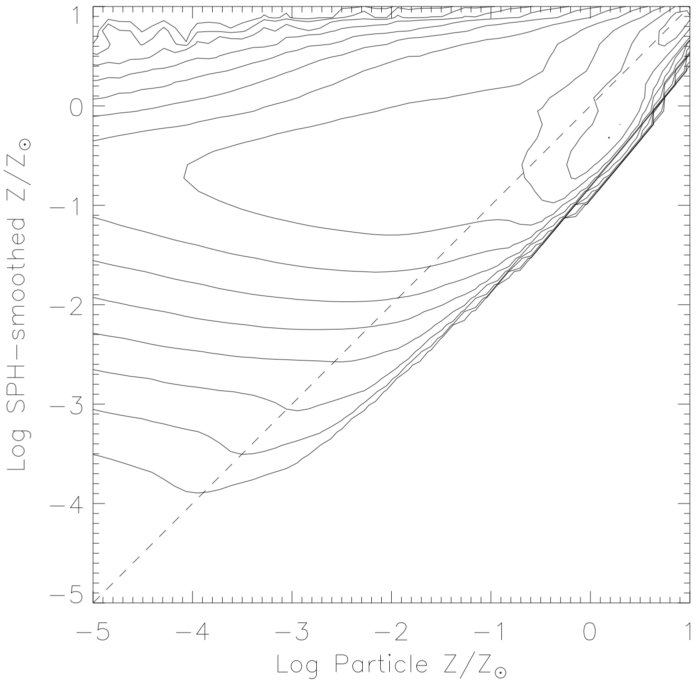

**Figure 3.12**: Two-dimensional probability density function of particle number density in the smoothed metallicity - particle metallicity plane for the L100N512 simulation at $z = 0$. The contours are spaced logarithmically by 0.5 dex. The two metallicity definitions agree in highly enriched regions where the metals are well mixed, but at lower metallicities the smoothed metallicities are typically higher. The lowest possible smoothed metallicity for a particle with non-zero particle metallicity corresponds to the case when all its neighbours are metal-free and agrees with the lower envelope visible in the plot.

seen from Figure 3.11 (blue curve), the result is much closer to the simulation using smoothed abundances (but without the reduction factor) than to the simulation using particle abundances. Hence, the increase in the total stellar mass is mostly due to the increase in the metal mixing.

This example demonstrates that the poor performance of SPH with regards to metal sampling and mixing is an important problem that can have a very large effect on the predicted star formation history. On the other hand, we expect the differences to be smaller for our higher resolution simulations. The fact that non-conservation of metal mass is much less important than metal mixing and that the mismatch between the total metal masses becomes very small for our highest resolution simulations, support our decision to use smoothed abundances during the simulations. In the rest of this chapter we will therefore only make use of simulations that employed smoothed abundances for the calculation of the cooling rates.

In figure 3.12 we directly compare the $z = 0$ smoothed and particle metallicities in the L100N512 simulation. The contours show the logarithm of the particle number density in the $Z_{\rm sm} - Z_{\rm part}$ plane. The dashed line indicates 1-1 correspondence. The two metallicities are strongly correlated for high metallicities, although significant scatter exists. This is expected, because high-metallicity gas will have been enriched by many star particles during many time steps and we therefore expect the metals to be well mixed. For low particle metallicities, however, the two metallicity definitions become essentially uncorrelated and the smoothed metallicities are typically higher than the particle metallicities. This is because a single enriched particle can give its neighbours a range of smoothed abundances depending on their distances.

For a given particle metallicity, there is a well defined lower limit to the smoothed

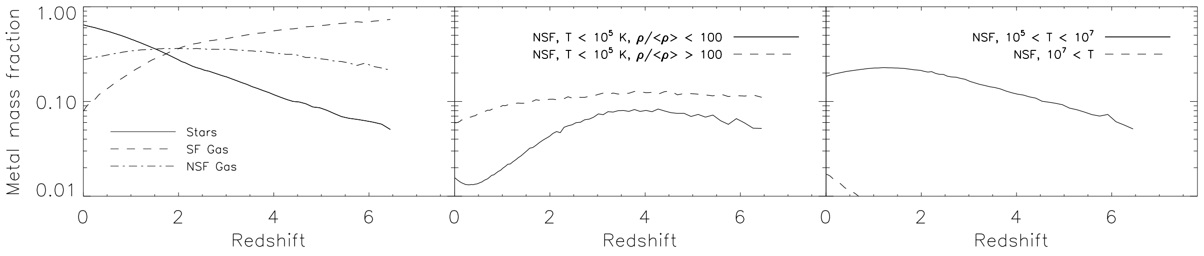

**Figure 3.13**: Evolution of fractional metal mass in various components for the L100N512 simulation. Left: Stars (solid), star-forming gas (dashed) and non-star-forming gas (dot-dashed). Note that these curves add up to unity. Centre: Cold-warm IGM (non-star-forming, $\rho < 100\langle\rho\rangle$, $T < 10^5\,\mathrm{K}$) (solid), and cold-warm halo gas (non-star-forming, $\rho > 100\langle\rho\rangle$, $T < 10^5\,\mathrm{K}$) (dashed). Right: WHIM (non-star-forming, $T > 10^5\,\mathrm{K}$) (solid) and ICM (non-star-forming, $T > 10^7\,\mathrm{K}$) (dashed). The parts of the curves corresponding to redshifts for which the total metal mass is smaller than $10^{-6}$ of the total baryonic mass have been omitted because they become very noisy. While most metals initially reside in star-forming gas, by $z = 0$ most are locked up in stars. At present most of the gaseous metals reside in the WHIM.

metallicity. This minimum smoothed metallicity corresponds to that of a metal-bearing particle that is surrounded by metal-free particles. It is visible as the lower envelope of the contours parallel to the dashed line in figure 3.12. From equations (3.21) and (3.23) we can see that the minimum smoothed metallicity is $Z_{\mathrm{sm},i} = m_{\mathrm{Z},i} W(0, h_i)/\rho_i$. Using the fact that for GADGET the value of the kernel at zero displacement is $W(0, h_i) = 8/(\pi h_i^3)$ and that for particles with $m_i \approx m$ the kernel satisfies $4\pi\rho_i h_i^3/3 \approx N_{\mathrm{ngb}} m$ (where the number of SPH neighbours $N_{\mathrm{ngb}} = 48$ in our simulations), it is easy to show that $Z_{\mathrm{sm},i} \approx 2Z_{\mathrm{part},i}/9$.

In summary, we use smoothed abundances during the simulation because it is consistent with the SPH method and because it reduces, though not eliminates, the metal sampling problem. Smoothed and particle metallicities are very close in high-metallicity regions but in low-metallicity regions the smoothed abundances will typically exceed the particle ones. Using SPH simulations to study low-metallicity gas and stars is hence problematic because the results are sensitive to the definition of metallicity that is used. The use of smoothed abundances increases the number of particles for which metal cooling is important and thus the star formation rate, particularly when the resolution is low.

## 3.7 THE PREDICTED DISTRIBUTION OF METALS

In this section we will investigate the cosmic metal distribution predicted by our simulations. We will only present results from the simulations listed in Table 3.2, which are drawn from the reference simulations of the OWLS set. While the simulations analysed here differ in terms of their box sizes and particle numbers, they all used the same simulation code and the same prescription for star formation, galactic winds and cooling. In chapter 4 we use the full OWLS set to study the effect of changes in the baryonic

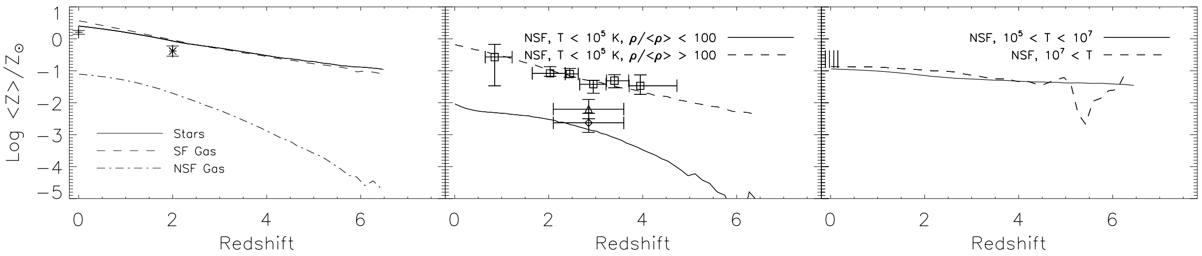

**Figure 3.14**: Evolution of the mass-weighted metallicities of various components for the L100N512 simulation. The panels and line styles are identical to those shown in Fig. 3.13. The metallicity of stars and the ISM evolves much more weakly than that of cold-warm diffuse gas. The mean metallicity of the WHIM is $\sim 10^{-1}\,Z_\odot$ at all times. Symbols indicate observational estimates of metallicities in various phases - stars: (Gallazzi et al. 2008) (plus sign) and (Halliday et al. 2008) (cross symbol); cold halo gas: (Prochaska et al. 2003) (squares); diffuse IGM: (Aguirre et al. 2008) (triangle) and (Schaye et al. 2003) (diamond); ICM: (Simionescu et al. 2009) (orange region).

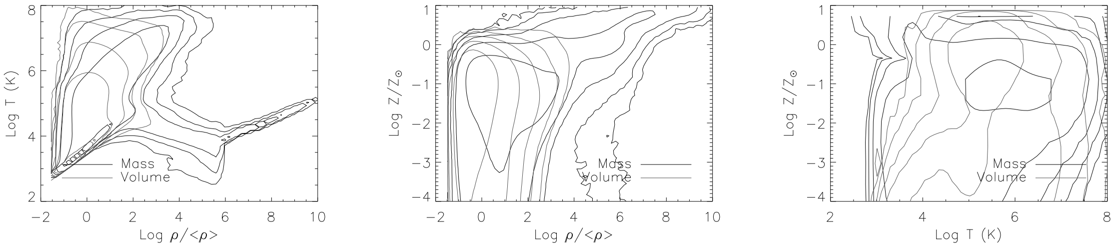

**Figure 3.15**: Gas distribution weighted by mass (black) and volume (grey) in the temperature - density (left), metallicity - density (centre), and metallicity - temperature (right) planes at $z = 0$ for the L100N512 simulation. Note that star-forming gas has been excluded from the right-hand panel. The contours are spaced by 1 dex. While low-density gas displays a wide range of metallicities, there is a strong positive gradient of metallicity with density that becomes narrower for higher densities. Combined with the fact that low-density gas must account for a larger fraction of the volume than the mass, the metallicity-density correlation implies that volume-weighting favors lower metallicities than mass weighting. There is no well defined relation between temperature and metallicity.

processes on the metal distribution, which turns out to be very important. Here we will instead focus on convergence tests and on the effect of different metallicity definitions.

There are a number of approaches we can take to study the cosmic metal distribution in our simulations. Before analysing the metal distribution at $z = 0$ in more detail, we will investigate the evolution of the metal mass fractions in various components. We will then proceed to discuss the dependence of the results on the definition of metallicity (§3.7.1), the size of the simulation box (appendix 3.A) and the numerical resolution (appendix 3.B). While appendices 3.A and 3.B will make use of the full suite of simulations listed in Table 3.2, we will only consider the L100N512 (which contains $2 \times 512^3$ particles in a box that is $100\ h^{-1}\,\mathrm{Mpc}$ on a side) run in the rest of this section.

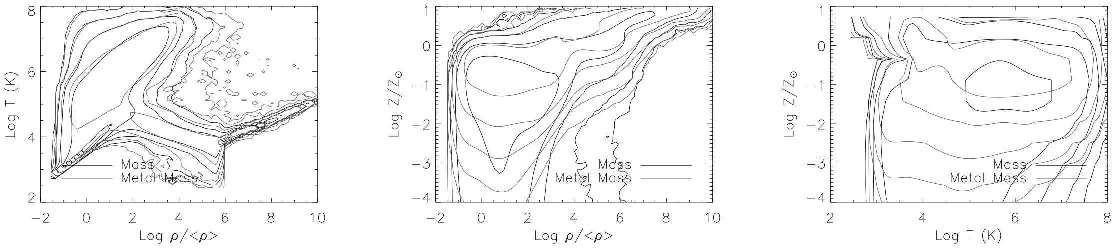

**Figure 3.16**: Gas mass (black) and gas metal mass (grey) distribution in the temperature - density (left), metallicity - density (centre), and metallicity - temperature (right) planes at $z = 0$ for the L100N512 simulation. Note that star-forming gas has been excluded from the right-hand panel. The contours are spaced by 1 dex. While gaseous metals track the general gas mass distribution at high densities (or metallicities), at the densities corresponding to diffuse structures ($\rho \lesssim 10^2 \langle\rho\rangle$) metals reside in gas that is both hotter and more metal-rich than is typical for these densities.

We note, however, that our much higher resolution L025N512 simulation (which was, however, stopped at $z = 1$) gives qualitatively similar results.

Figure 3.13 shows the evolution of the fraction of the metal mass contained in various components. By isolating the gaseous metals into various phases, we can develop a picture of where the metals are at a given redshift. To that end we have plotted the total fraction of the metal mass in stars (left, solid), star-forming gas (left, dashed), and non-star-forming gas (left, dot-dashed). Recall (see §3.2) that by star-forming we mean gas particles that are allowed to form stars and for which we impose an equation of state. These particles all have densities $n_{\rm H} > 10^{-1}\,{\rm cm}^{-3}$ and can be thought of as ISM gas. We have divided the non-star-forming gas into cold-warm ($T < 10^5\,{\rm K}$; middle) and warm-hot ($T > 10^5\,{\rm K}$; right) components. The cold-warm gas has been further subdivided into diffuse ($\rho < 10^2 \langle\rho\rangle$; middle, solid) and halo ($\rho > 10^2 \langle\rho\rangle$; middle, dashed) gas and we have subdivided the warm-hot, non-star-forming gas into the warm-hot IGM (WHIM) ($10^5\,{\rm K} < T < 10^7\,{\rm K}$; right, solid), and the intracluster medium (ICM) ($T > 10^7\,{\rm K}$; right, dashed).

Focusing first on the left-hand panel of Fig. 3.13, we see that the most prominent trend is the strong decrease in the fraction of the metals in star-forming gas. While this phase harbors most of the metals at $z = 8$, by $z = 0$ it contains only a small fraction. The opposite is true for the stars: while most of the metals are initially in the gas phase, today the majority of the metals are locked up in stars. The metal fraction contained in non-star-forming gas varies between twenty and forty per cent.

Davé & Oppenheimer (2007) have recently used a cosmological SPH simulation (using $256^3$ gas particles in a $32\,h^{-1}\,{\rm Mpc}$ box) to investigate the cosmic distribution of metals. While we postpone a detailed comparison to chapter 4, we note a clear, qualitative difference in the results. While Davé & Oppenheimer (2007) find that initially (at $z = 6$) the diffuse IGM contains much more metal than the ISM, we find the opposite. Schaye et al. (2009) showed this difference mostly reflects the higher initial mass loading of galactic winds assumed by Davé & Oppenheimer (2007). This difference illustrates the importance of varying the subgrid recipes used in the simulations. We will report on such variations chapter 4.

The other two panels of Fig. 3.13 show that while the metal fraction in cold-warm gas decreases with time, the fraction contained in warm-hot and hot gas increases. This is not unexpected, as growth of structure will result in more and stronger accretion shocks, heating an increasing fraction of the gas to high temperatures. While most of the metals in non-star-forming gas are initially cold, more than half of them reside in the WHIM for $z < 2$. The ICM, on the other hand, still contains only a few percent of the metal mass by $z = 0$, an order of magnitude less than the WHIM.

Besides the metal mass fractions, the metallicities of the various components are also of interest. Together with the evolution of the baryonic mass fractions, which we will present in Dalla Vecchia et al. (in prep), the metallicities determine the metal mass fractions. Figure 3.14 shows the evolution of the mass-weighted mean metallicities of the same components that were shown in Fig. 3.13.

As expected, the metallicity of the star-forming gas roughly traces the metallicity of the stars throughout the simulation, although the ratio of the mean stellar metallicity to the mean ISM metallicity decreases slightly with time. The stellar and ISM metallicities increase relatively slowly with time. At $z = 3$ the mean stellar metallicity is about 0.5 dex lower than at $z = 0$. Interestingly, the WHIM and the ICM have a metallicity $\sim 10^{-1}\, Z_{\odot}$ at all times. This lack of evolution is in stark contrast to the behavior of the cold-warm, diffuse gas whose metallicity increases rapidly with time. Consequently, the differences in the metallicities of the various components become smaller at lower redshifts. However, even by $z = 0$ the metallicity of the diffuse, cold-warm IGM is only of order 1 per cent of solar.

Although our primary aim is not to perform a direct comparison to observations, we have included in Fig. 3.14 a number of observational estimates of metallicity[11] in various phases. In the left panel we show the estimates for the mean stellar metallicity at $z = 0$ and $z = 2$ from Gallazzi et al. (2008) and Halliday et al. (2008), respectively. Our simulations fall about 0.2 dex above the redshift zero point and land about 0.3 dex above the higher redshift point. We note however, that Halliday et al. (2008) find their result to be low compared to that of Erb et al. (2006). They explained that this could represent an alpha enhancement at high redshift (Erb et al. 2006 measured oxygen while Halliday et al. 2008 measured iron). We compare our predictions for overdense, cold, non-starforming gas to the observations of damped Ly$\alpha$ (DLA) systems of Prochaska et al. (2003) and find excellent agreement. Our measurement of the mean metallicity of the $z \approx 3$ IGM agrees with the measurement based on carbon of Schaye et al. (2003), but falls slightly below that based on oxygen of Aguirre et al. (2008). In appendix 3.B we show that the metallicity of this phase is particularly sensitive to resolution and that higher resolution simulations may predict higher diffuse IGM metallicities. Finally, the metallicity of the low-redshift ICM falls along the lower range of cluster measurements compiled by Simionescu et al. (2009). For this we compiled a range of all metallicity measurements in the most outer regions of the clusters (regions which should dominate the mass averaged metallicity). We note that since most radial profiles flatten at outer radii, this should be a safe assumption. From these comparisons we conclude

---

[11] The observations were converted to our solar abundances where necessary.

that our simulation is in reasonable agreement with a range of observations. Although these values for mean metallicity are often luminosity weighted, we wish to avoid for now further uncertainties introduced by modelling the emission so we simply compare with our mass-weighted values.

Before investigating the robustness of these results to numerical effects, we will study the $z = 0$ metal distribution in more detail. To interpret the results, it is, however, helpful to first consider the gas mass rather than the metal mass distribution.

The solid contours in the left-hand panel of figure 3.15 indicate the $z = 0$ gas mass-weighted 2-dimensional (2-D) probability density function (PDF) in the temperature-density plane. That is, the contour values correspond to $dM_{\rm g}/(M_{\rm g,tot} d\log\frac{\rho}{\langle\rho\rangle} d\log T)$. Similarly, the red contours show the volume-weighted[12] 2-D PDF, i.e., $dV/(V_{\rm tot} d\log\frac{\rho}{\langle\rho\rangle} d\log T)$. All contour plots in this section show contours spaced by one dex, with each plot containing the same levels for both linestyles.

There are a number of distinct features in this temperature-density diagram. Much of the mass, and nearly all of the volume, resides in a narrow strip ranging from about $(\log\rho/\langle\rho\rangle, \log T) \sim (-1.5, 3)$ to $\sim (1.5, 4.5)$, which corresponds to the diffuse, photo-ionized IGM. The relation between temperature and density of this component is set by the balance between photo-heating and adiabatic cooling (Hui & Gnedin 1997). For gas at higher overdensities photo-heating is balanced by radiative rather than adiabatic cooling and the temperature slowly decreases with increasing density. The plume of much hotter gas corresponds to gas that has been shock-heated, either through gravitationally induced accretion shocks or galactic winds. For gas with densities $\rho/\langle\rho\rangle \gtrsim 10^2$ there is less mass at temperatures $T \sim 10^5\,{\rm K}$ than there is at lower and higher temperatures because the radiative cooling rates peak at these temperatures (due mostly to collisional excitation of oxygen, carbon, and helium), resulting in a bimodal distribution of the temperature in that density regime. The well-defined $T$-$\rho$ relation at the highest densities reflects the equation of state $P \propto \rho_g^{4/3}$, which we impose on gas with densities exceeding our star formation threshold of $n_{\rm H} = 0.1~{\rm cm}^{-3}$ ($\rho/\langle\rho\rangle \sim 10^6$ at $z = 0$). As discussed in §3.2, the temperature of this gas merely reflects the imposed effective pressure of the unresolved multiphase ISM.

The middle and right panels of Fig. 3.15 show how the gas mass (black) and the volume (red) are distributed in the metallicity-density and the metallicity-temperature planes, respectively. We have excluded star-forming gas from the right-hand panel since its temperature would merely reflect the pressure of the equation of state that we have imposed. We will exclude this component from all plots investigating temperature dependencies, except for temperature-density diagrams such as the left-hand panel of Fig. 3.15 (because in that case the gas density can be used to identify the star-forming gas).

While there is a clear positive correlation between metallicity and density for highly overdense gas (see the black contours in the middle panel), gas at low overdensities can have a large range of metallicities extending all the way to zero (outside the plotted range). Note that the highest density gas is highly supersolar. This reflects the fact that

---

[12] Volume weighting was implemented as weighting by $h_i^3/\sum_j h_j^3$, where $h_i$ is the SPH smoothing length of particle $i$. We verified that using $m/\rho$ instead of $h^3$ gives nearly identical results.

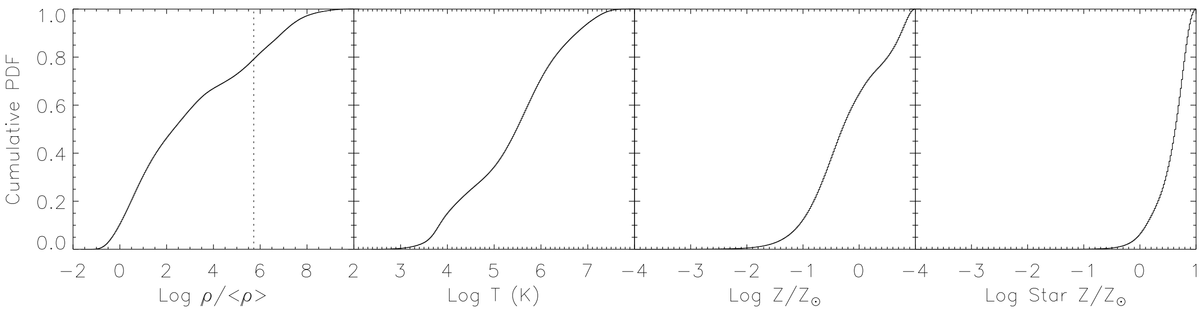

**Figure 3.17**: Cumulative probability density function of the gas metal mass as a function of gas density (*left*), temperature (*centre-left*), and metallicity (*centre-right*) at $z = 0$ for the L100N512 simulation. The vertical, dotted line in the left panel indicates our star formation threshold. Also note that star-forming gas has been excluded from the temperature plot. The right-hand panel shows the cumulative PDF of the stellar metal mass as a function of the stellar metallicity. While the gas metal mass is distributed over a wide range of densities and temperatures, it is concentrated in gas that has a relatively high (local) metallicity.

massive galaxies in this simulation have too high metallicities because galactic winds cannot escape their high-pressure ISM. In chapter 4 we will show that this problem is not present for some other implementations of galactic winds driven by SNe and, particularly, for more efficient feedback mechanisms such as energy injected by active galactic nuclei. The right-hand panel shows that there is no well-defined relation between metallicity and temperature. Gas at a given temperature displays a wide range of metallicities.

Figure 3.16 uses the same panels as Fig. 3.15 to compare the distribution of gas mass (black) and metal mass (red). Since we use smoothed metallicities, metal mass is defined as $Z_{\rm sm} M_{\rm g}$. Note that the black contours are identical to those shown in Fig. 3.15. Focusing first on the left-hand panel, which shows the distributions in the temperature-density plane, we see that while metal and gas mass track each other well for high overdensities (although the gas mass is distributed over a narrower range of temperatures for a given density), they differ in one important respect for $\rho / \langle \rho \rangle \lesssim 10^2$. Whereas most of the mass is concentrated at the lowest densities and temperatures, this diffuse, photo-ionized IGM contains only a small fraction of the metals. Instead, the vast majority of metals in low-density gas are hot ($T \gtrsim 10^5$ K). This is probably caused by the fact that high-velocity winds are required to transport metals to regions far from galaxies and that such winds shock-heat the medium. This agrees with Theuns et al. (2002) and Aguirre et al. (2005), who also found that most of the diffuse metals reside in hot gas, using different implementations of feedback from star formation and using simulations that did *not* include metal-line cooling. Aguirre et al. (2005) speculated that the inclusion of radiative cooling by metals might be important, but our simulations show that even when metal-line cooling is included, the WHIM ($5 < \log T < 7$, $\rho / \langle \rho \rangle \lesssim 10^3$) is an important reservoir of cosmic metals. From the right-hand panel of Fig. 3.15 we can see that although some WHIM gas has very low metallicities, much of it has $Z \gtrsim 10^{-1}\ Z_\odot$.

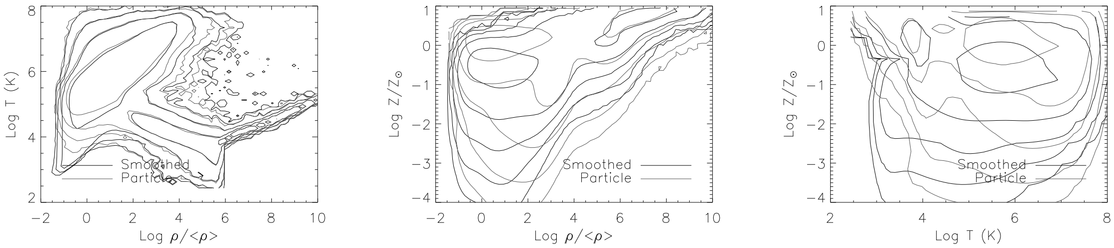

**Figure 3.18**: Gas smoothed metal mass (black) and gas particle metal mass (grey) distribution in the temperature - density (left), metallicity - density (centre), and metallicity - temperature (right) planes at $z = 0$ for the L100N512 simulation. Note that star-forming gas has been excluded from the right-hand panel. The contours are spaced by 1 dex. Except for low-metallicity gas, which mostly has low densities and temperatures, smoothed and particle metallicities yield similar results.

The left-hand panel of Fig. 3.17 shows the cumulative PDF for the gas metal mass as a function of $\log \rho/\langle\rho\rangle$, i.e., $\frac{1}{M_{Z_{\rm sm,tot}}}\int_0^\rho d\rho' \frac{d(M_{\rm g}Z_{\rm sm})}{d\rho'}$, where $M_{Z_{\rm sm,tot}}$ is the total smoothed metal mass in gas. Similarly, the second and third panels from the left show the cumulative PDF of the gas metal mass as a function of temperature and metallicity and the right-hand panel shows the cumulative PDF of the stellar metal mass as a function of metallicity. While the gas metal mass is spread over remarkably large ranges of densities and temperatures, it is concentrated in relatively high-metallicity gas. Note, however, that metallicity is evaluated locally, at the resolution limit of the simulation. High metallicity gas therefore includes patches of enriched gas embedded in structures whose overall metallicity is low.

Considering one variable at a time, ninety percent of the $z = 0$ gas metal mass resides in gas with $10^{-0.5} \lesssim \rho/\langle\rho\rangle \lesssim 10^{7.5}$, $10^4\,{\rm K} \lesssim T \lesssim 10^{6.5}\,{\rm K}$, or $10^{-1.5} \lesssim Z_{\rm sm}/Z_\odot \lesssim 10^{0.7}$. Half the gaseous metal mass resides in gas with $\rho < 10^2\langle\rho\rangle$ which implies that diffuse and collapsed structures contain similar amounts of metal mass. In terms of temperature the midpoint lies at about $10^5$ K, which means that half the gas metal mass resides in shock-heated gas. Clearly, any census aiming to account for most of the metal mass in gas will have to take a wide variety of objects and structures into account.

In the next section we will investigate the metal distribution and its evolution in more detail, including the sensitivity of the results to the definition of metallicity. The convergence of the predictions with respect to the size of the simulation box and the numerical resolution is studied in appendices 3.A and 3.B, respectively.

### 3.7.1 Smoothed vs. particle metallicity

As discussed in §3.6.2, there is some ambiguity in the definition of the metallicity in SPH. We have opted to use SPH smoothed metallicities $Z_{\rm sm} \equiv \rho_Z/\rho$ rather than particle metallicities $Z_{\rm part} \equiv m_Z/m$, because using smoothed abundances is consistent with the SPH method and because it partially counters the lack of metal mixing that results

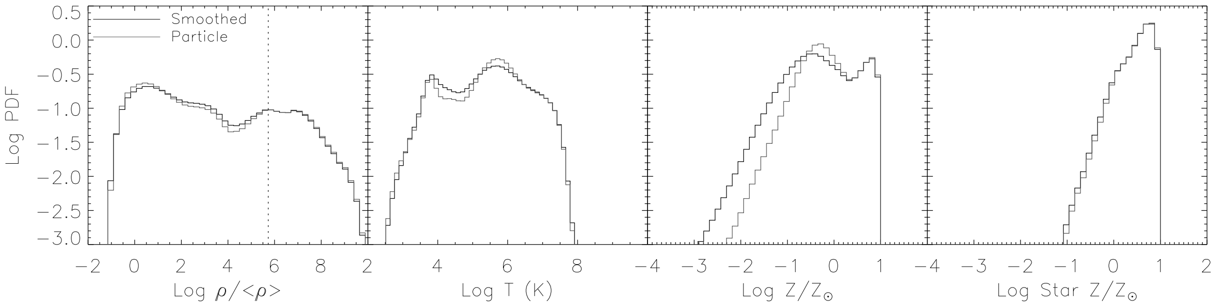

**Figure 3.19**: Probability density function of the gas density (left), temperature (centre-left) and smoothed/particle metallicity (centre-right) weighted by smoothed (black) and particle (grey) metal mass. The black (grey) histogram in the right-hand panel shows the PDF of the smoothed (particle) stellar metallicity weighted by smoothed (particle) metal mass. All panels correspond to the L100N512 simulation at $z = 0$. The vertical, dotted line in the left panel indicates the threshold for star formation. Note that star-forming gas was excluded from the temperature panel. The predictions for smoothed and particle metallicities only differ significantly for low-metallicity gas.

from the fact that metals are stuck to particles. We already demonstrated in §3.6.2 that the definition of metallicity is particularly important for low metallicity gas and that it has important consequences for gas cooling rates (and hence for the predicted star formation histories). Here we investigate its effect on the metal distribution by comparing the gas metal mass distributions computed using smoothed and particle metallicities. Note, however, that smoothed metallicities were always used during the simulation for the calculation of the radiative cooling rates, stellar lifetimes, and stellar yields.

Figure 3.18 compares the gas metal mass distribution using smoothed (black) and particle (red) metallicities in the temperature-density (left), metallicity-density (middle) and metallicity-temperature (right) planes. Note that the black contours are identical to the red contours in Fig. 3.16. The smoothed and particle metal distributions trace each other reasonably well, except for the diffuse, photo-ionized IGM ($\rho/\langle\rho\rangle < 10^2$, $T < 10^5$ K; left panel) and generally for low-metallicity gas ($Z \ll Z_\odot$; middle and right panels). When smoothed metallicities are used larger fractions of the metal mass reside in low-metallicity gas, which is consistent with Fig. 3.12.

The left-hand panel of figure 3.19 shows the 1-D gaseous metal mass weighted PDF for the gas density, i.e., $d(M_{\rm g}Z)/(M_{Z,{\rm tot}}d\log\frac{\rho}{\langle\rho\rangle})$ as a function of $\log\rho/\langle\rho\rangle$, where $Z$ is the smoothed/particle metallicity and $M_{Z,{\rm tot}}$ is the total smoothed/particle metal mass in gas. Thus, if the $y$-axis were linear (which it is not), the fraction of the area underneath the histogram that is in a given bin would correspond to the fraction of the gas metal mass in that bin. Similarly, the second and third panels from the left show the metal-mass weighted PDF of the temperature and metallicity, respectively, and the right-hand panel shows the metal mass-weighted PDF of the stellar metallicity. The distribution of metal mass over density is similar for smoothed and particle metallicities, but using smoothed metallicities results in a significant shift of metal mass from $T \sim 10^6$ K to $T < 10^5$ K. While the differences in the metal distributions as a function of metallicity are small for stars, presumably because they tend to form in well-mixed, high density gas, the differences are very substantial for the gas. As expected, the use of smoothed metallicities results in a prominent shift of gaseous metal mass to lower metallicities. For stars, the particle metallicity PDF exceeds that for smoothed abundances by about an order of magnitude in the range $-4 < \log Z < -2$ (i.e., outside the plotted range).

We stress, however, that because the metallicities are evaluated locally, i.e. at the spatial resolution limit, they may differ substantially from the overall mean metallicity of the structure containing the particles. For structures that contain many particles the mean metallicity will be insensitive to the definition of metallicity that is used. On the other hand, local gas metallicities are the ones that are used for the calculation of the cooling rates, so they are certainly important.

In summary, SPH simulations such as the ones presented here are not well-suited to study the metal distribution in low-metallicity gas. Because metals are stuck to particles, SPH suffers from a sampling problem which becomes worse in regions where only a small fraction of the particles have been enriched. Consequently, in the low-metallicity regime the distribution of mass is sensitive to the definition of metallicity. However, the bulk of the metals reside in gas of relatively high metallicity for which the predicted metal distribution is not strongly affected by the lack of metal mixing. Except for the small fraction of stars that have $Z \lesssim 10^{-1}\,Z_\odot$, the results are more robust for stars because they form in high-density gas that is better mixed. This is probably because high-density gas particles tend to be near star particles which means that they are likely to have received metals during many time steps.

## 3.8 SUMMARY

The elemental abundances of stars, galaxies, and diffuse gas are of great interest because they determine radiative cooling rates and the stellar initial mass function, because they can give insight into physical processes such as the interactions between galaxies and the IGM, because they change the strength of lines that are used as diagnostics of physical conditions and because they determine the observability of lines used as tracers of various gas phases. In this chapter we have presented a method to follow the timed release of individual elements by stars, including mass loss through stellar winds and SNe, and their subsequent dispersal through space.

The ingredients of our stellar evolution module include a choice of IMF (we use Chabrier), stellar lifetimes as a function of metallicity (which we take from Portinari et al. 1998), the rate of type Ia SNe for an SSP as a function of time (we use an empirical time delay distribution tuned to obtain agreement between the evolution of the observed, cosmic rates of SNIa and star formation), and stellar yields (we use Marigo 2001 for AGB stars, Portinari et al. 1998 for core collapse SNe, and the W7 model of Thielemann et al. 2003 for SNIa).

We compared different sets of nucleosynthetic yields taken from the literature after integrating them over the IMF. While the different studies predict similar total ejected masses, the predictions for heavy elements differ substantially. In particular, the ejected masses of individual elements differ by factors of a few for AGB stars and – for elements heavier than nitrogen – for core collapse SNe. Thus, even disregarding the fact that most nucleosynthetic yield calculations ignore potentially important effects such as rotation, the elemental ratios are uncertain by factors of a few for a fixed IMF. Predictions for abundances relative to iron are even less robust because much, perhaps even most, of the iron released by an SSP is produced by SNIa and the normalization of the SNIa rate is only known to within factors of a few.

Our implementation of mass transfer implicitly splits, for each element, the ejected mass into terms accounting for the mass that is produced (minus destroyed) and the mass that is simply passing through. The latter term is assumed to scale with the initial abundance, allowing us to correct for relative abundance variations with respect to solar at a fixed metallicity.[13] We have taken special care to correctly track the total metal mass even if not all elements are tracked explicitly.

We discussed two possible definitions of metallicity of SPH particles: the commonly used "particle metallicity", defined as the ratio of the metal to the total mass ($m_Z/m$), and the "smoothed metallicity", defined as the ratio of the metal mass density to the total mass density ($\rho_Z/\rho$), where each density is computed using the standard SPH formalism. We argued that smoothed metallicities (and, analogously, smoothed elemental abundances) are preferable because they are most consistent with the SPH formalism (particularly with regards to radiative cooling rates which depend explicitly on densities) and because they partially counter the lack of metal mixing that is inherent to SPH. We discussed in some detail the fact that SPH underestimates metal mixing because metals are stuck to particles and how this results in a sampling problem that may not become smaller when the resolution is increased. While the use of smoothed abundances eases this problem somewhat, it by no means eliminates it entirely (while also leaving the potential for small scale metal mixing due to physical processes unaddressed).

The use of smoothed abundances (which are frozen when a gas particle is converted into a star particle) leads to a slight non-conservation of metal mass, but we showed this to be negligible for our high-resolution simulations. A comparison of smoothed and particle metallicities (in a simulation that used smoothed abundances for the cooling rates and the stellar evolution) shows that while they are similar at high metallicities, they differ strongly at low metallicities, with smoothed abundances typically exceeding particle abundances by large factors. In particular, there are many more particles with non-zero smoothed metallicities than with non-zero particle metallicities. Since there is no overwhelming reason to prefer one definition of metallicity over the other, the fact that the choice matters indicates that care must be taken when interpreting the predictions of SPH simulations at low metallicities.

A comparison between two low-resolution simulations, one using smoothed abundances and the other using particle abundances for the calculation of the cooling rates, revealed large differences in the star formation rate. By redshift zero the simulation employing smoothed abundances had formed about 1.5 times as many stars as the

---

[13] Note that this treatment still ignores the fact that the nucleosynthesis may itself depend on the relative abundances.

run using particle metallicities. We demonstrated that this difference could not be attributed to non-conservation of metal mass and was instead caused by the increased mixing (i.e., metal cooling is important for more particles when smoothed abundances are used). Although the difference is expected to decrease with increasing resolution, we conclude that it will be necessary to solve the metal mixing problem before SPH simulations can be used to make precise predictions for the cosmic star formation rate.

We used a suite of large simulations with up to $2 \times 512^3$ particles to investigate the distribution of heavy elements. All simulations used identical physical parameters and sub-grid modules. The simulations made use of recently developed modules for star formation (Schaye & Dalla Vecchia 2008) and kinetic feedback from core collapse SNe (Dalla Vecchia & Schaye 2008). We followed all 11 elements (H, He, C, N, O, Ne, Mg, Si, S, Ca, Fe) that we found in chapter 2 to contribute significantly to the cooling of photo-ionized plasmas. Radiative cooling (including photo-heating) was implemented element-by-element, assuming the gas to be optically thin and in ionization equilibrium in the presence of an evolving photo-ionizing radiation background. We did this by making use of tables that had been pre-computed using CLOUDY following the methods in chapter 2. Element-by-element cooling and the inclusion of photo-ionization – not only for H and He, but also for heavy elements – are both novel features for cosmological simulations.

Our predictions for the metallicities of various baryonic phases are in reasonably good agreement with available observations. While most of the cosmic metal mass initially resides in gas of densities typical of the ISM ($n_{\rm H} > 10^{-1}\,{\rm cm}^{-3}$), by redshift zero stars have become the dominant reservoir of metal mass and the ISM contains only a small fraction of the metals. Diffuse gas ($n_{\rm H} < 10^{-1}\,{\rm cm}^{-3}$) contains a significant fraction of the metals at all times. Except at very high redshifts, most of the diffuse metals reside in the WHIM ($10^5\,{\rm K} < T < 10^7\,{\rm K}$), but the metal mass residing in the ICM ($T > 10^7\,{\rm K}$) is always negligible. By the present time, the gaseous metal mass is distributed over a wide range of densities (5, 50, and 95 per cent of the metal mass resides in gas with $\rho/\langle\rho\rangle \lesssim 10^{-0.5}$, $10^2$, and $10^{7.5}$, respectively) and temperatures (5, 50, and 95 per cent of the metal mass resides in gas with $T$ (K) $\lesssim 10^4$, $10^5$, and $10^{6.5}$, respectively), but is concentrated in gas that has a relatively high, local metallicity (95 per cent has $Z \gtrsim 10^{-1.5}\,Z_\odot$ averaged over the mass scale corresponding to the resolution limit). Clearly, any census aiming to account for most of the metal mass will have to take a wide variety of objects and structures into account.

Although the mean stellar metallicity slowly increases with time, it is already of order ten per cent of solar by $z = 8$. The evolution of the metallicity is much stronger for cold-warm ($T < 10^5\,{\rm K}$) diffuse gas, particularly for $\rho/\langle\rho\rangle < 10^2$. By redshift zero the diffuse, photo-ionized IGM has a metallicity $\sim 10^{-2}\,Z_\odot$, while the cold-warm gas in halos has $Z > 10^{-1}\,Z_\odot$. Interestingly, the metallicity of the WHIM and the ICM is $\sim 10^{-1}\,Z_\odot$ at all redshifts.

A comprehensive convergence study (see appendices 3.A and 3.B) revealed that, except for the ICM, a $50\ h^{-1}\,{\rm Mpc}$ box is sufficiently large to obtain a converged result for the cosmic metal mass fractions and metallicities down to $z = 0$ and $12.5\ h^{-1}\,{\rm Mpc}$ suffices for $z > 2$. The convergence with respect to numerical resolution was consistent with expectations based on a comparison with the Jeans scales. Our use of an effective equation of state for star-forming gas guarantees that the Jeans mass does not fall below $f_{\rm g}^{3/2}10^7\,h^{-1}\,{\rm M}_\odot$, where $f_{\rm g}$ is the local gas fraction, but even this scale is only marginally resolved in our highest resolution simulations (which have $m_{\rm g} \sim 10^6\,h^{-1}\,{\rm M}_\odot$). We found that it is much easier to obtain converged predictions for the metallicity of the different components than for their metal mass fractions. While the simulations presented here can provide (numerically) robust predictions for the metallicities at $z < 4$, higher resolution models may be required for higher redshifts.

Here we have investigated only a single set of physical parameters. We postpone such a comparison to chapter 4 that will investigate how the predictions for the metal distribution vary if we change the physical assumptions and sub-grid prescriptions, such as the cosmology, the star formation recipe, the implementation and efficiency of galactic winds, the cooling rates, and feedback from AGN. In this way we hope to isolate the processes that drive the evolution of the cosmic metal distribution.

## ACKNOWLEDGMENTS

We are grateful to Volker Springel for help with the simulations and to Laura Portinari and Robert Izzard for discussions about stellar yields. We are also grateful to Stefano Borgani, Andreas Pawlik, and the anonymous referee for their careful reading of the manuscript. This work was supported by Marie Curie Excellence Grant MEXT-CT-2004-014112.

## 3.A VARYING THE SIZE OF THE SIMULATION BOX

In this appendix we use the suite of cosmological simulations listed in Table 3.2 to test for convergence with the size of our simulation box. The size of the simulation box is important because it determines what kind of objects can form. Rare, large-scale structures (both high- and low-density peaks) can obviously only be sampled correctly if they are much smaller than the size of the box. Moreover, since Fourier components of the density field only evolve independently in the linear regime, the simulation box must be large compared with the scale that has last gone non-linear. Because this scale increases with time, larger boxes are required at lower redshifts. To isolate the effect of the size of the simulation volume, we will compare simulations that use different box sizes, *while holding the resolution constant*.

For this test we use two sets of simulations that differ in terms of their resolution. The first set consists of L100N512, L050N256, and L025N128 and the second set comprises L025N512, L012N256, and L006N128. Within each set the size of the box is thus decreased by factors of two and four, respectively. The second set uses a particle mass that is 64 times smaller than the first set, but these higher resolution runs were not continued down to $z = 0$.

The top and bottom rows of figure 3.20 show the evolution of the metal mass fractions in the various components for the low and high-resolution sets, respectively. The

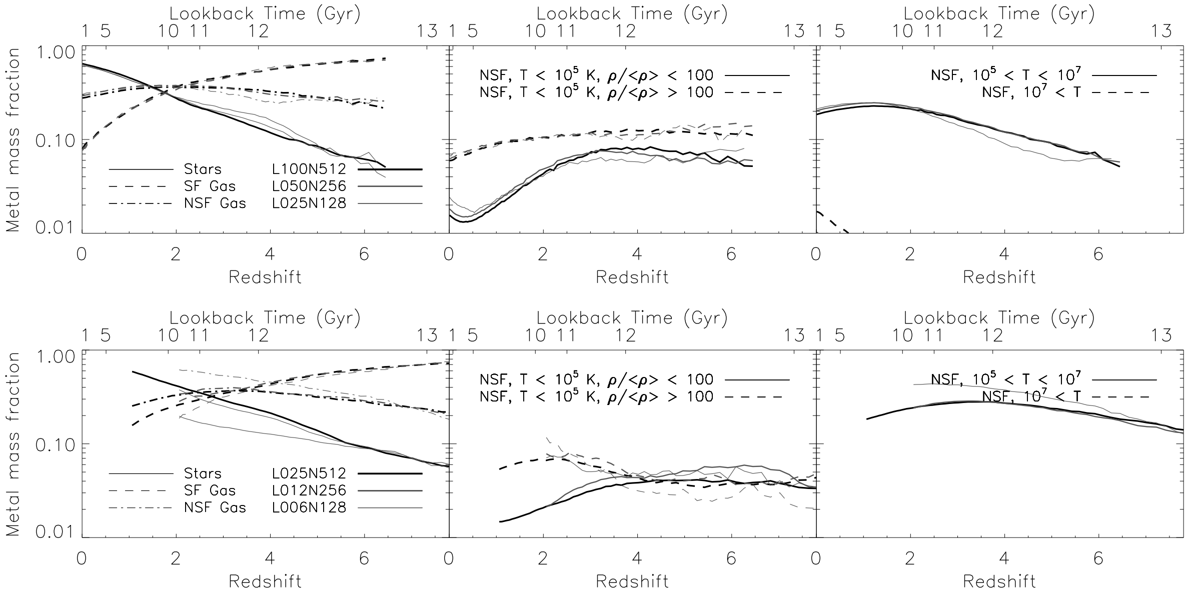

**Figure 3.20**: Dependence on the simulation box size of the evolution of the fractions of the metal mass in various components. The curves in the top panels correspond to the L100N512 (black, thick lines), L050N256 (grey, medium thick lines), and the L025N128 (grey, thin lines) simulations. The curves in the bottom panels are for the L025N512 (black, thick lines), L012N256 (grey, medium thick lines), and the L006N128 (grey, thin lines) simulations. The line styles are identical to those shown in Fig. 3.13. The parts of the curves corresponding to redshifts for which the total metal mass is smaller than $10^{-6}$ of the total baryonic mass have been omitted because they become very noisy. Except for the ICM ($T > 10^7\,\mathrm{K}$), the $50\ h^{-1}\,\mathrm{Mpc}$ and $12.5\ h^{-1}\,\mathrm{Mpc}$ boxes have nearly converged for $z < 2$ and $z > 2$, respectively.

panels are analogous to those shown in Fig. 3.13. In particular, the black curves in the top panels, which correspond to L100N512, are identical to those shown in Fig. 3.13. The top panels demonstrate that, except for the $T > 10^5\,\mathrm{K}$ gas (right panel), the results have already nearly converged for the $25\ h^{-1}\,\mathrm{Mpc}$ box. For the WHIM (right; solid) we require a $50\ h^{-1}\,\mathrm{Mpc}$ box, although even the $25\ h^{-1}\,\mathrm{Mpc}$ box seems to be nearly converged for $z < 2$. For the ICM (right; dashed), however, even the $50\ h^{-1}\,\mathrm{Mpc}$ box is too small. The bottom panels demonstrate that while a $12.5\ h^{-1}\,\mathrm{Mpc}$ box is sufficient for $z > 2$ (except for the ICM, which accounts for too few metals to be visible in the plot, and the photo-ionized IGM), boxes as small as $6.125\ h^{-1}\,\mathrm{Mpc}$ give spurious results for $z < 6$. The fact that we require larger boxes for hot gas is not surprising because objects with high virial temperatures are rare and large.

The evolution of the metallicities of the different components in the two sets of simulations is shown in Fig. 3.21. Interestingly, except for the ICM, the results appear to have converged already for our smallest simulation boxes (although this is not quite true for the stellar metallicity in L006N128). Together with Fig. 3.20 this suggests that it is easier to obtain convergence for the metallicity than for the metal mass fraction. This in turn implies that the lack of convergence of the metal mass fractions for the smallest boxes was caused by non-convergence of the baryonic mass fraction rather than the

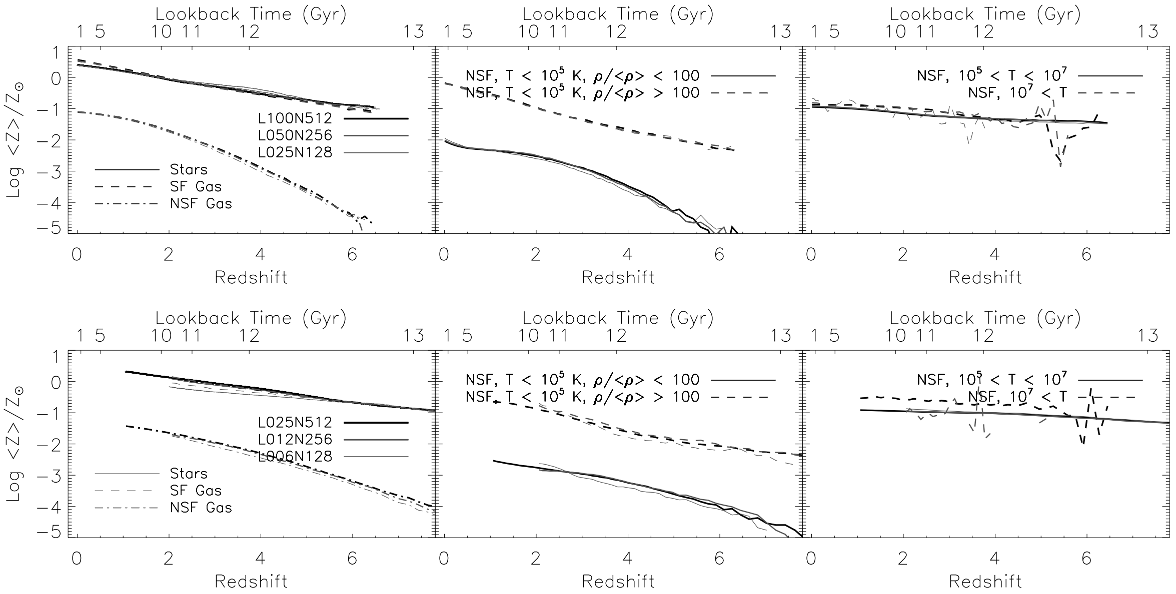

**Figure 3.21**: Dependence on the simulation box size of the evolution of the metallicities of various components. The colors and line styles are identical do those used in Fig. 3.20. The 25 $h^{-1}$ Mpc and 12.5 $h^{-1}$ Mpc boxes have converged for $z < 2$ and $z > 2$, respectively.

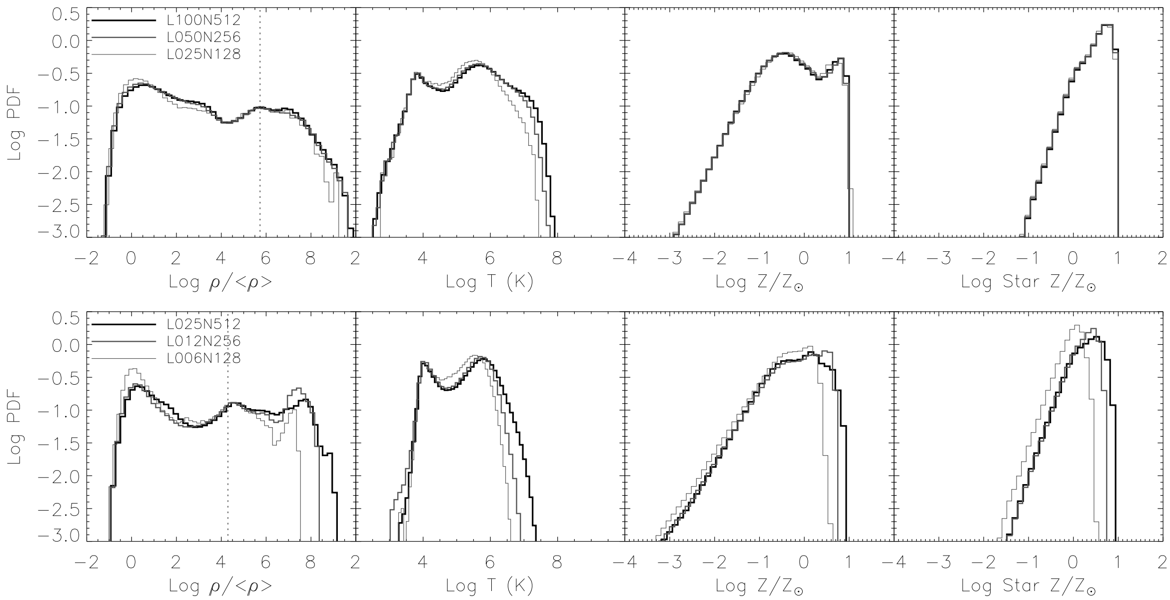

**Figure 3.22**: Dependence on the size of the simulation box of the probability density function, weighted by metal mass, of the gas density (left), temperature (centre-left), gas metallicity (centre-right), and stellar metallicity (right) at $z = 0$ (top) and $z = 2$ (bottom). The colors and line styles are identical to those used in Fig. 3.20. The vertical, dotted lines in the left panels indicate the threshold for star formation. Note that star-forming gas was excluded from the temperature panels. Except for the extremes of the distributions, the 50 $h^{-1}$ Mpc and 12.5 $h^{-1}$ Mpc boxes have nearly converged for $z < 2$ and $z > 2$, respectively.

metallicity.

However, part of the difference in appearance can be accounted for by the fact that the $y$-axis spans six decades in Fig. 3.21, but only two decades in Fig. 3.20. Closer inspection reveals that while this explanation may be viable for the stars, it does not hold for the gaseous components. Furthermore, the axis ranges differ for a reason: they show the range of interest. While we generally do not care whether the metal mass fraction in a particular component is $10^{-3}$ or $10^{-2}$ when drawing up a census of metals (both fractions are negligible), it is very interesting to know whether the diffuse IGM has a metallicity of $10^{-3}$ or $10^{-2}$ solar because the difference is measurable and because it has important consequences for enrichment scenarios.

Finally, we plot the probability density functions of the gas density, temperature and metallicity as well as the stellar metallicity, all weighted by metal mass, in Fig. 3.22. The results confirm the conclusions drawn from the previous two figures. This figure illustrates clearly that differences first show up at the extremes of the distribution, which is not surprising since those correspond to rare objects.

Summarizing, a $50~h^{-1}\,\mathrm{Mpc}$ box is sufficient to obtain a converged picture of the cosmic metal mass fractions and metallicities of most components down to $z = 0$. Somewhat smaller boxes may suffice if one is only interested in higher redshifts (except for the ICM, $12.5~h^{-1}\,\mathrm{Mpc}$ is sufficient for $z > 2$) or in low-mass objects. We caution the reader that it is possible that larger box sizes are needed if other aspects of the cosmic metal distribution are investigated (e.g., clustering strengths of metal absorption lines).

## 3.B VARYING THE RESOLUTION

While the size of the simulation box mainly determines the types of structures that can form, numerical resolution can even have a large effect on common objects. For example, simulations that do not resolve the Jeans scales may underestimate the fraction of the mass in collapsed structures and hence the total amount of metals produced. Moreover, processes like metal mixing (see §3.6.2) may depend on resolution. To isolate the effect of numerical resolution, it is important to hold the simulation box size constant (or to use a box sufficiently large for the result to have converged with respect to the size of the simulation box).

Before showing the results of the convergence tests, it is useful to consider what to expect. The temperature of substantially overdense[14] gas does not drop much below $10^4$ K in our simulations (see Fig. 3.15). In reality, gas at interstellar densities ($n_{\mathrm{H}} \gtrsim 10^{-1}\,\mathrm{cm}^{-3}$) is sufficiently dense and self-shielded to form a cold ($T \ll 10^4$ K), interstellar phase, allowing it to form stars (Schaye 2004). However, our simulations impose an effective equation of state for gas with densities exceeding our star formation threshold of $n_{\mathrm{H}} = 10^{-1}\,\mathrm{cm}^{-3}$. For our equation of state, $P \propto \rho^{4/3}$, the Jeans mass is independent of the density. Hence, provided we resolve the Jeans mass at the star formation threshold,

---

[14] Gas with very low overdensities can have temperatures substantially below $10^4$ K due to adiabatic expansion, but the Jeans scales corresponding to these low densities are nevertheless large.

we resolve it everywhere. The Jeans mass is given by

$$M_{\rm J} \approx 1 \times 10^7 \, h^{-1} \, {\rm M}_\odot f_{\rm g}^{3/2} \left( \frac{n_{\rm H}}{10^{-1}\,{\rm cm}^{-3}} \right)^{-1/2} \left( \frac{T}{10^4\,{\rm K}} \right)^{3/2} , \qquad (3.25)$$

where $f_{\rm g}$ is the local gas fraction. Hence, we do not expect convergence unless the gas particle mass $m_{\rm g} \ll 10^7 \, M_\odot$. To achieve convergence, a simulation will, however, also need to resolve the Jeans length $L_{\rm J}$, which implies that the maximum, proper gravitational softening, $\epsilon_{\rm prop}$, must be small compared with the Jeans Length

$$L_{\rm J} \approx 1.5 \, h^{-1} \, {\rm kpc} \, f_{\rm g}^{1/2} \left( \frac{n_{\rm H}}{10^{-1}\,{\rm cm}^{-3}} \right)^{-1/2} \left( \frac{T}{10^4\,{\rm K}} \right)^{1/2} . \qquad (3.26)$$

Note that since $L_{\rm J}$ scales as $L_{\rm J} \propto \rho^{-1/3}$ for our equation of state, the softening scale will always exceed $L_{\rm J}$ for sufficiently large densities. However, since the Jeans mass does not decrease with density, runaway collapse is not expected for star-forming gas. Comparing the above equations with the particle mass and softening scales listed in Table 3.2, we see that while our highest resolution simulation (L025N512) marginally resolves the Jeans scales for $f_{\rm g} \approx 1$, this is not the case for the simulations that go down to $z = 0$, although L050N512 has $m_{\rm g} \approx M_{\rm J}$ and $\epsilon_{\rm prop} \approx L_{\rm J}$ and is therefore not far off.

However, resolving the Jeans scales post-reionization may not even be sufficient, given that the simulations start at $z \gg z_{\rm reion}$. Prior to reionization the gas temperature can be much lower in which case we have no hope of resolving the Jeans scales at the threshold for star formation. On the other hand, a photo-dissociating UV background may well prevent the collapse of haloes with virial temperatures smaller than $10^4\,{\rm K}$. In any case, we expect the duration of this period to be comparatively short. Our simulations assume $z_{\rm reion} = 9$ and include a photo-dissociating background for $z > 9$ (see §3.2). Hence, in our simulations the formation of haloes with $T_{\rm vir} \ll 10^4\,{\rm K}$ will be efficiently suppressed.

We test for convergence with resolution using two sets of simulations, which use different box sizes. The first set consists of L100N256, L100N512, and L050N512 and the second set comprises L025N128, L025N256, and L025N512. Within each set the mass (spatial) resolution is thus increased by factors of 8 and 64 (2 and 4), respectively. Note that L050N512, the highest resolution run of the first set, uses a $50 \, h^{-1}\,{\rm Mpc}$ box whereas the other runs of this set used a $100 \, h^{-1}\,{\rm Mpc}$ box. However, as we have shown in appendix 3.A, $50 \, h^{-1}\,{\rm Mpc}$ is sufficiently large to give converged results for all phases but the ICM. We do not show L100N128 because most of its predictions are completely unreliable due to its extremely low resolution. The second set of simulations uses a box size of only $25 \, h^{-1}\,{\rm Mpc}$, but these higher resolution runs were not continued down to $z = 0$.

Figures 3.23 – 3.25 are analogous to figures 3.20 – 3.22 but show the effect of varying the resolution rather than the size of the simulation box. The top row of Fig. 3.23 shows no evidence for full convergence, but the difference between L100N512 (black) and L050N512 (dark green) is small for $z < 1$. From the bottom row of panels we can see that L025N512, while certainly not fully converged, is similar to L025N256 for $z < 4$.

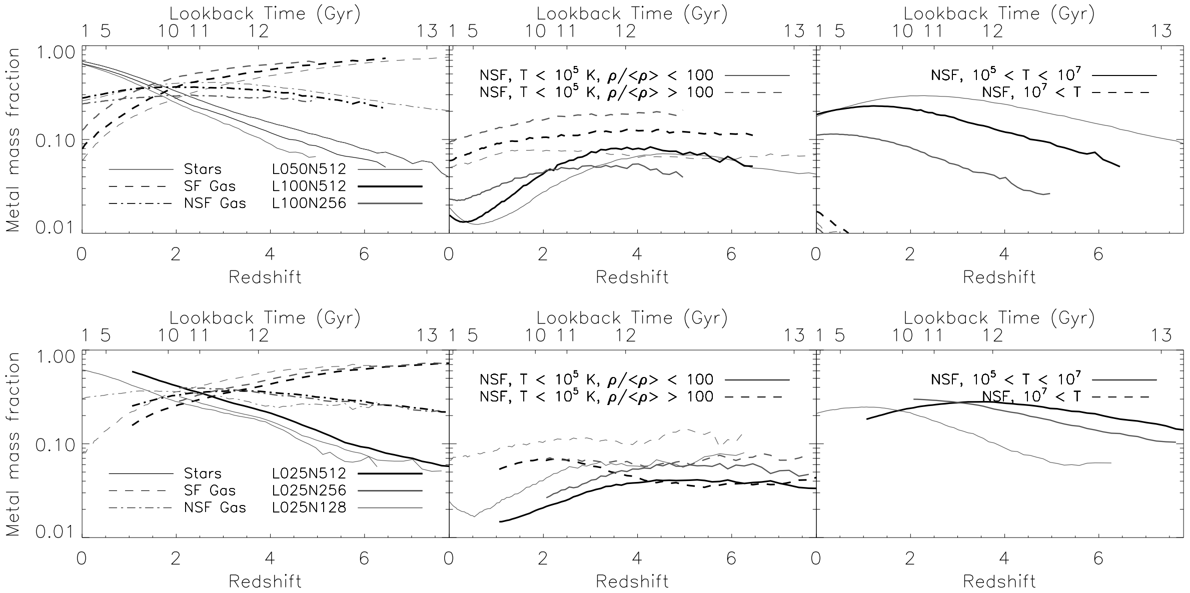

**Figure 3.23**: Dependence on the numerical resolution of the evolution of the fractions of the metal mass in various components. The curves in the top panels correspond to the L050N512 (grey, thin lines), L100N512 (black, thick lines), and the L050N256 (grey, medium thick lines) simulations. The curves in the bottom panels are for the L025N512 (black, thick lines), L025N256 (grey, medium thick lines), and the L025N128 (grey, thin lines) simulations. The line styles are identical to those shown in Fig. 3.13. The parts of the curves corresponding to redshifts for which the total metal is smaller than $10^{-6}$ of the total baryonic mass have been omitted because they become very noisy. Convergence is relatively poor for $z > 2$ in the top row and for $z > 4$ in the bottom row.

As the resolution is increased, the fractions of the metal mass in stars and the WHIM tend to increase, while the fractions in non-star-forming gas with $T < 10^5\,\mathrm{K}$ tend to decrease.

It is not surprising that convergence is better at lower redshift, because the typical mass of star-forming haloes increases with decreasing redshift which means it will be sampled with more particles per halo. In particular, lower resolution simulations will start forming stars later and it takes some time for the resultant underestimate of the metal mass to become negligible.

Figure 3.24 shows that it is much easier to get convergence for the metallicity of the different components than it is to get converged predictions for the metal mass fractions. As for convergence with box size, this partly reflects the fact that we do not require as much precision for the metallicities since the dynamic range of interest is much larger than it is for the metal mass fractions. The metallicities are nearly converged in the L050N512 run for $z < 2$ and in the L025N512 for $z < 4$. Finally, Fig. 3.25 confirms the finding from Fig. 3.23 that increasing the resolution mainly moves metals from cold-warm halo and ISM gas to the WHIM. In addition, Fig. 3.25 shows that the high-density cut-off to the gas distribution is mainly set by resolution, which is expected because many particles and small softening lengths are needed to sample

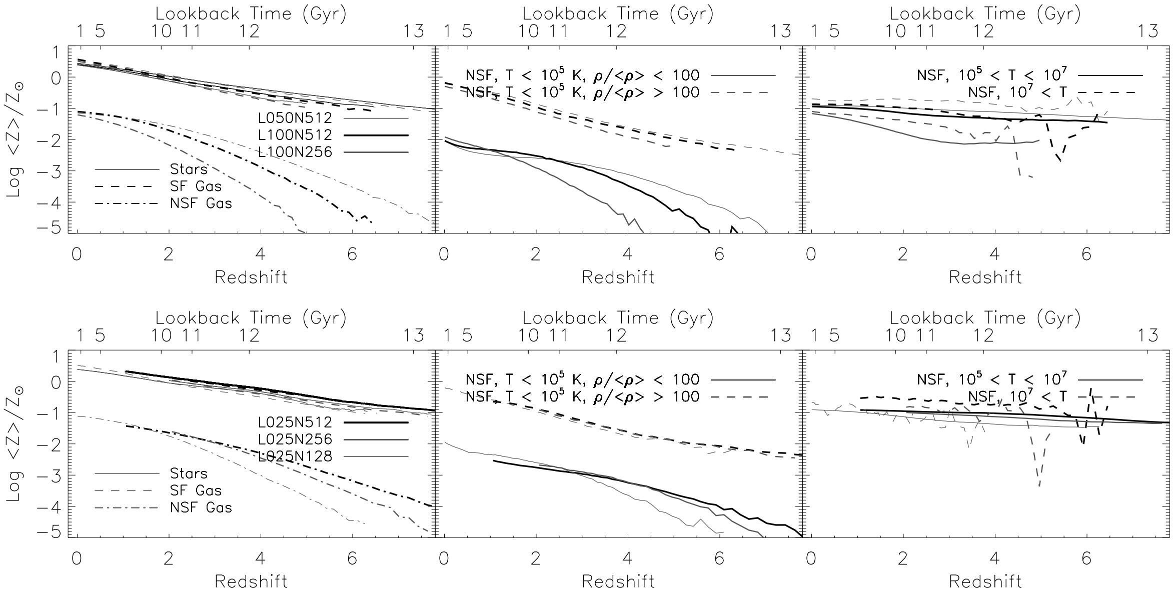

**Figure 3.24**: Dependence on numerical resolution of the evolution of the metallicities of various components. The colors and line styles are identical to those used in Fig. 3.23. Convergence is good for $z < 2$ in the top row and for $2 < z < 4$ in the bottom row.

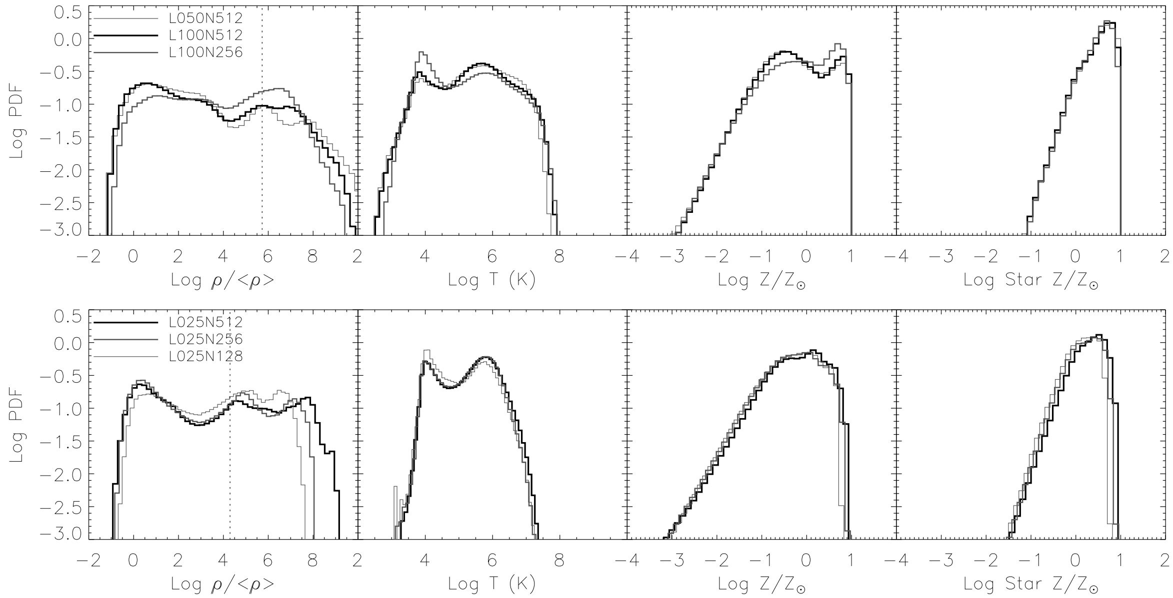

**Figure 3.25**: Dependence on numerical resolution of the probability density function, weighted by metal mass, of the gas density (left), temperature (centre-left), gas metallicity (centre-right), and stellar metallicity (right) at $z = 0$ (top) and $z = 2$ (bottom). The colors and line styles are identical to those used in Fig. 3.23. The vertical, dotted lines in the left panels indicate the threshold for star formation. Note that star-forming gas was excluded from the temperature panels. The highest resolution simulations have nearly converged.

the tail of the density distribution. The main conclusion we draw from this figure is, however, that the convergence is sufficiently good to draw interesting conclusions, particularly for the $25\,h^{-1}\,\mathrm{Mpc}$ box at $z = 2$ and the $50\,h^{-1}\,\mathrm{Mpc}$ box at $z = 0$.

Thus, the results of the convergence tests mostly agree with the expectations based on comparisons of the numerical resolution with the Jeans scales. The resolution of the L100N512 run ($m_g \approx 9 \times 10^7\,h^{-1}\,\mathrm{M}_\odot$) is sufficient to draw qualitative conclusions regarding the mass fractions in various phases and for $z < 2$ the L050N512 ($m_g \approx 1 \times 10^7\,h^{-1}\,\mathrm{M}_\odot$) may be close to convergence. Run L100N512 already has sufficient resolution to obtain interesting, quantitative predictions for the metallicities of the different phases at $z < 2$. For $z > 2$ we need higher resolution. While the mass fractions are still not fully converged for L025N512 ($m_g \approx 1 \times 10^6\,h^{-1}\,\mathrm{M}_\odot$), its predictions for the metallicities are robust for $z < 4$.

## REFERENCES

Abel T., Haehnelt M. G., 1999, ApJ, 520, L13

Aguirre A., Dow-Hygelund C., Schaye J., Theuns T., 2008, ApJ, 689, 851

Aguirre A., Schaye J., Hernquist L., Kay S., Springel V., Theuns T., 2005, ApJ, 620, L13

Allende Prieto C., Lambert D. L., Asplund M., 2001, ApJ, 556, L63

Allende Prieto C., Lambert D. L., Asplund M., 2002, ApJ, 573, L137

Alongi M., Bertelli G., Bressan A., Chiosi C., Fagotto F., Greggio L., Nasi E., 1993, Ap&SS, 97, 851

Arimoto N., Yoshii Y., 1987, A&A, 173, 23

Barris B. J., Tonry J. L., 2006, ApJ, 637, 427

Berczik P., 1999, A&A, 348, 371

Blanc G. e. a., 2004, A&A, 423, 881

Borgani S., Fabjan D., Tornatore L., Schindler S., Dolag K., Diaferio A., 2008, Space Science Reviews, 134, 379

Brachwitz F., Dean D. J., Hix W. R., Iwamoto K., Langanke K., Martínez-Pinedo G., Nomoto K., Strayer M. R., Thielemann F.-K., Umeda H., 2000, ApJ, 536, 934

Bradamante F., Matteucci F., D'Ercole A., 1998, A&A, 337, 338

Bruzual G., Charlot S., 2003, MNRAS, 344, 1000

Bryan G. L., Machacek M., Anninos P., Norman M. L., 1999, ApJ, 517, 13

Cappellaro E., Evans R., Turatto M., 1999, A&A, 351, 459

Carigi L., 2000, Revista Mexicana de Astronomia y Astrofisica, 36, 171

Carigi L., 2003, MNRAS, 339, 825

Ceverino D., Klypin A., 2007, ArXiv e-prints, 712

Chabrier G., 2003, PASP, 115, 763

Chieffi A., Domínguez I., Limongi M., Straniero O., 2001, ApJ, 554, 1159

Chieffi A., Limongi M., 2004, ApJ, 608, 405

Crowther P., Smartt S., 2007, Astronomy and Geophysics, 48, 010000

Dahlen T., Strolger L.-G., Riess A. G., Mobasher B., Chary R.-R., Conselice C. J., Ferguson H. C., Fruchter A. S., Giavalisco M., Livio M., Madau P., Panagia N., Tonry J. L., 2004, ApJ, 613, 189

Dalgarno A., McCray R. A., 1972, ARA&A, 10, 375

Dalla Vecchia C., Schaye J., 2008, MNRAS, 387, 1431

Davé R., Oppenheimer B. D., 2007, MNRAS, 374, 427

David L. P., Forman W., Jones C., 1990, ApJ, 359, 29

de Avillez M. A., Breitschwerdt D., 2007, ApJ, 665, L35

Della Valle M., Panagia N., Padovani P., Cappellaro E., Mannucci F., Turatto M., 2005, ApJ, 629, 750

Erb D. K., Shapley A. E., Pettini M., Steidel C. C., Reddy N. A., Adelberger K. L., 2006, ApJ, 644, 813

Fechner C., Richter P., 2008, ArXiv e-prints

Ferland G. J., Korista K. T., Verner D. A., Ferguson J. W., Kingdon J. B., Verner E. M., 1998, PASP, 110, 761

Forestini M., Charbonnel C., 1997, Ap&SS, 123, 241

Förster F., Wolf C., Podsiadlowski P., Han Z., 2006, MNRAS, 368, 1893

François P., Matteucci F., Cayrel R., Spite M., Spite F., Chiappini C., 2004, A&A, 421, 613

Gallazzi A., Brinchmann J., Charlot S., White S. D. M., 2008, MNRAS, 383, 1439

Gavilán M., Buell J. F., Mollá M., 2005, A&A, 432, 861

Goswami A., Prantzos N., 2000, A&A, 359, 191

Governato F., Willman B., Mayer L., Brooks A., Stinson G., Valenzuela O., Wadsley J., Quinn T., 2007, MNRAS, 374, 1479

Greggio L., Renzini A., 1983, A&A, 118, 217

Greif T. H., Glover S. C. O., Bromm V., Klessen R. S., 2008, ArXiv e-prints

Haardt F., Madau P., 2001, in Neumann D. M., Tran J. T. V., eds, Clusters of Galaxies and the High Redshift Universe Observed in X-rays Modelling the UV/X-ray cosmic background with CUBA

Hachisu I., Kato M., Nomoto K., 1999, ApJ, 522, 487

Halliday C., Daddi E., Cimatti A., Kurk J., Renzini A., Mignoli M., Bolzonella M., Pozzetti L., Dickinson M., Zamorani G., Berta S., Franceschini A., Cassata P., Rodighiero G., Rosati P., 2008, A&A, 479, 417

Hardin D. e. a., 2000, A&A, 362, 419

Hirschi R., Meynet G., Maeder A., 2005, A&A, 433, 1013

Holweger H., 2001, in Wimmer-Schweingruber R. F., ed., Joint SOHO/ACE workshop "Solar and Galactic Composition" Vol. 598 of American Institute of Physics Conference Series, Photospheric Abundances: Problems, Updates, Implications. pp 23–+

Hui L., Gnedin N. Y., 1997, MNRAS, 292, 27

Iben I., Truran J. W., 1978, ApJ, 220, 980

Iwamoto K., Brachwitz F., Nomoto K., Kishimoto N., Umeda H., Hix W. R., Thielemann F.-K., 1999, ApJS, 125, 439

Izzard R. G., Tout C. A., Karakas A. I., Pols O. R., 2004, MNRAS, 350, 407

Karakas A. I., Lattanzio J. C., Pols O. R., 2002, Publications of the Astronomical Society of Australia, 19, 515

Kawata D., 1999, PASJ, 51, 931

Kawata D., 2001, ApJ, 558, 598

Kawata D., Gibson B. K., 2003, MNRAS, 346, 135

Kennicutt Jr. R. C., 1998, ApJ, 498, 541

Kippenhahn R. W. A., Weigert A., 1994, Stellar Structure and Evolution. Stellar Structure and Evolution, XVI, 468 pp. 192 figs.. Springer-Verlag Berlin Heidelberg New York. Also Astronomy and Astrophysics Library

Kobayashi C., 2004a, MNRAS, 347, 740

Kobayashi C., 2004b, MNRAS, 347, 740

Kobayashi C., Springel V., White S. D. M., 2007, MNRAS, 376, 1465

Kobayashi C., Tsujimoto T., Nomoto K., 2000, ApJ, 539, 26

Kodama T., 1997, Ph.D. Thesis

Komatsu E., Dunkley J., Nolta M. R., Bennett C. L., Gold B., Hinshaw G., Jarosik N., Larson D., Limon M., Page L., Spergel D. N., Halpern M., Hill R. S., Kogut A., Meyer S. S., Tucker G. S., Weiland J. L., Wollack E., Wright E. L., 2008, ArXiv e-prints, 803

Kroupa P., Tout C. A., Gilmore G., 1993, MNRAS, 262, 545

Kuznetsova N., Barbary K., Connolly B., Kim A. G., Pain R., Roe N. A., Aldering G., Amanullah R., Dawson K., Doi M., Fadeyev V., Fruchter A. S., Gibbons R., Goldhaber G., Goobar A., Gude A., 2008, ApJ, 673, 981

Lia C., Portinari L., Carraro G., 2002, MNRAS, 330, 821

Liang Y. C., Zhao G., Shi J. R., 2001, A&A, 374, 936

Lindner U., Fritze-v. Alvensleben U., Fricke K. J., 1999, A&A, 341, 709

Madgwick D. S., Hewett P. C., Mortlock D. J., Wang L., 2003, ApJL, 599, L33

Maeder A., 1987, A&A, 173, 247

Maeder A., 1992, A&A, 264, 105

Maeder A., Meynet G., 1989a, A&A, 210, 155

Maeder A., Meynet G., 1989b, A&A, 210, 155

Mannucci F., Della Valle M., Panagia N., 2006, MNRAS, 370, 773

Mannucci F., Della Valle M., Panagia N., Cappellaro E., Cresci G., Maiolino R., Petrosian A., Turatto M., 2005, A&A, 433, 807

Marigo P., 2001, A&A, 370, 194

Matteucci F., 2001, Nature, 414, 253

McCarthy I. G., Schaye J., Ponman T. J., Bower R. G., Booth C. M., Dalla Vecchia C., Crain R. A., Springel V., Theuns T., Wiersma R. P. C., 2009, ArXiv e-prints

Miller G. E., Scalo J. M., 1979, ApJS, 41, 513

Mori M., Umemura M., 2006, Nature, 440, 644

Mosconi M. B., Tissera P. B., Lambas D. G., Cora S. A., 2001, MNRAS, 325, 34

Nagashima M., Lacey C. G., Baugh C. M., Frenk C. S., Cole S., 2005, MNRAS, 358, 1247

Navarro J. F., White S. D. M., 1993, MNRAS, 265, 271

Neill J. D. e. a., 2006, AJ, 132, 1126

Nomoto K., Hashimoto M., Tsujimoto T., Thielemann F.-K., Kishimoto N., Kubo Y., Nakasato N., 1997, Nuclear Physics A, 616, 79

Nomoto K., Iwamoto K., Kishimoto N., 1997, Science, 276, 1378

Nomoto K., Iwamoto K., Nakasato N., Thielemann F.-K., Brachwitz F., Tsujimoto T., Kubo Y., Kishimoto N., 1997, Nuclear Physics A, 621, 467

Nomoto K., Thielemann F.-K., Yokoi K., 1984, ApJ, 286, 644

Nomoto K., Tominaga N., Umeda H., Kobayashi C., Maeda K., 2006, Nuclear Physics A, 777, 424

Nykytyuk T. V., Mishenina T. V., 2006, A&A, 456, 969

Okamoto T., Eke V. R., Frenk C. S., Jenkins A., 2005, MNRAS, 363, 1299

Oppenheimer B. D., Davé R., 2006, MNRAS, 373, 1265

Oppenheimer B. D., Davé R., 2008, MNRAS, 387, 577

Padovani P., Matteucci F., 1993, ApJ, 416, 26

Pain R. e. a., 2002, ApJ, 577, 120

Pawlik A. H., Schaye J., 2008, MNRAS, 389, 651

Pearce F. R., Jenkins A., Frenk C. S., Colberg J. M., White S. D. M., Thomas P. A., Couchman H. M. P., Peacock J. A., Efstathiou G., The Virgo Consortium 1999, ApJ, 521, L99

Podsiadlowski P., Mazzali P., Lesaffre P., Han Z., Förster F., 2008, New Astronomy Review, 52, 381

Portinari L., Chiosi C., Bressan A., 1998, A&A, 334, 505

Portinari L., Moretti A., Chiosi C., Sommer-Larsen J., 2004, ApJ, 604, 579

Poznanski D., Maoz D., Yasuda N., Foley R. J., Doi M., Filippenko A. V., Fukugita M., Gal-Yam A., Jannuzi B. T., Morokuma T., Oda T., Schweiker H., Sharon K., Silverman J. M., Totani T., 2007, MNRAS, 382, 1169

Prochaska J. X., Gawiser E., Wolfe A. M., Castro S., Djorgovski S. G., 2003, ApJL, 595, L9

Raiteri C. M., Villata M., Navarro J. F., 1996, A&A, 315, 105

Rauscher T., Heger A., Hoffman R. D., Woosley S. E., 2002, ApJ, 576, 323

Recchi S., Matteucci F., D'Ercole A., 2001, MNRAS, 322, 800

Renzini A., Voli M., 1981, A&A, 94, 175

Ricotti M., Gnedin N. Y., Shull J. M., 2000, ApJ, 534, 41

Romano D., Chiappini C., Matteucci F., Tosi M., 2005, A&A, 430, 491

Romeo A. D., Sommer-Larsen J., Portinari L., Antonuccio-Delogu V., 2006, MNRAS, 371, 548

Salpeter E. E., 1955, ApJ, 121, 161

Scannapieco C., Tissera P. B., White S. D. M., Springel V., 2005, MNRAS, 364, 552

Scannapieco E., Bildsten L., 2005a, ApJL, 629, L85

Scannapieco E., Bildsten L., 2005b, ApJ, 629, L85

Schaye J., 2004, ApJ, 609, 667

Schaye J., Aguirre A., Kim T.-S., Theuns T., Rauch M., Sargent W. L. W., 2003, ApJ, 596, 768

Schaye J., Dalla Vecchia C., 2008, MNRAS, 383, 1210

Schaye J., Dalla Vecchia C., Booth C. M., Wiersma R. P. C., Theuns T., Haas M. R., Bertone S., Duffy A. R., McCarthy I. G., van de Voort F., 2009, ArXiv e-prints

Schaye J., Theuns T., Rauch M., Efstathiou G., Sargent W. L. W., 2000, MNRAS, 318, 817

Seljak U., Zaldarriaga M., 1996, ApJ, 469, 437

Simionescu A., Werner N., Böhringer H., Kaastra J. S., Finoguenov A., Brüggen M., Nulsen P. E. J., 2009, A&A, 493, 409

Sommer-Larsen J., Romeo A. D., Portinari L., 2005, MNRAS, 357, 478

Springel V., 2005, MNRAS, 364, 1105

Springel V., Hernquist L., 2003, MNRAS, 339, 289

Steinmetz M., Mueller E., 1994, A&A, 281, L97

Steinmetz M., Muller E., 1995, MNRAS, 276, 549

Stinson G., Seth A., Katz N., Wadsley J., Governato F., Quinn T., 2006, MNRAS, 373, 1074

Sutherland R. S., Dopita M. A., 1993, ApJS, 88, 253

Theis C., Burkert A., Hensler G., 1992, A&A, 265, 465

Theuns T., Leonard A., Efstathiou G., Pearce F. R., Thomas P. A., 1998, MNRAS, 301, 478

Theuns T., Leonard A., Schaye J., Efstathiou G., 1999, MNRAS, 303, L58

Theuns T., Viel M., Kay S., Schaye J., Carswell R. F., Tzanavaris P., 2002, ApJ, 578, L5

Thielemann F.-K., Argast D., Brachwitz F., Hix W. R., Höflich P., Liebendörfer M., Martinez-Pinedo G., Mezzacappa A., Nomoto K., Panov I., 2003, in From Twilight to Highlight: The Physics of Supernovae Supernova Nucleosynthesis and Galactic Evolution. pp 331–+

Thielemann F.-K., Nomoto K., Hashimoto M., 1993, in Origin and Evolution of the Elements . pp 299–+

Timmes F. X., Woosley S. E., Weaver T. A., 1995, ApJS, 98, 617

Tonry J. L. e. a., 2003, ApJ, 594, 1

Tornatore L., Borgani S., Dolag K., Matteucci F., 2007, MNRAS, 382, 1050

Tornatore L., Borgani S., Matteucci F., Recchi S., Tozzi P., 2004, MNRAS, 349, L19

Travaglio C., Hillebrandt W., Reinecke M., Thielemann F.-K., 2004, A&A, 425, 1029

Tsujimoto T., Nomoto K., Yoshii Y., Hashimoto M., Yanagida S., Thielemann F.-K., 1995, MNRAS, 277, 945

Valdarnini R., 2003, MNRAS, 339, 1117

van den Hoek L. B., Groenewegen M. A. T., 1997, Ap&SS, 123, 305

Veilleux S., Cecil G., Bland-Hawthorn J., 2005, ARA&A, 43, 769

Wanajo S., Nomoto K., Janka H. ., Kitaura F. S., Mueller B., 2008, ArXiv e-prints

White S. D. M., 1994, ArXiv Astrophysics e-prints

Woosley S. E., Weaver T. A., 1995, ApJS, 101, 181

# CHAPTER 4

# Determining the cosmic distribution of metals.

Robert P. C. Wiersma, et. al

In preparation

USING a set of cosmological, hydrodynamical simulations, we investigate how a range of physical processes affect the cosmic metal distribution. Focusing on redshifts $z = 0$ and 2, we study the metallicities and metal mass fractions for stars as well as for the interstellar medium (ISM; $n_{\rm H} > 0.1~{\rm cm}^{-3}$), and several more diffuse gas phases: the intracluster medium ($T > 10^7\,{\rm K}$), cold halo gas ($T < 10^5\,{\rm K}$, $\rho > 10^2\,\langle\rho\rangle$), the diffuse intergalactic medium (IGM; $T < 10^5\,{\rm K}$, $\rho < 10^2\,\langle\rho\rangle$), and the warm-hot IGM (WHIM; $10^5\,{\rm K} < T < 10^7\,{\rm K}$). We vary the parameters and/or implementations of subgrid prescriptions for radiative cooling, star formation, the structure of the ISM, galactic winds driven by feedback from star formation, feedback from active galactic nucleii (AGN), the supernova type Ia time delay distribution, and reionization, and we also explore variations in the stellar initial mass function and the cosmology.

In all models stars and the WHIM constitute the dominant repositories of metals, while at high redshift the ISM is also important. Provided galactic winds are included, predictions for the metallicities of the various phases vary at the factor of two level and are broadly consistent with observations. The exception is the IGM, whose metallicity varies at the order of magnitude level if the prescription for galactic winds is varied, even for a fixed wind energy per unit stellar mass formed, and falls far below the observed values if winds are not included. At the other extreme, the metallicity of the ICM is insensitive to the presence of galactic winds, indicating that its enrichment is regulated by other processes. The mean metallicities of stars ($\sim Z_\odot$), the ICM ($\sim 10^{-1}\,Z_\odot$), and the WHIM ($\sim 10^{-1}\,Z_\odot$) are relatively constant, while those of the cold halo gas and the IGM increase by more than an order of magnitude from $z = 5$ to 0.

Models that result in higher velocity outflows are more efficient at transporting metals to low densities, but actually predict lower IGM metallicities since the winds shock-heat the low-density gas to high temperatures, thereby increasing the fraction of the metals residing in the WHIM. However, the metallicity of the WHIM, as opposed to the corresponding metal mass fraction, is insensitive to the velocities of the galactic winds. Besides galactic winds driven by feedback from star formation, the metal distribution is most sensitive to the inclusion of metal-line cooling and feedback from AGN. We conclude that observations of the metallicity of the low-density IGM and WHIM have the potential to constrain the poorly understood feedback processes that are central to current models of the formation and evolution of galaxies.

## 4.1 INTRODUCTION

The spatial distribution of elements synthesised in stars (henceforth 'metals') provides an archaeological record of past star formation activity and of the various energetic phenomena that stirred and mixed these metals. Recent cosmological simulations of galaxy formation follow the different stellar evolutionary channels through which metals are produced, and include some processes that cause metals to escape from their parent galaxy. Here we will investigate to what extent these simulations produce realistic enrichment patterns, which physical processes affect the metal distribution, and how numerically robust these predictions are. The *relative* abundances of different metals depend on the details of the stellar evolution models as well as on how efficiently the ashes are dispersed. We begin by briefly reviewing how observations constrain metals in various phases: stars, the interstellar medium (ISM) of galaxies, the warm-hot (WHIM) and circum-galactic medium (CGM), the hot intracluster medium (ICM) and the low-density intergalactic medium (IGM).

Observations can constrain integrated stellar and nebular (ISM) abundances of galaxies (for $z \lesssim 1$ see e.g. Kobulnicky & Zaritsky 1999; Kunth & Östlin 2000; Tremonti et al. 2004; Dunne et al. 2003, for $z \approx 1$ see Churchill et al. 2007, for $z \gtrsim 2$ see the Lyman-break abundances of Erb et al. 2006). Since these are inferred from (star) light, they are luminosity-weighted quantities and hence dominated by the metallicity of the centre of the galaxy (e.g. Tremonti et al. 2004); a metallicity gradient (Mehlert et al. 2003) must either be assumed or ignored.

Metals in cold gas can be observed in absorption against a background source, see the damped Lyman-alpha observations at $z \approx 3$ (Pettini et al. 1994; Prochaska et al. 2003) and at even higher redshift (Ando et al. 2007; Price et al. 2007). This technique can be applied to more diffuse gas as well, however the background source must be rather bright (e.g. Songaila & Cowie 1996; Cowie & Songaila 1998; Ellison et al. 2000; Schaye et al. 2000, 2003; Scannapieco et al. 2006; Aguirre et al. 2008). The metallicity of the ICM is inferred from X-ray observations (e.g. Mushotzky et al. 1996; de Plaa et al. 2006; Sato et al. 2007).

These observations use very different tools to observe a variety of elements in a variety of ionization states, and it is not always obvious how to convert all these measurements to a common 'metallicity'. Often this is done assuming the relative abundances of elements equal those measured in the Sun; unfortunately even the assumed metallicity of the Sun itself varies between authors. Here we assume $Z_\odot = 0.0127$, and solar abundances from the default settings of CLOUDY (version 07.02, last described by Ferland et al. 1998) and repeated in Table 3.1.

Convolving metallicity with the fraction of baryonic mass in each of the different phases then yields a census of cosmic metals (Fukugita et al. 1998) . It must be kept in mind though that a large fraction of the metals are potentially not accounted for in current data: for example, a large fraction of $z = 0$ baryons are thought to be in the WHIM, which has not yet been convincingly detected. Similarly, hot ($T \gtrsim 10^5$ K) metals at $z \gtrsim 2$ are currently very poorly constrained. Gas cooling, star formation, galaxy interactions, ram pressure stripping and galactic winds all cause gas and hence metals to be cycled between the different phases, which makes it complicated to relate the observed metal distribution to the original source and/or enrichment process.

A theoretical calculation of the census of cosmic metals must take into account their production by nucleo-synthesis, their initial distribution, and the mixing that occurs in later stages. Semi-analytical models (e.g. Kauffmann et al. 1993; Somerville & Primack 1999; Croton et al. 2006; Bertone et al. 2007) follow the production of elements using interpolation tables from stellar evolution calculations convolved with an assumed stellar initial mass function (IMF), and solve simple equations that describe the flux of metals between different phases. Numerical simulations that include such 'chemo-dynamics' have become increasingly sophisticated since the early work by Theis et al. (1992), usually concentrating on the metal abundance evolution of a single galaxy (Steinmetz & Muller 1995; Raiteri et al. 1996; Berczik 1999; Recchi et al. 2001; Kawata 2001; Kawata & Gibson 2003; Kobayashi 2004; Mori & Umemura 2006; Stinson et al. 2006; Governato et al. 2007), or a cluster of galaxies (e.g. Lia et al. 2002; Valdarnini 2003; Tornatore et al. 2004; Sommer-Larsen et al. 2005; Romeo et al. 2006; Tornatore et al. 2007) in a cosmological context. These simulations also include similar interpolation tables from stellar evolution calculations for the production of metals, but implement the enrichment processes explicitly, for example by kicking metal-enriched gas near a site of star formation to model a galactic wind. The fluxes of metals between phases due to gas cooling, and galaxy/gas interactions, are computed explicitly by these hydro-codes. Early simulations that were also used to look at the metals outside galaxies include Cen & Ostriker (1999), Mosconi et al. (2001) and Theuns et al. (2002). Subsequent authors implemented more physics while increasing resolution and box size in order to minimise numerical effects (Scannapieco et al. 2005; Oppenheimer & Davé 2006; Cen & Ostriker 2006; Kobayashi et al. 2007; Oppenheimer & Davé 2008, chapter 3, Shen et al. 2009; Tornatore et al. 2009).

In this chapter we use cosmological hydrodynamical simulations of the formation of galaxies to attempt to answer the question '*Where are the metals*?', by computing the fraction of metals in each phase, and how this depends on time. Our suite of numerical simulations (the OWLS suite of simulations - **O**verwhelmingly **L**arge **S**imulations, Schaye et al. 2010), includes runs that differ in resolution, physics, and numerical implementation of physical processes. We use it to investigate what physical processes are most important how reliable the predictions are, and to what extent these depend on the sometimes poorly understood physics. Chapter 3 introduced the method and described some of the numerical issues involved, while here we consider different implementations of the sub-resolution physics.

## 4.2 METHOD

OWLS (Schaye et al. 2010) is a suite of more than fifty large, cosmological, gas-dynamical simulations in periodic boxes, performed using the $N$-body Tree-PM, SPH code GADGET III; see Tables 1 and 2 in Schaye et al. (2010) for a full list of parameters. GADGET III is an updated version of GADGET II (Springel 2005), to which we added new physics modules for star formation (Schaye & Dalla Vecchia 2008), feedback from supernovae in the form of galactic winds (Dalla Vecchia & Schaye 2008), feedback from accreting black holes (Booth & Schaye 2009), radiative cooling and heating in the presence of an ionizing background (chapter 2), and stellar evolution (chapter 3). In this simulation suite, numerical and poorly known physical parameters are varied with respect to a 'reference' model, to assess which conclusions are robust, and which processes dominate the results. The cosmological parameters of the reference model, and the physical processes with their numerical implementation, are discussed briefly in the next section. GIMIC (Crain et al. 2009) is a complementary suite of simulations performed with the same simulation code, but employs a single set of parameters to investigate how star formation depends on environment, by simulating regions picked from the Millennium simulation (Springel 2005). Here we give a short overview of the code, concentrating especially on those processes that are directly relevant to metal enrichment.

### 4.2.1 The REFERENCE model

The REFERENCE model assumes a cosmologically flat, vacuum energy dominated ΛCDM universe with cosmological parameters $[\Omega_m, \Omega_b, \Omega_\Lambda, \sigma_8, n_s, h] = [0.238, 0.0418, 0.762, 0.74, 0.951, 0.73]$, as determined from the WMAP 3-year data and consistent[1] with the WMAP 5-year data. The assumed primordial helium mass fraction is $Y = X_{\rm He} = 0.248$. We used CMBFAST (version 4.1; Seljak & Zaldarriaga 1996) to compute the linear powerspectrum and employed the Zel'Dovich (1970) approximation to linearly evolve the particles down to the starting redshift $z = 127$. Simulations with given box size use identical initial conditions (phases and amplitudes of the Gaussian density field), enabling us to investigate in detail the effects of the imposed physics on the forming galaxies and the intergalactic medium. The simulations are performed with a gravitational softening that is constant in comoving variables down to $z = 2.91$, below which we switch to a softening that is constant in proper units. This is done because we expect two-body scattering to be less important at late times, when haloes contain more particles.

- *Gas cooling and photoionization* Radiative cooling and heating are implemented as described in chapter 2[2]. In brief, the radiative rates are computed element-by-element, in the presence of an imposed ionizing background and the CMB. We use the redshift-dependent ionizing background due to galaxies and quasars computed by Haardt & Madau (2001, hereafter HM01). Contributions to cooling and heating of eleven elements (hydrogen, helium, carbon, nitrogen, oxygen, neon, magnesium, silicon, sulphur, calcium, and iron), thermal Bremsstrahlung, and inverse Compton cooling, are tabulated as a function of density, temperature and redshift, using the publicly available photo-ionization package CLOUDY, last described by Ferland et al. (1998), assuming the gas to be optically thin and in (photo-)ionization equilibrium.

---

[1] Our value of $\sigma_8$ is 8 % lower than the best-fit WMAP 7-year data (Jarosik et al. 2010).

[2] We used equation (2.3) rather than (2.4) and CLOUDY version 05.07 rather than 07.02.

Hydrogen reionization is implemented by switching on the evolving, uniform ionizing background at redshift $z = 9$. Prior to this redshift the cooling rates are computed using the CMB and a photo-dissociating background which we obtain by cutting off the $z = 9$ HM01 spectrum above 1 Ryd, which suppresses $H_2$ formation and cooling at all redshifts (we do not resolve haloes in which Pop. III stars that form by $H_2$ cooling would form).

Our assumption that the gas is optically thin may lead to an underestimate of the temperature of the IGM shortly after reionization (e.g. Abel & Haehnelt 1999). It is well known that without extra heat input, hydrodynamical simulations underestimate the temperature of the IGM at $z \gtrsim 3$, the redshift around which helium reionization is thought to have ended (e.g. Theuns et al. 1998, 1999; Bryan et al. 1999; Schaye et al. 2000; Ricotti et al. 2000). We therefore inject $2\ \mathrm{eV}$ per proton in total, smoothed with a Gaussian in redshift with mean $z = 3.5$ and dispersion $\sigma = 0.5$. This mimics the non-equilibrium and radiative transfer effects not included in our optically-thin ionization equilibrium calculations. The resulting thermal evolution is then consistent with that inferred by (Schaye et al. 2000), see chapter 3.

- *Star formation* The interstellar medium of the Milky Way consists of multiple 'phases': a warm component in which hot super nova bubbles envelope and penetrate cold 'clouds'. Current cosmological galaxy formation simulations cannot resolve such a multi-phase ISM, and in addition not all the physics that governs the interaction between these phases, and the star formation in them, is included. Instead of trying to simulate these physical processes we use the following 'subgrid' model. ISM gas is assumed to follow a pressure-density relation

$$p = p_0(\rho_g/\rho_{\mathrm{crit}})^{\gamma_{\mathrm{eff}}}\,, \tag{4.1}$$

where $p_0/k = 1.08 \times 10^3\ \mathrm{cm}^{-3}\,\mathrm{K}$. We use $\gamma_{\mathrm{eff}} = 4/3$ for which both the Jeans mass and the ratio of the Jeans length to the SPH kernel are independent of the density, thus preventing spurious fragmentation due to a lack of numerical resolution. Finally, only gas dense enough to be gravo-thermally unstable, $n_{\mathrm{H}} \approx 10^{-2} - 10^{-1}\ \mathrm{cm}^{-3}$, is assumed to be multiphase and star-forming gas (Schaye 2004). The pressure-density relation (equation 4.1) is only imposed on gas above a critical density of $\rho_{\mathrm{crit}} = 0.1\, m_{\mathrm{H}}\, \mathrm{cm}^{-3}$.

Star formation in disk galaxies is observed to follow a power-law 'Kennicutt-Schmidt' (Kennicutt 1998) relation between the surface density of star formation, $\dot{\Sigma}_*$, and the gas surface density, $\Sigma_{\mathrm{g}}$,

$$\dot{\Sigma}_* = 1.5 \times 10^{-4}\,\mathrm{M}_\odot \mathrm{yr}^{-1}\mathrm{kpc}^{-2} \left(\frac{\Sigma_{\mathrm{g}}}{1\ \mathrm{M}_\odot \mathrm{pc}^{-2}}\right)^{1.4}. \tag{4.2}$$

A star formation rate which depends on ISM pressure as $\dot{\rho}_* \propto p^{\gamma_*}$, guarantees that simulated disk galaxies in which the disk is vertically in approximate hydrostatic equilibrium follow the observed law, independent of the value of $\gamma_{\mathrm{eff}}$ imposed on their ISM gas (Schaye 2004; Schaye & Dalla Vecchia 2008).

- *Galactic winds* Galactic winds are implemented as described in Dalla Vecchia & Schaye (2008). Briefly, after a short delay of $t_{\rm SN} = 3 \times 10^7$ yr, corresponding to the maximum lifetime of stars that end their lives as core-collapse supernovae, newly-formed star particles inject kinetic energy into their surroundings by kicking a fraction of their neighbouring gas particles in a random direction, as governed by,

$$\begin{aligned} \dot{M}_w &= \eta \dot{M}_* \\ \epsilon_{\rm SN}\, f_w &= \frac{1}{2}\, \eta\, v_w^2 \,. \end{aligned} \tag{4.3}$$

  The mass loading factor, $\eta$, relates the rate at which mass is launched in a wind, $\dot{M}_w$, to the star formation rate, $\dot{M}_*$. The product $\eta\, v_w^2$, where $\eta$ is the mass loading factor and $v_w$ is the initial wind velocity, is proportional to the fraction $f_w$ of the supernova energy produced per unit mass, $\epsilon_{\rm SN}$, that powers the wind. We usually characterise the wind implementation by the mass loading factor, and wind speed. The wind prescription is implemented as follows: each SPH neighbour $i$ of a newly-formed star particle $j$ has a probability of $\eta m_j / \sum_{i=1}^{N_{\rm ngb}} m_i$ of receiving a kick with a velocity $v_{\rm w}$. Here, the sum is over the $N_{\rm ngb} = 48$ SPH neighbours of particle $j$. The REFERENCE simulation described below has a mass loading of $\eta = 2$ and wind speed of $v_{\rm w} = 600~{\rm km\,s^{-1}}$ (i.e., if all baryonic particles had equal mass, each newly formed star particle would kick, on average, two of its neighbours, increasing their velocity by $v_{\rm w} = 600~{\rm km\,s^{-1}}$). Assuming that each star with initial mass in the range $6 - 100~{\rm M}_\odot$ injects $10^{51}$ erg of kinetic energy as it undergoes a core collapse supernova, these parameters imply that the total wind energy accounts for 40 per cent of the available kinetic energy for a Chabrier IMF and a stellar mass range $0.1 - 100~{\rm M}_\odot$ (if we consider only stars in the mass range $8 - 100~{\rm M}_\odot$ for type II SNe, this works out to be 60 per cent). The value $\eta = 2$ was chosen to roughly reproduce the peak in the cosmic star formation rate (Schaye et al. 2010). Note that contrary to the widely-used kinetic feedback recipe of Springel & Hernquist (2003), the kinetic energy is injected *locally* and the wind particles are *not* decoupled hydrodynamically. As discussed by Dalla Vecchia & Schaye (2008), these differences have important consequences.

- *Chemodynamics* We employ the method outlined in chapter 3. Briefly, a star particle forms with the elemental abundance of its parent gas particle. It then represents a single stellar population (SSP) with given abundance, and an assumed stellar IMF. The reference model uses the IMF proposed by Chabrier (2003), with mass limits of $0.1{\rm M}_\odot$ and $100{\rm M}_\odot$. At each time step, we compute the timed release of elements and of energy from three stellar evolution channels: (i) type II core collapse supernovae (SNe), (ii) type I SNe and (iii) asymptotic giant branch (AGB) stars. The stellar evolution prescriptions are based on the Padova models, using stellar lifetimes computed in Portinari et al. (1998) and the yields of low mass and high mass stars of Marigo (2001) and Portinari et al. (1998) respectively. The yields of Portinari et al. (1998) include ejecta from core collapse supernovae (SNII) along with their calculations of mass loss from high mass stars. Using these yields gives an element of consistency between the high and low mass stellar evolution. An e-folding delay time is used to describe the SNIa rate and with a fraction of $2.5\%$ of white dwarfs that become SNIa the REFERENCE model approximately reproduces the observed cosmic SNIa rate[3], see chapter 3. We use the 'W7' SNIa yields of Thielemann et al. (2003).

Elements produced by nucleo-synthesis are distributed to SPH particles neighbouring the star, weighted by an SPH kernel, as done by (e.g. Mosconi et al. 2001). The simulations track the abundance of eleven individual elements and we use an extra 'metallicity' variable to track the total metal mass of each particle (see chapter 3). The ratio $Z \equiv M_Z/M$ of metal mass over total mass is the 'particle metallicity' . For gas particles we also compute a 'smoothed metallicity' , as $Z_{\rm sm} \equiv \rho_{\rm Z}/\rho$ *i.e.* the ratio of the metal density computed using SPH interpolation, $\rho_{\rm Z}$, over the gas density, $\rho$. Stars inherit metal abundances of their parent gas particle: we record both the particle and smoothed metallicity. In chapter 3 we argue that the smoothed metallicity is more consistent with the SPH formalism than the particle metallicity. Using smoothed metallicities results in a spreading of metals over slightly greater volumes.

### 4.2.2 The Simulation Suite

Table 4.1 contains an overview the models of the OWLS suite. Simulation names contain a string 'LXXXNYYY' which specifies the co-moving size of the periodic box, L=XXX$h^{-1}$ Mpc, and the number of particles N=YYY$^3$ of (initial) gas and dark matter; most runs discussed here have L=25 or 100, and N=512. Comparing different L and N models allows us to investigate the effects of numerical resolution, and missing large-scale power. The table also contains a brief description of the physics in which a particular run differs from the REFERENCE model, see Schaye et al. (2010) for more details.

---

[3] The current observations on SNIa explosion rates are inconsistent, our assumed rates conform to the most recent data (see chapter 3).

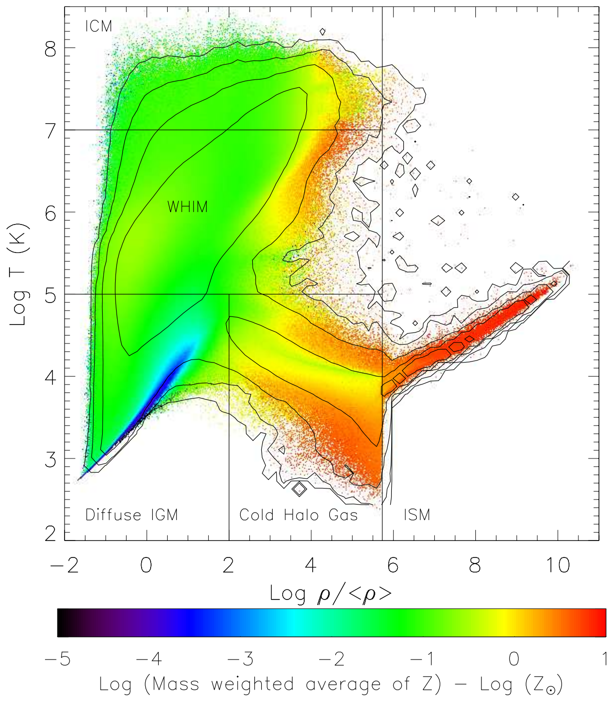

**Figure 4.1**: Mass weighted metal distribution in temperature-density space at $z = 0$ in simulation REFERENCE_L100N512. The colour scale gives the metallicity. The contours indicate the metal mass distribution and are logarithmically spaced by 1 dex. The straight lines indicate the adopted division of the gas into: star-forming gas (i.e., $n_{\rm H} > 0.1\,{\rm cm}^{-3}$), diffuse IGM ($\rho < 10^2\,\langle\rho\rangle$, $T < 10^5\,{\rm K}$), cold halo gas ($\rho > 10^2\,\langle\rho\rangle$, $T < 10^5\,{\rm K}$), WHIM ($10^5\,{\rm K} < T < 10^7\,{\rm K}$), and ICM ($T > 10^7\,{\rm K}$). The metals are distributed over a wide range of densities and temperatures

## 4.3 RESULTS

We begin by describing the metal distribution of the REFERENCE_L100N512 simulation in temperature-density space at redshift $z = 0$, figure 4.1. The colour shows the mass-weighted mean metallicity for a given temperature and density. The metallicity follows a clear density gradient, with the exception of a track of photo-ionized gas in the lower left hand corner, which has a very low metallicity. The contours, on the other hand show the distribution of total metal mass. Metals are found at virtually all temperatures and densities, from the high-densities in galactic disks, to extremely low densities.

It is useful to divide the $T - \rho$ plane into several 'phases', since as we will show, different enrichment processes dominate in different phases, and also because the observational constraints for different phases are inferred from different types of data. A first division distinguishes between star-forming gas (henceforth SF gas) on the imposed $p - \rho$ relation (equation 4.1), which we identify with the ISM in galaxies, and non-star-forming gas (NSF gas). The SF gas can be seen as the thin band of contours on the right of figure 4.1 at $\rho/\langle\rho\rangle > 10^6$. We further divide NSF gas into *hot gas*, typically found in halos of large groups or clusters (ICM, $T > 10^7 K$), *warm-hot intergalactic* and *circum-galactic gas* (WHIM, $10^5{\rm K} < T < 10^7$ K), *diffuse gas* (diffuse IGM, $\rho < 100\,\langle\rho\rangle$, $T < 10^5$ K), and *cold halo gas* ($\rho > 100\,\langle\rho\rangle$, $T < 10^5$ K. These phases are indicated in figure 4.1.

The spatial distribution of metals is shown at $z = 4$, 2 and 0, in figures 4.2 and 4.3. At $z = 4$ metals are strongly clustered around haloes, with circum-halo metallicities of $\log(Z/Z_\odot) \approx -3$ to -2, and large fractions of volume are enriched to exceed-

**Table 4.1**: Simulation Set

| Name | Box Size (Mpc/h) | Comment |
|---|---|---|
| AGN | 100/25 | Incorporates AGN model of Booth & Schaye (2009). |
| DBLIMFCONTSFV1618 | 100, 25 | Top-heavy IMF for $n_{\rm H} > 30~{\rm cm}^{-3}$;<br>$v_{\rm w} = 1618~{\rm km\,s}^{-1}$ |
| DBLIMFV1618 | 100, 25 | Top-heavy IMF for $n_{\rm H} > 30~{\rm cm}^{-3}$;<br>$v_{\rm w} = 1618~{\rm km\,s}^{-1}$,<br>$\dot{\Sigma}_*(0) = 2.083 \times 10^{-5}{\rm M}_\odot{\rm yr}^{-1}{\rm kpc}^{-2}$ |
| DBLIMFCONTSFML14 | 100, 25 | Top-heavy IMF for $n_{\rm H} > 30~{\rm cm}^{-3}$;<br>$\eta = 14.545$ |
| DBLIMFML14 | 100, 25 | Top-heavy IMF for $n_{\rm H} > 30~{\rm cm}^{-3}$;<br>$\eta = 14.545$, $\dot{\Sigma}_*(0) = 2.083 \times 10^{-5}{\rm M}_\odot{\rm yr}^{-1}{\rm kpc}^{-2}$ |
| REFERENCE | 100, 25 | |
| EOS1p0 | 100, 25 | Isothermal equation of state |
| EOS1p67 | 25 | Equation of state $p \propto \rho^{\gamma_*}$, $\gamma_* = 5/3$ |
| IMFSALP | 100, 25 | Salpeter IMF, SF law rescaled |
| MILL | 100, 25 | Millennium cosmology (WMAP1):<br>$(\Omega_m, \Omega_\Lambda, \Omega_b h^2, h, \sigma_8, n, X_{\rm He}) =$<br>$(0.25, 0.75, 0.024, 0.73, 0.9, 1.0, 0.249)$ |
| NOAGB_NOSNIa | 100 | AGB & SNIa mass & energy transfer off |
| NOHeHEAT | 25 | No He reheating |
| NOSN | 100, 25 | No SNII winds, no SNIa energy transfer |
| NOSN_NOZCOOL | 100, 25 | No SNII winds, no SNIa energy transfer, cooling uses primordial abundances |
| NOZCOOL | 100, 25 | Cooling uses primordial abundances |
| REIONZ06 | 25 | Redshift reionization = 6 |
| REIONZ12 | 25 | Redshift reionization = 12 |
| SFAMPLx3 | 25 | $\dot{\Sigma}_*(0) = 4.545 \times 10^{-4}{\rm M}_\odot{\rm yr}^{-1}{\rm kpc}^{-2}$ |
| SFAMPLx6 | 25 | $\dot{\Sigma}_*(0) = 9.090 \times 10^{-4}{\rm M}_\odot{\rm yr}^{-1}{\rm kpc}^{-2}$ |
| SFSLOPE1p75 | 25 | $\gamma_{\rm KS} = 1.75$ |
| SFTHRESZ | 25 | Metallicity-dependent SF threshold |
| SNIaGAUSS | 100 | Gaussian SNIa delay distribution |
| WDENS | 100, 25 | Wind mass loading and velocity determined by the local density |
| WML1V848 | 100, 25 | $\eta = 1$, $v_{\rm w} = 848{\rm km\,s}^{-1}$ |
| WML4 | 100, 25 | $\eta = 4$, $v_{\rm w} = 600{\rm km\,s}^{-1}$ |
| WML8V300 | 25 | $\eta = 8$, $v_{\rm w} = 300{\rm km\,s}^{-1}$ |
| WPOT | 100, 25 | 'Momentum driven' wind model (scaled with the potential) |
| WPOTNOKICK | 100, 25 | 'Momentum driven' wind model (scaled with the potential) without extra velocity kick |
| WVCIRC | 100, 25 | 'Momentum driven' wind model (scaled with the resident halo mass) |

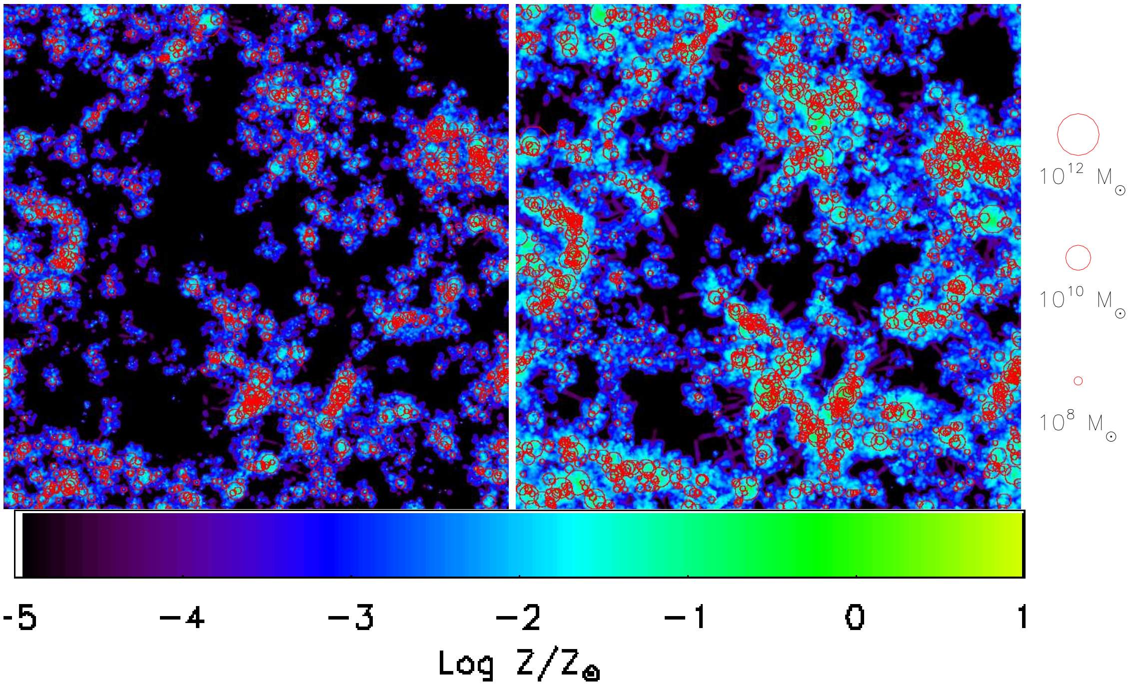

**Figure 4.2**: Metal enrichment in the REFERENCE_L025N512 simulation. Shown is a $5h^{-1}\,\mathrm{Mpc}$ (comoving) slice through the simulation box at $z = 4$ (left), and $z = 2$ (right). The colour coding shows smoothed metallicity, mass averaged along the line of sight; the colour scale is cut off below $\log(Z/Z_\odot)$ = -5 although metallicities extend to lower values. Red circles correspond to haloes identified by a friends-of-friends group finder, with radius proportional to the logarithm of the stellar mass of the halo, as indicated. The box (and therefore each panel) is $25h^{-1}\,\mathrm{Mpc}$ on a side. Metals are initially strongly clustered around haloes (left panel), but their volume filling factor increases as time progresses.

ingly low levels, or not at all. As time progresses circum-halo metallicities increase to $\log(Z/Z_\odot) \approx -2$ to -1 and the filling factor of metals also increases substantially, yet even at $z = 0$ there still are co-moving volumes which are barely enriched at all. Comparing the two resolutions (and box sizes), we note that although the abundance of circum-halo gas is similar at $z = 2$ in the L100N512 and L025N512 runs, the filling factor of metals is higher in the higher resolution simulation.

We begin our analysis by comparing the metallicities and metal mass fractions in different phases provided by the reference simulation with observations. We then turn our attention to a comparison of the different OWLS models.

### 4.3.1 Overview

We now introduce some of the observational data which are available for comparison in figure 4.4. Observationally metallicities are typically the easiest to measure and thus there are a number of sources giving cosmic metallicities as a function of redshift. The total mass of metals in a given phase is much harder to determine, and by extension the fraction of metals in a given phase. Figure 4.4 contains the evolution of all three

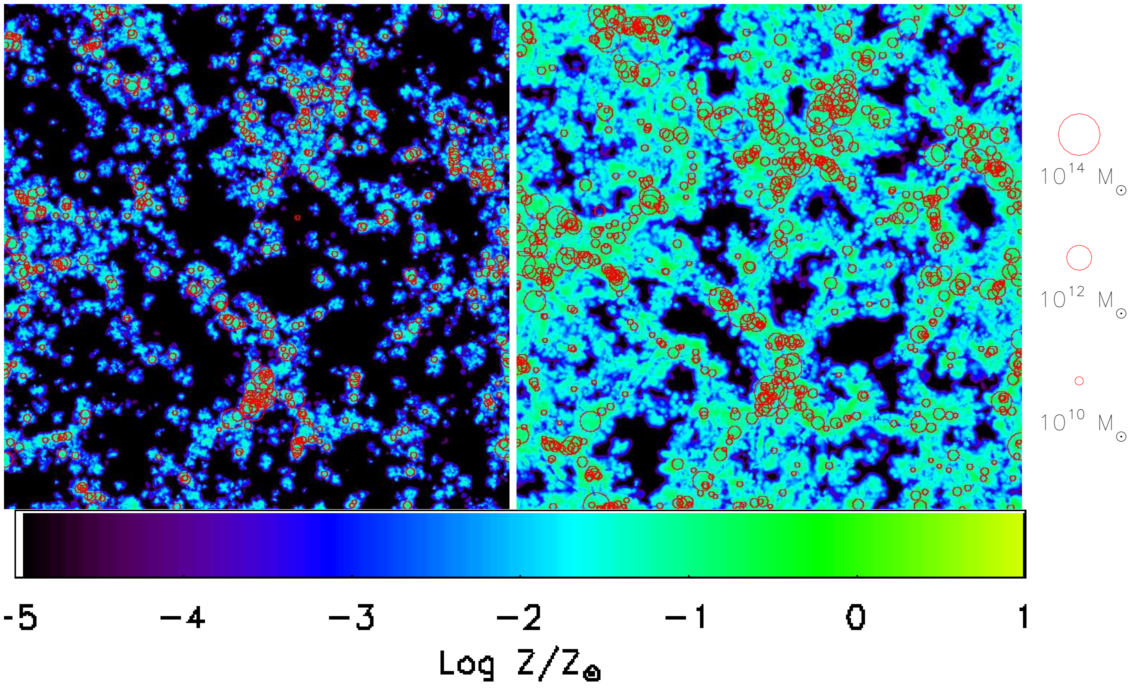

**Figure 4.3**: As in figure 4.2, but for the REFERENCE_L100N512 simulation. Shown is a $5h^{-1}$ Mpc (comoving) slice through the $100h^{-1}$ Mpc simulation box at $z = 2$ (left), and $z = 0$ (right). The filling factor of metals continues to increase to lower redshifts.

measure of metal abundance from the REFERENCE L100N512 simulation, compared to data[4]. The fraction of metals in a given phase is simply the ratio of the total amount of metals in that phase over the total amount of metals in all phases. The amount of metals in a phase is shown as $\Omega_Z \equiv \rho_Z/\rho_{\rm crit}$, the ratio of the metal mass density in a given phase over the critical density.

Now we briefly walk through the data (which we have converted to our adopted solar abundances) to which we are comparing:

- *Stars* For stellar metallicities, we compare to the global values obtained by Gallazzi et al. (2008, circle in the top-left panel) for $z = 0$ and Halliday et al. (2008, square in top left panel) for $z = 2$. Halliday et al. (2008) note that their metallicities are lower than what was found by Erb et al. (2006), speculating that since they observed oxygen, a non-solar [O/Fe] ratio might make their observations agree. We have also compared their point to [Fe/H] and indeed, the match to the data is better (see section 4.3.2 for a discussion of [O/Fe] in our simulations). The $z = 2.5$ point is taken from Bouché et al. (2007) which is compiled from their own previous measurements.

- *Star-forming gas* Bouché et al. (2007) give a value for ISM and/or dust at $z = 2.5$

---

[4] Note that for the remainder of this chapter, we use 'particle metallicities' (see section 4.2.1, although since we are considering mean metallicities of a given phase, they should differ little from the smoothed metallicities

and following Pagel (2008) we include it here as a filled red diamond in the top-left panel.

- *Diffuse IGM* For the metallicity we have included here both the carbon and oxygen Lyman-$\alpha$ forest measurements from Schaye et al. (2003, upwards pointed triangle in the top middle panel) and Aguirre et al. (2008, downwards pointed triangle in the top middle panel) respectively.

- *Cold Halo Gas* While the precise nature of DLAs is still somewhat uncertain, we surmise that circum-halo and intrahalo cold gas most likely have higher cross-sections than the ISM and thus we can consider observations of DLA and sub-DLA systems as tracing the cold halo gas. As such we have incorporated the compilation of DLA metallicities from Prochaska et al. (2003, leftwards pointed triangles in the top middle panel).

- *WHIM* The WHIM has long stood as a phase that promises to contain a wealth of baryons and metals, but is difficult to detect. As such, there is no direct measurement of the metallicity of the WHIM.

- *ICM* Measurements of ICM metallicities are also troublesome, although much less so. The main difficulty is measuring the metallicity out to large enough radii in order to get a good estimate of the mean metallicity. We have chosen to use the outermost measurements of cluster metallicities by Simionescu et al. (2009, hatched region in the top right panel), using a box to indicate the range of values in their sample.

In general the metallicities of our simulation follow the trends seen in the data. Converting from observed metallicities to estimates of the fractional metal distribution (middle row) or the total amount of metals in each phase (bottom row), require the metallicities for all phases to be precisely measured and a solid knowledge of the underlying baryon distribution. We will therefore focus on the metallicities throughout the rest of this work.

We want to investigate which physical processes are most important for determining the cosmic metal distribution in a given phase. We begin by discussing the metallicity and metal mass evolution for our full range of models.

The metallicity of the stars and star forming gas is numerically well converged (figure 4.5), with the stellar and SF gas abundances in simulations with 6 times lower mass resolution $\approx 0.2$ dex below that of the L025N512 models. The metallicities of the SF gas and stars track each other very closely, and in each of the models rises almost linear in redshift, $\log(Z/Z_{\odot}) \approx 0.3 - 1.1(z/6)$. The different models differ in stellar or SF metallicity about 0.2 dex, with some exceptions (see below). The metallicity of NSF gas is more resolution dependent and is unreliable in the lower resolution simulations above $z \approx 2$. The models here are reasonably consistent with the exception being the two models that do not include any feedback (the lower two lines in the bottom panel of figure 4.5).

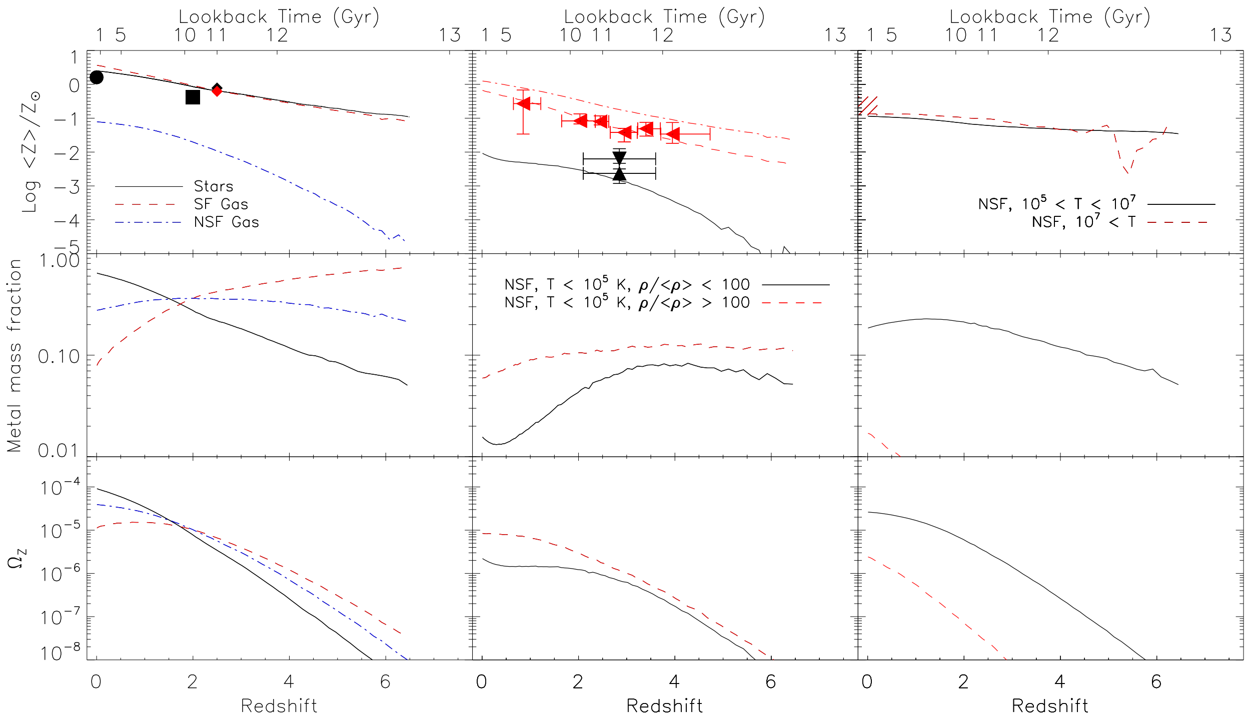

**Figure 4.4**: Metallicity (top row), metal mass fraction (middle row), and $\Omega_Z$ (bottom row) as a function of redshift for the various phases of baryons in the REFERENCE_L100N512 simulation compared to data. Lines refer to simulation results, with different line styles indicating various baryonic phases. *Left column*: stars (solid black), SF gas (dashed red), NSF gas (dot-dashed blue); *Middle column*: NSF hot gas (black), NSF cold gas (dashed red); *Right column*: WHIM (solid black line), ICM (dashed red). Data points are colour-coded to indicate to which phase they should be compared to in each panel. The diamonds at $z = 2.5$ are estimates of stellar and star-forming metallicities by Pagel (2008), with further stellar metallicities indicated by a circle Gallazzi et al. (2008) and a square Halliday et al. (2008). DLA measurements are from Prochaska et al. 2003, left pointing triangles, IGM pixel optical depth measurements in QSO spectra are from Aguirre et al. 2008, triangle pointed down and Schaye et al. 2003, triangle pointed up. The ICM measurements are from X-ray observations (Simionescu et al. 2009, hatched region)

We recall the numerical convergence results we discussed in appendices A and B of chapter 3. Box size does not play an important role for boxes larger than $12h^{-1}\,\mathrm{Mpc}$. On the other hand, resolution proves to be much more of a challenge. The stellar metal mass fraction just barely converges for the L025N512 resolution, although the difference is small by $z = 2$. The metal-mass fraction in the cold-phase NSF gas is converged to within a factor of two. Obtaining converged results tends to be more challenging at higher redshifts. Metallicity is generally better converged than the fraction of metals in a given phase, and is reasonably reliable for all phases at the resolution of the L100N512 simulations, with the exception of the metallicity of the diffuse IGM. Higher resolution simulations generally yield higher metallicities, especially at higher redshift, but even in this phase, the simulations are converged by $z = 2.5$ ($z = 3$) for

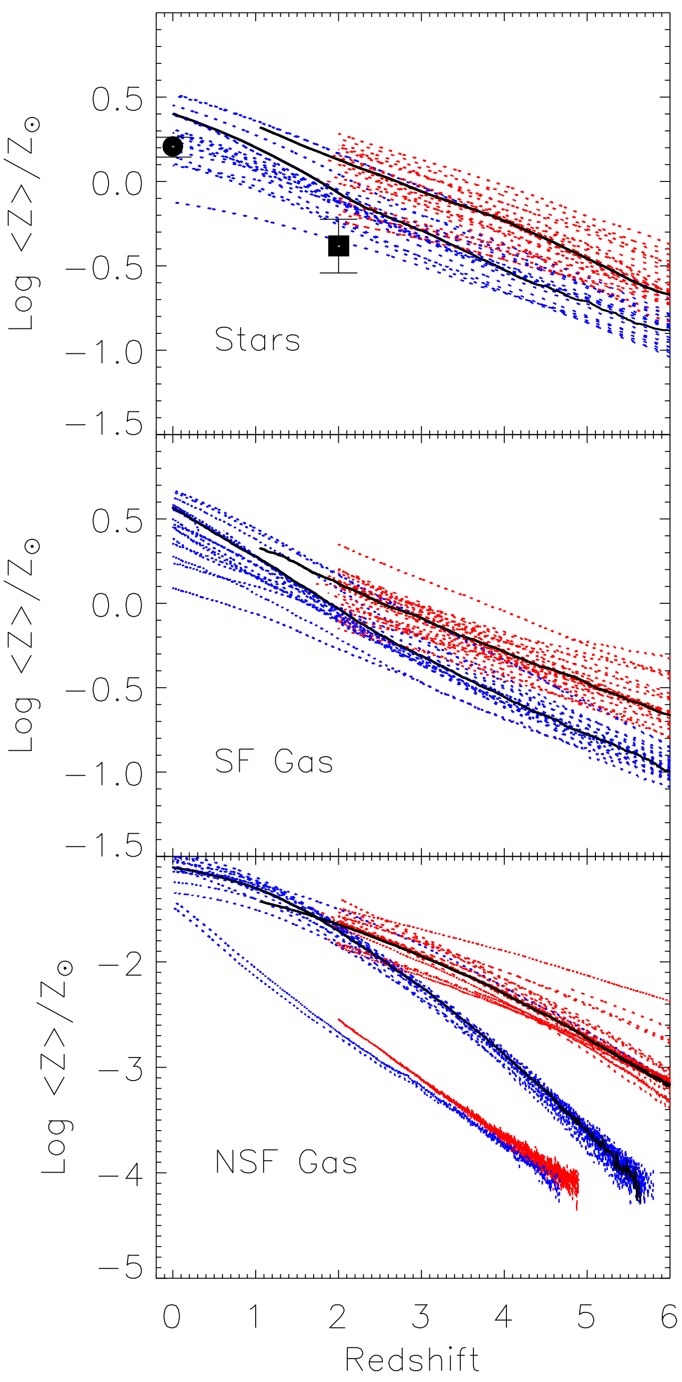

**Figure 4.5**: Metallicity in stars (top), star-forming gas (middle), and non-star-forming gas (bottom) as function of redshift for all OWLS simulations. Shown are the REFERENCE simulations (solid black), the rest of the (L025N512) simulations (dotted red,) and the rest of the (L100N512) simulations (dotted blue). The higher resolution (L025N512) simulations were stopped at $z = 2$ (with the exception of the REFERENCE model which was stopped just above $z = 1$), lower resolution simulations (L100N512) were continued to $z = 0$. The mean stellar metallicity in units of solar rise from $\approx -0.7$ dex at $z = 6$ to higher than solar at $z = 0$, closely tracking the metallicity of the SF gas. For these two phases, resolution plays a minor role, with a 64 times higher mass resolution resulting in higher metallicities by less than 0.3 dex. The metallicity of NSF gas is strongly resolution dependent at $z > 2$; in the higher resolution simulation it rises from $\mathrm{Log}\langle Z\rangle/Z_\odot = -3$ to $-1$ from $z = 6$ to $z = 0$. Points with error bars indicate observations of stellar metallicities at $z = 0$ and $z = 2$ by Gallazzi et al. (2008) and Halliday et al. (2008), respectively. Aside from the models without feedback (the lower lines in the bottom panel - note that NOSN_L025N512 and NOSN_NOZCOOL_L025N512 fall on top of each other), most of the different runs yield abundances that follow the REFERENCE model closely, indicating that the metallicities in our simulations are reasonably robust to model variations.

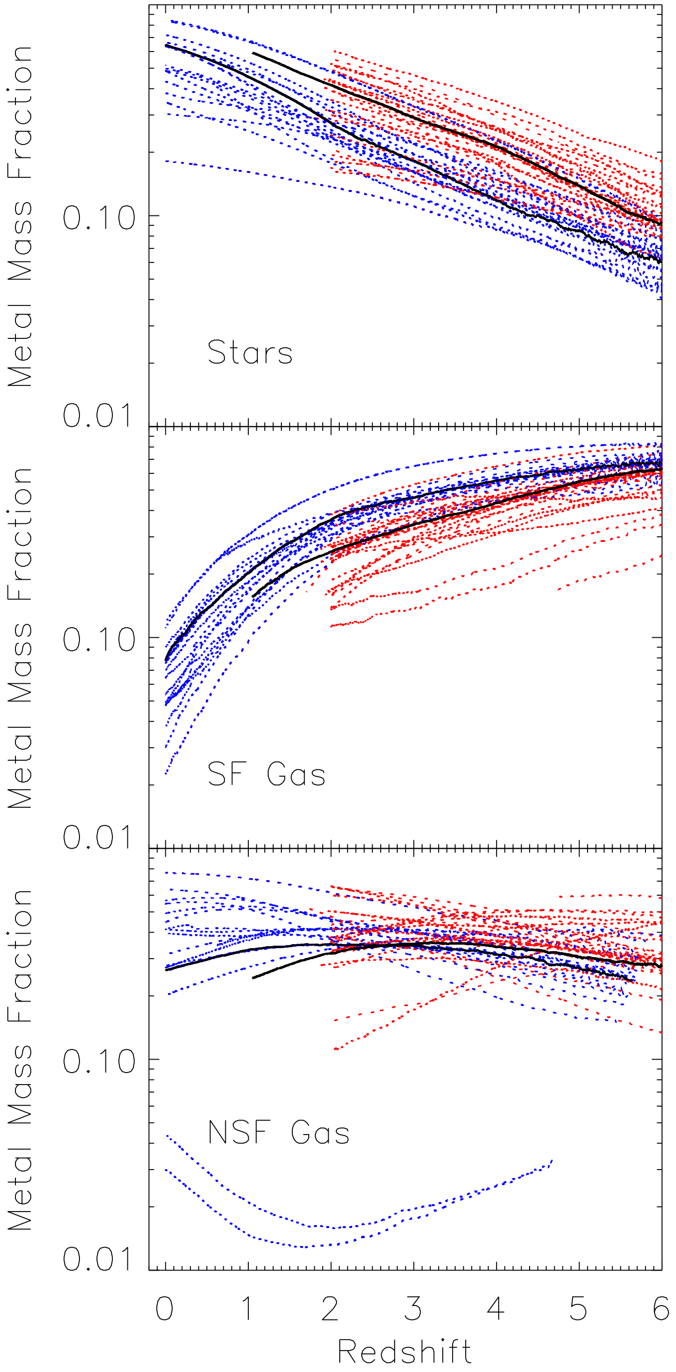

**Figure 4.6**: Same as figure 4.5, but for metal mass fractions. Comparing the two REFERENCE models shows that resolution affects the stellar metal mass in a discernible way, with higher resolution yielding a higher stellar metal fraction. The stellar metal mass increases towards $z = 0$, whereas the metal mass fraction in SF-gas decreases slowly to $z \approx 2$, then falls much more rapidly. The fraction of metals in NSF gas for a given model varies by less than a factor $\approx 2$ between $z = 6$ and $z = 0$ (with the exception of the models without feedback - the two lower lines in the bottom panel, note that here NOSN_L025N512 and NOSN_NOZCOOL_L025N512 fall below the plotting area).

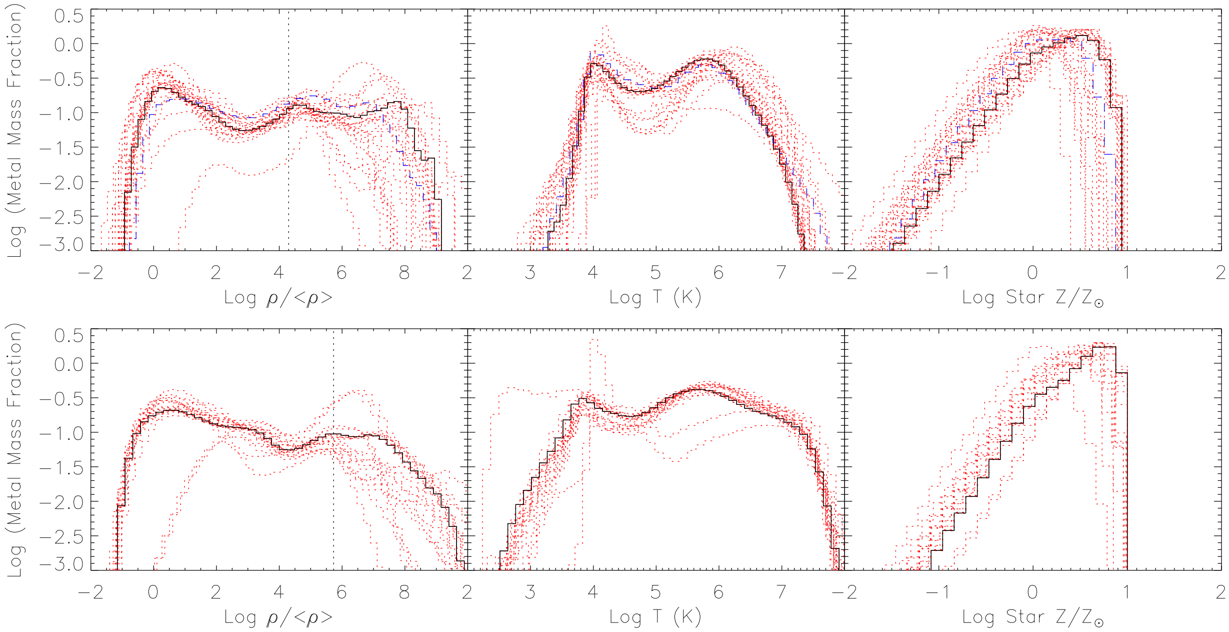

**Figure 4.7**: Fraction of metals in gas as a function of density (left), temperature (middle) and fraction of metals in stars as a function of stellar metallicity (right) for the same models as shown in figure 4.6 at $z = 2$ (top) and $z = 0$ (bottom). Each pdf is normalised to unity. The reference simulations are given in solid black, while the rest of the simulations are shown in dotted red. The REFERENCE_L100N512 model at $z = 2$ is shown in the top panel with the dashed blue line. SF gas is omitted from the central panel, since the 'temperature' of this multi-phase gas is set by the imposed $p - \rho$ relation. The dotted vertical line is the star formation threshold. While there are a few outliers, most models generally yield similar metal distributions, with the biggest differences occurring at high $\rho$ and small $T$.

L100N512 (L025N512) runs.

Resolution plays an important role for the fractional metal mass plots (figure 4.6), particularly for the WHIM[5]. In these models, the fraction of metals in stars rises from $\approx 6$ to $\approx 60$ per cent between $z = 6$ and $z = 0$, with a spread between models of about a factor of $\approx 2$, except in the most extreme models (the outliers with very low NSF gas metal mass are models without SN feedback). Interestingly, the fraction of metals in NSF gas in the other models is nearly constant over time at $\approx 30$ per cent. Initially, the majority of the metals reside in SF gas. At $z \approx 3$ metals are approximately equally distributed over the three different phases (stars, SF and NSF gas), with stars becoming the dominant repository of metals at lower redshift.

The distributions of metals at $z = 0$ and $z = 2$ are investigated in more detail in figure 4.7. The metal mass weighted probability distribution function (PDF) [6] shows

---

[5] Metal mass fraction and metallicity increase by a factor of a few between L100N256 and the 8 times better resolved L100N512 simulations, which itself is a still below a L050N512 simulation (chapter 3, Appendix B).

[6] We emphasise that the right most panel does *not* show the metallicity distribution function, as is commonly plotted. It rather shows how the metal mass is distributed among stars of various metallici-

several maxima in both density and temperature, with minima at $\rho \approx 10^3\langle\rho\rangle \approx 3$ and $\rho \approx 10^4\langle\rho\rangle \approx 3$ at $z = 2$ and $z = 0$ respectively, and at $T \approx 10^5\mathrm{K}$. All models have a relatively well pronounced maximum at $\rho \approx \langle\rho\rangle$: above this density gas tends to accrete quickly into haloes, where below it total amount of metals is small. The location of the secondary maximum is close to the star formation threshold for most models, although for some it is significantly higher. This is caused by the fact that star particles distribute their metals among their neighbours which tend to be star-forming themselves. The outliers at the low density end of the distribution result from turning off feedback (see figure 4.8), while the outliers at high density correspond to either strong feedback models (e.g. AGN) or models where the star formation efficiency is increased (e.g. SFAMPLX3).

The temperature minimum at $T \approx 10^5\mathrm{K}$ of is caused by a number of factors. First, gas cooling is very efficient at this temperature. Second, the winds tend to shock metals to temperatures higher than this value, causing a peak in the distribution at higher temperatures. Finally, the equilibrium temperature due to photoheating is lower than this temperature, causing a second peak. The temperature distribution of the metals shows less variation than the distribution with density. The two outliers again correspond to models without feedback (see figure 4.8). Such models have little shock-heated metals, resulting in much more low temperature metals. Without metal cooling, these metals pile up at $10^4$ K, whereas with metal cooling the metals are found to very low temperatures. This effect is diminished at $z = 2$, although note that the NOSN_L025N512 simulation is excluded because it was stopped at $z \approx 3$ due to computational costs. The metals appear to be distributed among the stellar metallicities very similarly in the different models, with the main deviation at high metallicity from the AGN simulation, which predicts more metal mass in lower metallicity stars.

These figures once more illustrate the large dynamic range in density and temperature over which metals are distributed. These distributions are mostly converged in both box size and resolution (figure 3.20 and figure 3.21), with some dependence of the temperature distribution on box size, and of the density distribution on resolution. Next, we will investigate in more detail how various physical processes affect the metal distribution.

### 4.3.2 Impact of energy feedback and metal-line cooling

Since the pioneering work of White & Rees (1978) it has been known that feedback plays an important role in controlling the growth of galaxies, with supernova driven winds (e.g. Dekel & Silk 1986) and AGN (e.g. Bower et al. 2008) the usual suspects, see e.g. Baugh (2006) for a review. Because metals are detected at low densities yet were synthesised inside galaxies, non-gravitational processes such as galactic winds that enrich the surroundings of galaxies, are clearly present, although other processes are at work as well. The OWLS simulations invoke energy feedback due to supernova explosions to power such galactic outflows. Here we investigate to what extent the metal distribution differs in models with and without energy feedback. In this section

---

ties.

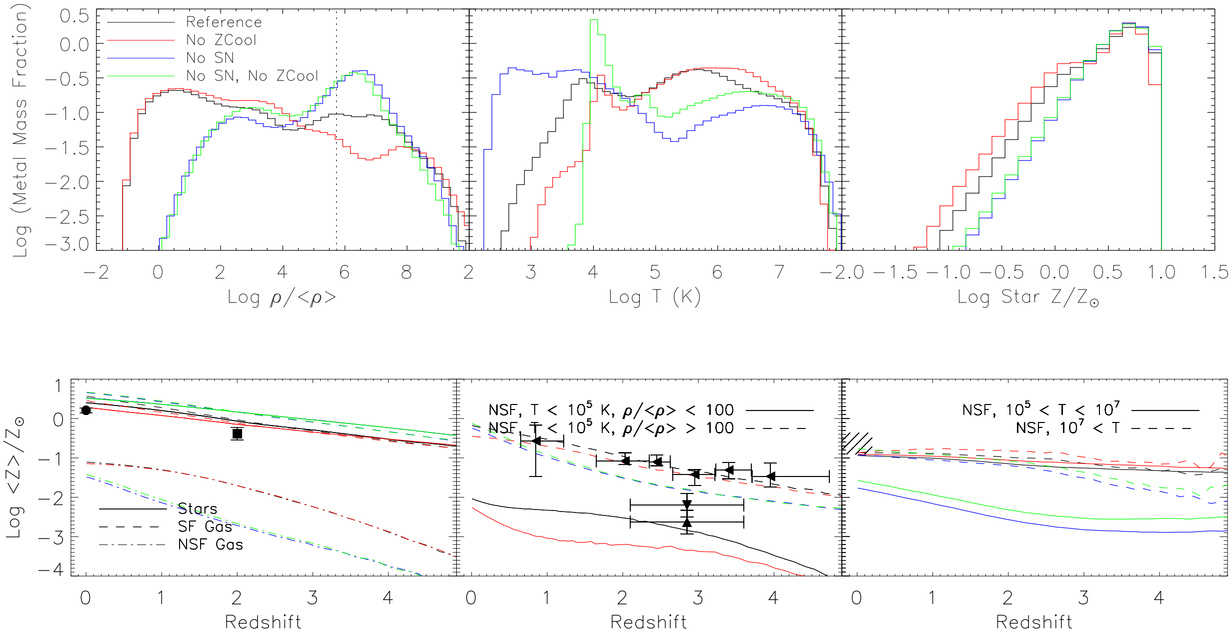

**Figure 4.8**: Distribution of metals for L100N512 simulations with different feedback and cooling prescriptions. *Top panels*: $z = 0$ metal mass weighted PDFs of density, temperature, and stellar metallicity. In the left-most panel, the star formation threshold is indicated by the dotted line. The gas that is on our equation of state was removed from the temperature PDF. *Bottom panels* : Metallicity as a function of redshift for various phases as defined in figure 1. The left panel shows stars (solid), SF gas (dashed) and NSF gas (dot-dashed). The middle panel shows cold IGM (NSF, $\rho < 10^2\langle\rho\rangle$, $T < 10^5\,\mathrm{K}$; solid), and cold halo and circum-halo gas (NSF, $\rho > 10^2\langle\rho\rangle$, $T < 10^5\,\mathrm{K}$; dashed). Finally, the right panel shows WHIM (NSF gas, $10^5\mathrm{K} < T < 10^7\,\mathrm{K}$; solid) and ICM (non-star-forming, $T > 10^7\,\mathrm{K}$; dashed). Shown are the REFERENCE simulation (black), a simulation which cools only using primordial abundances (NOZCOOL; red), a simulation which has no energy feedback (NOSN; blue), and a simulation which has no energy feedback and cools only using primordial abundances (NOSN_NOZCOOL; green), as indicated in the top left panel. Note that the metallicity of the diffuse IGM for the simulations without feedback is below the range in the bottom-middle panel. Data points indicate observations as in figure 4.4, where the points in the left panel correspond to stellar metallicities, the left pointed triangles in the middle panel correspond to the cold halo gas while the other (lower) set of triangles correspond to diffuse IGM measurements and the hatched region in the right panel shows an ICM metallicity measurement. metal-line cooling and especially feedback clearly play a major role in shaping the metallicity of the diffuse IGM. Without supernova feedback, the metallicities of the WHIM and the diffuse IGM are greatly reduced. The effect of feedback is surprisingly small for the metallicity of hot ($T > 10^7\mathrm{K}$) gas, stars, and SF gas.

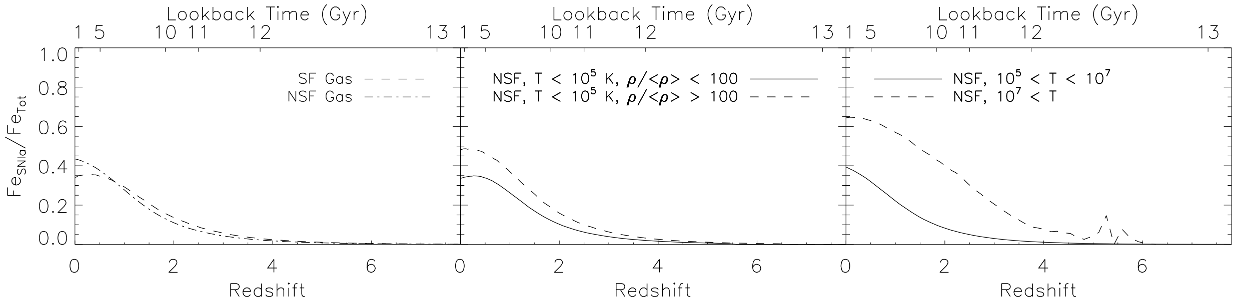

**Figure 4.9**: Evolution of the fraction of iron originating from type Ia SNe for the REFERENCE_L100N512 model, for different gas phases as indicated in the panels. For most phases, the contribution of type Ia SNe starts to build-up from ≈ 10 per cent at $z = 3$ to ≈ 40 per cent by $z = 0$, except in the ICM, where its contribution has reached nearly 65 per cent by $z = 0$. In all other phases, iron is produced predominantly by massive stars. Conversely, the high fraction of enrichment by type Ia SNe in the ICM implies that winds are not the only enrichment mechanism for the hot gas.

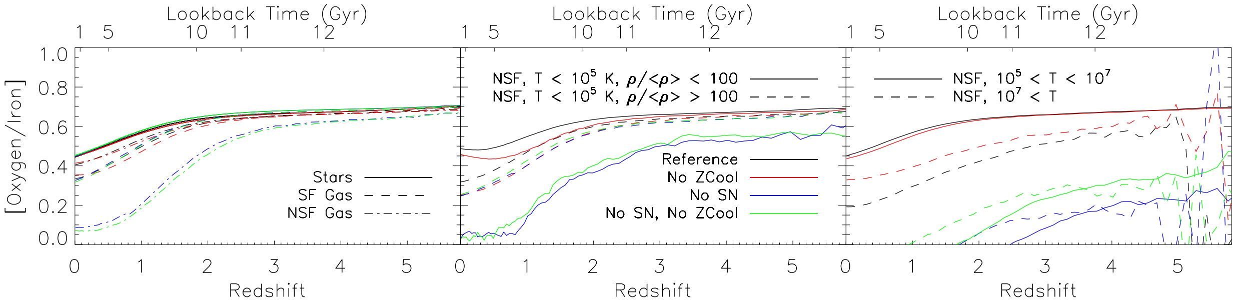

**Figure 4.10**: Evolution of [O/Fe] for the same L100N512 simulations as in figure 4.8, REFERENCE (black), NOZCOOL (red), NOSN (blue), and NOSN_NOZCOOL (green). Note that the solid lines in the left panel lie nearly on top of each other. In the REFERENCE simulation at high redshift all phases are highly overabundant in the $\alpha$-process element O (produced by type II SNe). metal-line cooling has little effect on the abundance ratio, but simulations without winds have lower O/Fe, especially in the diffuse IGM, ICM and WHIM, demonstrating that, not surprisingly, elements such as O are transported out of galaxies mainly by galactic winds powered by the SNe that produced $\alpha$-elements in the first place.

we discuss the effect of including galactic winds driven by supernovae and metal-line cooling on the metal distribution. We show that outflows are essential for enriching the IGM and that metal-line cooling strongly affects the temperature distribution of metals. On the other hand, the hot non-star-forming gas can obtain rather high metallicities without feedback, indicating that the ICM is enriched at least partly by some process that is not directly related to supernova feedback.

Relative to previous work, a significant improvement in the OWLS simulation suite is the cooling routine, which takes into account the contributions of all eleven individual elements that are important for the cooling rates in the presence of an imposed ionizing background. One motivation for this is that several simulations that included enrichment through winds or thermal feedback failed to match the observed CIII/CIV ratio as measured in the IGM (Aguirre et al. 2005), probably because the gas in the simulations was hotter than observed. metal-line cooling might alleviate this problem, and here we investigate how it affects the metal distribution itself.

In figure 4.8 we show the distribution of metals for simulations which treat cooling and feedback differently. Here the REFERENCE simulation is compared to a simulation without metal cooling (NOZCOOL), one without winds (NOSN; note that the blue lines in the lower left hand panel fall mainly under the green lines), and one with neither metal cooling nor winds (NOSN_NOZCOOL). These simulations differ not only in the way metals are distributed and cool, but also in their star formation history since cooling and feedback of course also affect the conversion of gas into stars (see Schaye et al. 2010).

The top panel shows metal mass weighted PDFs at $z = 0$. The simulation without metal cooling contains fractionally more metals than the REFERENCE model at $\rho \approx 10^2 \langle\rho\rangle$ at the expense of metals just above the star-formation threshold. Metal cooling thus allows metals to condense from low densities into star-forming gas. This clearly illustrates the importance of metal cooling in resolving accretion onto star-forming regions. Surprisingly, the presence of metal-line cooling has little effect on the temperature distribution where the cooling curve peaks ($T \approx 10^5$ K). This is most likely since the cooling times here are already short. The biggest difference is noticed in the low temperature regions (we remind the reader that this distribution excludes gas with densities above our star-formation threshold). Metals can cool gas well below $10^4$ K, while neglecting metal cooling abruptly cuts the distribution off. Finally, metal cooling slightly increases the fraction of metals locked up in high metallicity stars.

In the absence of galactic winds, only a negligible fraction of the metals reach densities $\rho \lesssim 10 \langle\rho\rangle$ (top-left panel of figure 4.8). This underlines the importance of feedback in reproducing the metals seen in the Lyman$-\alpha$ forest. Note that this is in opposition to Gnedin (1998) who found that feedback played only a minor role in enriching the IGM, but it agrees well with Aguirre et al. (2001a,b). Winds also serve to evacuate metals from the ISM as we can see that in the absence of feedback metals tend to pile up just above the star-formation threshold. The amount of metal at and below $10^4$K is much higher in the NOSN models than in any model that includes metal feedback from SNe in the absence of galactic winds (top-middle panel of figure 4.8). From to the severe dip in metals above $10^5$K, we infer that wind shocks, rather than accretion shocks, shape the metal distribution at these temperatures. Not only may metals be locked up in stars, they may be in star-forming gas which was excluded from the middle panel. We have checked and indeed a large amount of the metals in the NOSN simulations are in these two phases. For the star-forming gas we can see this in the top-left panel of figure 4.8.

In the bottom panels of figure 4.8 we show the metallicities as a function of redshift. As noted in chapter 3, in the REFERENCE model most of the metals are initially in the gas phase, while by the present day the majority of the metals are locked up into stars. The effect of neglecting metal cooling is small for the metallicity of either stars or SF gas, but is obvious for the metallicity of the IGM (which is *lower* by up to an order of magnitude in the absence of metal cooling) and the WHIM (*higher* by $\approx 0.2$ dex without metal cooling).

Without feedback from winds, more metals are in stars and significantly fewer in NSF gas, but the metallicities of stars, SF gas, dense NSF gas, and ICM are in fact not very different. The absence of feedback has a major effect on the metallicity of the IGM (low $T$ and low $\rho$ NSF gas) and the WHIM (hot, NSF gas), decreasing their metallicities by 2 and 1 orders of magnitude, respectively. Without galactic winds, metals are not efficiently transported to the lower densities of the diffuse IGM or WHIM. A careful census of the IGM metallicity, and its evolution, is therefore a powerful probe of the properties of galactic winds through the ages. Although the metallicity of the WHIM is much lower in the simulation without winds, the fraction of metals in the WHIM is also lower (see the temperature PDF in the top panel). Indeed, the fraction of gas in the WHIM phase at $z = 2$ decreases from $\approx 15$ per cent in the REFERENCE model to $\approx 6$ per cent in the NOSN_NOZCOOL model shocks from winds are responsible for increasing the fraction of baryons in the WHIM significantly. This contrasts with the results of Davé et al. (2001), who concluded from their suite of simulations that winds had little effect on WHIM properties. The lower WHIM fraction and its lower metallicity, in simulations without winds, make the predicted emission of the WHIM in UV and X-ray lines orders of magnitude less, as compared to the REFERENCE model (Bertone et al. 2010a,b).

Somewhat surprisingly, the ICM *metallicity* is not strongly affected by the presence or absence of winds, so how *do* metals get into the ICM? In the REFERENCE simulations winds are launched near sites of star formation. Therefore elements produced soon after star formation, such as the $\alpha$-enhanced elements synthesised in type II SNe, will be preferentially blown away by winds, whereas elements from type Ia SNe, that are produced much later on, will not. Comparing the iron distribution with that of $\alpha$-elements might thus help us to understand the importance of enrichment by winds. We have tracked the iron produced by type Ia SNe separately, and plot in figure 4.9 the fraction of iron that is due to type Ia SNe. Nearly 65 per cent of the ICM's iron is produced by type Ia SNe, as opposed to $< 50$ per cent in other phases. This suggests once more that in the ICM, winds are not the only mechanism contributing to the enrichment.

The impact of metal-line cooling and winds on the ratio of $\alpha$-elements to iron, as quantified by [O/Fe] is shown in figure 4.10. In the REFERENCE simulation, [O/Fe] decreases from $\approx 0.7$ to $\approx 0.45$ in most phases between $z = 6$ and $z = 0$; it is supersolar in all phases at all times. Note that Thomas et al. (2007) found values of [O/Fe]$\approx 0$ to 0.5 for local SDSS elliptical galaxies. Since a significant fraction of the stellar mass today is in elliptical galaxies, this suggests that the [O/Fe] values may not be unreasonable.

While uncertainties in the stellar yields and type Ia supernova rates make a detailed analysis of [O/Fe] troublesome, we can nonetheless use this ratio as a diagnostic tool. metal-line cooling has little effect on [O/Fe], but feedback from winds has a large effect, particularly for the IGM, WHIM, and ICM, where [O/Fe] is lower by $\approx 0.2 - 0.6$ dex without winds. Since our wind feedback is coupled to star formation, winds are especially good at transporting freshly synthesised $\alpha$ elements away from star-forming regions, but have clearly has much less impact on elements such as Fe which are also produced in significant quantities at later stages. In support of our postulate of a non-wind component to ICM enrichment, we note that for the REFERENCE simulation [O/Fe] is lowest (compared to the other phases) in the hot gas, indicating that older populations contribute to the metals in this phase.

There is some tension with the results of Oppenheimer & Davé (2008) who find WHIM metallicities of roughly $1\ \%$ solar in their model *with feedback* (as compared to our value of $10\ \%$ solar). Their metallicity is quoted in terms of [O/H] and we suspect that much of the difference lies in the different amount of oxygen and iron produced. Both Oppenheimer & Davé (2008) and Tornatore et al. (2009) have published the evolution of [O/Fe] in their models. If we compare our results with theirs, we notice that all three works arrive at very different values for [O/Fe], both at early and late times. On the other hand, all three of these investigations predict a similar shape for the evolution of [O/Fe], with the stars and the dense gas experiencing a drop of 0.2 dex from $z = 2$ to $z = 0$. Especially the differences between the models at high $z$ indicates suggest that the stellar evolution may be causing the difference.

Oppenheimer & Davé (2008) use the SNII yields of Limongi & Chieffi (2005), which span a mass range of $10\ \mathrm{M}_{\odot}$ to $35\ \mathrm{M}_{\odot}$, for the progenitor masses. These yields are averaged over this range to calculate the oxygen produced, which is extrapolated to the remaining SNII (from $35\mathrm{M}_{\odot}$ to $100\mathrm{M}_{\odot}$). Our yields already have slightly higher oxygen production for similar masses, but Portinari et al. (1998) found that oxygen production increases with mass. We therefore expect our simulations to predict higher Oxygen abundances than those of Oppenheimer & Davé (2008).

Tornatore et al. (2009) use the SNII yields of Woosley & Weaver (1995), which, like Limongi & Chieffi (2005), have values for $10\ \mathrm{M}_{\odot}$ to $35\ \mathrm{M}_{\odot}$, They thus miss the ejection of oxygen in the winds of high mass stars. In addition to yield uncertainties, there are also large uncertainties in the SNIa rates. Our adopted SNIa rate passes through the newer (lower) measurements of the cosmic SNIa rate, meaning that our iron from SNIa is likely to be lower than that of both authors. Such lower rates then also suggest a lower net production of iron, increasing our [O/Fe] above that of the other authors. In the end we stress that we use [O/Fe] merely as a diagnostic, since precise predictions of abundance ratios are impossible considering the uncertainties in the yields and the SNIa rate. Indeed, one could consider revising the yields based on a comparison of the predicted ratios with observations.

In summary, feedback from supernovae is essential for enriching the gas outside of haloes. Metal-line cooling, on the other hand, allows the cold phases for the non-star-forming gas to be enriched. The metallicity of the present day very hot gas is roughly $10\ \%$ solar and surprisingly insensitive to the presence of feedback. This implies a minimum metallicity for the ICM, and a non-feedback related enrichment component.

### 4.3.3 Wind Models

We have considered simply the effect of turning off feedback, but only in the context of a single feedback recipe. There are, however, a multitude of methods of implementing supernova feedback into simulations. We therefore exploit the power of the OWLS

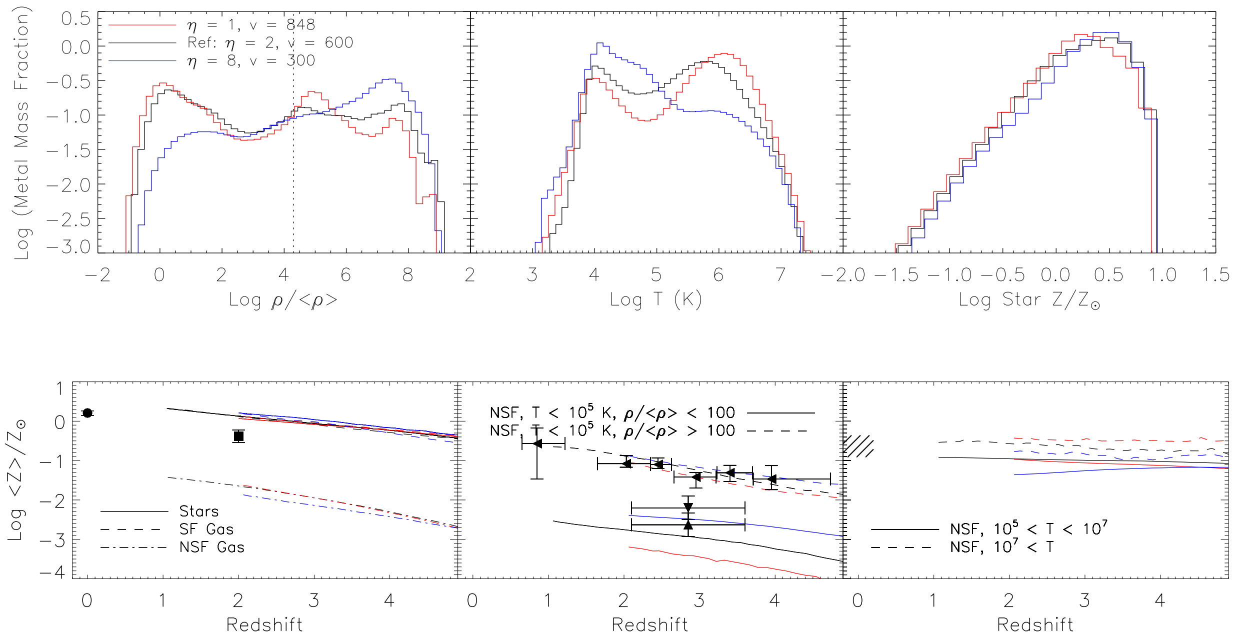

**Figure 4.11**: As figure 4.8, but for L025N512 simulations with different values for the mass loading, $\eta$, and wind speed, $v_w$. The metal mass weighted PDFs (top row) are for $z = 2$. Compared are the REFERENCE simulation ($\eta = 2$, $v_w = 600\ \mathrm{km\,s^{-1}}$; black), a simulation using a mass-loading of 1 ($\eta = 1$, $v_w = 848\ \mathrm{km\,s^{-1}}$; red), and a simulation using a mass-loading of 8 ($\eta = 8$, $v_w = 300\ \mathrm{km\,s^{-1}}$; blue) The density and temperature distributions of metals are strongly dependent on $\eta$. While the choice of $\eta$ has little effect on stellar metallicities, or those of SF gas, the metallicity of the IGM is significantly affected.

project and investigate a number of feedback recipes. We will show that the metallicity of the IGM is particularly sensitive to feedback implementation - some models are quite capable of enriching such low density gas, while others cannot. On the other hand, the metallicities of the stars and the star-forming gas are largely robust to differences in the wind model. The ICM and WHIM maintain a relatively constant metallicity with redshift if the feedback recipe is varied.

Winds in most of the simulations comprising the OWLS suite are characterised by two parameters: the mass loading factor, $\eta$, and the wind speed, $v_w$ (Dalla Vecchia & Schaye 2008; equation 4.3). All models shown in figure 4.11 use the same value of the product $\eta\, v_w^2$, hence assume that the same fraction of core collapse SN energy is used to power winds. The wind speed sets an approximate maximum depth of the potential well out of which the wind can push baryons: star formation will no longer be quenched significantly in a galaxy for which wind particles cannot escape. Note that since there are drag forces acting against the wind, the relationship between the wind speed and the potential well of the halo is non-trivial (see Dalla Vecchia & Schaye 2008). This parametrisation of winds is still very simple with little physical motivation: currently wind simulations should be guided by observations. Unfortunately determining the mass loading, and even relating observed wind speeds to $v_w$, has proven to be very problematic. For a complete description of the method and further motivation

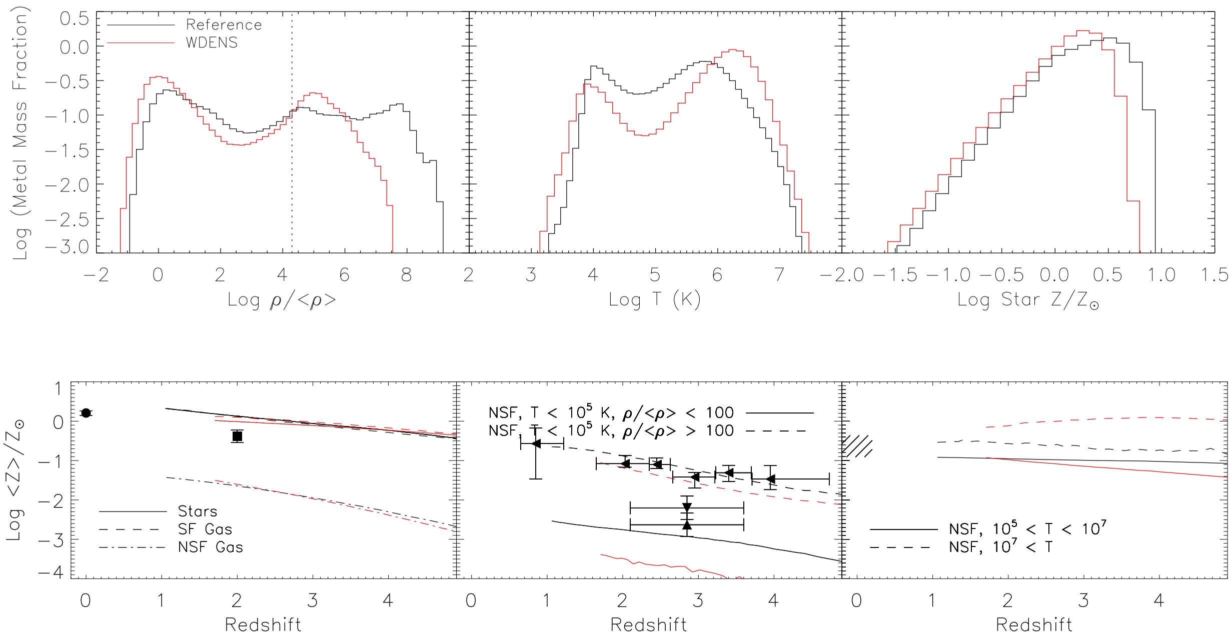

**Figure 4.12**: As figure 4.8, but for L025N512 simulations comparing the REFERENCE simulation (black) to model WDENS (red) in which wind speed is proportional to the local sound speed (equation 4.5). The metal mass weighted PDFs are for $z = 2$. The metallicities of both stars and SF gas are similar between these models, but low density gas is significantly *more* enriched in the WDENS model; the metallicity of the cold IGM though is lower in the WDENS model. The higher wind speeds in higher mass galaxies allow metals to escape from more massive galaxies in the WDENS models: this raises the ICM metallicity by a factor of a few. The WHIM metallicity is slightly lower initially, but becomes comparable to that of the constant wind model by $z \approx 3$.

see Dalla Vecchia & Schaye (2008).

At high $z$, when most stars form in low mass galaxies, even a low value of $v_w$ is enough for the gas to escape from most galaxies. For constant $\eta v_w^2$, a low wind speed implies high mass loading, and star formation is strongly suppressed early on. Metals are then very efficiently transported out of the galaxies, and end up predominantly in the cold NSF gas, since the wind velocities are low enough that strong shocks do not occur. However as time progresses, a low wind speed model can no longer suppress star formation in the increasingly more massive galaxies. The metals that are produced can no longer escape from the haloes and remain in the SF gas. For higher values of $v_w$ metals can escape from typical star-forming galaxies up to far lower $z$, ending-up in hotter gas because the winds get shocked to higher temperatures.

The dependence of the metal distribution on the wind speed and mass loading for $z = 2$ is shown in the top row of figure 4.11. As expected, a higher $v_w$ results in a larger fraction of metals at lower density and higher temperature. Conversely, low $v_w$ models have a considerably larger fraction of their metals at high density, and low $T \approx 10^4$ K. The low mass-loading model shows a peak in the density distribution of the metal mass just above the star formation threshold (vertical dotted line) that is similar to reference model, indicating that the location of this peak is not set by the wind

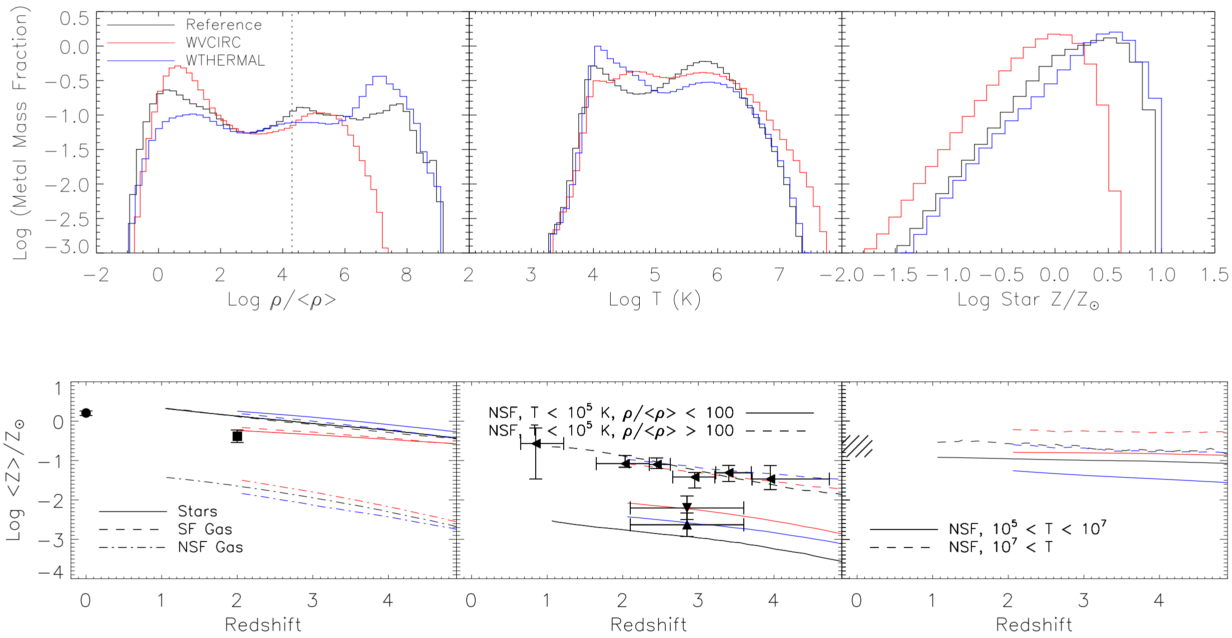

**Figure 4.13**: As figure 4.8, but for L025N512 simulations, comparing the REFERENCE simulation (black) to model WVCIRC (red), in which wind speed depends on the depth of the potential well (equation 4.6), and model WTHERMAL in which SN energy is injected thermally (blue). The metal mass weighted PDFs are for $z = 2$. The WVCIRC model is able to evacuate metals from high density regions, while at the same time, spreading the metals among a variety of temperatures. The WTHERMAL model differs less dramatically from the REFERENCE model, with *more* metals ending up in high density regions. These three models differ considerably in metallicity evolution in several phases, most notably in the IGM and WHIM; stellar metallicities are lowered in the WVCIRC model.

velocity (although the width and the height certainly are). There is another small peak at $\rho \approx 10^{7.5}\langle\rho\rangle$ in the metal-mass weighted density PDF of the low mass-loading model, which may be due to the largest haloes which have such high ISM pressures that even these high-velocity winds are quenched. The metal mass distributions in temperature show how higher wind velocities lead to more metals in hotter gas, due to metals in winds getting shocked to higher temperatures. A large portion of metals that are at $T \approx 10^5$ K in the REFERENCE model are heated to $\gtrsim 10^6$ K for $v_w = 848\ \mathrm{km\,s^{-1}}$. The stellar metal mass PDF is affected little by $v_w$.

While the distribution of the metals depends very strongly on the wind model, there is no significant difference in the *metallicity* between models with different $v_w$, with the exception of that of the IGM. In particular, the stellar and SF gas abundances are very little affected by the value of $v_w$.

The IGM metallicity in the high mass loading ($\eta = 8$) model is about an order of magnitude higher than in the REFERENCE ($\eta = 2$) model, despite the fact that a much smaller fraction of the metal mass resides at densities $\rho < 10^2\ \langle\rho\rangle$ for ($\eta = 8$). the increase in the metallicity of the IGM (which has $T < 10^5$ K by definition) with decreasing $v_w$ must therefore be due to a decrease in the temperature of the enriched low density gas. This wind implementation mostly moves gas together with its associated metals, which is why metallicity varies much less with $v_w$ than metal mass fraction does. However, this is of course not true for the diffuse IGM which was already in place: for this phase high wind speed models heat a significant fraction of the metals as the winds shock, and hence the metallicity of the cold IGM is lower than for a lower wind speed model. The metallicities of both the WHIM and the ICM remain strikingly constant with time at $\approx -1$ and $\approx -0.5$, respectively, all the way from $z = 6$ to $z = 1$ and, as shown in figure 4.8, even to $z = 0$. These values are clearly relatively robust with respect to the wind implementation.

In figure 4.11 the models are compared to the same data as was shown in figure 4.8; note that there may be significant biases in comparing these directly to the simulation. As remarked above, variations in $\eta$ have little effect on stellar metallicities (figure 4.11, top left panel); and the simulated values may be high compared to the $z = 2$ stellar metallicity of Halliday et al. (2008). The simulated cold but dense NSF gas has a similar metallicity as DLAs (Prochaska et al. 2003), again with $\eta$ having little effect. The IGM metallicity is sensitive to $\eta$, with the high mass loading $\eta = 8$ giving better agreement with the value inferred for oxygen by Aguirre et al. (2008), and well within the uncertainties of the Schaye et al. (2003) value for carbon. This is because most of the metals in the simulated IGM are ejected by small galaxies (see chapter 5): even low wind speeds can lift gas out of their potential wells, and a large mass loading then enriches the low-density IGM much more efficiently.

The simulations of Davé & Oppenheimer (2007) yield 'WHIM' (identified as shocked IGM, their figure 1) metallicities of $\log(Z/Z_\odot) \approx -1.8$ and $-1.4$ at redshifts $z = 2$ and 0, respectively (after converting to our solar abundances), significantly lower than our value of $\approx -1$ at all $z$, commenting that feedback strength may regulate the WHIM's metallicity. The wind models discussed so far have constant feedback energy, $\eta\, v_w^2 = \mathrm{constant}$, and we find that the WHIM metallicity is largely independent of $v_w$ (figure 4.11). We will show shortly that variable feedback energy also has little effect on the WHIM metallicity.

In the WDENS model, the fraction $\epsilon_{\rm SN} \propto \eta\, v_w^2$ (equation 4.3) of supernova energy that powers the wind is still kept fixed, but the values of $\eta$ and $v_w$ depend on the local sound speed, $c_s$. Since star-forming gas is on an imposed $p - \rho$ relation (equation 4.1), $c_s^2 = p/\rho \propto \rho^{\gamma_{\rm eff}-1} \propto \rho^{1/3}$, for our assumed value of $\gamma_{\rm eff} = 4/3$. The assumed wind parameters then correspond to a density dependence as

$$v_{\rm w} = v_0 \left(\frac{\rho}{\rho_{\rm crit}}\right)^{1/6} \text{and} \tag{4.4}$$

$$\eta = \eta_0 \left(\frac{\rho}{\rho_{\rm crit}}\right)^{-2/6} \tag{4.5}$$

where $\rho_{\rm crit}$ is the star formation threshold density. We chose $v_0 = 600\ \mathrm{km\,s^{-1}}$ and $\eta_0 = 2$, so that the wind parameters are the same as in the REFERENCE model at the star formation threshold. Such winds will remain efficient in regulating star formation for denser gas at the bottom of deeper potential wells, where the winds will have higher $v_w$.

The metal mass distribution in gas density and stellar metallicity (figure 4.12) confirm that the WDENS model is indeed able to reduce the build up of high density and high metallicity metals. The high density tail is truncated at $\rho/\langle\rho\rangle \approx 10^7$, resulting in a larger fraction of metals just above the star formation threshold. The metal mass weighted temperature PDF behaves as the high wind velocity model in figure 4.11: the higher wind speeds result in a larger fraction of metals at $T \gtrsim 10^6$ K due to winds getting shocked. With fewer metals in high-density SF gas, stellar metallicities are on average $\approx 0.1$ dex lower than in the REFERENCE model. The ICM is enriched to higher levels at nearly solar, with little evolution. The enrichment of the cold IGM is notably less advanced than in the REFERENCE model, with a metallicity nearly 1 dex lower.

This model is unable to achieve high metallicities in the cold IGM because it shock heats more of the escaping metals to temperatures for which the cooling time is long. In general, this model behaves like the $\eta = 1$ simulation shown in figure 4.11 at early times. Winds in the reference model do not have such high velocities and therefore the IGM metallicity is higher.

Although we stated in section 4.3.2 that the ICM metallicity is not shaped solely by feedback, we find that very efficient winds are able to further enrich the ICM, presumably since they can have very high wind velocities that give strong shocks and hence convert enriched winds into ICM (but note that our definition of ICM includes hot gas with densities much below that of the true intracluster medium).

In model WDENS the wind speed scales with the local sound speed to obtain efficient feedback in small galaxies at early times as well as in more massive haloes at later times. An alternative method to obtain a similar behaviour makes the wind speed depend directly on the depth of the potential well, as in the model discussed by Oppenheimer & Davé (2008), which is meant to mimic a case where the wind is driven by radiation pressure. Such a wind is implemented in our WVCIRC model as follows: an on-the-fly group finding algorithm is used to identify haloes, and the escape velocity, $v_{\rm circ}$, from the halo is estimated for each star particle within that halo. The wind speed $v_w$, then depends on $v_{\rm circ}$ as

$$v_{\rm w} = \frac{(3+\eta_0)}{\sqrt{2}} v_{\rm circ} \text{ and} \tag{4.6}$$

$$\eta = \frac{v_{\rm crit}/v_{\rm circ}}{\sqrt{2}}. \tag{4.7}$$

Here, $v_{\rm circ} = \sqrt{\frac{GM}{r}}$ is the circular velocity, and $v_{\rm crit} = 150\ {\rm km\,s^{-1}}$ and $\eta_0 = 2$ (note that Oppenheimer & Davé (2008) use the velocity dispersion of their groups instead of the circular velocity). In this model the effective value of $\epsilon_{SN}$ is no longer held constant, as the momentum carried by the wind is kept fixed instead.

In figure 4.13 we also show results from another model, WTHERMAL, discussed in Schaye et al. (2010) and Dalla Vecchia and Schaye (in prep.), in which the SN energy is deposited locally as *thermal* energy, instead of kinetic energy. As star formation occurs in high density regions that cool efficiently, such a feedback mechanism may be very inefficient if the multi-phase nature of the ISM is not resolved (e.g. Katz 1992). The implementation of thermal feedback avoids the cooling problem by giving the energy to only a few particles so that they can be heated to high enough temperatures that the cooling time is long (see also Theuns et al. 2002).

The WVCIRC model transports significantly more metals to lower densities (figure 4.13), leading to metals being locked up at lower stellar metallicities, similar to WDENS (figure 4.13). However the temperature distribution of the metals in this model is quite different from that of WDENS with a much smaller fraction of metals at $\approx 10^6$ K and a much larger fraction at $\approx 10^5$ K. The thermal feedback model WTHERMAL continues this trend with even less metals at $\approx 10^6$ K and more at $T \lesssim 10^5$ K. It also has less metals at low densities, but significantly more at high densities $\rho \gtrsim 10^6 \langle\rho\rangle$.

The metallicity evolution of these models are plotted in the bottom panel of figure 4.13. WVCIRC predicts the highest metallicities for the low-density components. In particular, the metallicity of the diffuse IGM is up to an order of magnitude higher than for the reference model. Stellar metallicities, on the other hand, are a factor of $\approx 2$ lower by $z \approx 2$. The high mass loading factors used in small galaxies and the extra wind energy in massive galaxies clearly result in more efficient metal transport from galaxies to the IGM. In addition, the low wind velocities in low-mass galaxies ensure that the metals are shocked to lower temperatures than for high-mass galaxies.

Compared to the REFERENCE model, model WTHERMAL predicts slightly higher stellar metallicities and slightly lower metallicities for the low-density phases. The exception is the cold IGM, whose metallicity is a factor of two higher. Apparently, the decrease in the temperature of wind-shocked gas is more important for this phase than the reduction of the fraction of the metals that reside in low-density gas. It is interesting that a model that heats metals (recall that the wind energy is injected directly in thermal form) in the end results in more metals in a cold phase.

Despite the fact that WVCIRC uses a wind recipe that is very similar to that of Oppenheimer & Davé (2008), we do not get a present day WHIM metallicity as low as $\approx 10^{-1.8} Z_\odot$ as they do (see section 4.2.1 of their paper). As noted before, their value is quoted in terms of the oxygen abundance which, due to a different choice in yields may correspond to a somewhat different value for the mean metallicity. On the other hand, a difference of an order of magnitude seems unlikely to be made up by such a discrepancy. Their simulations differ from ours in four other important respects: they do not use smoothed metallicities, their cooling routine neglects the effect of photoionization on the metal-line cooling, they decouple their winds hydrodynamically for a short period, and their feedback is not local to particular star-forming particles. The latter two points are holdovers from the original Springel & Hernquist (2003) GADGET model. This figure shows the 'particle' metallicity[7], thus any effect of using smoothed metallicities would have to be in the form of metal smoothing feeding back into the simulation (perhaps in the form of cooling). It is possible that the simulations of Oppenheimer & Davé (2008) experience over-cooling due to the assumption of collisional ionization equilibrium for the metals. Indeed, as shown in chapter 2, these temperatures and densities are precisely where such an effect would be seen (although in figure 4.8 indicates

---

[7] When averaged over the entire WHIM the difference between the smoothed and particle metallicities is nominal

that cooling likely does not play an major role in shaping the WHIM metallicity). We have checked the effect of decoupling the winds for the reference parameters, and find it increases the WHIM metallicity since the winds are going 'full-speed' when they reach the hot galactic corona[8] and shock the gas to higher temperatures. However, WVCIRC uses lower wind velocities and hence decoupling may primarily increase the metallicity of the cold IGM. We doubt that the locality of the wind plays a dominant role since star-forming particles should be well enriched. The simulations differ in other ways - star formation law, ISM physics, etc. - all of which could play some role.

In summary, the details of the wind implementation have a large impact on the metal census in the OWLS simulation suite. Metallicities are somewhat more independent of the wind model than the fraction of metals in various phases, with the metallicity of stars and SF gas especially robust, and also the WHIM and ICM metallicities varying by less than $\approx 0.3$ dex between most models. In all models, the ICM and WHIM metallicity are nearly independent of redshift. The IGM metallicity varies most between models, with both WML8V300, WVCIRC and WTHERMAL yielding metallicities close to the measurements of Schaye et al. (2003). Most models give stellar metallicities which may be slightly high compared to the data from Gallazzi et al. (2008) and Halliday et al. (2008), and cold halo gas abundances similar to those derived from DLAs (Prochaska et al. 2003). The temperature distribution of the metals also varies significantly between models, with higher wind velocities resulting in hotter metals It would be worthwhile to analyse the gas abundances in the simulations in a way which mimics the observational determinations in more detail.

### 4.3.4 Active Galactic Nuclei

Feedback from accreting black holes in Active Galactic Nuclei (AGN) has been invoked to reproduce the observed black hole scaling relations, the break in the galaxy luminosity function, the thermodynamic properties of groups of galaxies, to suppress star formation in massive galaxies at low $z$ allowing them to become 'red and dead', and also to quench cluster cooling flows (e.g. Silk & Rees 1998; Tamura et al. 2001; Kauffmann & Haehnelt 2000; Cattaneo 2001; Benson et al. 2003; Granato et al. 2004; Di Matteo et al. 2005; Springel et al. 2005; Bower et al. 2006; Croton et al. 2006; Lagos et al. 2008; Booth & Schaye 2009, 2010; McCarthy et al. 2010).

Our models for black hole formation and the associated AGN feedback which are modified versions of the model of Springel et al. (2005) are fully described in Booth & Schaye (2009) and we summarise it here. We seed groups with central black holes when contain 100 dark matter particles. The black holes are allowed to grow by mergers and gas accretion and the ambient gas is heated to a very high temperature at a rate proportional to the accretion rate. If a black hole is accreting at a low rate, the heat is saved up to ensure a particle is able to be heated completely (to ensure the heat is not radiated away before it is converted into kinetic form). This model reproduces

---

[8] This is an important point - the use of decoupled winds causes an underestimation of the amount of feedback needed to enrich these phases.

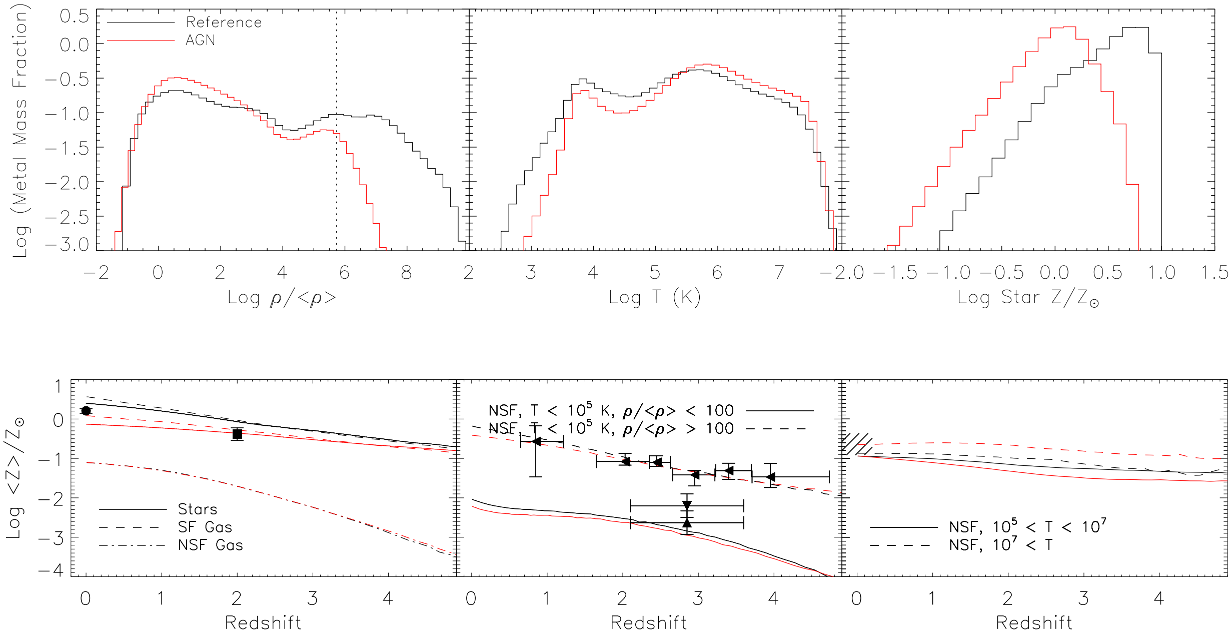

**Figure 4.14**: As figure 4.8, but for L100N512 simulations comparing the REFERENCE simulation (black) to model AGN(red) which incorporates feedback from AGN. The metal mass weighted PDFs are for $z = 0$. The AGN model is also able to evacuate metals from the high-density regions while decreasing the metallicity of stars at $z = 0$ by $\approx 0.5$ dex. The metallicities of most of the other phases remains largely unchanged with the exception of the hottest phase whose metallicity increases by a factor of two.

the Magorrian et al. (1998) relation, as well as the other observed black hole scaling relations.

In the top panel of figure 4.14 we show the distribution of metals at $z = 0$ for the AGN model. AGN feedback is able to remove metals from high-density regions and transport them outside haloes (i.e., $\rho < 200 \langle\rho\rangle$), all the while heating them to high temperatures. The peak of the stellar metallicity distribution is that lowered by almost a factor of 10.

The metallicity evolution reveals some interesting features (bottom panel of figure 4.14). Since there are less metals in the star-forming regions, it is not surprising that the AGN model has lower stellar metallicities as well, bringing this model more in line with the observed values.. However the WHIM's metallicity is also reduced, notwithstanding the much larger fraction of metals in the WHIM (as seen in the temperature PDF). Including AGN feedback (as implemented here) therefore increases the fraction of baryons in the WHIM by a large amount.

## 4.3.5 Stellar Initial Mass Function

We now consider the effect of changing the IMF on the cosmic metal distribution. We will show that employing a much flatter IMF in high pressure regions affects mainly the stellar metallicity, leaving the other phases mostly unchanged. This is mostly a

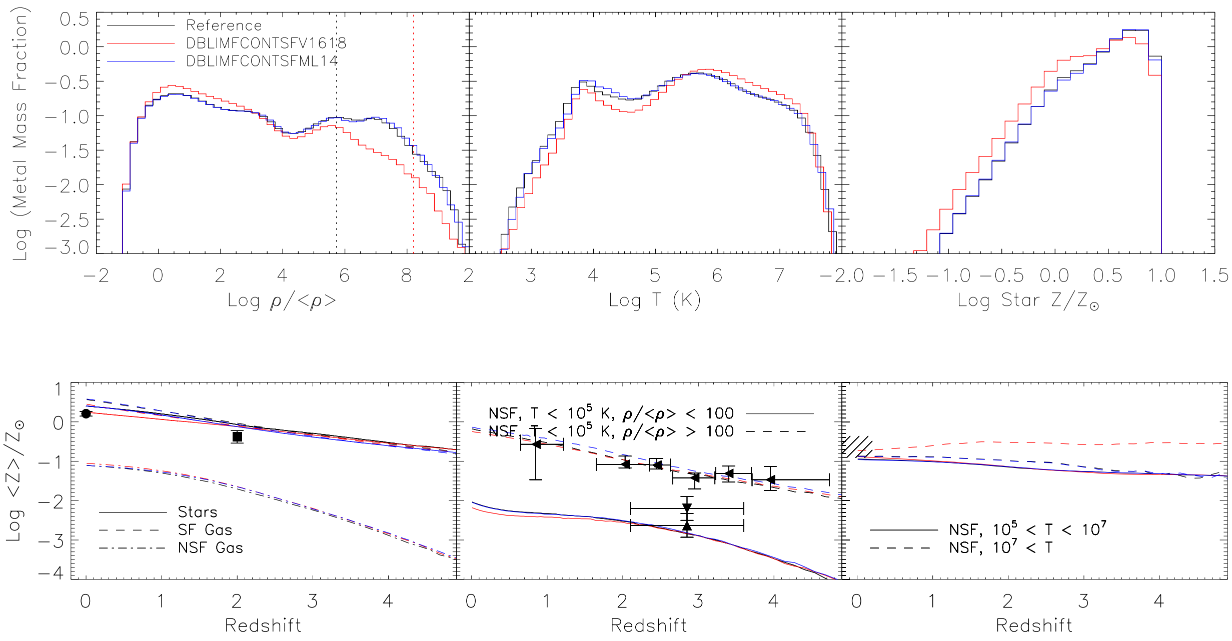

**Figure 4.15**: As figure 4.8, but for L100N512 simulations comparing the REFERENCE simulation (black), with two models with a top-heavy IMF at high-pressure; one in which the extra wind energy is used to increase the wind velocity ($v_w = 1618 \text{ km s}^{-1}$, DBLIMFCONTSFV1618, red), and one in which the extra wind energy is used to increase the mass loading ($\eta = 14$, DBLIMFCONTSFML14, blue). The metal mass weighted PDFs here are for $z = 0$. The black dotted line indicates the star formation threshold as before, and the red dotted line indicates the densities above which the top-heavy IMF is used. Using such an IMF has little effect unless the wind energy is used to increase the wind velocity.

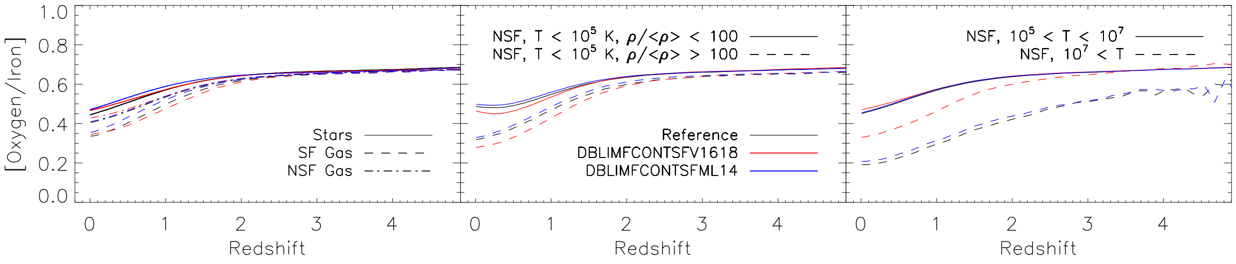

**Figure 4.16**: Evolution of [O/Fe] for different phases: the REFERENCE simulation (black), and two models with a top-heavy IMF at high-density, one where the extra supernova energy is used to increase the wind speed (DBLIMFCONSTV1618, red) and one where the extra supernova energy is used to increase the mass loading (DBLIMFCONSTML14, blue). This reinforces that the differences in figure 4.15 from the REFERENCE model are not due to enhancement of SNII products, but due to the added wind velocity.

result of the increased energy released from the supernovae which are more prevalent with a top-heavy IMF.

The IMF is the fraction of stars, $\Phi(M)\,dM$, born with mass $[M, M + dM]$. The low-mass tail of the IMF, which is thought to contain most of the mass, can only be probed very nearby, because low mass stars are faint. While slope in the low-mass end of the IMF does not have a strong effect on either the luminosity or the production rate of metals of a galaxy, it does affect the inferred stellar mass. In contrast, the high-mass end of the IMF has a big effect on both the luminosity and the metal production of a galaxy. The pioneering work of Salpeter (1955) described the IMF as a power-law,

$$\Phi(M) \equiv \frac{dN}{dM} \propto AM^{\alpha}\,. \tag{4.8}$$

A more recent fit by Chabrier (2003) is

$$M\Phi(M) = \left\{ \begin{array}{ll} Ae^{-(\log M - \log M_{\rm c})^2/2\sigma^2} & \text{if } M \leq 1\mathrm{M}_\odot \\ BM^{1+\alpha} & \text{if } M > 1\mathrm{M}_\odot \end{array} \right\}, \tag{4.9}$$

where $\alpha = -2.3$, $M_{\rm c} = 0.079$, $\sigma = 0.69$, and the coefficients $A$ and $B$ are set by requiring continuity at $1\ \mathrm{M}_\odot$, and by the normalization condition, $M \int \Phi(M)\,dM = 1\,\mathrm{M}_\odot$. Although the shape of the IMF above $1\ \mathrm{M}_\odot$ is very similar to Salpeter's, the lognormal decrease at the low mass end results in a much lower stellar mass-to-light ratio. For a recent review on the Milky Way's IMF see e.g. Kroupa (2002) or Chabrier (2003).

There is tentative observational evidence that the IMF in some environments is 'top-heavy' as compared to the solar neighbourhood, such as in intense star bursts (McCrady et al. 2003), or the inner parsec of the Galaxy (Maness et al. 2007). Models of galaxy formation hint that such a top-heavy IMF may be required to explain submm (Baugh et al. 2005) and Spitzer counts (Lacey et al. 2008), the metallicity in the ICM (Nagashima et al. 2005) and that of galaxies (De Lucia et al. 2004; Nagashima et al. 2005). Padoan et al. (1997) and Larson (2005) discuss theoretical motivations for environmental dependence and evolution of the IMF, see Lacey et al. (2008) for more discussion.

We have implemented an environment-dependent IMF in our simulations, labeled DBLIMF in Table 4.1, in which the IMF is changed from the Chabrier fit to become top-heavy, $\Phi(M) \propto M^{-1}$, above a density threshold of $n_{\rm H} = 30$ particles cm$^{-3}$ which corresponds to a pressure of $P/k = 2.0 \times 10^6 \mathrm{cm}^3\mathrm{K}$. Because the star formation rate density increases with pressure in this model the IMF becomes top-heavy in regions with high star formation densities, i.e. 'starbursts'.

A flat IMF will give an order of magnitude more high mass stars by number than a standard IMF. Such an increase should be accounted for in the supernova feedback. Our reference model has a mass-loading $\eta = 2$ with a wind velocity, $v = 600\ \mathrm{km\,s}^{-1}$. Assuming that each star with initial mass in the range $6 - 100\ \mathrm{M}_\odot$ injects $10^{51}\ \mathrm{erg}$ of kinetic energy, these parameters imply that the total wind energy accounts for 40 per cent of the available kinetic energy for a Chabrier IMF and a stellar mass range $0.1 - 100\ \mathrm{M}_\odot$ (if we consider only stars in the mass range $8 - 100\ \mathrm{M}_\odot$ for type II SNe, this works out to be 60 per cent). Given the relation (equation 4.3) between the supernova energy produced per unit mass in stars, $\epsilon_{\rm SN}$, and the wind parameters $\eta$ and $v_w$, a higher value of $\epsilon_{\rm SN}$ implies a higher value of $\eta\, v_w^2$. We explore two extremes, one uses a higher mass-loading but the standard wind speed, $(\eta = 14, v_w = 600~{\rm km\,s^{-1}})$, the other uses the standard mass loading but higher wind speed, $(\eta = 2, v_w = 1618~{\rm km\,s^{-1}})$; note that this change is only enacted above the density threshold for top-heavy star formation.

The change in IMF discussed here affects $\approx 10\%$ of the stars. For the sake of brevity, we restrict ourselves to the case in which the star formation law is continuous across the 'starburst' pressure threshold (see Schaye et al. 2010 for a full discussion of this point; see section 4.3.6 for the results of models in which this is not the case). We therefore plot the DBLIMFCONTSFV1618 $(\eta = 2, v_w = 1648~{\rm km\,s^{-1}})$ and DBLIMFCONTSFML14 $(\eta = 14, v_w = 600~{\rm km\,s^{-1}})$ models in figure 4.15. While the top-heavy IMF should increase the amount of metals produced in high density regions due to the enhanced fraction of high mass (high yield, short lifetime) stars, the increased feedback serves to move a lot of these metals to high temperatures and low densities, resulting in metals in stars of *lower* metallicity. Indeed, we see in the bottom panel lower mean stellar metallicities, and higher metallicities in the ICM. Channeling the extra feedback energy into a higher mass loading factor yields metallicities and metal mass distributions identical to that of the REFERENCE model.

The use of a top-heavy IMF in 'starbursts', as implemented in the DBLIMF models, has surprisingly little effect on the abundance of $\alpha$-enriched elements, produced by these massive stars (figure 4.16). The wind parameters determine to a large extent where the $\alpha$-enriched gas is deposited. When the wind speed is high, they are more effectively removed from the galaxy into the IGM, WHIM and ICM. For example, the ICM in the DBLIMFCONSTV1618 is $\approx 0.15$ dex more $\alpha$ enhanced at $z = 0$ compared to either the REFERENCE or the DBLIMFCONSTML14 models. Cold NSF gas, either diffuse IGM or cold halo gas, actually has a *lower* [O/Fe] ratio in model DBLIMFCONSTV1618: although the [O/Fe] of all metals is higher in this model, the $\alpha$-enhanced metals are deposited predominantly in the hot gas. A top-heavy IMF model with high mass loading has similar [O/Fe] as the REFERENCE model in all phases. This confirms that the differences between the REFERENCE model and the top-heavy IMF in starbursts models is driven not by the increased metal production, but the increased wind velocity.

Note that these models likely suffer from worse resolution issues than our REFERENCE model (see Schaye et al. 2010). In particular, the simulation needs to resolve densities above the starburst threshold. For lower resolution, this is more difficult in lower mass haloes.

In summary, models in which the IMF is changed to become top-heavy in star bursts have a higher value of $\epsilon_{\rm SN}$, the total supernova energy available to power winds per solar mass of star formed. It is this larger value of $\epsilon_{\rm SN}$ that to a large extent causes the differences in the metal distribution between models with a top-heavy IMF, and the REFERENCE model. If high values of $\epsilon_{\rm SN}$ are combined with an increase in wind speed, $v_w$, then the hot NSF gas becomes $\alpha$ enriched, up to 0.2 dex for the ICM at $z = 0$, with little change in [O/Fe] in stars, SF gas, or cold NSF gas. The higher $v_w$ models also result in around a factor 2 more metals in the hot NSF gas, but little change in its metallicity. This again implies that the *amount* of WHIM and ICM is higher in the model with a top-heavy IMF and associated higher wind speed, as compared to the REFERENCE model.

### 4.3.6 Other models

Although some processes can dramatically affect the cosmic metal distribution, we will see in figures 4.17 through 4.20 that there are a number of models that show little difference. It is remarkable that drastic changes in physical parameters and processes have such little affect on the metallicity and metal mass distribution. We briefly comment on each of the models that exhibit this behaviour.

**DBLIMFML14, DBLIMFV1618** - These models include a top-heavy IMF for densities over $n_{\rm H} = 30\,{\rm cm}^{-3}$. They are similar to the models we discussed in section 4.3.5, except that the star formation law is discontinuous across the 'starburst' threshold. Since no discontinuities in star formation density (as a function of gas density) have been observed, this model decreases the number of high-mass stars to produce a continuous UV flux as a function of density. These models show little difference to their DBLIMFCONTSF counterparts, though they are less effective at removing metals from the most dense regions.

**EOS1p0, EOS5o3** - In these models, the slope, $\gamma_{\rm eff}$, of the $p \propto \rho_{\rm eff}^{\gamma}$ relation imposed on star-forming gas, is changed from the value $\gamma_{\rm eff} = 4/3$ assumed in the REFERENCE model to 1 and 5/3, respectively. This change affects the density distribution of the ISM, and hence of the metals in the ISM and there is no significant effect on the metal distribution in other phases.

**IMFSALP, IMFSALPML1** - These models assume the Salpeter IMF , as opposed to the Chabrier IMF assumed in the REFERENCE model. The IMFSALPML1 model also has the mass loading of the wind model decreased in order to account for a different value of $\epsilon_{\rm SN}$ implied by a Salpeter IMF. The change in IMF results in a small increase of the fraction of metals in stars, but a decrease in stellar metallicity. The [O/Fe] ratio decreases in all phases, because the Salpeter IMF has a higher component of low mass stars which results in more type Ia SN, and thus more iron.

**MILL** - This model use the cosmological parameters of the Millennium simulation (Springel 2005), as opposed to the WMAP3 values. The most significant difference is the larger value of $\sigma_8$ in the MILL model, which implies that structure starts to form slightly earlier. This model has the wind mass loading increased ($\eta = 4, v_w = 600\ {\rm km\,s}^{-1}$) to match the peak of the cosmic star formation history (Schaye et al. 2010). Changing the cosmology has a large affect on the cosmic metal distribution, although the effect is dominated by the fact that structure forms earlier, shifting all of the curves in our REFERENCE simulations to higher redshift.

**NOAGB_NOSNIa** - In this model we have neglected the contribution of AGB and type Ia SNe to metal production and feedback. Compared to the REFERENCE model this has little effect on the distribution of metals and metallicity except that we find slightly fewer metals in cold, star-forming gas and lower stellar metallicities. In this model the abundance ratios evolve very little and reflect solely the SNII yields ([O/Fe]$\approx 0.7$ for all redshifts and phases).

**NOHeHEAT** - As discussed in section 4.2, we include some heating around $z \approx 3$ to account for the rise in the IGM temperature around the time of helium reionization. We have run a simulation with this turned off and have found no significant difference in the cosmic metal distribution by $z = 2$.

**NOREION, REIONZ06, REIONZ12** - We have also varied the reionization history of hydrogen in our simulations. Whereas the REFERENCE model assume HI reionization at $z_{\rm r} = 9$, these models have no reionization, $z_r = 6$ and $12$, respectively. We find that so long as the heating from reionization happens, the simulations have a very 'short' memory of their thermal history. If there is no heating from reionization, a large amount of the metals lie in cold gas.

**SFAMPLx3, SFAMPLx6, SFSLOPE1p75, SFTHRESZ** - In this set of models we vary the values of the normalisation, power-law index, and threshold gas density for star formation of the Kennicutt-Schmidt law (equation 4.2), with respect to those of the REFERENCE model. The first two models assume normalisations that are higher by factors of 3 and 6, respectively; the third model has a slope of 1.75 (as opposed to 1.4). In the last model the threshold for star formation is dependent on metallicity (see Schaye et al. 2010, for details). The cold halo phase is the most affected, increasing slightly in metallicity for the first 3 models and decreasing slightly for model SFTHRESZ.

**SNIaGAUS** - Given the large uncertainties in the normalisation and shape of the cosmic SNIa rate, we have run a model where it is based on a Gaussian delay function (rather than the e-folding delay function used in the REFERENCE model). This results in roughly the same number of SNIa, but they happen much later in the history of the universe. The evolution of the [O/Fe] ratio shows the expected differences (the dip to lower values occurring at lower redshift), but the overall distribution of metals and metallicity are nearly identical to the results for the REFERENCE model.

**WHYDRODEC** - Wind particles in our simulations are not decoupled, they interact hydrodynamically with their surroundings at all times. This model turns of this interaction and hence wind particles are hydrodynamically 'decoupled' as in the original Springel & Hernquist (2003) model. This modification has a significant effect, decreasing stellar metallicities and dramatically increasing the fraction of metals in, but not the metallicity of the WHIM. We have relegated this simulation to this overview due to space constraints, but it remains the most important variation of those listed in this section.

### 4.3.7 Summary

Figures 4.17 - 4.20 summarise our different models, comparing metal fractions and metallicities at redshifts $z = 0$ and $2$. We give observational estimates of metallicities to compare to, but we caution that these are only meant to give an idea as to what *reasonable* values correspond to, as the uncertainties are large. We have plotted the same set of observations as in figure 4.11 (i.e., stellar, $z = 2$ cold halo, and $z = 0$ ICM values).

At redshift $z = 0$, the models that stand out most in terms of the metal mass fractions are AGN, and NOSN, and NOSN_NOZCOOL (figure 4.17). The NOSN models

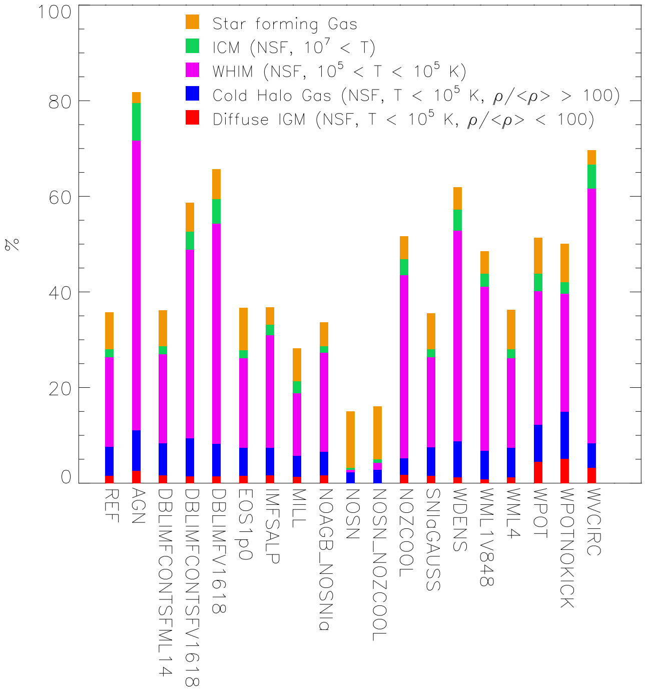

**Figure 4.17**: Fraction of metal mass in various phases for a selection of L100N512 models of the OWLS suite at $z = 0$. The orange, green, magenta, blue and red bars correspond to the metal mass fraction in star-forming gas, ICM, WHIM, cold halo gas, and diffuse IGM, respectively. The remainder of metals is locked up in stars. Metal fractions depend largely on the strength of feedback - models without feedback have very high stellar metal fractions, models with strong feedback do not.

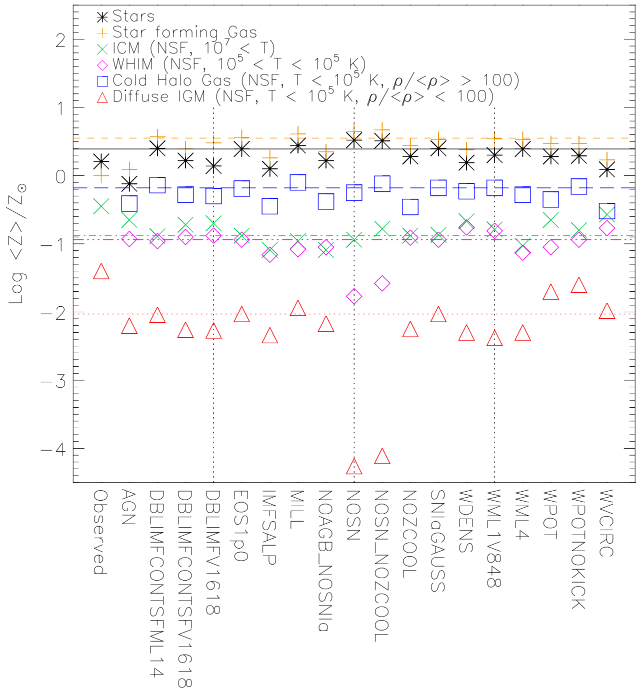

**Figure 4.18**: Metallicities of various phases for a selection of L100N512 models of the OWLS suite at $z = 0$ (colours correspond to the phases as in figure 4.17 - stars are added as black asterisks). The REFERENCE model is shown using horizontal lines: stars are shown in black solid, star-forming gas in orange dashed, ICM in green dot-dashed, WHIM in pink dot-dot-dot-dashed, cold halo gas in blue long dashed and diffuse IGM in red dotted. Observations shown are as follows: stars - Gallazzi et al. (2008) and ICM - Simionescu et al. (2009) with the rest coming from estimates compiled by Pagel (2008). The metallicities are surprisingly similar across most models, but models without feedback are clearly different.

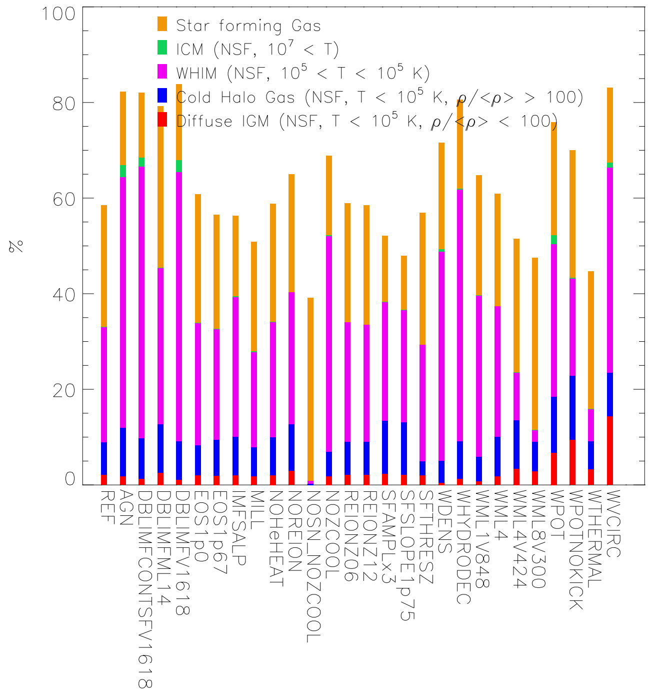

**Figure 4.19**: Fraction of metal mass in various phases for a selection of L025N512 models of the OWLS suite at $z = 2$ (colours correspond to the phases as in figure 4.18).

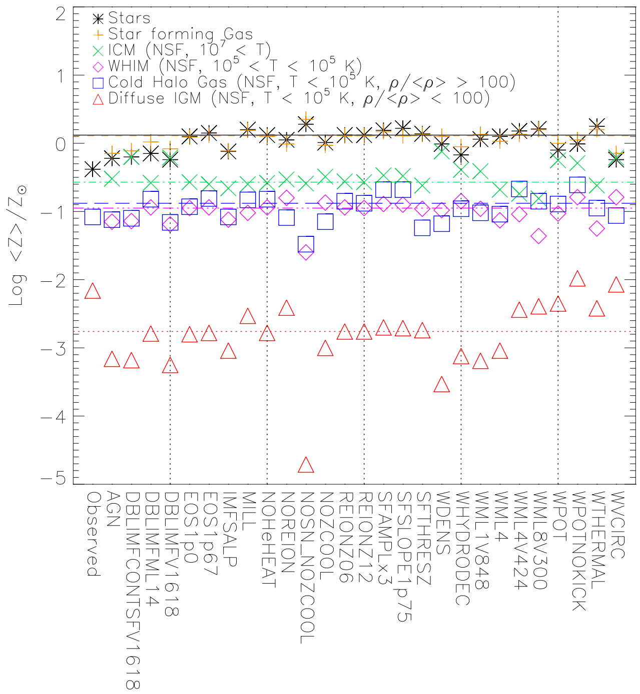

**Figure 4.20**: Metallicity of various phases for a selection of L025N512 models of the OWLS suite at $z = 2$ (colours and lines correspond to the phases as in figure 4.18). The horizontal lines show the REFERENCE model. Observations shown are as follows: stars - Halliday et al. (2008), cold halo gas - Prochaska et al. (2003), and diffuse IGM - Aguirre et al. (2008). The diffuse IGM shows the most variation among the different models.

(no energy feedback from SNe) have significantly more metals in stars, and also higher stellar and SF gas metallicities. Figure 4.18 shows that these models also stand out in terms of the low metallicity of their WHIM and diffuse IGM components. The variation between the other models is smaller, and they are mostly in reasonable agreement with the observations. Given that the stellar metallicities are probably the most reliable, the AGN model as well as the DBLIMF model with high wind speed (top-heavy IMF in bursts), and the WDENS model (where wind speed is scaled with the local sound speed), likely provide the best agreement. The models without feedback show the largest spread in metallicities, ranging from $[Z] \approx 0.4$ to $[Z] \approx -4.8$.

The data at $z = 2$ are more uncertain and more incomplete (figures 4.19 and 4.20). The same models stand out as at $z = 0$ (AGN and the no feedback models), although some other models also show an increasing difference in the fraction of metals that is in stars. For example the AGN, DBLIMFCONTSFV1618 (top-heavy IMF, high wind speed), WVCIRC ('momentum-driven' winds), and WDENS (wind speed scales with sound speed) models all have low stellar fractions. The spread in metallicities is small, within 0.3 dex for most models and most phases. The observed stellar metallicity is *low* compared to all models.

Models with more efficient feedback predict that a larger fraction of the metals resides in the WHIM, mostly at the expense of the metal fractions in stars and star-forming gas. Except for the models without any feedback, the different models predict similar metallicities for the different phases. The metallicity of the diffuse IGM is most sensitive to variations in the input physics.

## 4.4 CONCLUSIONS

We have investigated the distribution of metals predicted by simulations taken from the *O*verwhelmingly *L*arge *S*imulations project (OWLS). We considered different recipes and physical parameters in order to determine what the significant factors are that shape the distribution of metals as a function of the gas density, temperature, and metallicity. This builds on our previous work where we introduced our method and demonstrated the effect of simulation box size and resolution (chapter 3).

A common result runs through all our comparisons. This is that while the probability density functions and fractional distributions of metals can vary significantly, metallicity (when expressed on a log scale) varies little from model to model (although it does evolve significantly over the lifetime of the universe for some phases). This point is pertinent since the observations are measured on this scale and their errors (measurement uncertainties as well as physical variance) are often of order of 0.5 dex.

Our results can be divided between statements of how the physical processes affect the metal mass distribution and statements about the metal mass distribution itself as learned from varying the physics. The former can be summarised as follows:

- Metal-line cooling increases the fraction of the metals that reside in star-forming gas and stars, at the expense of the fraction in highly overdense warm-hot gas. Metal-line cooling increases the metallicities of all cold phases. In particular, it increases the metallicities of the diffuse IGM and cold, halo gas by about a factor of two.

- While there are other mechanisms which can enrich the warm-cold IGM (ram pressure stripping, mergers), without SN feedback, its metallicity is far smaller and is strongly ruled out by observations of QSO absorption lines.
- Processes other than outflows driven by feedback from star formation and AGN contribute significantly to the enrichment of the ICM.
- Even for a constant energy per unit stellar mass formed (i.e. a fixed efficiency), the freedom given by the parameters of sub-grid implementations of galactic winds is very large. At a fixed efficiency, higher wind velocities (and thus correspondingly low mass loading factors) increase the fraction of the metals that reside in low-density ($\rho < 10^2 \langle\rho\rangle$) gas. However, since higher wind velocities also shift metals to higher temperatures, the metallicity of the diffuse, warm-cold IGM is in fact higher for lower wind velocities.
- The metallicity of the warm-cold diffuse IGM is most sensitive to the implementation of galactic winds.
- By varying the parameters of the wind model with local properties, one can significantly affect the metal distribution in the IGM. For example, a model in which low-mass galaxies drive highly mass-loaded, slow winds while high-mass galaxies drive fast winds with low mass loading factors (e.g. Oppenheimer & Davé 2008) can efficiently enrich the diffuse warm-cold IGM while still limiting the build up of metals in the stellar components of more massive galaxies.
- Feedback from AGN strongly reduces the fractions of metals that reside in the ISM and stars as well as the metallicities of these two components. Fast galactic winds in massive galaxies, e.g. resulting from a top-heavy IMF at high gas pressures, work in the same direction but have a smaller effect than AGN. Efficient feedback in high-mass galaxies only has a relatively small effect on the metallicities of the diffuse gas components.
- Changes in the star formation law, the structure of the ISM, the reionization history, the cosmology, and the IMF all play a role, but are less important than the inclusion and implementation of metal-line cooling and, most importantly, outflows driven by feedback from star formation and accreting supermassive black holes.

We summarise the metal mass distribution as follows:

- Stars and the WHIM are the dominant depositories of metals. At high redshift the ISM also contains a large fraction of the metals. In all our models, and at both $z = 0$ and $z = 2$, the remaining components (diffuse cold-warm IGM, cold halo gas, and ICM) together contain less than a quarter of the metals.

- The mean metallicities of stars, WHIM, and ICM are nearly constant in time. In contrast, the metallicities of the cold halo gas and the diffuse IGM, increase by more than an order of magnitude from $z = 5$ to 0.

- All our models predict, both for $z = 0$ and 2, mean metallicities of $Z \approx Z_\odot$ for stars and ISM, and $10^{-1}\,Z_\odot \lesssim Z < Z_\odot$ for the ICM and for cold halo gas (the latter component has $Z \approx 10^{-0.3}\,Z_\odot$ at $z = 0$ and $Z \approx 10^{-1}\,Z_\odot$ at $z = 2$). Except for the models without SN feedback, all simulations predict, both for $z = 0$ and 2, mean metallicities of $Z \approx 10^{-1}\,Z_\odot$ for the WHIM and $10^{-3}\,Z_\odot \lesssim Z \lesssim 10^{-2}\,Z_\odot$ for the diffuse cold-warm IGM.

The inclusion and implementation of outflows driven by feedback from star formation and AGN is most important for predictions of the distribution of metals. As cosmological simulations will need to continue the use of sub-grid implementations of these processes for the foreseeable future, this implies that predicting the distribution of metals will remain difficult for ab initio models. However, as we have shown, provided that some feedback is included, the mean metallicities of many different components can be robustly predicted to order of magnitude.

The sensitivity of some of the results to the implementation of feedback can also be regarded as fortunate. It gives us a useful tool to study the effects of outflows, which are an essential but very poorly understood ingredient of models of galaxy formation and evolution. The enrichment of the diffuse warm-cold IGM, which can be constrained using QSO absorption lines, is particularly sensitive to variations in the models and is therefore a very promising probe of the physics of galactic outflows.

## REFERENCES

Abel T., Haehnelt M. G., 1999, ApJ, 520, L13

Aguirre A., Dow-Hygelund C., Schaye J., Theuns T., 2008, ApJ, 689, 851

Aguirre A., Hernquist L., Schaye J., Weinberg D. H., Katz N., Gardner J., 2001a, ApJ, 560, 599

Aguirre A., Hernquist L., Schaye J., Katz N., Weinberg D. H., Gardner J., 2001b, ApJ, 561, 521

Aguirre A., Schaye J., Hernquist L., Kay S., Springel V., Theuns T., 2005, ApJ, 620, L13

Ando M., Ohta K., Iwata I., Akiyama M., Aoki K., Tamura N., 2007, PASJ, 59, 717

Baugh C. M., 2006, Reports on Progress in Physics, 69, 3101

Baugh C. M., Lacey C. G., Frenk C. S., Granato G. L., Silva L., Bressan A., Benson A. J., Cole S., 2005, MNRAS, 356, 1191

Benson A. J., Bower R. G., Frenk C. S., Lacey C. G., Baugh C. M., Cole S., 2003, ApJ, 599, 38

Berczik P., 1999, A&A, 348, 371

Bertone S., De Lucia G., Thomas P. A., 2007, MNRAS, 379, 1143

Bertone S., Schaye J., Dalla Vecchia C., Booth C. M., Theuns T., Wiersma R. P. C., 2010a, arXiv:0910.5723

Bertone S., Schaye J., Dalla Vecchia C., Booth C. M., Theuns T., Wiersma R. P. C., 2010b, arXiv:1002.3393

Booth C. M., Schaye J., 2009, MNRAS, 398, 53

Booth C. M., Schaye J., 2010, arXiv:1005.0844

Booth C. M., Theuns T., 2007, MNRAS, 381, L89

Booth C. M., Theuns T., Okamoto T., 2007, MNRAS, 376, 1588

Bouché N., Lehnert M. D., Aguirre A., Péroux C., Bergeron J., 2007, MNRAS, 378, 525

Bower R. G., Benson A. J., Malbon R., Helly J. C., Frenk C. S., Baugh C. M., Cole S., Lacey C. G., 2006, MNRAS, 370, 645

Bower R. G., McCarthy I. G., Benson A. J., 2008, MNRAS, 390, 1399

Brüggen M., Kaiser C. R., 2002, Nature, 418, 301

Bryan G. L., Machacek M., Anninos P., Norman M. L., 1999, ApJ, 517, 13

Cattaneo A., 2001, MNRAS, 324, 128

Cattaneo A., Faber S. M., Binney J., Dekel A., Kormendy J., Mushotzky R., Babul A., Best P. N., Brüggen M., Fabian A. C., Frenk C. S., Khalatyan A., Netzer H., Mahdavi A., Silk J., Steinmetz M., Wisotzki L., 2009, Nature, 460, 213

Cen R., Ostriker J. P., 1999, ApJ, 519, L109

Cen R., Ostriker J. P., 2006, ApJ, 650, 560

Chabrier G., 2003, PASP, 115, 763

Churchill C. W., Kacprzak G. G., Steidel C. C., Evans J. L., 2007, ApJ, 661, 714

Cowie L. L., Songaila A., 1998, Nature, 394, 44

Crain R. A., Theuns T., Dalla Vecchia C., Eke V. R., Frenk C. S., Jenkins A., Kay S. T., Peacock J. A., Pearce F. R., Schaye J., Springel V., Thomas P. A., White S. D. M., Wiersma R. P. C., 2009, MNRAS, 399, 1773

Croton D. J., Springel V., White S. D. M., De Lucia G., Frenk C. S., Gao L., Jenkins A., Kauffmann G., Navarro J. F., Yoshida N., 2006, MNRAS, 365, 11

Dalla Vecchia C., Bower R. G., Theuns T., Balogh M. L., Mazzotta P., Frenk C. S., 2004, MNRAS, 355, 995

Dalla Vecchia C., Schaye J., 2008, MNRAS, 387, 1431

Davé R., Cen R., Ostriker J. P., Bryan G. L., Hernquist L., Katz N., Weinberg D. H., Norman M. L., O'Shea B., 2001, ApJ, 552, 473

Davé R., Oppenheimer B. D., 2007, MNRAS, 374, 427

De Lucia G., Kauffmann G., White S. D. M., 2004, MNRAS, 349, 1101

de Plaa J., Werner N., Bykov A. M., Kaastra J. S., Méndez M., Vink J., Bleeker J. A. M., Bonamente M., Peterson J. R., 2006, A&A, 452, 397

Dekel A., Silk J., 1986, ApJ, 303, 39

Di Matteo T., Colberg J., Springel V., Hernquist L., Sijacki D., 2008, ApJ, 676, 33

Di Matteo T., Springel V., Hernquist L., 2005, Nature, 433, 604

Dunne L., Eales S. A., Edmunds M. G., 2003, MNRAS, 341, 589

Ellison S. L., Songaila A., Schaye J., Pettini M., 2000, AJ, 120, 1175

Erb D. K., Shapley A. E., Pettini M., Steidel C. C., Reddy N. A., Adelberger K. L., 2006, ApJ, 644, 813

Ferland G. J., Korista K. T., Verner D. A., Ferguson J. W., Kingdon J. B., Verner E. M., 1998, PASP, 110, 761

Fukugita M., Hogan C. J., Peebles P. J. E., 1998, ApJ, 503, 518

Gallazzi A., Brinchmann J., Charlot S., White S. D. M., 2008, MNRAS, 383, 1439

Gnedin N. Y., 1998, MNRAS, 294, 407

Governato F., Willman B., Mayer L., Brooks A., Stinson G., Valenzuela O., Wadsley J., Quinn T., 2007, MNRAS, 374, 1479

Granato G. L., De Zotti G., Silva L., Bressan A., Danese L., 2004, ApJ, 600, 580

Haardt F., Madau P., 2001, in Neumann D. M., Tran J. T. V., eds, Clusters of Galaxies and the High Redshift Universe Observed in X-rays Modelling the UV/X-ray cosmic background with CUBA

Halliday C., Daddi E., Cimatti A., Kurk J., Renzini A., Mignoli M., Bolzonella M., Pozzetti L., Dickinson M., Zamorani G., Berta S., Franceschini A., Cassata P., Rodighiero G., Rosati P., 2008, A&A, 479, 417

Jarosik N., Bennett C. L., Dunkley J., et al., 2010, ArXiv e-prints

Jubelgas M., Springel V., Enßlin T., Pfrommer C., 2008, A&A, 481, 33

Katz N., 1992, ApJ, 391, 502

Kauffmann G., Haehnelt M., 2000, MNRAS, 311, 576

Kauffmann G., White S. D. M., Guiderdoni B., 1993, MNRAS, 264, 201

Kawata D., 2001, ApJ, 558, 598

Kawata D., Gibson B. K., 2003, MNRAS, 346, 135

Kennicutt Jr. R. C., 1998, ApJ, 498, 541

Kobayashi C., 2004, MNRAS, 347, 740

Kobayashi C., Springel V., White S. D. M., 2007, MNRAS, 376, 1465

Kobulnicky H. A., Zaritsky D., 1999, ApJ, 511, 118

Kroupa P., 2002, Science, 295, 82

Kunth D., Östlin G., 2000, A&A Rev., 10, 1

Lacey C. G., Baugh C. M., Frenk C. S., Silva L., Granato G. L., Bressan A., 2008, MNRAS, 385, 1155

Lagos C. D. P., Cora S. A., Padilla N. D., 2008, MNRAS, 388, 587

Larson R. B., 2005, MNRAS, 359, 211

Lia C., Portinari L., Carraro G., 2002, MNRAS, 330, 821

Limongi M., Chieffi A., 2005, in Turatto M., Benetti S., Zampieri L., Shea W., eds, 1604-2004: Supernovae as Cosmological Lighthouses Vol. 342 of Astronomical Society of the Pacific Conference Series, Presupernova Evolution and Explosive Nucleosynthesis of Massive Stars at Various Metallicities from Z=0 to Z=Zsun. pp 122–+

Magorrian J., Tremaine S., Richstone D., Bender R., Bower G., Dressler A., Faber S. M., Gebhardt K., Green R., Grillmair C., Kormendy J., Lauer T., 1998, AJ, 115, 2285

Maness H., Martins F., Trippe S., Genzel R., Graham J. R., Sheehy C., Salaris M., Gillessen S., Alexander T., Paumard T., Ott T., Abuter R., Eisenhauer F., 2007, ApJ, 669, 1024

Marigo P., 2001, A&A, 370, 194

McCarthy I. G., Schaye J., Ponman T. J., Bower R. G., Booth C. M., Vecchia C. D., Crain R. A., Springel V., Theuns T., Wiersma R. P. C., 2010, arXiv:0911.2641

McCrady N., Gilbert A. M., Graham J. R., 2003, ApJ, 596, 240

McNamara B. R., Wise M. W., Nulsen P. E. J., David L. P., Carilli C. L., Sarazin C. L., O'Dea C. P., Houck J., Donahue M., Baum S., Voit M., O'Connell R. W., Koekemoer A., 2001, ApJ, 562, L149

Mehlert D., Thomas D., Saglia R. P., Bender R., Wegner G., 2003, A&A, 407, 423

Mori M., Umemura M., 2006, Nature, 440, 644

Mosconi M. B., Tissera P. B., Lambas D. G., Cora S. A., 2001, MNRAS, 325, 34

Murray N., Quataert E., Thompson T. A., 2005, ApJ, 618, 569

Mushotzky R., Loewenstein M., Arnaud K. A., Tamura T., Fukazawa Y., Matsushita K., Kikuchi K., Hatsukade I., 1996, ApJ, 466, 686

Nagashima M., Lacey C. G., Baugh C. M., Frenk C. S., Cole S., 2005, MNRAS, 358, 1247

Nagashima M., Lacey C. G., Okamoto T., Baugh C. M., Frenk C. S., Cole S., 2005, MNRAS, 363, L31

Oppenheimer B. D., Davé R., 2006, MNRAS, 373, 1265

Oppenheimer B. D., Davé R., 2008, MNRAS, 387, 577

Padoan P., Nordlund A., Jones B. J. T., 1997, MNRAS, 288, 145

Pagel B. E. J., 2008, in Knapen J. H., Mahoney T. J., Vazdekis A., eds, Pathways Through an Eclectic Universe Vol. 390 of Astronomical Society of the Pacific Conference Series, Where Are the Missing Baryons and Metals?. pp 483–+

Pettini M., Smith L. J., Hunstead R. W., King D. L., 1994, ApJ, 426, 79

Portinari L., Chiosi C., Bressan A., 1998, A&A, 334, 505

Price P. A., Songaila A., Cowie L. L., Bell Burnell J., Berger E., Cucchiara A., Fox D. B., Hook I., Kulkarni S. R., Penprase B., Roth K. C., Schmidt B., 2007, ApJ, 663, L57

Prochaska J. X., Gawiser E., Wolfe A. M., Castro S., Djorgovski S. G., 2003, ApJL, 595, L9

Raiteri C. M., Villata M., Navarro J. F., 1996, A&A, 315, 105

Recchi S., Matteucci F., D'Ercole A., 2001, MNRAS, 322, 800

Ricotti M., Gnedin N. Y., Shull J. M., 2000, ApJ, 534, 41

Romeo A. D., Sommer-Larsen J., Portinari L., Antonuccio-Delogu V., 2006, MNRAS, 371, 548

Salpeter E. E., 1955, ApJ, 121, 161

Sato K., Tokoi K., Matsushita K., Ishisaki Y., Yamasaki N. Y., Ishida M., Ohashi T., 2007, ApJL, 667, L41

Scannapieco C., Tissera P. B., White S. D. M., Springel V., 2005, MNRAS, 364, 552

Scannapieco E., Pichon C., Aracil B., Petitjean P., Thacker R. J., Pogosyan D., Bergeron J., Couchman H. M. P., 2006, MNRAS, 365, 615

Schaye J., 2004, ApJ, 609, 667

Schaye J., Aguirre A., Kim T.-S., Theuns T., Rauch M., Sargent W. L. W., 2003, ApJ, 596, 768

Schaye J., Dalla Vecchia C., 2008, MNRAS, 383, 1210

Schaye J., Dalla Vecchia C., Booth C. M., Wiersma R. P. C., Theuns T., Haas M. R., Bertone S., Duffy A. R., McCarthy I. G., van de Voort F., 2010, MNRAS, 402, 1536

Schaye J., Rauch M., Sargent W. L. W., Kim T. S., 2000, ApJ, 541, L1

Schaye J., Theuns T., Rauch M., Efstathiou G., Sargent W. L. W., 2000, MNRAS, 318, 817

Seljak U., Zaldarriaga M., 1996, ApJ, 469, 437

Shen S., Wadsley J., Stinson G., 2009, ArXiv e-prints

Silk J., Rees M. J., 1998, A&A, 331, L1

Simionescu A., Werner N., Böhringer H., Kaastra J. S., Finoguenov A., Brüggen M., Nulsen P. E. J., 2009, A&A, 493, 409

Somerville R. S., Primack J. R., 1999, MNRAS, 310, 1087

Sommer-Larsen J., Romeo A. D., Portinari L., 2005, MNRAS, 357, 478

Songaila A., Cowie L. L., 1996, AJ, 112, 335

Springel V., 2005, MNRAS, 364, 1105

Springel V., Di Matteo T., Hernquist L., 2005, MNRAS, 361, 776

Springel V., Hernquist L., 2003, MNRAS, 339, 289

Steinmetz M., Muller E., 1995, MNRAS, 276, 549

Stinson G., Seth A., Katz N., Wadsley J., Governato F., Quinn T., 2006, MNRAS, 373, 1074

Tamura T., Kaastra J. S., Peterson J. R., Paerels F. B. S., Mittaz J. P. D., Trudolyubov S. P., Stewart G., Fabian A. C., Mushotzky R. F., Lumb D. H., Ikebe Y., 2001, A&A, 365, L87

Theis C., Burkert A., Hensler G., 1992, A&A, 265, 465

Theuns T., Leonard A., Efstathiou G., Pearce F. R., Thomas P. A., 1998, MNRAS, 301, 478

Theuns T., Leonard A., Schaye J., Efstathiou G., 1999, MNRAS, 303, L58

Theuns T., Viel M., Kay S., Schaye J., Carswell R. F., Tzanavaris P., 2002, ApJ, 578, L5

Thielemann F.-K., Argast D., Brachwitz F., Hix W. R., Höflich P., Liebendörfer M., Martinez-Pinedo G., Mezzacappa A., Nomoto K., Panov I., 2003, in From Twilight to Highlight: The Physics of Supernovae Supernova Nucleosynthesis and Galactic Evolution. pp 331–+

Thomas D., Maraston C., Schawinski K., Sarzi M., Joo S., Kaviraj S., Yi S. K., 2007, in A. Vazdekis & R. F. Peletier ed., IAU Symposium Vol. 241 of IAU Symposium, Environment and the epochs of galaxy formation in the SDSS era. pp 546–550

Tornatore L., Borgani S., Dolag K., Matteucci F., 2007, MNRAS, 382, 1050

Tornatore L., Borgani S., Matteucci F., Recchi S., Tozzi P., 2004, MNRAS, 349, L19

Tornatore L., Borgani S., Viel M., Springel V., 2009, ArXiv e-prints

Tremonti C. A., Heckman T. M., Kauffmann G., Brinchmann J., Charlot S., White S. D. M., Seibert M., Peng E. W., Schlegel D. J., Uomoto A., Fukugita M., Brinkmann J., 2004, ApJ, 613, 898

Valdarnini R., 2003, MNRAS, 339, 1117

White S. D. M., Frenk C. S., 1991, ApJ, 379, 52

White S. D. M., Rees M. J., 1978, MNRAS, 183, 341

Wise J. H., Abel T., 2008, ApJ, 685, 40

Woosley S. E., Weaver T. A., 1995, ApJS, 101, 181

Zel'Dovich Y. B., 1970, A&A, 5, 84

# CHAPTER 5

# The enrichment history of cosmic metals

Robert P. C. Wiersma, Joop Schaye, Claudio Dalla Vecchia, C. M. Booth,
Tom Theuns, and Anthony Aguirre

Accepted for publication in the Monthly Notices of the Royal Astronomical Society

We use a suite of cosmological, hydrodynamical simulations to investigate the chemical enrichment history of the Universe. Specifically, we trace the origin of the metals back in time to investigate when various gas phases were enriched and by what halo masses. We find that the age of the metals decreases strongly with the density of the gas in which they end up. At least half of the metals that reside in the diffuse intergalactic medium (IGM) at redshift zero (two) were ejected from galaxies above redshift two (three). The mass of the haloes that last contained the metals increases rapidly with the gas density. More than half of the mass in intergalactic metals was ejected by haloes with total masses less than $10^{11}$ $\mathrm{M}_{\odot}$ and stellar masses less than $10^{9}$ $\mathrm{M}_{\odot}$. The range of halo masses that contributes to the enrichment is wider for the hotter part of the IGM. By combining the 'when' and 'by what' aspects of the enrichment history, we show that metals residing in lower density gas were typically ejected earlier and by lower mass haloes.

## 5.1 INTRODUCTION

Despite the fact that 'metals' - heavy elements produced by stars - make up a very tiny portion of the cosmic matter budget, they are of critical importance to our understanding of the Universe. From a diagnostic point of view, they are very useful in constraining star formation and tracing feedback from massive stars and supernovae. More importantly, however, metals impact the rate at which gas cools, affecting structure formation on scales of galaxy clusters down to dust grains. This effect should not go understated since, depending on the temperature, metals can reduce the cooling time by over an order of magnitude for solar metallicity (e.g. Sutherland & Dopita 1993; Gnat & Sternberg 2007, chapter 2).

Observations clearly show that a substantial fraction of the diffuse intergalactic medium (IGM) has been enriched with heavy elements (e.g. Cowie & Songaila 1998; Schaye et al. 2000; Ellison et al. 2000; Schaye et al. 2003; Simcoe et al. 2004; Aracil et al. 2004; Schaye et al. 2007; Aguirre et al. 2008; Danforth & Shull 2008; Cooksey et al. 2010; Pieri et al. 2009). However, the physical mechanism, the timing and the sources of the enrichment all remain unknown. The IGM may have been enriched by the first generations of stars and galaxies at very high redshifts, or it may have been polluted by more massive galaxies at intermediate redshifts. Metals may be carried out into intergalactic space by galactic winds driven by supernovae, radiation pressure from star light, or by active galactic nuclei (AGN) (e.g. Cen & Ostriker 1999; Aguirre et al. 2001a,b; Madau et al. 2001; Theuns et al. 2002; Tornatore et al. 2004; Aguirre et al. 2005; Oppenheimer & Davé 2006; Davé & Oppenheimer 2007; Oppenheimer & Davé 2008; Scannapieco et al. 2006; Kawata & Rauch 2007; Kobayashi et al. 2007; Sommer-Larsen & Fynbo 2008; Shen et al. 2010; Tornatore et al. 2010; Choi & Nagamine 2010, chapter 3). In dense environments such as groups and clusters of galaxies metals may also be efficiently dispersed via processes such as ram pressure stripping or tidal stripping (see e.g. Borgani et al. 2008 for a review).

The most straightforward way to investigate when the IGM received its metals, is to plot the metallicity or metal mass as a function of redshift, as we did for a series of cosmological simulations in chapter 3. By comparing models with different physical implementations, one can obtain information about the processes that are important for IGM enrichment. However, the metals that reside in the IGM at high redshift may not be the same metals that are in the IGM at the present day. What is hot IGM gas at high redshift, may have cooled by low redshift. Intergalactic metals may also accrete onto galaxies and end up in the ISM or in stars.

Here we also use cosmological simulations to study the enrichment of the cosmos - noting that the IGM is of particular interest - but we take a novel approach in that we classify the gas based on its state at the redshift of interest (we choose $z = 0$ and $z = 2$) and trace its enrichment history back in time with the aim of understanding how the observed metals were put into place. Specifically, we will address the following two questions: When did gas that resides in the IGM at $z = 0$ and $z = 2$ receive its metals? And what are the masses of the haloes that last contained these metals?

This paper is organised as follows. In Section 5.2 we describe the simulations used, emphasising the details that are particularly pertinent here. Section 5.3 discusses *when* the gas was enriched, taking each sub-phase in turn. In Section 5.4 we investigate *what* enriched the gas, using a halo-finder to determine what kinds of objects are mainly responsible for the enrichment of various gas phases. We connect the two ideas in Section 5.5, relating enrichment time with the last halo that contained the metals that end up in the IGM. Finally, we summarise our findings in Section 5.6.

## 5.2 SIMULATIONS

The simulations presented here are part of the OverWhelmingly Large Simulations (OWLS) project (Schaye et al. 2010), which consists of a large suite of cosmological, hydrodynamical simulations that include chemodynamics. We use a substantially modified version of the $N$-body Tree-PM, smoothed particle hydrodynamics (SPH) code GADGET III, which is itself a modified version of the code GADGET II (Springel 2005). The code includes new modules for radiative cooling and heating (chapter 2), star formation (Schaye & Dalla Vecchia 2008), chemodynamics (chapter 3), and feedback from supernovae (Dalla Vecchia & Schaye 2008). Below we will give a brief overview of the simulation ingredients that are most relevant for this work. More details can be found in Schaye et al. (2010) and the references given above.

We assume a flat ΛCDM universe with the cosmological parameters $[\Omega_m, \Omega_b, \Omega_\Lambda, \sigma_8, n_s, h, Y] = [0.238, 0.0418, 0.762, 0.74, 0.951, 0.73, 0.248]$, as determined from the WMAP 3-year data and consistent[1] with the WMAP 7-year data (Jarosik et al. 2010).

We use the radiative cooling tables presented in chapter 3[2]. In brief, net radiative cooling rates are computed element-by-element in the presence of the cosmic microwave background (CMB) and the Haardt & Madau (2001) model for the UV/X-ray background radiation from quasars and galaxies. The contributions of the eleven elements hydrogen, helium, carbon, nitrogen, oxygen, neon, magnesium, silicon, sulphur, calcium, and iron are interpolated as a function of density, temperature, and redshift from tables that have been pre-computed using the publicly available photo-ionization package CLOUDY, last described by Ferland et al. (1998), assuming the gas to be optically thin and in (photo-)ionization equilibrium.

Stars are formed from gas particles as per Schaye & Dalla Vecchia (2008). Gas at sufficiently high densities ($n_{\rm H} \gtrsim 10^{-1}\,{\rm cm}^{-3}$) is expected to be multiphase and star-forming (Schaye 2004). Because we lack the resolution and the physics to model the cold interstellar phase, we impose an effective equation of state with pressure $P \propto \rho_{\rm g}^{4/3}$ for densities exceeding $n_{\rm H} = 0.1~{\rm cm}^{-3}$, normalised to $P/k = 1.08 \times 10^3~{\rm cm}^{-3}\,{\rm K}$ at the threshold. For this slope of the equation of state both the Jeans mass and the ratio of the Jeans length and the SPH kernel are independent of the density, thus preventing spurious fragmentation due to a lack of numerical resolution. Star-forming gas particles are stochastically converted into star particles at a pressure-dependent rate that is determined analytically from the observed Kennicutt-Schmidt star formation law.

---

[1] The most significant discrepancy is in $\sigma_8$, which is 8% lower than the value favoured by the WMAP 7-year data.

[2] We used their equation (3) rather than (4) and CLOUDY version 05.07 rather than 07.02.

Supernova feedback is injected in kinetic form, as described in Dalla Vecchia & Schaye (2008). After a short delay of $t_{\rm SN} = 3 \times 10^7$ yr, corresponding to the maximum lifetime of stars that end their lives as core-collapse supernovae, newly-formed star particles inject kinetic energy into their surroundings by kicking a fraction of their neighbours in a random direction. The reference simulations presented here use the default parameters of Dalla Vecchia & Schaye (2008), which means that each SPH neighbour $i$ of a newly-formed star particle $j$ has a probability of $\eta m_j / \sum_{i=1}^{N_{\rm ngb}} m_i$ of receiving a kick with a velocity $v_{\rm w}$, where $N_{\rm ngb} = 48$ is the number of SPH neighbours. We choose $\eta = 2$ and $v_{\rm w} = 600$ km s$^{-1}$ (i.e. if all baryonic particles had equal mass, each newly formed star particle would kick, on average, two of its neighbours). Assuming that each star with initial mass in the range $6 - 100$ M$_\odot$ injects $10^{51}$ erg of kinetic energy, these parameters imply that the total wind energy accounts for 40 per cent of the available kinetic energy for a Chabrier IMF and a stellar mass range $0.1 - 100$ M$_\odot$ (if we consider only stars in the mass range $8 - 100$ M$_\odot$ for type II supernovae, this works out to be 60 per cent). The value $\eta = 2$ was chosen to roughly reproduce the peak in the cosmic star formation rate (see Schaye et al. 2010).

For the chemo-dynamics, we employ the method described in chapter 3. We use a Chabrier (2003) stellar initial mass function, with mass limits of $0.1$ M$_\odot$ and $100$ M$_\odot$. We consider enrichment due to mass loss from AGB and massive stars as well as type Ia and II supernovae (SNIa and SNII respectively). Our prescription for stellar evolution is heavily based on the Padova models as we use the lifetimes of Portinari et al. (1998) and the yields of low mass and high mass stars of Marigo (2001) and Portinari et al. (1998), respectively. The yields of Portinari et al. (1998) include ejecta from SNII along with estimates of mass loss from high mass stars. Using these yields gives an element of consistency between the low and high mass stars. Finally, we use the 'W7' SNIa yields of Thielemann et al. (2003).

As the precise channels of SNIa progenitors are uncertain, we employ SNIa explosion rates that roughly reproduce the observed cosmic SNIa rate. We note that the observations from different surveys are not consistent and that our rates conform to the most recent data. An e-folding delay time is used to describe the SNIa rate and we use a corresponding efficiency (i.e. number of white dwarfs that become SNIa) of $2.5\%$.

We use SPH-smoothed metallicities for cooling and stellar evolution purposes, where $Z_{\rm sm} \equiv \rho_{\rm Z}/\rho_{\rm g}$ for gas particles, and star particles inherit the smoothed metallicities of their progenitors. In chapter 3 we argued that this definition is more consistent with the SPH formalism than the more commonly used particle metallicity, $Z_{\rm part} \equiv m_{\rm Z}/m_{\rm g}$. Using smoothed metallicities results in a spreading of metals over greater volumes, increasing the average rates of cooling and star formation.

Since SPH is a Lagrangian scheme, metals move with the particles they are attached to, and hence a high-metallicity particle may in principle be completely surrounded by low-metallicity gas. Introducing smoothed metallicities partially mitigates this numerical artefact. However, SPH codes may underestimate the true amount of gas mixing as compared to grid codes in case of instabilities (Agertz et al. 2007) or turbulence (Mitchell et al. 2009). It would thus be very interesting to investigate whether the metal distribution in such grid simulations is similar to that obtained with SPH. On

**Table 5.1**: List of simulations. From left-to-right the column show: simulation identifier, dark matter particle mass, baryonic particle mass, maximum physical gravitational softening (the softening is held fixed in comoving coordinates above $z = 2.91$), final redshift, and a brief description.

| Simulation | $m_{\rm dm}$ ($h^{-1}\,{\rm M}_{\odot}$) | $m_{\rm b}$ ($h^{-1}\,{\rm M}_{\odot}$) | $\epsilon_{\rm prop}$ ($h^{-1}\,{\rm kpc}$) | $z_{\rm end}$ | Comment |
|---|---|---|---|---|---|
| *L025N512* | $6.3 \times 10^6$ | $1.4 \times 10^6$ | 0.5 | 1.45 | Reference model |
| *L050N512* | $5.1 \times 10^7$ | $1.1 \times 10^7$ | 1.0 | 0 | Reference model |
| *L025N256* | $5.1 \times 10^7$ | $1.1 \times 10^7$ | 1.0 | 2 | Reference model |
| *L050N256* | $4.1 \times 10^8$ | $8.7 \times 10^7$ | 2.0 | 0 | Reference model |
| *L100N512* | $4.1 \times 10^8$ | $8.7 \times 10^7$ | 2.0 | 0 | Reference model |
| *AGN_L100N512* | $4.1 \times 10^8$ | $8.7 \times 10^7$ | 2.0 | 0 | Includes AGN |
| *WDENS_L100N512* | $4.1 \times 10^8$ | $8.7 \times 10^7$ | 2.0 | 0 | Wind vel. prop. to local sound speed (SN energy as *REF*) |

the other hand, we note that Shen et al. (2010) included turbulent diffusion of metals in cosmological SPH simulations but found its effect to be small.

Of the OWLS suite of simulations (described in Schaye et al. 2010), we use the subset listed in Table 5.1. Here we make use of the notation $LXXXNYYY$, where the simulation cube has a comoving side length of XXX $h^{-1}\,{\rm Mpc}$ and uses YYY$^3$ dark matter particles and YYY$^3$ baryonic particles. Table 5.1 also lists the dark matter and the initial baryonic particle masses, $m_{\rm dm}$ and $m_{\rm b}$, the maximum proper gravitational softening (the softening is fixed to this value in comoving coordinates above $z = 2.91$), $\epsilon_{\rm prop}$, the redshift at which the simulation was stopped, $z_{\rm end}$, and a short description.

We explore two variations on the reference model (*REF*). Run *AGN_L100N512* includes the prescription of Booth & Schaye (2009) for the growth of supermassive black holes by gas accretion and mergers, and for feedback from AGN. The black holes inject 1.5 per cent of the accreted rest mass energy as thermal energy in the surrounding interstellar medium. This model reproduces not only the the local black hole scaling relations (Booth & Schaye 2009), but also the observed entropy, temperature, and metallicity profiles of groups of galaxies and the stellar masses that they contain (McCarthy et al. 2009).

For run *WDENS_L100N512* the parameters of the winds are dependent on the local density, keeping the energy per unit stellar mass formed constant. They scale such that in high-density environments the wind velocity is higher:

$$v_{\rm w} = v_{\rm w}^{*}\left(\frac{n_{\rm H}}{n_{\rm H}^{*}}\right)^{1/6}, \tag{5.1}$$

$$\eta = \eta_{*}\left(\frac{n_{\rm H}}{n_{\rm H}^{*}}\right)^{-1/3}, \tag{5.2}$$

where $v_{\rm w}^{*} = 600\ {\rm km\,s^{-1}}$ and $\eta_{*} = 2$ such that the model agrees with the reference model at the threshold for star formation. For higher gas pressures the velocity increases in

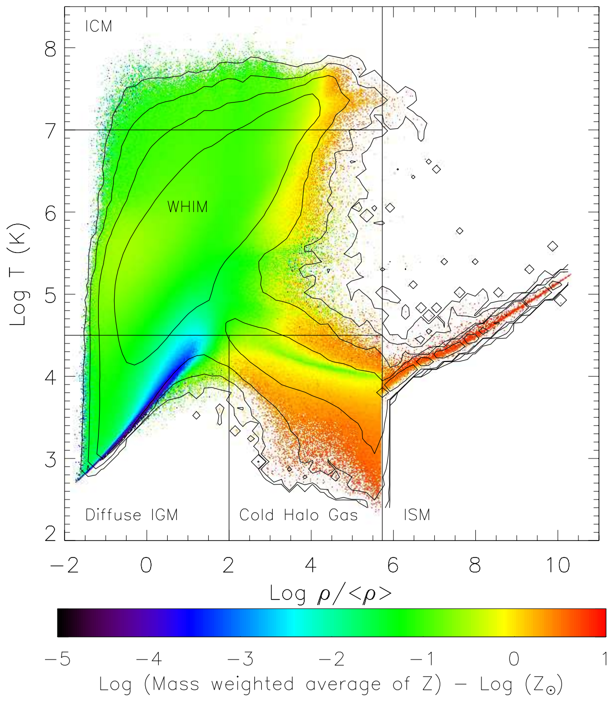

**Figure 5.1**: Mass weighted metal distribution in temperature-density space at $z = 0$ in simulation *L050N512*. The colour scale gives the metallicity. The contours indicate the metal mass distribution and are logarithmically spaced by 1 dex. The straight lines indicate the adopted division of the gas into: non-star-forming gas (i.e., $n_{\rm H} < 0.1~{\rm cm}^{-3}$), diffuse photo-ionised IGM ($\rho < 10^2\,\langle\rho\rangle$, $T < 10^{4.5}\,{\rm K}$), cold halo gas ($\rho > 10^2\,\langle\rho\rangle$, $T < 10^{4.5}\,{\rm K}$), WHIM ($10^{4.5}\,{\rm K} < T < 10^7\,{\rm K}$), and ICM ($T > 10^7\,{\rm K}$). The metals are distributed over a wide range of densities and temperatures.

proportion with the local sound speed. Schaye et al. (2010) find that this model is much more efficient at suppressing star formation in massive galaxies, though not as efficient as the model that includes AGN.

## 5.3 WHEN WAS THE GAS ENRICHED?

In this section we will investigate how the time at which a gas element was enriched varies with its density and temperature at some later time. We will evaluate the enrichment history of the gas as a function of its physical state at both $z = 0$ and $z = 2$. Before doing so, it is, however, instructive to look at the distribution of metal mass at the present time, which we show in Fig. 5.1.

Fig. 5.1 indicates how we can divide the temperature-density plane in several regions of interest. For $n_{\rm H} > 0.1\,{\rm cm}^{-3}$ (which corresponds to $\rho/\langle\rho\rangle > 5.3\times10^5$ at $z = 0$ and $\rho/\langle\rho\rangle > 2.0\times10^4$ at $z = 2$) we impose an effective equation of state and assume the gas to be star-forming. We divide the non-star-forming gas into hot gas typically found in haloes of large groups or clusters (ICM, $T > 10^7\,{\rm K}$), warm-hot intergalactic gas (WHIM, $10^{4.5}\,{\rm K} < T < 10^7\,{\rm K}$), diffuse photo-ionised IGM ($\rho < 10^2\,\langle\rho\rangle$, $T < 10^{4.5}\,{\rm K}$), and cold halo gas ($\rho > 10^2\,\langle\rho\rangle$, $T < 10^{4.5}\,{\rm K}$). While we have divided the cold ($T < 10^{4.5}\,{\rm K}$) gas into low- and high-density components (diffuse IGM and cold halo gas, respectively), we have not done the same for hotter gas. We find that if we split the WHIM at $\rho = 10^2\,\langle\rho\rangle$, the enrichment history of the low-density component is very similar to that of the WHIM in total, whereas that of the high-density component is more similar to the enrichment history of the ICM. The high-density component contains less than

**Table 5.2**: Fractional distribution of metals in the reference models at $z = 0$ and $z = 2$.

| Phase | Fraction of metals (%) |
|---|---|
| L050N512 ($z = 0$) | |
| Stars | 68.2 |
| SF Gas | 5.8 |
| ICM | 1.3 |
| WHIM | 19.0 |
| Cold Halo Gas | 4.6 |
| Diffuse IGM | 1.0 |
| L025N512 ($z = 2$) | |
| Stars | 42.0 |
| SF Gas | 25.8 |
| ICM | $< 0.1$ |
| WHIM | 24.0 |
| Cold Halo Gas | 7.2 |
| Diffuse IGM | 0.9 |

one quarter of the WHIM metals at $z = 0$ and less than one sixteenth at $z = 2$.

In chapter 3 we showed that the metallicities predicted for these phases[3] by our reference model are in agreement with the observations, although the metallicity for the diffuse IGM may be slightly too low and is not yet fully converged with respect to the numerical resolution (it increases with increasing resolution).

The contours in Fig. 5.1 show how the metal mass is distributed in temperature-density space. The metals are spread over a wide range of phases. The metallicity (that is, the ratio of metal mass to total mass), indicated by the colour scale, ranges significantly between the various regions. That the contours do not always trace the regions with the highest metallicities highlights the fact that the metals are distributed rather differently from the rest of the baryons. Table 5.2 summarises the $z = 0$ and $z = 2$ metal mass distributions for the reference model.

We will make frequent use of what we will term "metal-mass-weighted mean redshifts", $z_Z$. This quantity, which we compute on the fly for all gas particles in our simulations, is defined as the mean redshift of enrichment events weighted by the metal mass imparted by each event:

$$z_Z \equiv \frac{\sum_i \Delta m_{\mathrm{Z};i} z_i}{m_{\mathrm{Z}}}, \tag{5.3}$$

where $\Delta m_{Z;i}$ is the metal mass received by the gas particle at redshift $z_i$ ($i$ indicates a time-step) and $m_Z$ is the total metal mass of the particle. Thus, if a gas particle received all its metals over a short interval (which is typical for particles that have been ejected from haloes), this quantity gives the redshift at which it was enriched. Note that $z_Z$ does not correspond to the time at which the metals were created. Stars may create metals long before they are released and metals may be cycled through multiple

---

[3] Note that in chapter 3 we used $T = 10^5$ K as the dividing temperature for WHIM and cold gas; we lower the limit here so that we can better isolate the components visible in Fig. 5.2.

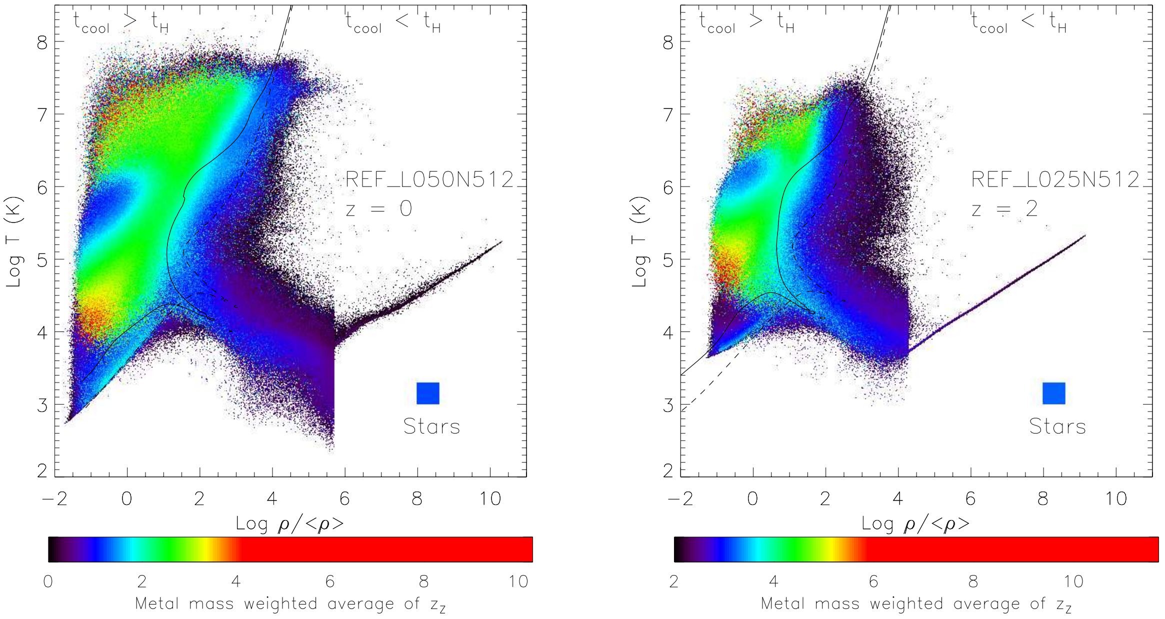

**Figure 5.2**: Enrichment redshift in temperature-density space. The colour scale gives the metal mass weighted mean enrichment redshift as a function of the gas density and temperature at $z = 0$ in *L050N512* (left panel) and at $z = 2$ in *L025N512* (right panel). Each pixel shows the metal mass weighted average value of $z_Z$ for all particles that fall into the corresponding temperature-density bin. The rectangles in the bottom-right parts of the diagrams indicate the corresponding values for the metals locked up in stars. Also plotted are $t_{\rm cool} = t_{\rm H}$ contours for solar (solid) and primordial (dashed) abundances. Note that we have stretched the colour scale to emphasise the different components (only a handful of pixels correspond to high values of $z_Z$) and that the two panels use different colour scales. Denser gas was typically enriched later. The enrichment redshift is particularly small for gas with a short cooling time.

generations of stars. We will nevertheless sometimes refer to the metals residing in gas with higher values of $z_Z$ as being "older". In §5.4 we will show that for intergalactic metals $z_Z$ is typically close to the redshift at which the metals last resided in a halo.

Fig. 5.2 shows $z_Z$ in temperature-density space for *L050N512* at $z = 0$ (left panel) and for *L025N512* at $z = 2$ (right panel). Note that this figure contains no information about how much metal mass is actually in a given bin (for instance, the diffuse IGM contains relatively little metal mass, but this is not obvious from this plot). We can, however, refer back to Fig. 5.1 to see the metal distribution. For reference, computing the metal mass weighted average over all gas (stars) yields $z_Z \approx 1.5$ ($z_Z \approx 1.2$) for *L050N512* at $z = 0$ and $z_Z \approx 3.1$ ($z_Z \approx 3.2$) for *L025N512* at $z = 2$.

The most prominent trend visible in Fig. 5.2 is a strong overall gradient with density, with higher density gas being enriched more recently. This agrees with the predictions of Oppenheimer & Davé (2009) for the low-redshift, diffuse IGM as traced by O VI absorbers. Of all components, the star-forming gas (i.e., the ISM) has been enriched most recently. This is not unexpected, as this is the gas that surrounds the stars that are releasing the metals. Moreover, much of the metal mass that was injected into the ISM a long time ago, will already have been locked up in stars. Indeed, the metals locked up in stars were, on average, released (by other, older stars) earlier than the metals that reside in the ISM as can be seen by comparing the colour of the rectangles in the bottom-right parts of the panels to that of the ISM. The fact that the increase of $z_Z$ with decreasing density continues all the way to the lowest densities, suggests that travel-time is a limiting factor for the enrichment of the IGM, as suggested by Aguirre et al. (2001b).

Fig. 5.2 also reveals some interesting trends with the gas temperature. For high gas densities, the dependence on temperature reflects a dependence on the radiative cooling time. We can see this by comparing to the solid and dashed contours, which show where the net radiative cooling time[4], $t_{\rm cool}$, equals the Hubble time, $t_{\rm H}$, for gas with solar and primordial abundances, respectively. The two contours that enter the diagram at high and low temperatures correspond to net cooling and heating, respectively. They converge at high densities and intermediate temperatures at the equilibrium temperature. There the contours should really extend further to the bottom right, approximately to the star formation threshold (above which we impose an effective equation of state), but they stop due to the finite resolution of the grid on which we have computed the cooling time. Gas to the right of the contours has $t_{\rm cool} < t_{\rm H}$, but gas to the left of the contours cannot cool. Clearly, the enrichment redshift is a decreasing function of the cooling time if $t_{\rm cool} < t_{\rm H}$. Since the gas cannot remain in the same area of the temperature-density plane for more than a cooling time, this implies that the time since enrichment is correlated with the time since the gas parcel moved significantly in the $T - \rho$ diagram. This is for example expected if the gas was enriched and shock-heated at roughly the same time, as in a galactic wind. It would, however, also happen if the enrichment led to a strong reduction in the cooling time.

In the long cooling time regime (i.e. to the left of the contours) the enrichment redshift also depends on the gas temperature. We will show later (see Fig. 5.3) that some of the features for $\rho \lesssim \langle\rho\rangle$ and $T > 10^4\,{\rm K}$ are sensitive to the implementation of feedback. However, the finding that the coldest part of the diffuse IGM was enriched more recently than the WHIM, is robust. Note, however, that the diffuse IGM contains very few metals compared to the WHIM (see Fig. 5.1). We will show in section 5.4 (Fig. 5.11) that most of the metals in the cold, underdense part of the diffuse IGM have never been part of a (resolved) halo. This suggests that this gas may have been enriched by winds from intermediate-mass, intergalactic stars (presumably formed in galaxies and then ejected). Apparently, gas that has been enriched and ejected by galactic winds ends up in the WHIM at higher temperatures, probably because it has been put onto a higher adiabat as a result of shock-heating. Once the gas has entered the region where $t_{\rm cool} > t_{\rm H}$, it can no longer decrease its entropy, preventing low-density WHIM gas from moving into the diffuse, photo-ionised region of the diagram.

The left panel of Fig. 5.3 shows $z_Z(T,\rho)$ at $z = 0$ for the *L100N512* version of the reference model. Comparison with the left panel of Fig. 5.2, which showed the prediction for a simulation with 8 (2) times higher mass (spatial) resolution shows that the trends have converged numerically.

---

[4] We plot only the radiative cooling time, but note that the actual cooling rates in the simulation are dominated by adiabatic expansion for low densities.

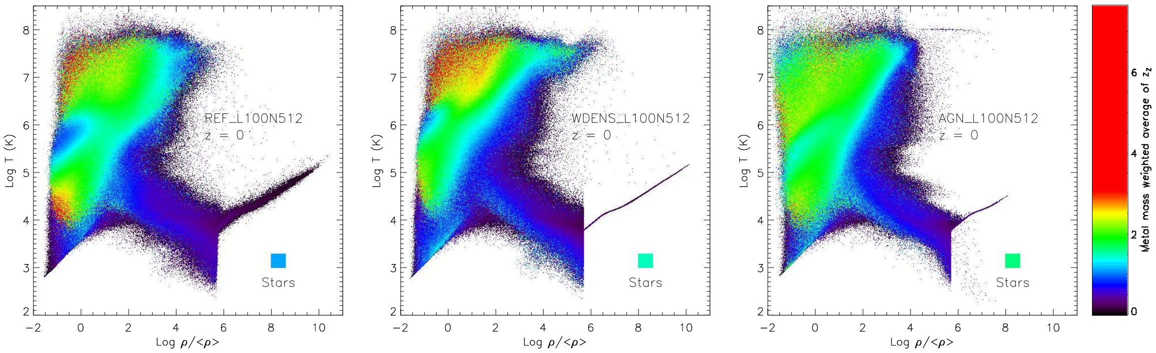

**Figure 5.3**: A comparison of the enrichment redshifts for simulations including different feedback processes. The colour scale gives the metal mass weighted mean enrichment redshift as a function of the gas density and temperature at $z = 0$ for simulations *REF_L100N512* (left panel), *WDENS_L100N512* (middle panel), and *AGN_L100N512* (right panel). Model *WDENS* uses an implementation of supernova-driven winds that is more efficient in massive haloes than that of model *REF*. Model *AGN* uses the same prescription for supernova feedback as model *REF*, but includes feedback from AGN. The rectangles in the bottom-right parts of the diagrams indicate the values of $z_Z$ for the metals locked up in stars. For numerical reasons that are explained in the main text, the unresolved multiphase ISM (Log $\rho/\langle\rho\rangle \gtrsim 6$) follows a much tighter equation of state for models *WDENS* and *AGN* than for model *REF*. While the features seen at $(\rho, T) \sim (10^{-1}\ \langle\rho\rangle\,, 10^{4.3}\,\mathrm{K})$ and $(10^{-0.5}\ \langle\rho\rangle\,, 10^{5.7}\,\mathrm{K})$ for model *REF* depend on the implementation of galactic winds, the other trends are robust.

The remaining panels of Fig. 5.3 show the enrichment redshift predicted by two other simulations from the OWLS project. The middle panel shows model *WDENS*, for which the wind velocity scales with the local sound speed, while keeping the total energy per unit stellar mass identical to that used in model *REF*. In this model the supernova driven winds remain efficient up to higher halo masses, which results in a lower global star formation rate at low redshift (Schaye et al. 2010). The right panel shows the results for model *AGN*, which uses the same prescription for supernova feedback as model *REF*, but which also includes feedback from accreting supermassive black holes. Since AGN feedback is most relevant for high halo masses, the star formation rate, and thus the rate at which metals are both produced and locked up in stars, decreases much faster below $z = 2$ than for the other models (Schaye et al. 2010). This explains the increase in the metal mass weighted mean enrichment redshift of the stars, from $z_Z \approx 1.1$ for model *REF* to 1.5 for *WDENS* to 1.6 for *AGN* (the corresponding values for the gas are $z_Z \approx 1.1$, 1.3, and 1.5, respectively).

The gas on the equation of state (Log $\rho/\langle\rho\rangle \gtrsim 6$), which represents the unresolved, multiphase ISM, displays much less scatter for *WDENS* and *AGN* than for *REF*. This reflects the fact that for the latter model the output time corresponded to a global time-step whereas passive particles were caught 'drifting' adiabatically between time-steps in the reference run, resulting in temperatures that deviate slightly from our imposed equation of state. Note that this does not represent any difference in how the hydrodynamical forces were calculated among the three simulations. Observe also that some of the particles in the right panel fall on a line near $10^8$ K. This corresponds to the AGN heating temperature (see Booth & Schaye 2009) and thus implies that these particles have been heated very recently.

Comparing the three panels, we see that the features seen at $(\rho, T) \sim (10^{-1} \langle\rho\rangle,$ $10^{4.3}\,\mathrm{K})$ and $(10^{-0.5} \langle\rho\rangle, 10^{5.7}\,\mathrm{K})$ for model *REF* depend on the implementation of supernova-driven winds. All other trends of $z_Z$ with $T$ and $\rho$ are, however, robust. Even AGN feedback does not change the trends discussed above. Since the differences between the simulations are small compared to the similarities, we will only make use of our higher resolution reference model for the remainder of this section. It should be kept in mind, however, that this model probably underestimates the typical enrichment redshift due to the absence of an efficient feedback mechanism in massive galaxies.

Figs. 5.2 and 5.3 do not allow us to infer what the typical enrichment time is of metals as a function of just density or just temperature, because the diagrams do not take into account the distribution of metal mass in the $T - \rho$ plane. The solid curves in Fig. 5.4 therefore show the metal mass weighted mean enrichment redshift as a function of density (left panel) or temperature (right panel). The black and red curves show results for *L050N512* at $z = 0$ and for *L025N512* at $z = 2$, respectively.

Focusing first on the left panel, we see strong gradients with the gas density. While gas that is diffuse at $z = 0$ was typically enriched at $z \approx 2$, metals that reside in collapsed structures (i.e. $\rho \gtrsim 10^2 \langle\rho\rangle$) at the present time, were on average released much more recently. The enrichment redshift continues to decrease down to the highest densities. The same holds at $z = 2$, although the gradient is less steep at high densities. Gas that is diffuse at $z = 2$ typically received its metals at $z > 3$ and metals residing in underdense gas at $z = 2$ were on average ejected at $z > 4$.

Similarly, the right panel of Fig. 5.4 shows the metal mass weighted enrichment redshift as a function of the gas temperature at $z = 0$ (black) and $z = 2$ (red) for all gas (solid) as well as for gas with density smaller (dot-dashed) or greater (dashed) than $10^2 \langle\rho\rangle$. The enrichment redshift peaks for $T \sim 10^5 - 10^6\,\mathrm{K}$, but this merely reflects the more fundamental trend with density: metals in this temperature range mostly reside in diffuse gas while lower and higher temperatures are dominated by higher densities.

So far we have only plotted the metal mass weighted enrichment redshift averaged over all gas particles in some temperature and/or density bin. Such plots do not reveal information about the distribution in the values of $z_Z$ of the particles that fall into the bin. Fig. 5.5 provides this information by plotting the metal mass weighted cumulative probability distribution function of $z_Z$. In other words, it shows the fraction of the metal mass that resides in gas particles for which $z_Z$ exceeds the value that is plotted along the $x$-axis. The different columns and line styles show the different regions in $T-$ $\rho$ space defined in Fig. 5.1 and the different colours correspond to different resolutions. The top and bottom rows are for $z = 0$ and 2, respectively.

Fig. 5.5 shows that the metals residing in a particular gas phase typically span a wide range of enrichment redshifts. Note that this plot underestimates the true range, because it shows the distribution of $z_Z$ for gas particles, which have themselves been averaged over all past enrichment events (weighted by metal mass). That is, even though a particle may have experiences multiple enrichment events, it only has a single

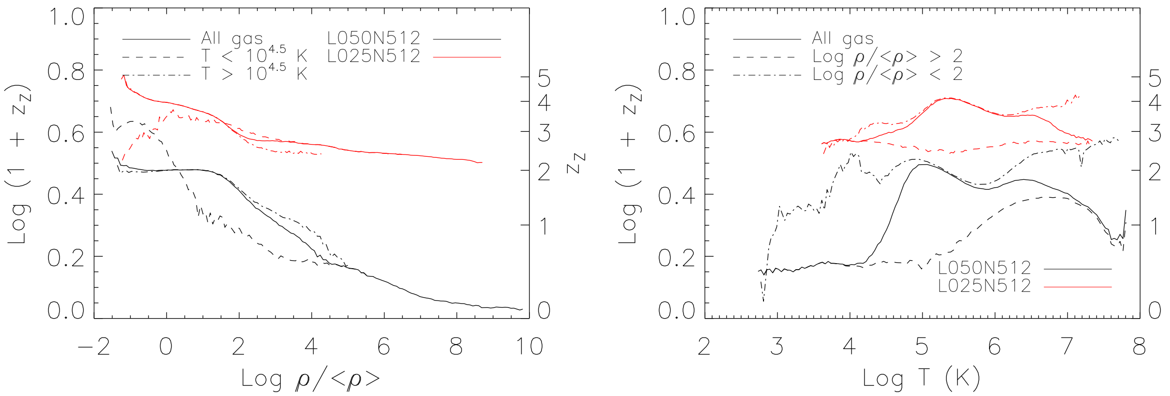

**Figure 5.4**: Metal mass weighted mean enrichment redshift as a function of the gas density (left panel) or the gas temperature (right panel) at $z = 0$ for model *L050N512* (black) and at $z = 2$ for *L025N512* (red). The different line styles correspond to cuts in the temperature (left panel) or density (right panel) as indicated in the legends. The curves were cut when the number of particles per bin falls below 200. The enrichment redshift decreases rapidly with increasing density. Metals residing in gas with intermediate temperatures ($T \sim 10^5 - 10^6$ K) are typically older, but this merely reflects the fact that metals at these temperatures reside mostly in lower density gas than metals at lower or higher temperatures, as can be seen by comparing the different line styles in the right panel.

value of $z_Z$. The distribution is particularly wide if the average enrichment redshift is high. While the average value of $z_Z$ is about 2 for the diffuse IGM at $z = 0$, a quarter of the metal mass resides in particles with $z_Z < 1$ and another quarter has $z_Z > 3$.

Comparison of the different line colours shows that the convergence with numerical resolution is excellent for stars, the ISM, cold halo gas, and the ICM, but that it is less good for the diffuse IGM and the WHIM, particularly at $z = 0$. It is likely that our highest resolution simulation at this redshift, *L050N512*, still significantly underestimates the typical enrichment redshift of these low-density components. We will show in the next section that this is because low-mass haloes dominate the enrichment of low-density gas.

## 5.4 HOW MASSIVE WERE THE OBJECTS THAT ENRICHED THE GAS?

Now that we have a general impression of when the cosmic gas was enriched, we would like to investigate what types of galaxies were responsible for the enrichment. That is, do galaxies residing in certain halo masses preferentially enrich a typical phase of gas? We will address this question by determining the mass of the halo from which the metals were last ejected.

We identify haloes using a friends-of-friends group finder with a linking length of 0.2. This group finder is run on the dark matter particles in the simulation. Baryonic

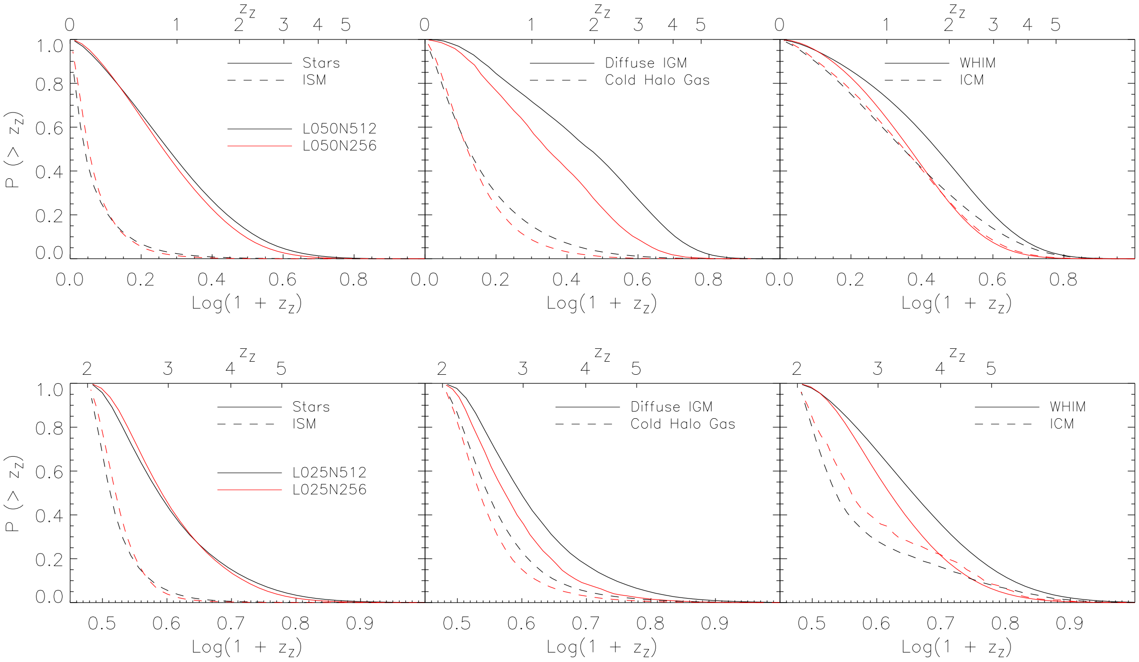

**Figure 5.5**: Cumulative probability distribution of the enrichment redshift, weighted by metal mass, of metals at $z = 0$ (top row) and $z = 2$ (bottom row) for stars and for the different gas phases defined in Fig. 5.1. The different colours correspond to different numerical resolutions. The results are converged with respect to resolution except for the diffuse IGM and the WHIM. For this gas even our highest resolution runs may underestimate the enrichment redshift. There is substantial scatter in the enrichment redshift, particularly for the phases whose metals are, on average, older.

particles are associated with their nearest dark matter neighbour. We include only haloes with at least 100 dark matter particles, because we found that this limit results in excellent agreement with the Sheth et al. (2001) fit to the dark matter halo mass function. For model *L100N512* this lower limit corresponds to a typical $z = 0$ stellar mass of $\sim 10^{9.0}\,\mathrm{M}_\odot$ and this is also roughly the value below which the stellar mass function cuts off due to the limited resolution. For models *L050N512* and *L025N512*, however, the stellar mass already cuts off below about $10^{2.5}$ dark matter particles, which corresponds to stellar masses of $\sim 10^{8.3}\,\mathrm{M}_\odot$ for *L050N512* at $z = 0$ and $\sim 10^{7.7}\,\mathrm{M}_\odot$ for *L025N512*. We therefore expect that we will underestimate the importance of the lowest mass haloes that we consider, particularly for these last two models.

To make the connection between metals and the haloes out of which they were ejected, we perform the following calculation. For each enriched particle, we begin at $z = 0$ ($z = 2$ for the *L025N512* simulation) and search for that particle (using its unique ID) in the friends-of-friends halo catalogue. If said particle is found, we note the total mass of the halo ($m_{\mathrm{halo}}$), and the corresponding redshift, $z_{\mathrm{halo}}$. For all particles not found in this output, we choose halo outputs at successively higher redshifts[5], until we

---

[5] Halo catalogues were generated at all simulation output redshifts. These are spaced at $\Delta z = 0.125$

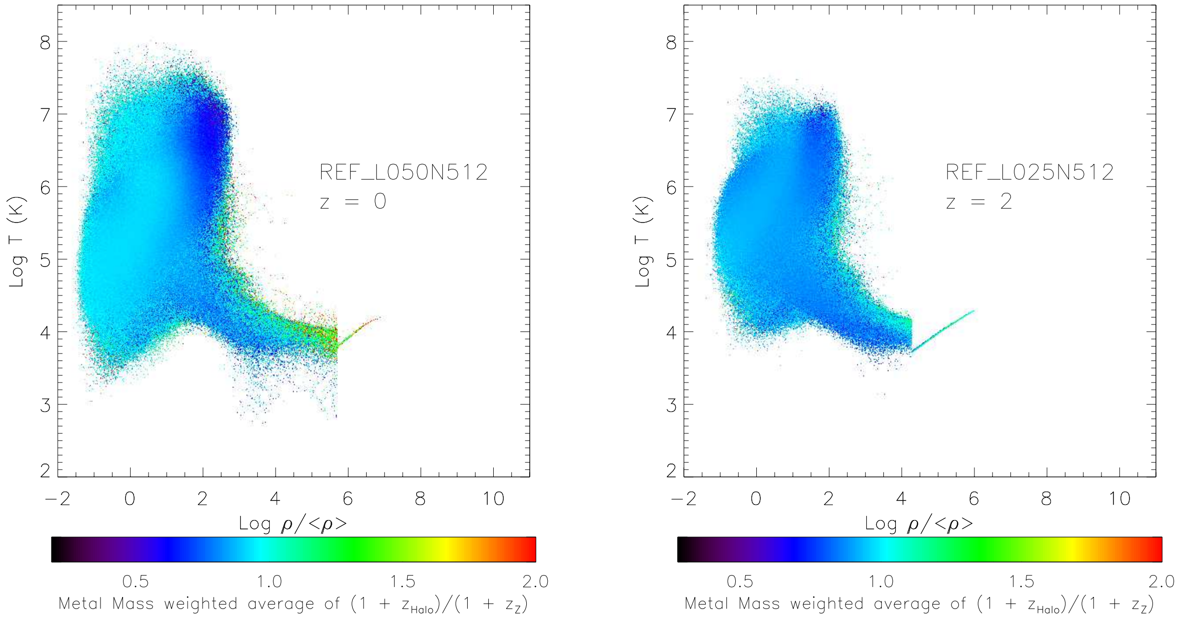

**Figure 5.6**: Ratio of $(1+z_{\rm halo})/(1+z_Z)$ as a function of gas density and temperature in *L050N512* at $z=0$ (left panel) and at $z=2$ for *L025N512* (right panel). Only gas that is not currently part of a resolved halo is included. The metal mass weighted mean enrichment redshift, $z_Z$, is typically similar to, but slightly higher than $z_{\rm halo}$, the metal mass weighted mean redshift at which the metals last resided in a resolved halo. This implies that the gas was ejected from the halo shortly after it was enriched.

have exhausted all of them. For every particle we thus have values for the temperature, density, and metal mass as well as $z_{\rm halo}$ and $m_{\rm halo}$ (unless no corresponding halo is found in our outputs). Note that the temperature and density recorded are for $z=0$ (or $z=2$), whereas $m_{\rm halo}$ is the mass of the host halo at redshift $z_{\rm halo}$.

Before showing the results of such calculations, we investigate the relation between the metal mass weighted enrichment redshift, $z_Z$, and $z_{\rm halo}$ for gas that has been part of, but that is not currently in, a resolved halo. If metals in the IGM were ejected from the haloes in which they formed shortly after they were released by stars, then the two redshifts should roughly agree. We would expect the two to be similar, as both metal enrichment and outflows are driven by massive stars, with $z_{\rm halo}$ somewhat smaller than $z_Z$, simply because it takes some time for gas that has been ejected to reach the virial radius and leave the halo. However, even if enrichment and ejection happen nearly simultaneously, we would expect differences of the order of the time scales corresponding to the time intervals between snapshots. Fig. 5.6 shows that $z_{\rm halo}$ and $z_z$ do indeed agree very well for almost all temperatures and densities. This is true for both $z=0$ and $z=2$. An exception is hot, dense gas ($10^6{\rm K} \lesssim T \lesssim 10^7{\rm K}, \rho \sim 10^2\,\langle\rho\rangle$) at $z=0$, for which $z_{\rm halo}$ is significantly smaller than $z_Z$. This may be because this gas recently moved from the ICM across (our definition of) the halo boundary, but was

---

for $0 \leq z \leq 0.5$, at $\Delta z = 0.25$ for $0.5 \leq z \leq 4$, and at $\Delta z = 0.5$ for $4 \leq z \leq 9$. We also have outputs for $z = 10$, 12.5, 15, and 20.

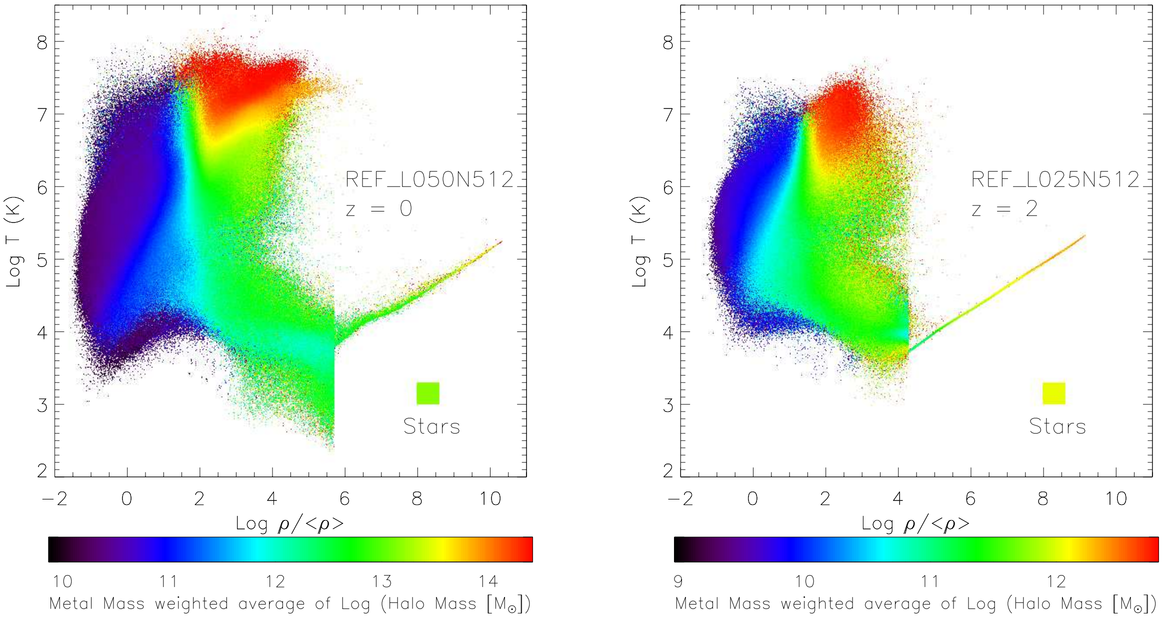

**Figure 5.7**: Metal mass weighted mean $\log_{10} m_{\rm halo}$, where $m_{\rm halo}$ is the total mass of the halo that last contained the metals, as a function of the gas density and temperature at $z = 0$ in *L050N512* (left panel) and at $z = 2$ in *L025N512*. Each pixel shows the metal mass weighted average value of $\log_{10} m_{\rm halo}$ for all particles that fall into the corresponding temperature-density bin. The rectangles in the bottom-right parts of the diagrams indicate the corresponding values for the metals locked up in stars. Only particles that have resided in haloes with more than 100 dark matter particles are included. Note that the two panels use different colour scales. Metals residing in lower density gas originate from lower mass haloes. Because high-density gas ($\rho \gtrsim 10^2 \langle\rho\rangle$) currently resides in haloes, the increase in halo mass with temperature reflects their virial temperatures. The diffuse IGM is nearly completely missing from this plot because it is enriched by unresolved haloes and/or intergalactic stars.

enriched at relatively high redshift. Note that gas with $\rho \gtrsim 10^2 \langle\rho\rangle$ is probably part of unresolved haloes. Most of the gas with these densities is in resolved haloes and has thus been excluded from the plot.

The colour scale in Fig. 5.7 indicates the metal mass weighted mean $\log_{10} m_{\rm halo}$ as a function of the gas temperature and density for *L050N512* at $z = 0$ (left) and for *L025N512* at $z = 2$ (right). Particles that were never part of a halo containing at least 100 dark matter particles were excluded. These particles account for about 4 and 0.3 percent of the total metal mass in gas at $z = 0$ and 2, respectively. Recall that gas with $\rho \gtrsim 10^2 \langle\rho\rangle$ typically resides in a halo.

There is a strong gradient with density in both panels. The lower the density, the lower the mass of the objects that were responsible for the enrichment. The enrichment of the low-density IGM ($\rho < 10\,\langle\rho\rangle$) is dominated by the smallest, resolved haloes, particularly at $z = 0$. This explains the relatively poor convergence that we found for these components in the previous section. Comparing with Fig. 5.2, we see that the low-density photo-ionised IGM ($\rho < 10\,\langle\rho\rangle$, $T < 10^{4.5}$K) is nearly completely missing from Fig. 5.7. This gas phase has therefore only been enriched by haloes below our res-

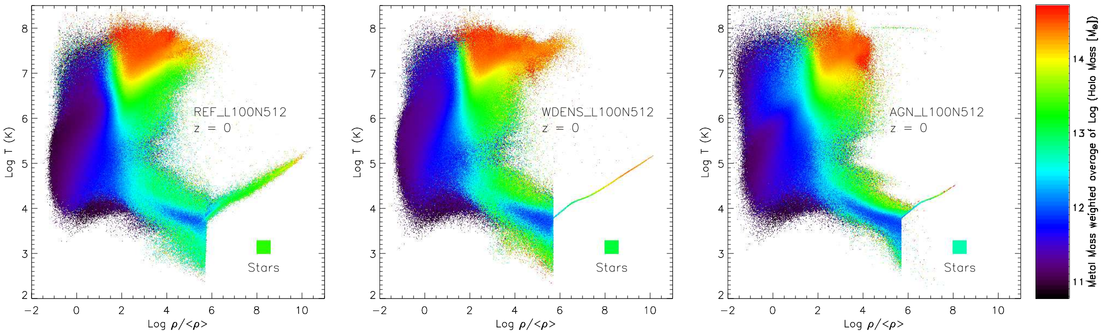

**Figure 5.8**: As Fig. 5.7 but for simulations *REF_L100N512* (left panel), *WDENS_L100N512* (middle panel), and *AGN_L100N512* (right panel), all at $z = 0$. Model *WDENS* uses an implementation of winds driven by supernovae that is more efficient in massive haloes than the prescription used in model *REF*. Model *AGN* uses the same recipe for supernova feedback as model *REF*, but also includes feedback from AGN. While there are some small differences, the trends are very similar for the three models.

olution limit and/or by intergalactic stars. The latter can occur when stars are ejected from galaxies via some dynamical process and then enrich the ambient IGM.

There is a positive gradient of $m_{\rm halo}$ with $T$ for high densities ($\rho \gtrsim 10^2 \langle\rho\rangle$). Since most of these particles reside in haloes, this merely reflects the fact that the virial temperature is an increasing function of mass.

Fig. 5.8 compares the reference model to model *WDENS*, which uses an implementation of galactic winds that makes them more efficient in high-mass haloes, and to model *AGN*, which includes AGN feedback. While there are some small differences, the trends are identical. Thus, the results are robust to variations in the numerical implementation of galactic winds and to the inclusion of AGN feedback. Henceforth we will therefore only consider the reference model.

Comparison of the left panel of Fig. 5.8 to the left panel of Fig. 5.7, which uses a mass (spatial) resolution that is eight (two) times higher, we see that the trends are also robust with respect to the numerical resolution. However, there are clear quantitative differences (note that the colour scales differ), with the higher resolution simulation giving lower halo masses, particularly for masses near the resolution limit.

Fig. 5.9 shows the metal mass weighted mean $\log_{10}$ of the halo mass that last contained the metals as a function of density (left panel) and temperature (right panel) for *L050N512* at $z = 0$ (black) and for *L025N512* at $z = 2$ (red). This plot therefore shows projections of Fig. 5.7, weighted by the metal mass in each pixel of that figure. The solid curves show the results for all the gas, while the other line styles correspond to cuts in the temperature (left) or density (right). Note that due to the finite resolution of the simulation, we may strongly overestimate the typical halo mass of origin when it is predicted to be of the order the minimum resolved halo mass.

The solid curves in the left panel follow the dot-dashed curves at low densities ($\rho \lesssim 10^2 \langle\rho\rangle$) because most of the metals residing in diffuse gas are hot ($T > 10^{4.5}\,{\rm K}$). Conversely, for densities of order or greater than the star formation threshold, most of the metals are cold and the solid curves follow the dashed curves. We see similar

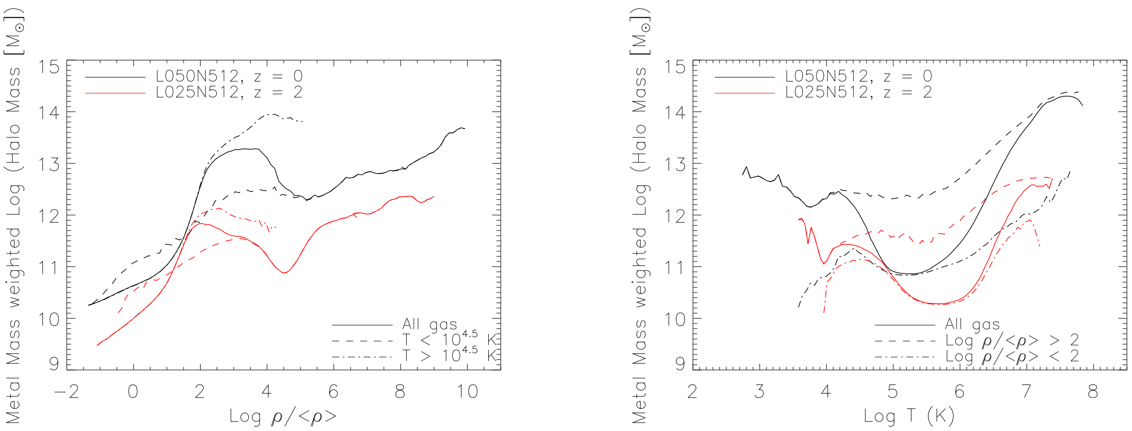

**Figure 5.9**: Metal mass weighted mean $\log_{10} m_{\rm halo}$, where $m_{\rm halo}$ is the total mass of the halo that last contained the metals, as a function of the gas density (left panel) or the gas temperature (right panel) at $z = 0$ for model *L050N512* (black) and at $z = 2$ for *L025N512* (red). The different line styles correspond to cuts in the temperature (left panel) or density (right panel) as indicated in the legends. The curves were cut when the number of particles per bin falls below 200. For both the diffuse IGM and the ISM, the typical halo mass that last contained the metals increases with the gas density. Gas at intermediate temperatures ($T \sim 10^5 - 10^6$ K) typically received its metals from lower mass haloes, but this merely reflects the fact that metals at these temperatures reside mostly in lower density gas than metals at lower or higher temperatures, as can be seen by comparing the different line styles in the right panel.

behaviour in the right panel.

The typical halo mass out of which the metals residing in the diffuse IGM were ejected increases strongly with the gas density. As the density increases above that typical of collapsed objects ($\rho \sim 10^2 \langle\rho\rangle$), $m_{\rm halo}$ firsts declines, because cold metals begin to account for a substantial fraction of the metal mass and for lower mass haloes a greater fraction of the gas is in clumps. Beyond the star formation threshold the mean halo mass increases again as more massive haloes sample higher pressure and thus, given our imposed equation of state for star-forming gas, higher density gas. The right panel shows that, for a fixed temperature, metals in higher density gas originate in higher mass haloes. The typical halo mass that last contained the metals reaches a minimum at intermediate temperatures ($T \sim 10^5 - 10^6$ K), because at these temperatures most of the metals reside at low-densities ($\rho < 10^2 \langle\rho\rangle$), while high-density gas dominates the metal content at both low ($T \lesssim 10^4$ K) and high ($T \gtrsim 10^7$ K) temperatures.

In order to gain insight into the distribution of halo masses that contribute to the enrichment of a particular gas phase, we show the cumulative probability distribution function of $m_{\rm halo}$ in Fig. 5.10. Phrased differently, the figure shows the fraction of the metal mass that last resided in halo masses exceeding those plotted along the $x$-axis. The different columns and line styles correspond to the different regions in $T - \rho$ space shown in Fig. 5.1 and the different colours show the results for different resolutions. The top and bottom rows are for $z = 0$ and $z = 2$, respectively.

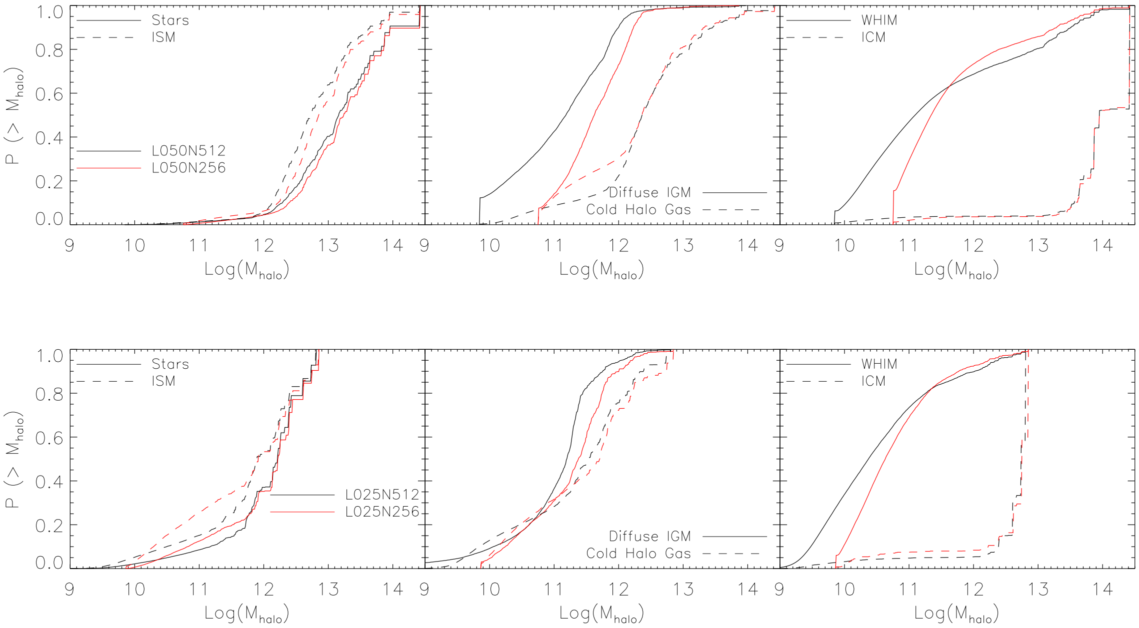

**Figure 5.10**: Cumulative probability distribution of the halo mass that last contained the metals, weighted by metal mass, at $z = 0$ (top row) and $z = 2$ (bottom row) for stars and for the different gas phases defined in Fig. 5.1. The different colours correspond to different numerical resolutions. For metals that have never resided in a halo with more then 100 dark matter particles we set $m_{\rm halo}$ to the minimum resolved halo mass. The results are close to converged with respect to resolution except for the diffuse IGM and the WHIM. For these phases even our highest resolution runs may overestimate the halo mass. A wide range of halo masses contribute to the enrichment.

For metals that never resided in a resolved halo we set $m_{\rm halo}$ to the dark matter mass of the smallest resolved haloes. The fraction of the metal mass ejected by unresolved haloes is greatest for the diffuse IGM at $z = 0$, for which it is about 12 percent. Comparing the two resolutions, we see that the results for the low-density phases, i.e. the diffuse IGM and the WHIM, are not converged. The situation is worst for the diffuse IGM at $z = 0$. Note that within these phases, convergence will be worse at lower densities as we have already demonstrated that the mean halo mass of origin decreases with decreasing density. Fig. 5.10 clearly shows that a wide range of halo masses contributes to the enrichment of most gas phases. More than half of the metal mass in the diffuse IGM and the WHIM originated from haloes with total mass $M < 10^{11}\,{\rm M}_{\odot}$, which corresponds to stellar masses smaller than $10^{9}\,{\rm M}_{\odot}$. For the WHIM at $z = 2$ this fraction is about 80%. As we noted in §5.3, if we separate the WHIM at $\rho = 100\langle\rho\rangle$ (not shown), then the low-density component behaves similarly to the full WHIM, while the high-density component is more similar to the ICM.

Finally, Fig. 5.11 shows the fraction of the metal mass that resided in a resolved halo in at least one of our snapshots as a function of the temperature and the density. As we had already observed, most of the metal mass in the colder part of the diffuse IGM

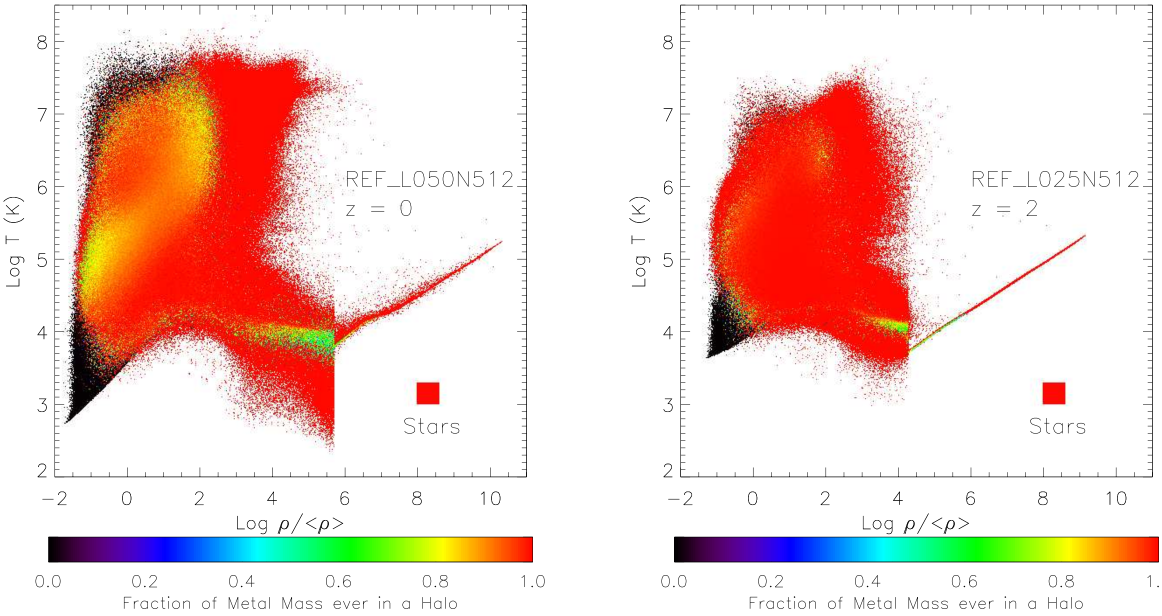

**Figure 5.11**: Fraction of metal mass that has been in a halo with at least 100 dark matter particles as a function of density and temperature for *L050N512* at $z = 0$ (left panel) and for *L025N512* at $z = 2$ (right panel). Most of the metals in the colder part of the diffuse IGM have never been part of a resolved halo.

has never been part of a resolved halo. The same is true for a small fraction of the cold, dense gas. This reinforces our conclusion that the enrichment of the low-density IGM is dominated by very low-mass haloes with a possible contribution from intergalactic stars.

## 5.5 WHAT ENRICHED THE IGM AND WHEN?

We conclude by simultaneously addressing the two questions that we investigated in the two previous sections: When was the IGM enriched and by what? Fig. 5.12 shows the metal mass distribution as a function of both $z_Z$ and $m_{\rm halo}$ for model *L050N512* at $z = 0$ (left column) and for model *L025N512* at $z = 2$ (right column). The top and bottom rows show the results for metals residing in the diffuse IGM and the WHIM, respectively. Metals that are currently part of a halo were excluded (note that this corresponds to a large fraction of the metals for the case of the WHIM). As discussed before, the finite resolution of our simulations will cause us to underestimate the importance of haloes with masses near and below the minimum halo mass that we consider.

Focusing first on the diffuse IGM at $z = 0$ (the top-left panel of Fig. 5.12), we see that there is a strong anti-correlation between the enrichment redshift and the mass of the halo from which the metals were ejected. Early enrichment is more strongly dominated by lower mass galaxies. For metals residing in the diffuse IGM at $z = 2$ (top-right panel) this is also the case, but the enrichment seems to have been dominated by objects with $m_{\rm halo} \sim 10^{11}\,{\rm M}_\odot$ (which corresponds to a stellar mass $m_* \sim 10^9\,{\rm M}_\odot$), which

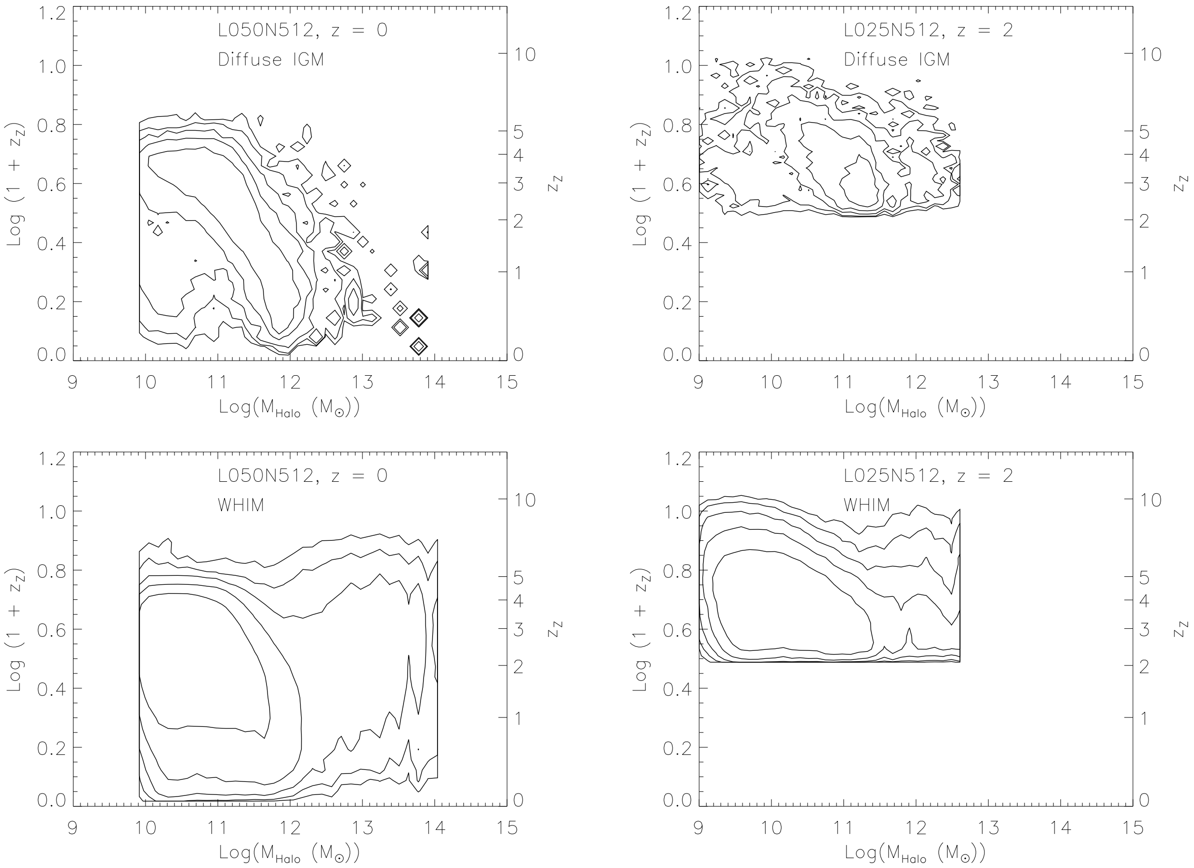

**Figure 5.12**: Distribution of metal mass as a function of $m_{\rm halo}$, the metal mass weighted mean mass of the last resolved halo that contained the metals, and $z_Z$, the metal mass weighted mean enrichment redshift. Results are shown for the diffuse IGM (top row) and the WHIM (bottom row) at $z = 0$ for *L050N512* (left column) and at $z = 2$ for *L025N512* (right column). The contours are logarithmically spaced by 0.5 dex. Metals that are currently in a halo and metals that have never been part of a resolved halo were both excluded. Older metals were typically ejected by lower mass haloes, particularly if they end up in the diffuse IGM. The WHIM was enriched by a wide range of halo masses.

is about two orders of magnitude greater than the minimum halo mass we consider. The smaller role for the lowest mass haloes at $z = 2$ is also apparent from a comparison of the solid curves in the middle panels of Fig. 5.10. It appears that the resolution of the *L025N512* simulation is nearly sufficient to model the enrichment of the diffuse IGM at $z = 2$.

We must keep in mind, however, that the diffuse IGM is not a single phase. We have already demonstrated that $z_Z$ and $m_{\rm halo}$ are strongly increasing resp. decreasing functions of the gas density (see Figs. 5.4 and 5.9). For example, for the diffuse IGM at $z = 2$ the metal mass weighted mean $\log_{10} m_{\rm halo}$ decreases from $\approx 12$ for an overdensity of $10^2$ to $\approx 10$ (i.e. too close to the resolution limit to be converged) at the mean density.

It is likely that a significant fraction of the metal mass that resides at the high-density end of the diffuse IGM at $z = 2$, which is typically ejected by more massive haloes, will have fallen back into haloes by $z = 0$ and will therefore no longer be part of the diffuse IGM. This effect can help explain why $m_{\rm halo}$ is smaller at $z = 0$ than at $z = 2$ and why there is an anti-correlation between $z_Z$ and $m_{\rm halo}$. Evolution of the halo mass function is likely also an important part of the explanation. At higher redshifts the masses of the haloes producing metals are typically lower.

The enrichment history of the WHIM (bottom row of Fig. 5.12) shows some interesting differences from that of the diffuse IGM. At $z = 0$ the anti-correlation between $z_Z$ and $m_{\rm halo}$ is much weaker. Relatively recent enrichment by low-mass haloes is more important for the WHIM. Presumably, metals that are ejected recently are shock-heated by the winds that carry them and many of them may not have had sufficient time to cool down to the temperatures of the diffuse IGM. High-mass haloes are also more important for the WHIM. This may largely be because high-mass haloes tend to be embedded in gas that is heated by gravitational accretion shocks and is therefore sufficiently hot to be considered part of the WHIM.

The results for the other OWLS models considered here are very similar (not shown), although higher mass haloes are slightly more important for *WDENS* and *AGN*, presumably because in these models feedback is more efficient in such objects.

## 5.6 CONCLUSIONS

We have used cosmological, hydrodynamical simulations that include radiative cooling, star formation, stellar evolution and supernova feedback, and, in some cases, AGN feedback, to investigate the metal enrichment history of the Universe. Specifically, we took advantage of the Lagrangian nature of our simulations to investigate when gas that ends up in a particular gas phase at redshift $z = 0$ or $z = 2$ received its metals and what the masses were of the haloes that last contained these metals.

We considered different physical models, all taken from the OWLS project, including simulations with a different implementation of supernova feedback and a model that includes AGN feedback. While there are some small differences, such as slightly higher enrichment redshifts for models with more efficient feedback in massive galaxies, the main trends are strikingly similar for all models. Although we cannot rule out that some of our conclusions may depend on the details of our method (e.g. the use of SPH), the similarities between different feedback models suggest that our conclusions are robust.

The time since the enrichment varies most strongly with the gas density. Metals in lower density gas are typically much older than metals in high-density gas, a trend that extends over ten orders of magnitude in gas density. At least half of the metals that reside in the diffuse IGM at $z = 0$ ($z = 2$) were ejected above redshift two (three).

The enrichment redshift also varies with the temperature of the gas, but this mostly reflects the fact that the typical gas density of enriched gas varies with its temperature. For gas that is dense enough to be able to cool, the time since enrichment correlates well with the cooling time. Gas with shorter cooling times received its metals more recently.

The typical mass of the haloes from which the metals residing in the IGM were ejected, increases rapidly with the gas density. At least half of the metal mass was ejected by haloes with total masses less than $10^{11}\,\mathrm{M}_\odot$, which corresponds to stellar masses smaller than $10^{9}\,\mathrm{M}_\odot$. For the low-redshift IGM the mass of the dominant IGM polluters may be substantially smaller than this because our predictions for present day low-density gas are not close to converged with respect to the numerical resolution.

The age of the metals ending up in the diffuse IGM is strongly anti-correlated with the mass of the haloes from which they were ejected. In other words, older metals were typically ejected by lower mass haloes. This anti-correlation is less strong for the hotter part of the IGM (the WHIM), for which recent enrichment by low-mass haloes is more important. While massive haloes ($> 10^{12}\,\mathrm{M}_\odot$) are unimportant for the enrichment of the diffuse IGM, they do contribute to the pollution of the warm-hot IGM at low redshift.

Our main and strongest conclusion is that metals residing in lower density gas were typically ejected earlier and by lower mass haloes. This suggests that travel-time is a limiting factor for the enrichment of the IGM, as proposed by Aguirre et al. (2001b). Metals that have been ejected recently simply have not had sufficient time to reach the low-density gas far from galaxies. The anti-correlation between metal age and halo mass would then follow because typical galaxy masses are lower at higher redshifts. Another mechanism that could explain the trends is fall back onto galaxies. If metals ejected by lower mass galaxies are less likely to fall back (e.g. Oppenheimer et al. 2009) or if they typically leave the haloes with larger velocities, then we would expect lower mass galaxies to be more important for gas that is further away. Finally, low-mass galaxies are more weakly clustered than high-mass galaxies, thus low-density gas is more accessible to low-mass galaxies.

It is not immediately obvious how one could compare this result with observations. One way would be to consider abundance ratios of elements in various phases as a function of density and redshift in an attempt to find a signature that could be searched for in high-redshift observations. However, uncertainties in the nucleosynthetic yields and the type Ia supernova rates (see chapter 3), as well as in the ionization corrections, may make such a comparison troublesome. Correlations between absorbers and the distances to different types of galaxies may also help shed light on the enrichment mechanism (e.g. Steidel et al. 2010; Chen & Mulchaey 2009; Wilman et al. 2007; Stocke et al. 2006), although is is important to keep in mind that the metals that are observed to be near a galaxy may have been injected by its lower-mass progenitors (Porciani & Madau 2005; Scannapieco 2005). In fact, our results would imply that this is likely to be the case for metals in low-density gas. We leave an analysis of abundance ratios and other observational comparisons to a future work.

The importance of low-mass galaxies is a challenge for simulations of the enrichment of the IGM, as it implies the need for high-resolution in large volumes. On the other hand, our results suggest that the low-density IGM provides us with an exciting opportunity to study the consequences of feedback in low-mass galaxies, a key but poorly understood ingredient of models of galaxy formation, and that it provides us with a fossil record of galaxy formation in the high-redshift Universe.

## ACKNOWLEDGEMENTS

We are very grateful to Volker Springel for invaluable help with the simulations and for a careful reading of the manuscript. We would also like to thank Ben Oppenheimer for a careful reading of the manuscript. The simulations presented here were run on Stella, the LOFAR Blue Gene/L system in Groningen, on the Cosmology Machine at the Institute for Computational Cosmology in Durham as part of the Virgo Consortium research programme and on Darwin in Cambridge. This work was sponsored by National Computing Facilities Foundation (NCF) for the use of supercomputer facilities, with financial support from the Netherlands Organization for Scientific Research (NWO), Marie Curie Excellence Grant MEXT-CT-2004-014112, an NWO VIDI grant, NSF grants AST-0507117 and AST-0908910, and DFG Priority Program 1177.

### REFERENCES

Agertz O., Moore B., Stadel J., Potter D., Miniati F., Read J., Mayer L., Gawryszczak A., Kravtsov A., Nordlund Å., Pearce F., Quilis V., Rudd D., Springel V., Stone J., Tasker E., Teyssier R., Wadsley J., Walder R., 2007, MNRAS, 380, 963

Aguirre A., Dow-Hygelund C., Schaye J., Theuns T., 2008, ApJ, 689, 851

Aguirre A., Hernquist L., Schaye J., Katz N., Weinberg D. H., Gardner J., 2001a, ApJ, 561, 521

Aguirre A., Hernquist L., Schaye J., Weinberg D. H., Katz N., Gardner J., 2001b, ApJ, 560, 599

Aguirre A., Schaye J., Hernquist L., Kay S., Springel V., Theuns T., 2005, ApJ, 620, L13

Aracil B., Petitjean P., Pichon C., Bergeron J., 2004, A&A, 419, 811

Booth C. M., Schaye J., 2009, MNRAS, 398, 53

Borgani S., Fabjan D., Tornatore L., Schindler S., Dolag K., Diaferio A., 2008, Space Science Reviews, 134, 379

Cen R., Ostriker J. P., 1999, ApJ, 519, L109

Chabrier G., 2003, PASP, 115, 763

Chen H., Mulchaey J. S., 2009, ApJ, 701, 1219

Choi J., Nagamine K., 2010, ArXiv e-prints

Cooksey K. L., Thom C., Prochaska J. X., Chen H., 2010, ApJ, 708, 868

Cowie L. L., Songaila A., 1998, Nature, 394, 44

Dalla Vecchia C., Schaye J., 2008, MNRAS, 387, 1431

Danforth C. W., Shull J. M., 2008, ApJ, 679, 194

Davé R., Oppenheimer B. D., 2007, MNRAS, 374, 427

Ellison S. L., Songaila A., Schaye J., Pettini M., 2000, AJ, 120, 1175

Ferland G. J., Korista K. T., Verner D. A., Ferguson J. W., Kingdon J. B., Verner E. M., 1998, PASP, 110, 761

Gnat O., Sternberg A., 2007, ApJS, 168, 213

Haardt F., Madau P., 2001, in Neumann D. M., Tran J. T. V., eds, Clusters of Galaxies and the High Redshift Universe Observed in X-rays Modelling the UV/X-ray cosmic background with CUBA

Jarosik N., Bennett C. L., Dunkley J., et al., 2010, ArXiv e-prints

Kawata D., Rauch M., 2007, ApJ, 663, 38

Kobayashi C., Springel V., White S. D. M., 2007, MNRAS, 376, 1465

Madau P., Ferrara A., Rees M. J., 2001, ApJ, 555, 92

Marigo P., 2001, A&A, 370, 194

McCarthy I. G., Schaye J., Ponman T. J., et al., 2009, arXiv:0911.2641

Mitchell N. L., McCarthy I. G., Bower R. G., Theuns T., Crain R. A., 2009, MNRAS, 395, 180

Oppenheimer B. D., Davé R., 2006, MNRAS, 373, 1265

Oppenheimer B. D., Davé R., 2008, MNRAS, 387, 577

Oppenheimer B. D., Davé R., 2009, MNRAS, 395, 1875

Oppenheimer B. D., Davé R., Kereš D., Fardal M., Katz N., Kollmeier J. A., Weinberg D. H., 2009, ArXiv e-prints

Pieri M. M., Frank S., Mathur S., Weinberg D. H., York D. G., Oppenheimer B. D., 2009, ArXiv:0908.2001

Porciani C., Madau P., 2005, ApJ, 625, L43

Portinari L., Chiosi C., Bressan A., 1998, A&A, 334, 505

Scannapieco E., 2005, ApJ, 624, L1

Scannapieco E., Pichon C., Aracil B., Petitjean P., Thacker R. J., Pogosyan D., Bergeron J., Couchman H. M. P., 2006, MNRAS, 365, 615

Schaye J., 2004, ApJ, 609, 667

Schaye J., Aguirre A., Kim T.-S., Theuns T., Rauch M., Sargent W. L. W., 2003, ApJ, 596, 768

Schaye J., Carswell R. F., Kim T., 2007, MNRAS, 379, 1169

Schaye J., Dalla Vecchia C., 2008, MNRAS, 383, 1210

Schaye J., Dalla Vecchia C., Booth C. M., et al., 2010, MNRAS, 402, 1536

Schaye J., Rauch M., Sargent W. L. W., Kim T.-S., 2000, ApJ, 541, L1

Shen S., Wadsley J., Hayfield T., Ellens N., 2010, MNRAS, 401, 727

Sheth R. K., Mo H. J., Tormen G., 2001, MNRAS, 323, 1

Simcoe R. A., Sargent W. L. W., Rauch M., 2004, ApJ, 606, 92

Sommer-Larsen J., Fynbo J. P. U., 2008, MNRAS, 385, 3

Springel V., 2005, MNRAS, 364, 1105

Steidel C. C., Erb D. K., Shapley A. E., Pettini M., Reddy N. A., Bogosavljević M., Rudie G. C., Rakic O., 2010, ArXiv e-prints

Stocke J. T., Penton S. V., Danforth C. W., Shull J. M., Tumlinson J., McLin K. M., 2006, ApJ, 641, 217

Sutherland R. S., Dopita M. A., 1993, ApJS, 88, 253

Theuns T., Viel M., Kay S., Schaye J., Carswell R. F., Tzanavaris P., 2002, ApJ, 578, L5

Thielemann F.-K., Argast D., Brachwitz F., et al., 2003, in From Twilight to Highlight: The Physics of Supernovae Supernova Nucleosynthesis and Galactic Evolution. pp 331–+

Tornatore L., Borgani S., Matteucci F., Recchi S., Tozzi P., 2004, MNRAS, 349, L19

Tornatore L., Borgani S., Viel M., Springel V., 2010, MNRAS, 402, 1911

Wilman R. J., Morris S. L., Jannuzi B. T., Davé R., Shone A. M., 2007, MNRAS, 375, 735

# Bibliography

## REFEREED PAPERS

*Chemical enrichment in cosmological, smoothed particle hydrodynamics simulations*
**Wiersma, R. P. C.**, Schaye, J., Theuns, T., Dalla Vecchia, C., Tornatore, L.
2009, Monthly Notices of the Royal Astronomical Society, Volume 399, pp. 574–600

*The effect of photoionization on the cooling rates of enriched, astrophysical plasmas*
**Wiersma, R. P. C.**, Schaye, J., Smith, B. D.
2009, Monthly Notices of the Royal Astronomical Society, Volume 393, pp. 99–107

*The Effect of Pre-Main-Sequence Stars on Star Cluster Dynamics*
**Wiersma, R.**, Sills, A., Portegies Zwart, S.
2006, The Astrophysical Journal, Volume 637, pp. 838–849

## CONFERENCE PROCEEDINGS

*Observations of Metals in the Intra-Cluster Medium*
Werner, N.; Durret, F.; Ohashi, T.; Schindler, S.; **Wiersma, R. P. C.**
2008, Space Science Reviews, Volume 134, pp. 337–362

# Het simuleren van de Chemische Verrijking van het Intergalactisch Medium

Onze planeet draait om een enkele ster, de Zon, een van vele in ons Melkwegstelsel, die zelf een van de miljarden sterrenstelsels is die deel uitmaken van het heelal. Vroeg in de twintigste eeuw begonnen astronomen buiten de grenzen van ons eigen melkwegstelsel te kijken, op zoek naar aanwijzingen over de oorsprong van het heelal. Na de ontdekking van een schijnbaar oneindige uitgestrektheid van sterrenstelsels realiseerden astronomen zich dat er natuurkunde is die werkt op schalen veel groter dan eerder gedacht. Tegenwoordig is kosmologie een ver ontwikkeld gebied met nauwkeurige voorspellingen en observationele tests.

Het zeer vroege heelal bestaat vermoedelijk uit slechts waterstof en helium, met enkele sporen van lithium en beryllium. In de loop van de tijd produceren sterren zwaardere elementen (hierna ”metalen”genoemd), die de omliggende ruimte met elementen zwaarder dan helium ‘vervuilen’. Een paar specifieke metalen werden gekozen om te condenseren rond een schijnbaar onbeduidende ster in een planeet die we nu kennen als ‘Aarde’.

Naast deze misschien romantische redenen is het van cruciaal belang voor ons begrip van het heelal om te kunnen verklaren hoe metalen gemaakt en vervoerd worden en wat hun effecten zijn op de verdere structuurvorming. Niet alleen fungeren metalen als een ’fossil record’ van de stervormingsgeschiedenis van het heelal, ze kunnen ons ook vertellen hoe gas ontsnapt uit stervormingsgebieden. Metalen doen echter veel meer dan fungeren als een diagnostiek. Ze dienen ter versnelling van de afkoeling van gaswolken, een effect dat de vorming van sterrenstelsels drastisch verandert. Zonder een solide begrip van het gedrag van metalen is ons vermogen om de evolutie van het heelal te verklaren onvolledig.

## De bronnen van metalen

Met uitzondering van de witte dwergen ondergaat elke ster in het heelal kernfusie. Het proces van het creëren van zwaardere elementen van lichtere elemeneten wordt nucleosynthese genoemd. Dit proces gebeurt diep in het binnenste van een ster, dus er moet een mechanisme zijn om metalen uit een ster te krijgen.

Voor alle sterren is er een stellaire ‘wind’, die massa uit de ster drijft via stralingsdruk. Omdat massieve sterren meer licht produceren, neemt dit effect toe met de massa van de ster. Dit kan een belangrijk mechanisme zijn voor het vervoer van metalen uit sterren.

Tegen het einde van hun levensduur ondergaan sterren met een massa van meer dan 8 keer die van de zon een supernova explosie. Tijdens een dergelijke explosie wordt niet alleen een groot deel van de inhoud van de ster uitgeworpen maar treden ook de condities op die ideaal zijn voor snelle nucleosynthese. Het is tijdens dit proces dat de meeste van de elementen zwaarder dan ijzer vormen. Deze vorm van supernovae, die ‘kern-ineenstorting’ wordt genoemd, is verantwoordelijk voor het merendeel van de metalen die worden geproduceerd in de vroege stadia van een stellair systeem. Van dit type supernova is bekend dat het de belangrijkste producent van elementen zoals zuurstof, neon, silicium en zwavel is.

Deze supernova explosies genereren ook een grote hoeveelheid energie, die vrijkomt in het interstellaire medium (ISM). Deze energie kan bijdragen aan de turbulentie van het ISM of resulteren in de uitstroom van gas uit het sterrenstelsel. Omdat sterren vaak gevormd worden in een uitbarsting, kan het effect van de explosies worden vergroot indien er meerder supernovae in harmonie afgaan.

Voor de sterren met een massa van minder dan 8 maal de massa van de zon is er geen explosief eind aan het leven. Deze sterren zullen in plaats daarvan een periode ervaren van significant massaverlies aan het eind van hun leven. Hierin blazen de buitenlagen op en deze worden uiteindelijk afgestoten. De uitwerpselen zijn samengesteld uit waterstof en helium, verrijkt met metalen, voornamelijk koolstof en stikstof.

Een andere methode van metaalverrijking is afkomstig van ‘type Ia supernovae’. Dit zijn explosies die zich voordoen wanneer twee lage massa sterren, die om elkaar heen draaien oud worden en samensmelten of massa met elkaar beginnen te delen. Op een bepaald punt wordt de activiteit te sterk het systeem wordt ontbonden in een explosie. Omdat de omstandigheden rond de explosie heel anders zijn dan de explosies van hoge massa sterren, zijn ook de nucleosynthetische producten verschillend. In deze explosies ontstaat een groot deel van het ijzer en nikkel.

Sterren die hun leven eindigen in een van de bovenstaande twee processen leven lang, maar niet allemaal even lang, zodat astronomen de verhouding van bepaalde elementen als “klokken” kunnen gebruiken, die de leeftijd van een groep sterren aan kan geven. Metalliciteit (dat is de massa in metalen ten opzichte van de totale massa) moet met de tijd oplopen, omdat opeenvolgende generaties sterren het interstellaire medium (ISM) zullen verrijken. De hoeveelheid zuurstof ten opzichte van ijzer, silicium t.o.v. koolstof, en stikstof t.o.v. neon zijn allemaal voorbeelden van chemische verhoudingen die moeten afnemen met de tijd.

## De vorming van sterrenstelsels

Omdat sterren zijn gegroepeerd in sterrenstelsels, kan men op een kosmische schaal sterrenstelsels zien als fabrieken, die het intergalactische medium met metalen vervuilen. Als zodanig is het begrip van de vorming en evolutie van sterrenstelsels essentieel om te begrijpen hoe de metalen worden verdeeld en hoe die distributie tot stand kwam.

Sterrenstelsels vormen voornamelijk op twee manieren, door het geleidelijk aanvoeren van materiaal aan een oorspronkelijke concentratie van massa en door de samensmeltingen van kleinere systemen in grotere. In werkelijkheid vormt dit een continuüm van dien aard dat het moeilijk kan worden onderscheiden wat geleidelijk aanvoeren en wat samensmelten is. Terwijl botsingsvrije materie (dat willen zeggen dat er geen gasdruk is, samengesteld uit sterren en de zogenaamde 'donkere materie') weinig problemen heeft een gebonden systeem in te tuimelen, zal gas aan interne energie winnen die de aanwas van massa via gasdruk kan ontkrachten. Dergelijke interne energie kan echter worden uitgestraald. Dit proces staat bekend als afkoeling.

Afkoeling kan optreden op sub-atomair, atomair en moleculair niveau. Vrije elektronen kunnen verstrooien aan passerende fotonen (lichtdeeltjes), waarbij ze wat energie aan de fotonen mee kunnen geven. Ze kunnen ook afkoelen via bremsstrahlung, wat betekent dat ze energie uitstralen tijdens het passeren van een ander geladen deeltje. Atomen kunnen koelen door van een aangeslagen elektronenconfiguratie naar een energetisch lagere toestand te gaan. Dit is de reden waarom metalen zo belangrijk kunnen zijn. Omdat er veel meer configuraties bestaan in metaalatomen (omdat zij meer elektronen hebben), koelen zij ook veel efficiënter. Dit effect kan koeling tot een orde van grootte (een factor tien) laten toenemen. Moleculen kunnen ook efficiënte koelers zijn, bij temperaturen die laag zijn in vergelijking met het intergalactische medium (IGM). Deze temperaturen zijn typisch voor bepaalde fasen van het ISM en dat gas is dus gevoelig voor moleculaire koelers. Moleculen zoals CO kunnen dan overheersen en dit is een andere reden waarom metalen zo belangrijk zijn. Dit proefschrift behandelt schalen veel groter dan die waarop stervorming plaatsvindt, dus laten we de details van moleculaire koelers achter ons en richten we ons op wat er gebeurt net buiten sterrenstelsels en proto-stelsels.

Gas bij voldoende lage dichtheden zal geen sterren vormen. Na reïonisatie (dat is nadat het IGM werd geïoniseerd), heeft de straling van de sterrenstelsels en quasars in het heelal invloed op de manier waarop een gaswolk afkoelt. Deze achtergrondstraling zal niet alleen het gas opwarmen, maar het zal ook van invloed zijn op de ionisatiebalans van de wolk: het verandert de elektronische configuratie van de atomen aanzienlijk.

In figuur 7.1 we zien hoe de afkoelingsfunctie afhangt van de temperatuur. De doorgetrokken lijn laat zien hoe deze functie zich gedraagt als het gas door fotonen is geïoniseerd, wat heel anders is dan wanneer het gas alleen wordt geïoniseerd door botsingen (stippellijn). Vaak nemen berekeningen van de kosmische afkoeling alleen het laatste geval mee, wat leidt tot veel hogere waarden voor de afkoelsnelheid. Aan de andere kant negeren andere simulaties vaak de bijdrage van metalen, die kan worden gezien door vergelijking van de streep-stippellijn met de stippellijn. Het is duidelijk dat beide effecten moeten worden beschouwd.

Aangezien de productie van metalen de manier waarop sterrenstelsels vormen beïnvloedt en dus ook de manier waarop verder metalen worden geproduceerd, staat de productie van elementen bekend als een feedback mechanisme. De effectiviteit van deze feedback betekent dat elke gedetailleerd model van galactische systemen metalen

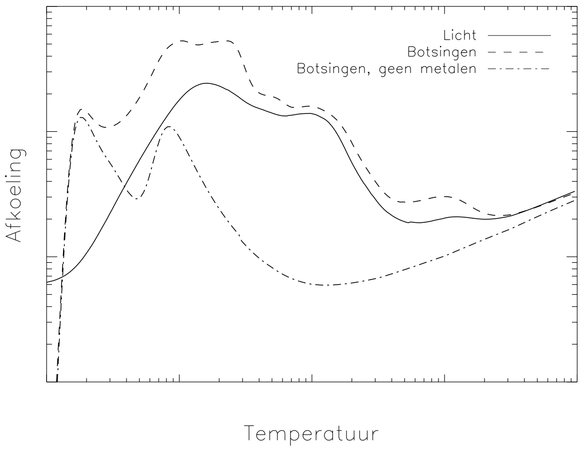

**Figuur 7.1**: Afkoelsnelheden voor gas dat afkoelt terwijl geoniseerd door fotonen (doorgetrokken lijn), geoniseerd door botsingen (stippellijn) en geoniseerd door botsingen zonder metalen dat metalen worden meegenomen (streepstippellijn).

en hun invloed zo nauwkeurig mogelijk zullen moeten meenemen.

## SIMULATIES

Om tot een volledig begrip van de vorming en evolutie van sterrenstelsels, zoals ook de verdeling van kosmische metalen, te komen is het vaak wenselijk om computersimulaties uit te voeren. Dergelijke simulaties kunnen dienen om waarnemingen te interpreteren en hebben duidelijke voordelen ten opzichte van andere theoretische methoden. Simulaties laten je terugkijken in de tijd zonder de beperkingen die inherent zijn aan waarnemingen (niet dat simulaties zelf zonder beperkingen zijn).

Bij het uitvoeren van een simulatie van het heelal, moet men rekening houden met twee soorten materie, donkere materie en baryonische materie. De simulaties in dit proefschrift maken gebruik van de populaire hydrodynamica-code GADGET. Met deze code wordt de donkere materie gemodelleerd als een botsingsvrije vloeistof die alleen de zwaartekracht ervaart. De baryonen kunnen verder onderverdeeld worden in gas en sterren. Het gas wordt gediscretiseerd tot deeltjes met behulp van de 'uitgesmeerd deeltje hydrodynamica' ('Smoothed Particle Hydrodynamics' in het Engels - SPH) methode. Elk deeltje vertegenwoordigt een vloeistofelement die zijn dichtheid "uitsmeert" over haar naburige deeltjes terwijl ze ook druk uitoefent op hen. Deze deeltjes worden ook meegenomen in de berekening van de zwaartekracht. Sterren worden gemaakt van gas op basis van enkele criteria, waarna deze baryonische deeltjes ook botsingsvrij worden en ze dus geen gasdruk meer uitoefenen op hun omgeving.

Door computationele beperkingen moeten wij in plaats van de vorming van individuele sterren hele populaties van sterren tegelijk vormen. We moeten dus aannemen dat de sterren in zo'n populatie allemaal worden geboren op hetzelfde moment. Op deze manier, uitgaande van een initiële verdeling van stermassa's, kunnen we het uitrekenen hoeveel metalen er worden uitgestoten door zowel hoge als lage massa sterren.

Natuurlijk moeten we voor deze berekening vertrouwen op berekeningen van het verlies van metalen uit deze verschillende sterren door eerdere onderzoekers. Niet alleen moeten we zorgvuldig een passende reeks van stellaire 'opbrengsten' (de hoeveelheid van verschillende metalen die de sterren produceren) kiezen, maar wij moeten ook schattingen maken van de distributie van stellaire geboortemassa's, de levensduur van sterren, en het tempo waarin type Ia supernovae exploderen. De onzekerheden van al deze ingredinten resulteren in grote onzekerheden in de relatieve abundanties van de elementen.

## HET OWLS PROJECT

Om simulaties beter te kunnen interpreteren, werd het overweldigend grote simulaties ('OverWhelming Large Simulations' in het Engels - OWLS) project bedacht. Het idee achter dit project is het uitvoeren van een grote verzameling van simulaties, met in elke simulatie een iets andere fysisch model of numerieke parameter (dat wil zeggen, de grootte van de simulatie of de typische deeltjesmassa). In vergelijking met eerdere inspanningen zullen de meeste simulaties in een groot volume en met hoge resolutie uitgevoerd worden. Dus zowel de omvang van het project als de individuele simulaties zijn groot.

Simulaties van deze soort hebben een aantal 'sub-grid' recepten om fysische processen te modelleren, waarvoor de resolutie van de simulatie nog niet goed genoeg is. Inzicht in de beperkingen en onzekerheden in dergelijke recepten is essentieel om de vorming van sterrenstelsels en de verdeling van metalen te begrijpen. De recepten die zijn opgenomen in onze simulatie (we hebben elke module gevarieerd op een bepaalde manier) zijn:

- Gas afkoeling
- Stervorming
- Verdeling van massa's van sterren bij de geboorte ('Initial Mass Function' in het Engels - IMF)
- Stellaire feedback, en
- Actieve galactische kernen ('Active Galactic Nuclei' in het Engels - AGN).

Figuur 7.2 toont drie opeenvolgende zoom-ins op een doorsnede door een van onze simulaties. In het linker paneel kan men de grote schaal structuur van de kosmos zien, terwijl het rechter paneel lijkt op een sterrenstelsel. Het dynamisch bereik is zeer groot en vereist een zorgvuldige 'boekhouding' van de fysische processen.

## DIT PROEFSCHRIFT

Dit proefschrift is sterk gebaseerd op het OWLS project. De eerste helft beschrijft een aantal van de natuurkundige modellen die in het referentie-model van het project zijn

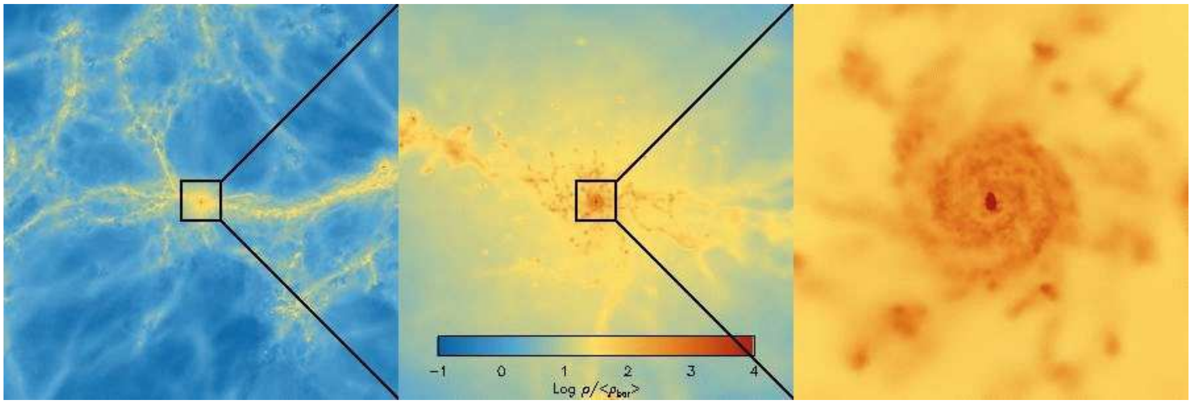

**Figuur 7.2**: Opeenvolgende zoom-ins op een doorsnede door een van onze simulaties. De kleurenschaal geeft gasdichtheid.

gegaan, terwijl de tweede helft zich meer richt op de analyse van de simulaties.

## Hoofdstuk 2

Hoofdstuk 2 bespreekt hoe metalen en een fotooniserende achtergrond kunnen de afkoeling door straling van kosmisch gas kunnen beïnvloeden. Dit wordt gepresenteerd in de kader van gas met eigenschappen die typisch zijn (in dichtheid, temperatuur, en ioniserende achtergrond) voor het intergalactische medium en proto-stelsels. Metaalverrijking dient meestal ter versnelling van het afkoelen (vanwege de toename van het aantal gebonden elektronen) en ionisatie dient typisch ter verlaging van de koelsnelheid (als gevolg van het verminderd aantal gebonden elektronen beschikbaar en via de opwarming door de fotonen). Hoewel beide effecten eerder zijn besproken in isolement, combineren we de twee en berekenen we de relatieve bijdrage van beide effecten voor een reeks dichtheden en temperaturen. We vinden dat het verschil van de vorige berekeningen tot ongeveer een factor tien kan zijn. Dit effect treedt op, op een niet-triviale manier, zodat zelf-consistente berekeningen noodzakelijk zijn voor een nauwkeurig afkoelsnelheid.

We laten zien hoe de berekening van de bijdragen van elk element aan de afkoeling uitgevoerd moet worden, zodat we de veronderstelling dat de relatieve abundanties van de elementen in het gas universeel is kunnen laten vallen. Zelfs in goed gemengd gas, kunnen relatieve abundanties veranderen met een factor van een paar als het wordt verrijkt door verschillende processen. Dit is zeer belangrijk omdat de individuele pieken van de koeling curve zeer gevoelig zijn voor abundanties en ionisatiegraad. De berekeningen van de afkoeling, gepresenteerd in dit hoofdstuk, worden gebruikt in de simulaties gepresenteerd in de rest van dit proefschrift.

## Hoofdstuk 3

In hoofdstuk 3 beschrijven we de chemodynamica zoals die in onze simulaties zit. Wij bekijken elk ingrediënt op zijn beurt, om de onzekerheden te illustreren. De onzekerheden in de stellaire opbrengsten, en met name in de supernova type Ia snelheid, bedragen verschillen van factoren van een paar in de hoeveelheid metaalproductie. Vervolgens bekijken we de verspreiding van metalen in het referentie model van het Overweldigend Grote Simulaties (OWLS) project, die onze methode gebruikt. We vinden dat het veranderen van de definitie van de metalliciteit in de simulaties kan leiden tot een factor anderhalf verschil in stellaire massa in het huidige heelal, een illustratie van de numerieke moeilijkheden die inherent zijn aan een dergelijke berekening.

De metalen in onze simulaties zijn relatief gelijkmatig verdeeld tussen kosmische gasfasen ongeveer 10 miljard jaar geleden en ze volgen niet de relatieve verdelingen van baryonen, die zich veelal ofwel in een schok-verwarmde, warme tot hete fase rondom sterrenstelsels, ofwel in een koude, diffuse fase bevinden. Tegenwoordig zijn de meeste metalen opgesloten in sterren.

## Hoofdstuk 4

De kracht van het OWLS project wordt helemaal duidelijk in hoofdstuk 4. Hier vergelijken we de verschillende fysische modellen die gebruikt worden in de verschillende simulaties in het kader van de kosmische metaaldistributie. We onderzoeken de werking van koeling, galactische wind modellen, stellaire IMF en feedback van AGN in detail.

We vinden dat een sterke feedback nodig is om efficiënt metalen uit halo’s van alle massa’s te verwijderen. Dit kan gebeuren door middel van een bijzonder sterk wind model, een IMF met extra veel zware sterren in gebieden van hoge druk, of feedback van AGN. In overeenstemming met eerder werk, vinden we dat de metalliciteit van het Warm-Hete Intergalactisch Medium (WHIM) - waar zich een groot deel van de baryonen in het lokale heelal bevinden - ongeveer $10\%$ is van wat is waargenomen in de zon, en dat dit weinig evolutie ondergaat. Tussen alle modellen varieert deze waarde met minder dan een factor drie. De enige uitzondering zijn de modellen die geen feedback in de vorm van stellaire winden en supernovae meenemen.

De metalliciteit van de gebieden in het heelal met de laagste dichtheid – het diffuse IGM – is zeer gevoelig voor de precieze parameters en de uitvoering van de feedback. Deze afhankelijkheid kan dus nuttig zijn bij het vaststellen van de geldigheid van de verschillende modellen.

We vinden in alle modellen dat de gemiddelde stellaire metalliciteit van het heelal vrij hoog is op hoge roodverschuiving (ver weg en vroeg in het heelal).

## Hoofdstuk 5

Hoofdstuk 5 gaat in op de oorsprong van de metalen die we vandaag de dag om ons heen zien. We bouwen een verrijkingsgeschiedenis voor de verschillende fasen van het gas in het referentiemodel van de hoogste resolutie. Zoals verwacht vinden we een sterke afhankelijkheid van dichtheid, waarbij gas van hogere dichtheid later wordt verrijkt. Wij bekijken niet alleen *wanneer* dit gas is verrijkt, maar ook door *wat*. Software die sterrenstelsels zoekt wordt gebruikt om de karakteristieke massa van sterrenstelsels te bepalen die gas van een bepaalde dichtheid en temperatuur verrijkt. Ook hier vinden we een sterke dichtheidsgradiënt. Lage massa sterrenstelsels verrijken het lage dichtheid IGM terwijl hoge massa sterrenstelsels het hete gas van gemiddelde dichtheid verrijken. Dit is onafhankelijk van het feedback-model. Het koude, diffuse, lage dichtheid IGM bevat zeer weinig metalen, de metalen die er zijn, zijn voornamelijk afkomstig uit intergalactische sterren. Het feit dat veel van de IGM verrijking wordt aangedreven door de laagste massa sterrenstelsels die we kunnen simuleren, suggereert dat de karakteristieke massa van sterrenstelsels waardoor het IGM wordt verrijkt, afhankelijk kan zijn van de resolutie.